Laboratoire Kastler Brossel, Université Pierre et Marie Curie,

National Nanotechnology Laboratory, Università del Salento

Phd thesis to obtain the title of Docteur de l'université Pierre et Marie Curie

and the title of Dottore in scienze e tecnologie multidisciplinari

Single Photon Sources Based on Colloidal Nanocrystals and Two Photon Polariton Laser

Ferruccio Pisanello

defended on July 11, 2011

Jury :

Jean-François Roch, reviewer

Gerd Leuchs, reviewer

Pascale Senellart, examinator

Agnès Maître, examinator

Luigi Carbone, examinator

Alberto Bramati, Ph. D. advisor

Massimo De Vittorio, Ph. D. advisor

Acknowledgements

A Ph. D. is certainly not a solo effort. Of course, during these years I acquired strong experimental skills and knowledge, but such experience allows you to meet a variety of people in academic and non-academic settings, that have directly and indirectly contributed to this thesis.

First, I thank Prof. Alberto Bramati and Prof. Massimo De Vittorio for their patience and guidance. They have given me an amazing amount of academic freedom, allowing me to pursue a variety of ideas. They were always present during these years and they are enthusiastic and motivating supervisors. It does not surprise me that I continue to learn from them as time goes on.

I thank professors Jean-François Roch, Gerd Leuchs, Pascale Senellart, Agnès Maître and Luigi Carbone for having accepted to be part of the jury of my thesis and for their careful reading of the text. Their positive comments and remarks were very helpful for producing the final version of the manuscript. I thank also Paul Indelicato, director of the Laboratorire Kastler Brossel, for having welcomed me in this fantastic laboratory.

A special thank must be spent for Alberto Amo and Luigi Martiradonna. They have the merit of setting my scientific aspirations very high, and showing me every day what it takes to become a truly accomplished researcher. Working with them has been challenging, fun, and rewarding. The enthusiasm of Alberto and Gigi in doing research is at the same time stimulating and encouraging, and their optimism has been essential through my graduate student experience and my life outside the lab. As well as them, Antonio Qualtieri and Tiziana Stomeo played a very important role during these years. Their help and their expertise were essential through the ups and downs of this work, and the scientific knowledge I absorbed from them is incredible. During this Ph. D. I've had the great pleasure to work with Piernicola Spinicelli. When I started in the group, I was several times obsessed about the wrong details, but Piernicola had every time the good answers to my questions, pushing me toward the solutions. I thank also Jean-Pierre Hermier, his suggestions on the physics of colloidal nanocrystals have been essential to obtain several results presented in this thesis. I thank Elisabeth Giacobino for her comments and thoughts during these years and for the help in the redaction of this manuscript. Her enthusiasm, even during the times when everything had

mischievously decided not to work as we intended, has been very much appreciated.

I'm grateful to Pietro Lombardi, who helped me a lot during my first year in Paris, also in furnishing my flat. As well as Pietro, also Riccardo Messina helped in setting up my house, but I thank him also for the help in choosing the most important purchase of my life. I thank Giuseppe Patera, in particular because during our long discussions on physics he was able to stimulate my mind toward new ideas and new research fields. A special thought goes to Chiara Molinelli: with her we shared the last months before the Ph. D. defense, through optimism, depression and bureaucracy.

I've had great luck to work with a very talented and motivated young researcher for almost the whole Ph. D., Godefroy Leménager. He greatly challenged me with his sharp thinking and richness of research ideas. We worked together days and nights, aligning mirrors and lasers, moving labs, performing measurements and, most important, drinking coffee!

I thank the various members of the two labs that I had the pleasure to interact with over the years, for their help and for their good moods: Virginia, Lucile, Rym, Roman, Vera, Romain, Daria, Michael, Oxana, Panayotis, Pu, Claire, Etienne, Stefano, Marco, Vincenzo and Pascal in Paris, and Benedetta, Maria, Alessandro, Alessandra, Gianmichele, Serena, Viviana, Ilaria, Valentina, Leo, Fabrizio, Loris, Valeria, Peppone, Virgilio, Piero, Vittorianna, Teresa, Paolo, Gianmichele, Tonio, Stefatia, Betta, Elisabetta, Adriana Passaseo, Adriana, Iolena, Marco Grande, Marco Esposito, Ilaria Ingrosso and Cristian in Lecce.

I thank my parents. From when I was a child, they inculcate in me the right approach to life, and if I today I had the possibility to reach a Ph. D. degree, a big part of the work is to be ascribed to them. When the time came to choose a career, they advised me to choose the field I liked the most. Their support has been unwavering over the years, and I thank them for being by my side in every moments of my life.

I thank my brother, Marco. The job he did for me during my stay in Paris has been amazing, proofreading my papers and polishing my presentations. He pushed me forward in any difficulty that I faced in my research and he was always proud of my every little success.

Finally, I would like to express my deep gratitude to Pamela. No words would be able to describe what she did for me, without her I would not be what I am today. This thesis is dedicated to her.

Abstract: When scaled down up to nanometer size, semiconductors can exhibit quantum confinement effects for both electrons and photons. One interesting feature of nano-sized materials is the strong size dependence of their optical properties, that allows to master classical and non-classical light generation.

This work concerns the development and the characterization of new sources for the generation of classical and non-classical light states with isolated and coupled confined systems for photons and electrons. In particular: (i) a new type of semiconductor colloidal nanocrystals (NCs) is studied with the goal to obtain an efficient single photon generation at room temperature in the visible spectral range and (ii) NCs coupling with photonic crystals nanocavities has been obtained by using several methods; finally, (iii) in the last part of the manuscript the development of a two-photons excitation technique for microcavity polaritons is discussed with the final goal to obtain non-classical light generation.

The first part of the manuscript is focused on the emission properties of a particular type of colloidal nanocrystals, called dot-in-rod (DR), in which a spherical cadmium selenide (CdSe) core is surrounded by a rod-like cadmium sulfide (CdS) shell. By virtue of their electronic properties, colloidal nanocrystals can emit single photons at room temperature. However the application of colloidal nanocrystals has been so far limited by two phenomena: the blinking of their photoluminescence and a non-polarized emission. The streaky point of dot-in-rods is that their emission properties are strongly dependent on their geometrical parameters. Here we show that by carefully choosing the diameter of the core, as well as the thickness and the length of the shell, the blinking behavior can be strongly reduced and a high degree of linear polarization of the emitted photons obtained.

The second part of the thesis is devoted to the development of a silicon nitride photonic crystals cavity platform for applications in the visible spectral range. The weak coupling of these nanocavities with dot-in-rods has been achieved by using several deposition methods and we obtained a modification of the spontaneous emission by means of the *Purcell effect*. The possibility to reach the strong coupling regime by using this technology is also discussed from the theoretical point of view.

The last part of the work studies a semiconductor system in which the strong coupling between quantum well excitons and a cavity mode gives rise to quasi-particles called *polari-*

tons. When polaritons experience a sufficiently strong three-dimensional confinement, they can exhibit a quantum blockade phenomenon. Indeed, in the case of ultra small cavity modal volume just one polariton at time can exist in the structure, while the injection of other polaritons is forbidden by virtue of strong polariton-polariton repulsive interactions. With the purpose to reach this operation regime, an original excitation technique based on a resonant two-photon absorption (TPA) process has been developed. Moreover, TPA has been exploited to resonantly inject high polariton density in pillar microcavities, reaching an emission regime called *two-photon polariton laser*.

Key words: nanocrystal, single photon, photonic crystal, nanocavity, nanolaser, polariton laser, two-photon.

Résumé : Ce travail est consacré à l'étude de plusieurs types de systèmes confinés pour les électrons et/ou les photons. En particulier : (i) un nouveau type de nanocristaux semiconducteurs est étudié pour obtenir une source efficace de photons uniques à température ambiante dans le domaine spectral du visible ; (ii) leur couplage avec des cavités à cristaux photoniques en nitrure de silicium est obtenu par plusieurs techniques de déposition. (iii) Enfin, le développement d'une technique d'excitation à deux photons pour les polaritons dans les microcavité semiconductrices est décrit dans la dernière partie du travail de thèse.

La première partie du manuscrit étudie les propriétés d'émission d'un type particulier de nanocristaux semiconducteurs, appelé dots-in-rod, dans lesquels un cœur de séléniure de cadmium (CdSe) est entouré par une coquille en sulfure de cadmium (CdS) de forme allongée. Depuis les année 2000, il est bien connu que les nanocristaux semiconducteurs sont des sources de photons uniques à température ambiante. Cependant, les applications des nanocristaux sont affectées entre autre par deux caractéristiques de leur photoluminescence: le scintillement et l'émission non polarisée. Nous avons montré qu'il est possible de modifier l'émission des dots-in-rod en agissant sur leurs paramètres géométriques, c'est-à-dire le diamètre du cœur ainsi que l'épaisseur et la longueur de la coquille, aboutissant à la suppression du scintillement et à un degré élevé de polarisation linéaire des photons émis.

Dans la deuxième partie, la thèse démontre la réalisation des cavités à cristaux photoniques en nitrure de silicium (Si_3N_4) pour le domaine spectral du visible. Le couplage de ces cavités

avec des dot-in-rods a été étudié en régime de couplage faible et nous avons obtenu une modification de l'émission spontanée par *effet Purcell*. La possibilité d'obtenir le régime de couplage fort dans ce système est aussi discutée du point de vue théorique.

Dans la dernière partie du manuscrit nous avons étudié des systèmes semiconducteurs tels que les microcavités et le micropiliers dans lesquels le régime de couplage fort exciton-photon donne naissance aux polaritons. Dans le cas de polaritons confinés, les interactions répulsives entre polaritons peuvent porter à un régime appelé *polariton quantum blockade*, dans le quel un seul polariton peut être excité dans la structure, ce régime est très prometteur pour la réalisation de sources à photons uniques basées sur les polaritons en cavité. Dans ce travail, nous développons une technique original et flexible basée sur une excitation résonante à deux photons pour attendre le *polariton quantum blockade*. Enfin, un nouveau régime d'émission appelé *two-photon polariton laser* est étudié toujours à la technique d'excitation résonante à deux photons.

Mots clés : nanocristaux, semiconducteurs, photons uniques, polariton, excitation à deux photons, cristaux photoniques

Prefazione: Questo lavoro ha come oggetto lo studio di vari tipi di sistemi confinati per elettroni e/o fotoni. In particolare: (i) un nuovo tipo di nanocristalli semiconduttori è stato ingegnerizzato al fine di ottenere la generazione efficiente di un flusso di singoli fotoni a temperatura ambiente nel dominio spettrale del visibile; (ii) tali nanocristalli sono poi stati accoppiati con cavità a cristallo fotonico utilizzando varie tecniche di deposizione al fine di controllarne le proprietà di emissione; (iii) nella parte conclusiva del lavoro è descritto lo sviluppo di una tecnica di eccitazione a due fotoni di polaritoni in microcavità.

Nella prima parte della tesi è presentato lo studio spettroscopico di una tipologia di nanocristalli colloidali chiamati dot-in-rod, nei quali un *core* di selenurio di cadmio (CdSe) è incapsulato in una shell di solfuro di cadmio (CdS) di forma allungata. Dai primi anni 2000 è ben noto che, grazie alle loro proprietà elettroniche, i nanocristalli colloidali sono sorgenti a singolo fotone a temperatura ambiente. Tuttavia, l'applicazione dei nanocristalli colloidali come sorgenti a singolo fotone è stata finora limitata da due problemi: la fotoluminescenza intermittente, chiamata *"blinking"* e l'emissione non polarizzata. La particolarità dei dots-

in-rod consiste nella forte influenza dalle loro caratteristiche geometriche sulle loro proprietà ottiche: questo lavoro dimostra che, scegliendo opportunamente il diametro del core, lo spessore della shell e la sua lunghezza, è possibile ottenere un'emissione fortemente polarizzata e una drastica riduzione del *blinking*.

La seconda parte del lavoro concerne lo sviluppo di una piattaforma tecnologica per la realizzazione di cavità a cristallo fotonico in nitruro di silicio (Si_3N_4) risonanti nello spettro del visibile. L'accoppiamento di queste cavità con i dot-in-rod è stato studiato nel regime di accoppiamento debole (*weak coupling*), ottenendo una modifica dell'emissione spontanea delle nanoparticelle grazie al così detto *effetto Purcell*, mentre la possibilità di ottenere il regime di accoppiamento forte è discussa dal punto di vista teorico.

La parte finale della tesi si occupa invece dello studio di un sistema semiconduttore nel quale l'accoppiamento forte (*strong coupling*) tra gli eccitoni di una *quantum well* e un modo di cavità portano alla nascita di nuove quasi-particelle chiamate *polaritoni*. Come eccitoni e fotoni, anche i polaritoni possono essere confinati in tre dimensioni. Se tale confinamento è sufficiente, si possono creare forti interazioni repulsive tra polaritoni, fino al punto di impedire che due di essi possano coesistere nella stessa cavità. Questo fenomeno, noto come *polariton quantum blockade*, è molto promettente per la realizzazione sorgenti a singolo fotone basate sui polaritoni. In questo lavoro viene sviluppata una tecnica innovativa di eccitazione riosonante a due fotoni per ottenere il regime di *polariton quantum blockade*. Infine, il manoscritto descrive anche un nuovo regime di emissione, chiamato *two-photon polariton laser*.

Parole chiave: nanocristalli, singolo fotone, semiconduttori, polaritone, eccitazione a due fotoni, cristalli fotonici

Contents

Chapter 1

Introduction

During a class at Caltech, Richard P. Feynman affirmed that to scientist of early 1900's it was extremely hard to think to wave-particle duality and that about the double nature of light "it was jokingly said by someone that light was waves on Mondays, Wednesdays, and Fridays; it was particles on Tuesdays, Thursdays, and Saturdays, and on Sundays, we think about it!" [1]. This funny sentence found its fundament in a general state of confusion, because at that time it looked like that you had to know which experiment you were analyzing in order to tell if light was waves or particles.

After one hundred years of experiments, the puzzle seems now much more complete, and advances in nanotechnologies made possible to master classical and non-classical radiations. One striking feature of nano-sized materials is the strong size dependence of their physical properties. The first observation of size dependent optical properties dates the early 80's [2, 3] and the suitability of such small materials to serve as potential building blocks in future applications has driven many research groups to focus on the study of fully confined semiconductor systems. When scaled down up to De Broglie wavelength, semiconductors can exhibit quantum confinements effects for both electrons and photons, forbidding their motion in all or few directions, and, moreover, making these two particles to interact in several ways.

This thesis focuses on the design, the development and the characterization of new sources for the generation of classical and non-classical light states with isolated and coupled confined systems for photons and electrons. The most common ways to obtain these types of systems are reviewed in **chapter 2**, with particular emphasis on colloidal semiconductor nanocrystals, photonic crystals nanocavities and microcavity polaritons.

An example of fully confined systems for electrons are *colloidal semiconductor nanocrystals*, i.e. ultra-small compounds composed by tens to thousands atoms arranged in a crystal structure similar to that of bulk material, but with dimensions of few nanometers. Although their crystalline structure is the same of bulk semiconductor, in nanocrystals continuous energy bands are not formed, due to the confinement potential at sizes lower than De Broglie's wavelength. The distribution of allowed energy states for electrons is now discrete and represents an intermediate regime between single atoms and molecules [4, 5]. By virtue of their well separated energy states in both conduction and valence bands, the quantum confinement in colloidal nanocrystals is efficient also at room-temperature, making these nanoparticles promising for various applications such as light emitting devices, nanoelectronic circuits and fluorescence tagging in biological applications [6–10]. It is well known that colloidal nanocrystals can emit non-classical light also at room temperature [11]. However, in the field of single photon generation, other nano-materials are considered to be the state of art, including color centers in diamond nanocrystals [12], Stransky-Krastanow quantum dots [13] and organics molecules [14]. This is mainly due to the fact that NCs exhibit sharp photoluminescence intensity fluctuations, known as blinking [15]. Despite two different approaches have been recently proposed to avoid blinking [16, 17], no one of them show blinking-free PL preserving a single photon emission suitable for applications. The **third chapter** of this work is devoted to show that by properly surrounding a CdSe dot with an elongated CdS shell, it is possible to obtain an almost non-blinking source of single photons at room temperature with a high degree of linear polarization. The single-photon flux is generated with an efficiency assessed to be $\sim 70\%$, thus approaching the state of the art of single photon sources based on other materials.

A possible way to confine photons is to use integrated photonics and, in particular, photonic crystals technology. Photonic crystals are periodic structures made of dielectric materials: regions with different dielectric constants alternate periodically with a period of the order of the wavelength of light. By virtue of constructive and

destructive interferences, they can mold the flow of light by defining allowed and forbidden energy states and bands for photons; building up nanoresonators able to confine light in volumes even smaller than a cubic wavelength is therefore enabled. Photonic crystals emerged in 80's, when it was realized that the effect of a three-dimensionally periodic material can be similar to the effect of semiconductors on electrons [18]. This opened new perspectives in photonics and nowadays photonic crystals integrated circuits are well developed in the infrared spectral range. However the interest on linear and non linear applications in the visible spectral range boosts up research activity on photonic crystals at these unusual wavelengths [19–21], making technical and scientific communities asking for a versatile technology able to answer to the needs of this field. **Chapter 4** proposes Silicon Nitride two-dimensional photonic crystal resonators as flexible technological platform to realize photonic devices based on spontaneous emission engineering of nanoemitters in the visible spectral range. In order to demonstrate the versatility of this photonic platform, the resonators have been coupled with (i) DNA strands marked with Cyanine 3 organic dyes, (ii) antibodies bounded to fluorescent proteins and (iii) colloidal semiconductor nanocrystals localized in the maximum of the resonant electric field, showing also the possibility to use this technology in biosensing devices.

It has been already mentioned that fully confined systems can make the confined particles interacting. In semiconductors, the fundamental excitation is called exciton, i.e. an electron-hole pair bound through Coulomb's interaction. When this quasi-particle is fully confined and when it can interact with confined photons, the strong coupling between them can results in another quasi-particle called polariton. In first approximation, a polariton can be defined as a quasi-particle formed of half-light and half-matter. Polaritons so far showed a huge amount of intriguing quantum phenomena arising from strong polariton-polariton interactions due to their excitonic part. As in cold atoms gasses, polaritons can condensate in the state with minimum energy and can behave as a quantum fluid in supersonic, subsonic or superfluid regime [22,

23]. This quantum fluid can generate turbulences such as vortex singularities [24], moving vortex pairs [25] or dark solitons propagating within the fluid [26]. Moreover, when interactions are sufficiently strong, a coherent emission can be recovered from polaritons states also if the system is optically pumped in an incoherent way. Being also characterized by a pronounced narrowing of the emission linewidth, this phenomenon is know as *polariton laser* and can show thresholds almost two order of magnitude lower than standard photon laser [27, 28].

A phenomenon of remarkable interest obtainable by strongly interacting polaritons is the so-called *polariton quantum blockade*, which allows strongly coupled systems to emit on-demand single photons [29]. A sufficiently strong polariton-polariton interaction can indeed forbid two photons to coexist in the structure: if only one polariton is excited in the cavity, it can re-emit only one photon, thus resulting in a strongly anti-bunched radiation. **Chapter 5** proposes a coherent two-photon pumping technique to excite microcavity polaritons in GaAs-based nanostructures, with the goal to obtain polariton quantum blockade. We also show that the two-photon excitation technique is effective to obtain a new operation regime which present several similarities with polariton laser, here called *two-photon polariton laser*.

Chapter 2

Fully confined systems

Contents

In the last twenty years the development of nanotechnologies made possible to realize nanostructures able to confine photons and electrons, freezing their motion in the space. A consequence of that is a significant enhancement of quantum effects, that lead to a number of novel physical phenomena in both coupled and uncoupled systems. When experiencing strong confinement, these two fundamental particles can interact, giving rise to linear and non-linear effects and making possible to boost up the performances of several opto-electronic devices, such as lasers, optical amplifiers, single photon sources, solar cells, biosensor etc. This chapter introduces the working principle of nanostructures able to confine both photons and electrons and will describe how the dynamics of the photon-exciton coupling can strongly modify the optical and electronic properties of these systems.

2.1 Multidimensional confinement of electrons

Although the most important properties of bulk crystalline materials are well understood from solid-state physics, below a certain size, they start to change and become size-dependent. After a brief review on electronic confinement in nanometer sized semiconductors, this section describes a particular type of semiconductor quantum dots,

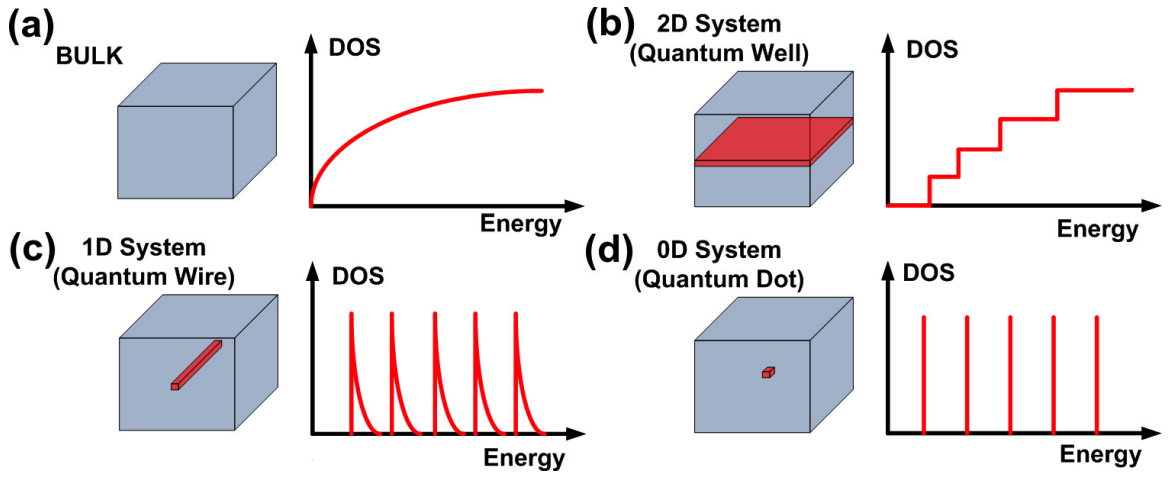

Figure 2.1: Sketch of the density of allowed energy states in the conduction band of bulk semiconductors **(a)**, quantum wells **(b)**, quantum wires **(c)** and quantum dots **(d)**.

also called semiconductor nanocrystals (NCs), composed of a few thousands of atoms arranged in a crystal structure similar to that of the bulk material, but with dimensions of few nanometers. At that size, comparable to De Broglie wavelength, semiconductors exhibit quantum confinement effects and are one of the most promising structures to realize innovative electronic and photonic devices.

Limiting the electron motion dramatically alters the electron energy spectrum, leading to a modification the *Density Of allowed energy States* (DOS), which is defined as the number of states at a given energy level. Figure 2.1 schematically illustrates the changes in the density of states when the electrons motion is limited in one, two or three dimensions. Confinement therefore creates different types of structures known as *quantum wells* (electrons free to move in a plane and step-like DOS), *quantum wires* (electrons confined in two directions), and *quantum dots* (electrons confined along the three cartesian axes and Dirac's delta-like DOS).

2.1.1 Bulk excitons

In the case of direct band gap bulk semiconductors (Fig. 2.1(a)), in the vicinity of the wavevector value $\mathbf{k} = \mathbf{0}$, valence and conduction band dispersions can be approximated by a parabola and, supposing zero the value of the energy at the maximum of the valence band, these dispersions are described by the following relations

$$E_c(k) = E_g + \frac{\hbar^2 k^2}{2m_c^*}, \quad E_v(k) = -\frac{\hbar^2 k^2}{2m_v^*}, \tag{2.1}$$

where E_g is the semiconductor energy gap and m_v^* and m_c^* are the effective mass of the valence and conduction band, respectively.

The absorption of a photon with energy $\hbar\omega > E_g$ allows the optical excitation of an electron from the valence to the conduction band, and the free place left by the electron in the valence band constitutes a quasi-particle called *hole*, with effective charge $+e$ and a momentum opposite to the one of the excited electron. In that case a free electron-hole pair (e-h) is formed in the semiconductor. If the free e-h pair is the most obvious excitation, however it is not the elementary electronic excitation. Indeed, by taking into account the Coulomb interaction, the electron and the hole have bound states, resulting in a quasi-particle called *exciton*. The exciton energy lies below the energy gap and is given by the relation

$$E_X(k_X) = E_g - E_b + \frac{\hbar^2 k_X^2}{2m_X^*}, \tag{2.2}$$

where E_b is the binding energy, k_X the exciton momentum and m_X its effective mass. The Hamiltonian of the exciton system is analog to the one of the hydrogen atom and its levels have the same orbital structure (1s, 2s, 2p, ...).

2.1.2 Quantum wells

In a quantum well the excitons are free to move into the plane of the well, while their motion is forbidden in the perpendicular direction. Dingle and co-workers [30] were the first to report about the quantum confinement in a AlGaAs-GaAs-AlGaAs quantum

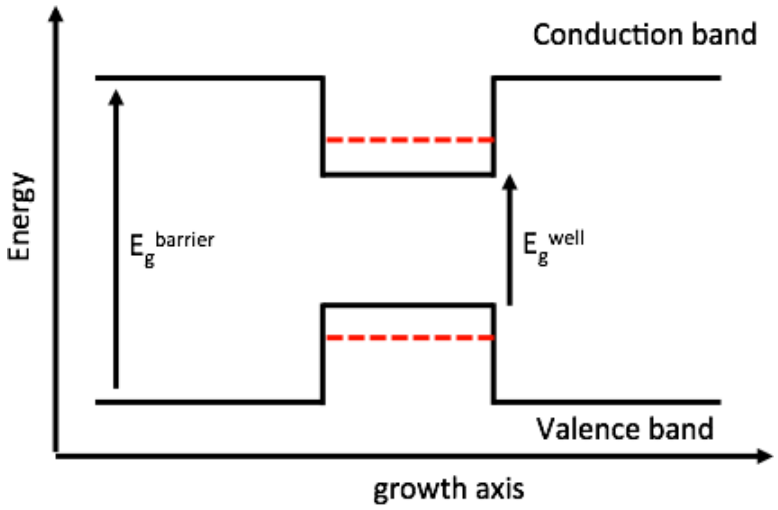

Figure 2.2: Schematic of a quantum well bandstructure.

well, showing the existence of four discrete energy levels for both heavy and light-hole[1] excitons. This confined behavior can be obtained by inserting a thin semiconductor layer (with energy gap E_g^{well}) between two thicker layers of another semiconductor with larger bandgap ($E_g^{barrier}$), leading to the heterostructure reported in Fig. 2.2. Because of the confinement, the energy difference between the maximum of the valence band the minimum of the conduction band (i.e. the band gap E_g) is shifted with respect to the bulk material of a value ΔE, (i.e. $E_g = E_g^{well} + \Delta E$). The energy state of the quantum well excitons can be computed via the formula

$$E_{X,n}^{well} = E_g^{well} + \Delta E - \frac{1}{(n+1/2)^2} \frac{\mu}{\epsilon_0 m_e} E_I, \tag{2.3}$$

where μ is the electron-hole reduced mass, $E_I = m_e e^4/(2\hbar^2)$ the hydrogen atom ionization energy [2], $e^2 = q^2/(4\pi\epsilon_0)$ the rescaled electron charge, ϵ_0 the dielectric constant in the vacuum, and m_e the electron mass at the rest. The Bohr radius in quantum wells is one half of the Bohr radius in bulk materials.

[1] The valence band is, in turn, composed of few bands. The two bands with maxima at $\mathbf{k} = \mathbf{0}$ are the heavy- and the light-hole bands. For instance, in silicon the light hole mass is $m_l^* = 0.16 m_0$, while the heavy-hole mass is $m_h^* = 0.46 m_0$, where m_0 is the free electron mass.

[2] It depends on the parallelism with the hydrogen orbitals mentioned in section 2.1.

In QWs the translational symmetry in the direction of the confinement is thus broken by the confinement [31], while it is preserved in the in plane direction. It is important to point out that for confined excitons it is possible to calculate the exciton radiative lifetime via the Fermi's golden rule [32]. In order to do that a quantity called *oscillator strength* f_{osc} is usually introduced. f_{osc} is proportional to the probability for an electron in the valence band to create an exciton by absorbing a photon and it is related to the exciton lifetime τ_X by the relation [33]

$$\frac{1}{\tau_X} = \frac{e^2}{2\epsilon_0 m_0 c} f^*_{osc}, \tag{2.4}$$

where f^*_{osc} is the oscillator strength for surface unity. As detailed in sections 2.3 and 4.5, the oscillator strength is an important parameter to obtain the strong coupling regime between excitons and photons.

2.1.3 Quantum dots

When charge carriers motion is frozen along all directions, the fully confined system is called *quantum dot* (QD), and the quantization take place along all the cartesian's axes. In that case the quasi-continuous distribution of states collapses in to a series of Dirac functions [Fig. 2.1(d)] and in the case of flat potential with infinite boundaries the level spacing increases with the energy. The energy of the n-th allowed state is [34]

$$E_n = \frac{h^2\pi^2}{2m^*_e a^2} n^2, \tag{2.5}$$

where a is the size of the quantum dot[3].

Because the energy levels of the quantum dots are discrete rather than continuous, changes in the box sizes have the effect of altering the boundaries of the bandgap. Indeed, by changing the geometry of the surface of the quantum dot it is possible to change the bandgap energy, with the resulting effect of a tunability of the emission and

[3]Equation (2.5) is derived by solving the basic one-dimensional Schröedinger equation for a flat potential well with infinite boundaries and for a spherical quantum dot it is valid along the three axes.

absorption spectra. In particular, the higher the confinement, the larger the energy gap. It is, therefore, possible to predict that by shrinking the dimensions of a quantum dot its absorption spectrum will be shifted towards higher energies, as confirmed also by the eq.(2.5).

Since 1982, when the concept of quantum dots was first proposed by Arakawa and Sakaki [35], their peculiar properties have been applied to a number of photonic devices, and impressive results in the synthesis and application of these nanostructures have been demonstrated. Epitaxial QDs, obtained by the Stranski-Krastanov (SK) self-organized growth method [36], have demonstrated their potential as light sources for ultrafast semiconductor lasers and optical amplifiers for optical communications, showing new functionalities and performances such as high gain and efficiency, ultra-low threshold current densities and weak sensitivity to temperature variations [37–39]. A different approach for the fabrication of quantum dots is based on wet-chemistry for the synthesis of colloidal QDs. These colloidal nanocrystals (NCs) are good candidates for photonic applications in different fields such as health, energy, environment and aerospace due to their low fabrication costs, high quantum efficiency at room temperature, high versatility in the chemical synthesis, and broad tunable emission range [40]. Both epitaxy and wet chemistry have demonstrated to be valuable for the fabrication of triggered non-classical sources of single photons based on QDs. However, epitaxial QDs exhibit single photon emission only at cryogenic temperature [41], whereas single colloidal NCs based on II-VI compounds exhibit photon antibunching at room temperature [11, 42] by virtue of their specific electronic properties.

2.1.4 Colloidal Nanocrystals

As already mentioned, an alternative to SK QDs are colloidal nanocrystals. Being synthesized using wet-chemistry, they are free-standing structures dispersed in solution. Therefore, they can be produced in large quantities in a reaction flask and can then be transferred to any desired substrate. Moreover, due to their cheap, easy and

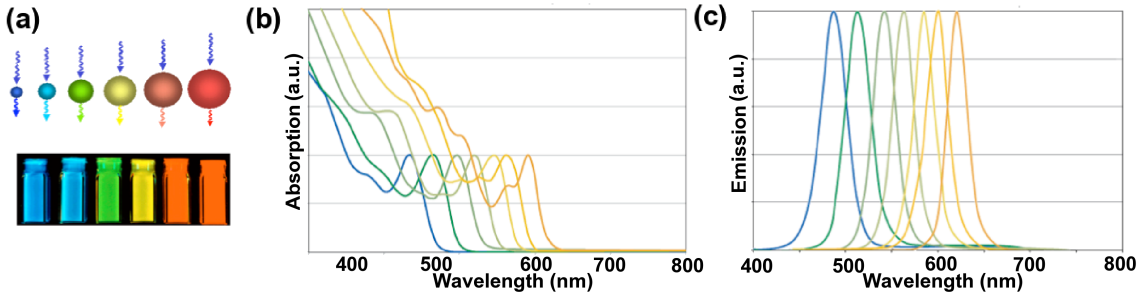

Figure 2.3: Size-tunable emission properties of quantum dots. **(a)** Vials of CdSe/ZnS colloidal nanocrystals having different diameters; **(b)** and **(c)** Typical absorption and emission spectra of CdSe/ZnS quantum dots with diameters ranging from $2nm$ (blue lines) to $5nm$ (red line). [Reproduced from ref. [45]]

high throughput synthesis, colloidal NCs are highly versatile nanoparticles allowing to arbitrarily engineering the grown structure according to the requested optical properties [40]. In section 2.1.3 the possibility to tune the QDs absorption band by tuning their dimension has been mentioned, and colloidal nanocrystals make possible to simply do that. As an example, Fig.2.3(b) reports several absorption spectra of CdSe nanocrystals capped by a ZnS shell. It is well known that in bulk CdSe at room temperature the energy gap is $E_g = 1.75eV$. However, by reducing the size of quantum dots from $5nm$ (red line in Fig.2.3(b), $E_g \sim 2eV$) to $2nm$ (blue line in Fig.2.3(b), $E_g \sim 2.69eV$) E_g can be increased in order to scan the whole visible spectral range. Similarly, the emission spectra, whose peak position is typically slightly detuned to lower energies from the absorption peak by a quantity called *Stokes shift* [43, 44], undergoes the same spectral tuning due to the size engineering. Figure 2.3(a) displays the luminescence of CdSe/ZnS NCs in liquid solution and illuminated by an ultraviolet source: the whole visible spectral range is easily covered, as confirmed by the corresponding emission spectra in Fig. 2.3(c). By changing the material and therefore the E_g^{bulk}, NCs emission in the ultraviolet and infrared bands can be also obtained. For instance, using PbS and PbSe, emission from 800 nm to 1600 nm can be obtained.

As a drawback, being in solution, NCs are not embedded in a semiconductor matrix

as for SK QDs. The lack of a matrix can cause strong sensitivity of NCs optical properties to the local environment, leading to the phenomena described in the next two sections.

2.1.4.1 Spectral diffusion and emission linewidth

This environmental dependence leads to the so-called *spectral diffusion* of the NC emission peak: the photoluminescence spectrum of the single particle, which is typically narrower than $0.1meV$ at cryogenic temperatures, exhibits significant fluctuations in time. These spectral shifts are typical small on the scale of $100ps$ and more pronounced ($\sim 80meV$) on the scale of seconds [46, 47]. The macroscopic effect of this spectral modifications is the broadening of the FWHM of the single dot PL when integrated for long times, and the impossibility to reduce the FWHM of colloidal nanocrystals below several meV. Spectral diffusion is one of the most important causes of line-width broadening, acting on the emission spectrum of the single nanoparticle. When the emission spectrum of ensembles of NCs is measured, FWHMs even larger are observed, due to the size dispersion of the nanoparticles resulting from the synthesis procedure.

2.1.4.2 Blinking

A second spectroscopic feature of colloidal nanocrystals is the photoluminescence blinking: the emission of a single quantum dot exhibits a dramatic on/off behavior, with off times that may vary from milliseconds to several minutes [15, 48]. A typical trace where blinking is evident is reported in Fig. 2.4. Although the reason for this behavior is still under discussion, the ionization of the nanocrystal is the most commonly invoked cause. Both the interaction of the nanocrystal with the environment and the charge-carrier dynamics can lead to the nanocrystal ionization. Indeed, a possible ionizing mechanism involves the so-called *Auger photoionization*: when two excitons are simultaneously present in the NC, the energy lost in the recombination of the first one can be transferred to the second one, ejecting one of the carriers into the envi-

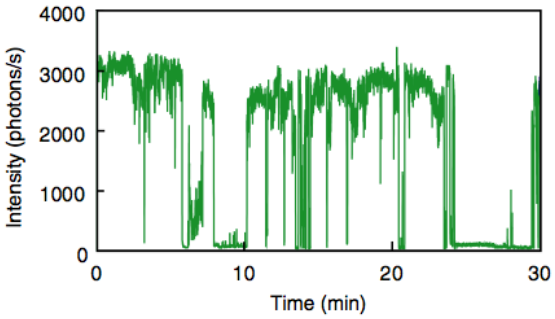

Figure 2.4: A typical photoluminescence time trace of a blinking nanocrystal. [Reproduced from ref. [51]]

ronment of the quantum dot (for instance on surface traps). The quantum dot is now charged, and the following excitons created into the QD efficiently recombine via ultra-fast non-radiative processes involving the ionization charge still present in the dot (for instance the Auger non-radiative energy transfer described in section 3.4). The dot remains in the off state until other interactions with the environment or with excitons neutralize the charged state. This mechanism also explains why multiexciton states emission is not usually observed in NCs. Several studies are currently analyzing the relationship between spectral shift and blinking in colloidal QDs [47, 49, 50]. On the other hand, recent developments on nanocrystals growth show a clear reduction of the blinking probability by increasing the shell thickness or properly modeling the potential well [16, 17]. A full comprehension of these mechanisms would allow to prevent these phenomena, making colloidal nanocrystals optically stable in time and robust as the epitaxially grown quantum dots.

2.2 Multidimensional confinement of photons

As electrons, also photons can be confined in low dimensional systems, breaking the linear dispersion of the vacuum $\omega = ck$. From the theory of the electromagnetic field based on Maxwell's equations, it is well known that discretized transversal modes can be guided in metallic structures and that the resonant frequencies in a metallic resonator constitute an infinite set of discrete values. This section discusses how a refractive index periodicity in one or two dimensions can induce photon confinement in ultra small volumes.

2.2.1 Working principles of photonic crystals

Photonic crystals (PhCs) are structures made of different dielectric materials arranged in a periodic lattice. The striking property of PhCs is that they can act on photons in the same way as crystals act on electrons [18]. If in crystalline semiconductors the periodical potential induces an energy band gap, a periodic disposition of materials with different refractive indexes can induce an interval of wavelengths in which photons can not exist in the structure. This wavelength range is usually referred to as *Photonic Band Gap* (PBG). The refractive-index periodicity can be realized along one or more axis, leading to the possibility to realize one-, two- or three- dimensional photonic crystals [18].

The one-dimensional case is the simplest, and relies in the alternation of several dielectric slabs with different refractive indexes. In the case of non-homogeneous materials and without applied sources, Maxwell's equations can be written as

$$\nabla \times \mathbf{E} = -\mu \frac{\partial \mathbf{H}}{\partial t}, \tag{2.6}$$

$$\nabla \times \mathbf{H} = \varepsilon(\mathbf{x}) \frac{\partial \mathbf{E}}{\partial t}, \tag{2.7}$$

where $\mathbf{x}$ is the position vector, $\varepsilon(\mathbf{x})$ the dielectric constant and $\mathbf{E}$ and $\mathbf{H}$ the electric and magnetic field vectors, respectively. From eq.s (2.6) and (2.7) the following eigenvalue

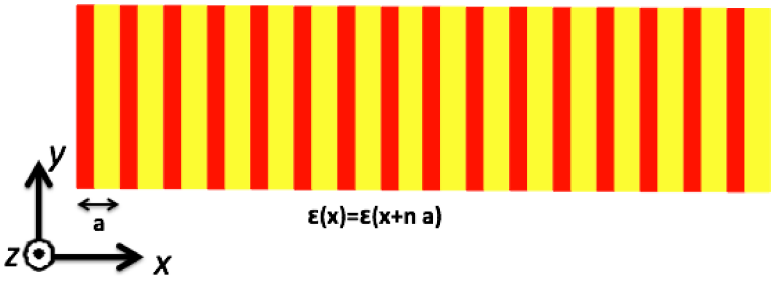

Figure 2.5: Structure with a refractive-index periodicity in one dimension. Materials in red and yellow have different refractive indexes. $n \in \{0, 1, 2, \dots\}$.

problem in the phasorial domaine can be extrapolated

$$\nabla \times \frac{1}{\varepsilon\left(\mathbf{x}\right)} \nabla \times \mathbf{H} = \frac{\omega^2}{c^2} \mathbf{H}. \tag{2.8}$$

$\mathbf{H}(\mathbf{x}, t)$ in general depends on both time and position. However, if the eigen-operator $\nabla \times \frac{1}{\varepsilon(\mathbf{x})} \nabla \times$ is periodic, from the differential equations theory it can be derived that the eigenfunctions can be written using the Bloch formalism, i.e. as a plane wave modulated by a periodic envelop $\mathbf{H}_{\mathbf{k}}(\mathbf{x})$ [18]

$$\mathbf{H}\left(\mathbf{x}\right) = e^{i\mathbf{k}\cdot\mathbf{x}} \mathbf{H}_{\mathbf{k}}\left(\mathbf{x}\right) = e^{i\mathbf{k}\cdot\mathbf{x}} \mathbf{H}_{\mathbf{k}}\left(\mathbf{x} + \mathbf{R}\right), \tag{2.9}$$

where the periodicity vector $\mathbf{R}$ depends on the structure. Let us refer to the 1D periodic structure reported in Fig. 2.5, with $\epsilon(x) = \epsilon(x) + a$. Because of the continuous translational symmetry, the wave vector $\mathbf{k}$ can assume any value in the yz plane [18]. Along x the situation is instead different. A key feature of Bloch states along the direction of the periodicity is that the Bloch state with wave vector k_x and $k_x + m\frac{2\pi}{a}$ are identical (m is an integer number). The mode frequency is therefore periodic in k_x, i.e. $\omega(k_x) = \omega(k_x + m\frac{2\pi}{a})$, and the dispersion diagram assumes the behavior reported in Fig. 2.6. The representation of the eigenfrequencies can thus be limited to the interval $k_x \in \left[0, \frac{2\pi}{a}\right]$ [18], as well as in the interval $k_x \in \left[-\frac{\pi}{a}, \frac{\pi}{a}\right]$, called *irreducible Brillouin zone*, as shown in Fig. 2.7.

These considerations, valid for 1D-PhC, can be extended to two and three dimensions. In the case of two dimensions this can be done by reproducing the same dielectric

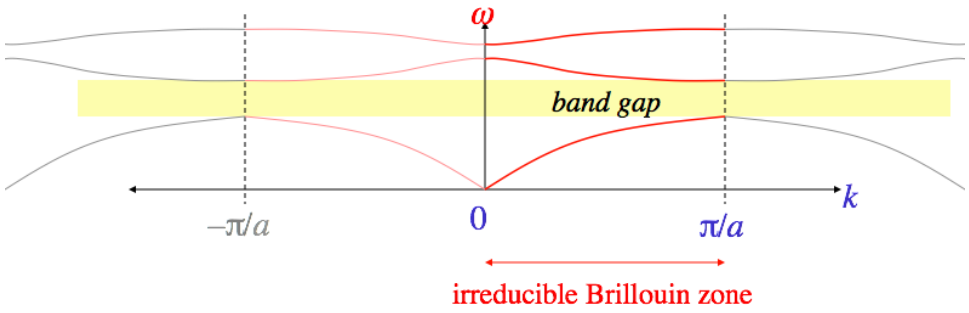

Figure 2.6: Dispersion behavior for the structure reported in Fig. 2.5. [Reproduced from ref. [52]].

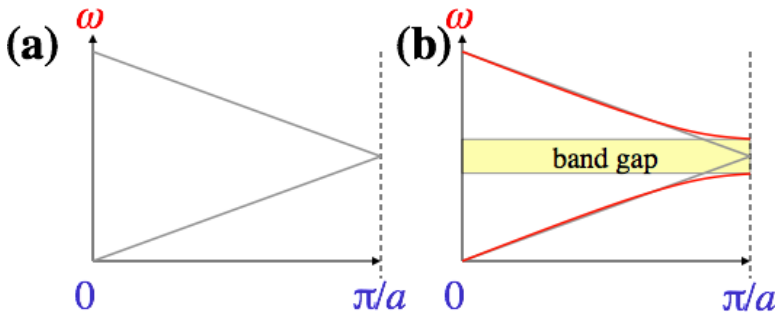

Figure 2.7: Dispersion curves for free photons **(a)** and for photons in a 1D-PhC **(b)**. [Reproduced from ref. [52]].

element in a plane following a defined lattice. For instance, one can periodically arrange dielectric columns of infinite height following a square or triangular lattice in the xy plane, as shown in Fig. 2.8. In such structures the electromagnetic field can be described as a linear combination of *transverse electric* (TE) and *transverse magnetic* (TM) modes and the Brillouin zone is now defined in two dimensions [4]. As a consequence, the dispersion diagram, also called *photonic band diagram* for analogy with semiconductor crystals, assumes the behavior reported in Fig. 2.8 for a square disposition of dielectric columns in air [Fig. 2.8(a)] and for a triangular lattice of air-columns in another dielectric medium [Fig. 2.8(b)]. It has been demonstrated that in the case of triangular lattices with radius comparable with the period of the structure a, it is

[4] The definition of TE and TM modes is ambiguous in the literature and here they will be redefined when needed. In this chapter, TE (TM) modes are modes with non-zero components of the electric (magnetic) field only in the plane in which the Brillouin zone is defined (i.e. the xz plane).

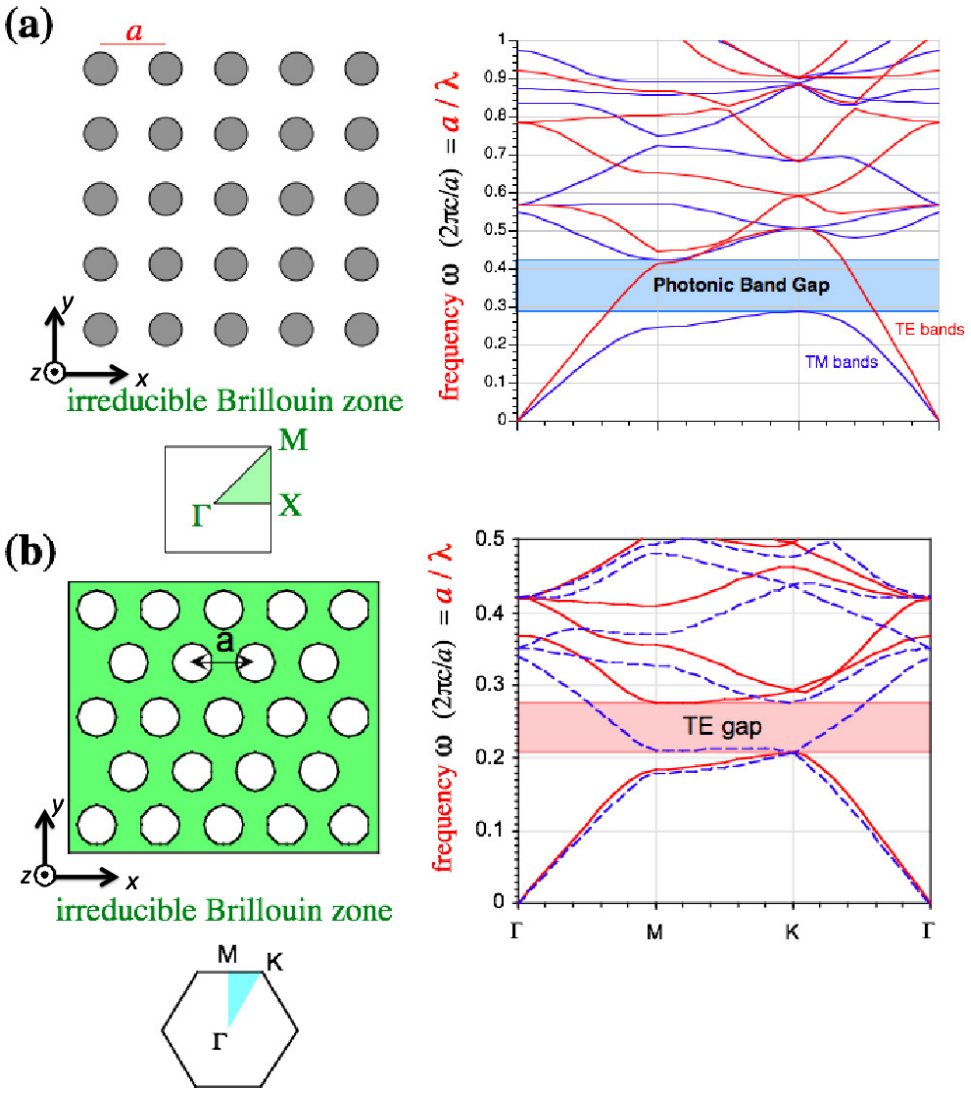

Figure 2.8: Band diagrams for two dimensional photonic crystals. Reproduced from ref. [52]

possible to obtain hybrid PBGs, valid at the same time for TE and TM modes, while for the other cases the band gap is obtained only for one of the two modal configurations (as also shown in Fig. 2.8) [18].

2.2.2 Planar microcavities

Let us consider again the 1D-photonic crystal reported in Fig. 2.5. Due to the PBG, each photon impinging on the structure with a wave vector perpendicular to the periodicity is reflected. This layered structure thus behaves as a wavelength selective

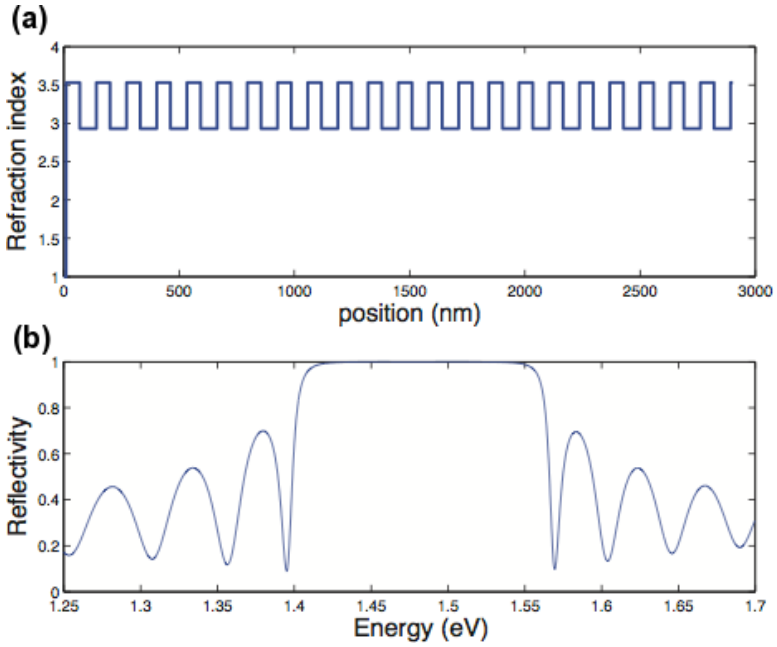

Figure 2.9: Real space refractive index distribution **(a)** and reflectivity as a function of photons energy **(b)** for a Bragg reflector in the near infrared. [Reproduced from ref. [53].]

mirror called *Bragg reflector* (an example of its reflectivity is reported in Fig. 2.9). The reflection band corresponds to the PBG defined in previous sections.

So far only structures with a perfect periodicity have been discussed. Let us now consider a multilayer film in which one of the elements is different from the others, introducing a defect in the periodic disposition. It is intuitive that for wavelengths (λ) far away from the size of the defect, the full periodicity of the system is recovered, and the band diagram should look like the one of the unperturbed system. However for λ comparable to the defect size, the broken periodicity may allow the localization of a mode in the PBG, which should exponentially decay when it goes out from the defect entering in the two periodic regions around it. As shown in Fig. 2.10, these two regions are indeed two Bragg's reflectors, one parallel to the other, and any light propagating along x with a wavelength defined by the defect size is trapped between them. Because the mirrors localize the light within a finite region, the modes are quantized into discrete frequencies and with discrete components of $\mathbf{k}$ along x, while there is no quantization

Figure 2.10: Example of a 1D-PhC cavity.

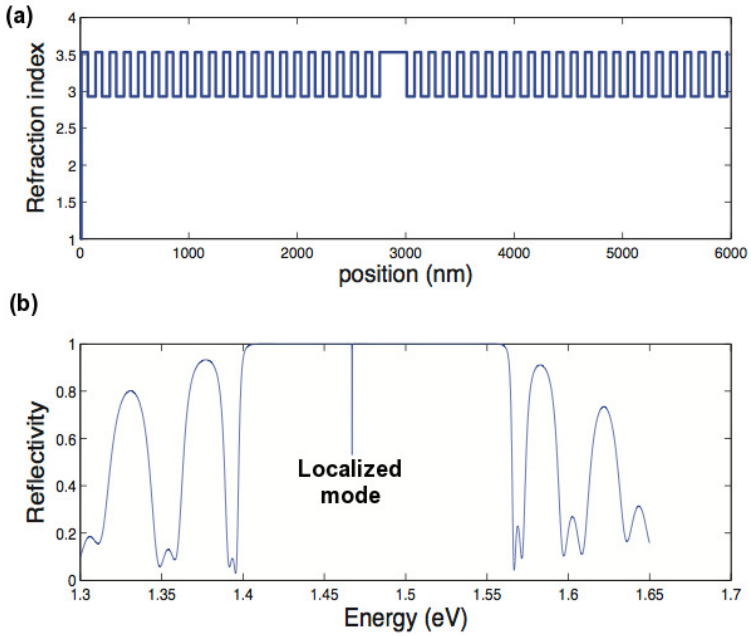

Figure 2.11: Refractive index distribution **(a)** and reflectivity as a function of photons energy **(b)** for a GaAs/AlAs based microcavity. [Reproduced from ref. [53]].

along z and y (where the structure is supposed to be infinitely extended). Figure 2.11 shows an example of the cavity reflectivity where the appearance of a reflection minimum inside the stop band of the Bragg reflectors confirms the storage of a mode inside the cavity. In the case reported in Fig. 2.11 the cavity was obtained by realizing a GaAs/AlAs multilayer and introducing a defect of size λ, which resulted to be the resonant frequency of the cavity.

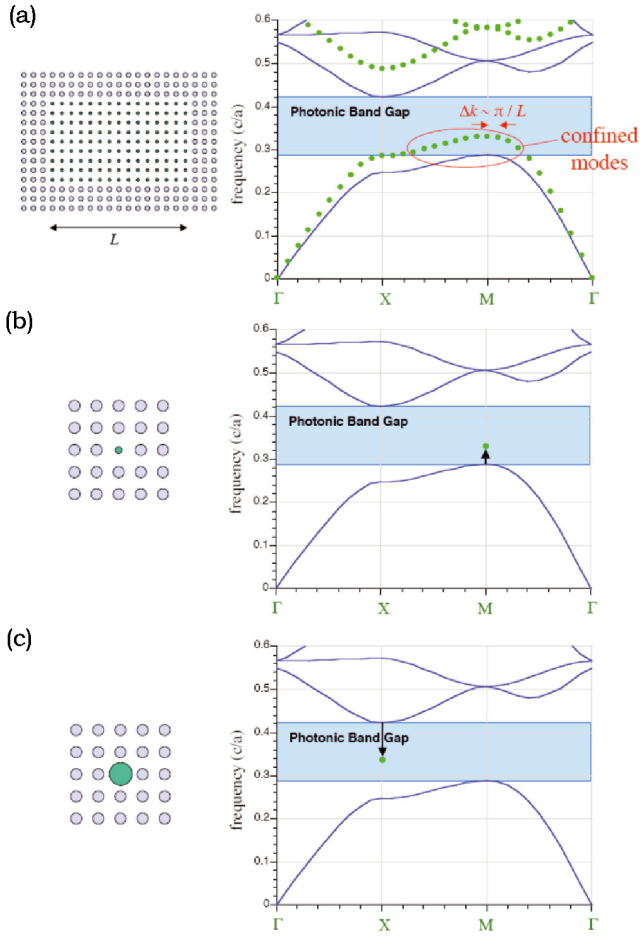

Figure 2.12: Example of electromagnetic defects in 2D-PhCs. [Reproduced from ref. [52]].

2.2.3 2D Photonic crystals cavities

Also in the case of cavities the considerations for 1D-PhC can be extended to the two dimensional case. A few examples of possible defects in 2D-PhC are reported in Fig. 2.12: the modification of the 2D periodicity can lead to localized modes at a given **k** (Fig. 2.12(b) and (c)) or to more complex configurations (Fig. 2.12(a)). Another possibility is to omit a periodic element, as shown in Fig. 2.13, thus leading to a localized mode for all in-plane wavevectors and for a given wavelength.

A figure of merit to evaluate the confinement of a micro or nanocavity is the so called *Quality factor* (Q-factor), defined as the ratio between the energy stored in the

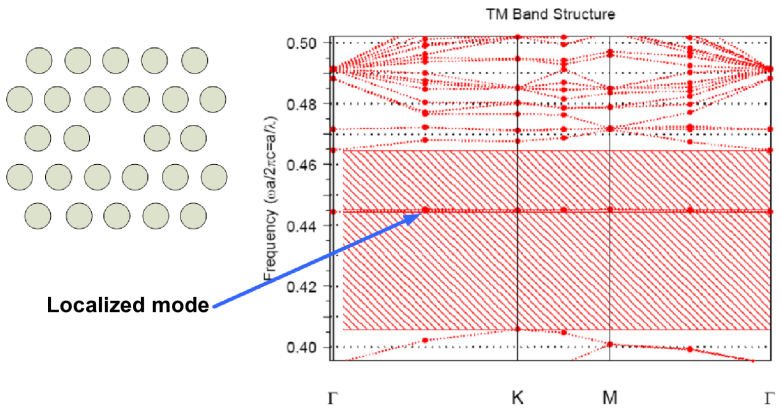

Figure 2.13: Example of a point defect obtained by eliminating a dielectric column in a triangular lattice.

cavity and the energy lost in each oscillation, i.e.

$$Q = 2\pi \frac{Stored \quad Energy}{Lost \quad Energy} = \omega \frac{\langle U \rangle}{\langle P \rangle}, \tag{2.10}$$

where ω is the resonant angular frequency, $\langle P \rangle$ is the far field radiation power and $\langle U \rangle$ is the energy stored in the cavity defined as

$$\langle U \rangle = \int_V \frac{1}{2} \left(\varepsilon E^2 + \mu H^2 \right) dV, \tag{2.11}$$

with V the volume of the structure and ε and μ the electric and magnetic permittivity.

However, this description for 2D-PhCs is ideal, since the periodic elements are supposed to be infinitely extended along z (see Fig. 2.8 for axes definitions). Obviously, it is not possible to realize such structures, and a finite value of total thickness t should be taken into account to model the resonators.

The first difference between finite and infinite 2D-PhC is the light confinement mechanism. As already mentioned, 2D-PhCs allow or forbid photons to be in well defined energy states. However, when the total thickness in not infinite, this is possible only in the plane in which the Brillouien zone can be defined, because along z the structure is not periodic and the light is thus confined by total internal reflection. For this reason it is impossible to define TE and TM modes, but the modal expansion results to be true for two other types of electric field configurations, called *TE-like* and

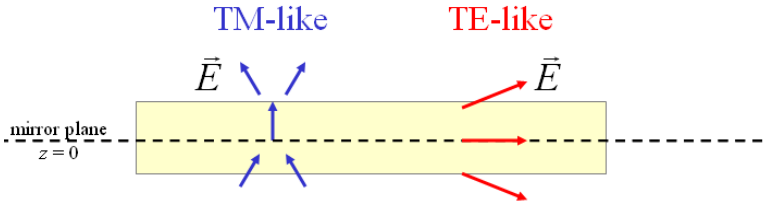

Figure 2.14: Definition of TE- and TM-like modes. [Reproduced from ref. [52].]

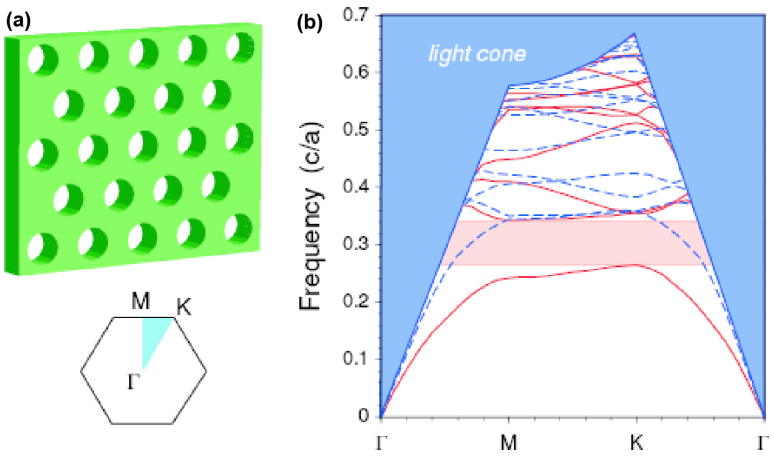

Figure 2.15: Band diagram for a 2D-PhC slab surrounded by an uniform cladding. [Reproduced from ref. [52].]

TM-like, allowing for small components of the electric and magnetic fields also in the plane in which the Brillouin zone is not defined [see Fig. 2.14].

Moreover, in addition to guided modes, in finite structures (also called PhC-slabs and sketched in Fig. 2.15(a)) spurious modes in the surrounding cladding materials appear. These modes are inside a zone called *light cone*, which is identified as the set of radiation modes not confined in the slab and it is represented by the blue area in Fig. 2.15(b). The light cone size is defined by the refractive index of the claddings: the higher the difference of the refractive index between the slab and the claddings, the higher the confinement within the PhC structure. Obviously, if more than one cladding is present, more light cones can be defined, each of which representing the radiations in the different materials. Also in the case of 2D PhC-slabs it is possible to have a PBG, which is considered a *complete PBG* if it is extended also in the light cone and

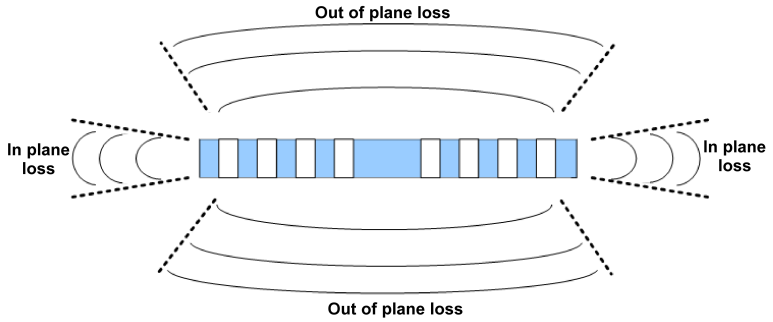

Figure 2.16: Sketch of radiation loss in the case of 2D-PhC slabs.

a *partial PBG* otherwise.

Let us now consider a 2D-PhC resonator with finite thickness t in an uniform cladding material with a refractive index $n_{cladding}$. Figure 2.16 sketchs the possible leakage channels that contribute to the final quality factor of the resonator. In eq.(2.10) these contributions are taken into account in the radiation losses $\langle P \rangle$, which should now be written as

$$\langle P \rangle = \left\langle P_{\parallel} \right\rangle + \langle P_{\perp} \rangle \,, \tag{2.12}$$

where $\left\langle P_{\parallel} \right\rangle$ is the in-plane loss due to the non-ideality of the PhC, while $\langle P_{\perp} \rangle$ is the radiation loss due to the total internal refraction perpendicular to the PhC plane. As a consequence the quality factor can be re-written in the form

$$\frac{1}{Q} = \frac{1}{Q_{\parallel}} + \frac{1}{Q_{\perp}}. \tag{2.13}$$

It is important to point out that Q is smaller than the smallest partial quality factor. $Q_{\parallel}$ can be arbitrarily increased increasing the number of lattice periodicity around the cavity, at least for well-localized modes inside the PBG. The upper bound to Q is thus given by the out-of-plane radiation losses, taken into account by $Q_{\perp}$.

2.3 Coupling of fully confined systems

When an optical emitter is placed in a resonant cavity and the energetic distributions of the two systems allow an interaction between the two oscillators, two different regimes,

known as *weak* and *strong coupling*, can be observed [54–56].

Let us focus this paragraph on the strong coupling between a quantum well and a planar microcavity, while the case of interaction between a quantum dot and a cavity mode well detailed in section 4.5. In the condition of weak exciton density the Hamiltonian of the coupled system is the following:

$$H = \sum_{\mathbf{k}} \hbar\omega_C(\mathbf{k}) a_{\mathbf{k}}^{\dagger} a_{\mathbf{k}} + \hbar\omega_X(\mathbf{k}) b_{\mathbf{k}}^{\dagger} b_{\mathbf{k}} + \frac{\hbar\Omega_R}{2}(a_{\mathbf{k}}^{\dagger} b_{\mathbf{k}} + b_{\mathbf{k}}^{\dagger} a_{\mathbf{k}}) \tag{2.14}$$

where $a_{\mathbf{k}}$ ($a_{\mathbf{k}}^{\dagger}$) and $b^{\dagger}$ ($b_{\mathbf{k}}^{\dagger}$) are the creation (annihilation) operators for a photon and an exciton, respectively, with in plane momentum $\mathbf{k}_{\parallel} = \mathbf{k}$ and $\hbar\Omega_R \propto \sqrt{f_{osc}}$ is the *Vaccum Rabi splitting* (VRS). After diagonalization, the Hamiltonian (2.14) become

$$H = \sum_{\mathbf{k}} \hbar\omega_{LP}(\mathbf{k}) p_{\mathbf{k}}^{\dagger} p_{\mathbf{k}} + \hbar\omega_{UP}(\mathbf{k}) q_{\mathbf{k}}^{\dagger} q_{\mathbf{k}}, \tag{2.15}$$

where the operators $\left(p_{\mathbf{k}}, p_{\mathbf{k}}^{\dagger}, q_{\mathbf{k}}, q_{\mathbf{k}}^{\dagger}\right)$ are related to the operators $\left(a_{\mathbf{k}}, a_{\mathbf{k}}^{\dagger}, b_{\mathbf{k}}, b_{\mathbf{k}}^{\dagger}\right)$ by the linear transformation

$$\begin{pmatrix} p_{\mathbf{k}} \\ q_{\mathbf{k}} \end{pmatrix} = \begin{pmatrix} -C_k & X_k \\ X_k & C_k \end{pmatrix} \begin{pmatrix} a_{\mathbf{k}} \\ b_{\mathbf{k}} \end{pmatrix} \tag{2.16}$$

and its own conjugate. The coefficients

$$X_{\mathbf{k}}^2 = \frac{\delta_{\mathbf{k}} + \sqrt{\delta_{\mathbf{k}}^2 + \Omega_R^2}}{2\sqrt{\delta_{\mathbf{k}}^2 + \Omega_R^2}} \tag{2.17}$$

$$C_{\mathbf{k}}^2 = -\frac{\delta_{\mathbf{k}} - \sqrt{\delta_{\mathbf{k}}^2 + \Omega_R^2}}{2\sqrt{\delta_{\mathbf{k}}^2 + \Omega_R^2}} \tag{2.18}$$

are the excitonic and photonic Hopfield factors with the unitary condition $X_{\mathbf{k}}^2 + C_{\mathbf{k}}^2 = 1$ and represent *excitonic* and *photonic content* of the polariton, respectively. The eigenvalues

$$\omega_{LP}(\mathbf{k}) = \frac{\omega_X(\mathbf{k}) + \omega_C(\mathbf{k})}{2} - \frac{1}{2}\sqrt{\delta_{\mathbf{k}}^2 + \Omega_R^2} \tag{2.19}$$

$$\omega_{UP}(\mathbf{k}) = \frac{\omega_X(\mathbf{k}) + \omega_C(\mathbf{k})}{2} + \frac{1}{2}\sqrt{\delta_{\mathbf{k}}^2 + \Omega_R^2} \tag{2.20}$$

are called *upper* (UP) and *lower* (LP) *polariton branches* and $\delta_{\mathbf{k}} = \omega_C(\mathbf{k}) - \omega_X(\mathbf{k})$ is the cavity-exciton detuning.

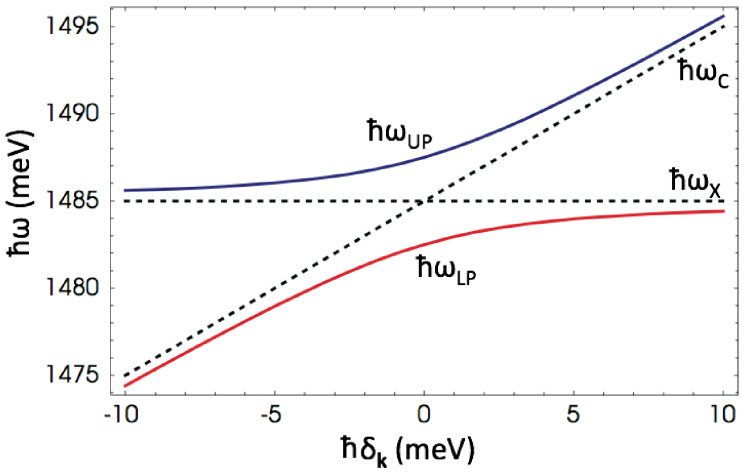

Figure 2.17: Example of lower and upper polariton branches minimum energies dependences as a function of cavity-exciton detuning.

A signature of strong coupling regime is the so-called *anticrossing behavior*, shown in Fig. 2.17 for $\mathbf{k} = \mathbf{0}$. When the cavity and the exciton energies are degenerate, i.e. $\omega_C = \omega_X$, the two polariton eigenstates are separated by an energy of twice the interaction energy between the oscillators which is the *Vacuum Rabi Splitting* $\hbar\Omega_R$. In Fig. 2.18 the typical behavior of polariton dispersions and lower branch exciton and photon weights are reported for different detunings. When $\delta_{\mathbf{k}} = 0$, $X_{\mathbf{k}}^2 = C_{\mathbf{k}}^2 = 1/2$ and polaritons can be considered as half-light half-matter quasi-particles.

Because of the selection rules on the in-plane momentum, a specific polariton state on the dispersion curve can be excited using a non-zero incident angle $\theta = (\theta_x, \theta_z)$ of electromagnetic field (see Fig. 2.19). The polariton momentum is equal to the photon momentum and the in-plane wavevector $\mathbf{k} = (k_x, k_z)$ can be calculated via the relations

$$k_x = k_L sin(\theta_x), \quad k_z = k_L sin(\theta_z), \tag{2.21}$$

where $k_L = \frac{2\pi}{\lambda_L}$ is the momentum of the laser beam at wavelength λ_L injecting the polaritons. Each photon emitted at a defined energy contains all the information (position, phase, momentum) of the polariton from which it has been emitted.

The hamiltonian (2.14) does not take into account the coupling between each

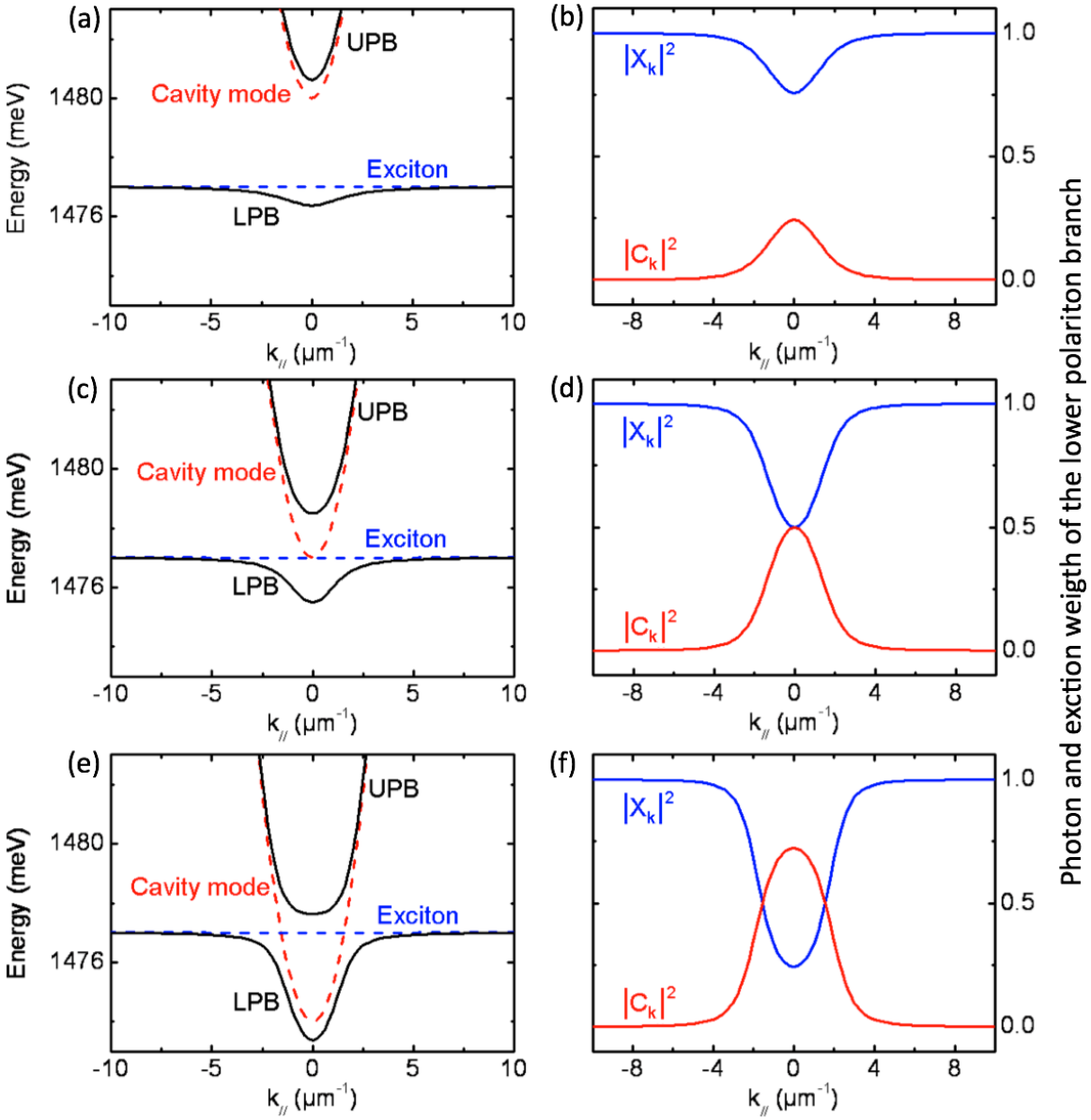

Figure 2.18: **(a,c,e)** Polariton (black lines), exciton (dashed blue lines) and cavity (dashed red lines) mode dispersions for different detunings. **(b,d,f)** Photon and exction weigth of the lower polariton branch for different detunings. [$\Omega_R = 3meV$, detuning values (a,b) $\delta = +3meV$, (c,d) $\delta = 0$, (e,f) $\delta = -3meV$, image reproduced from ref. [33]]

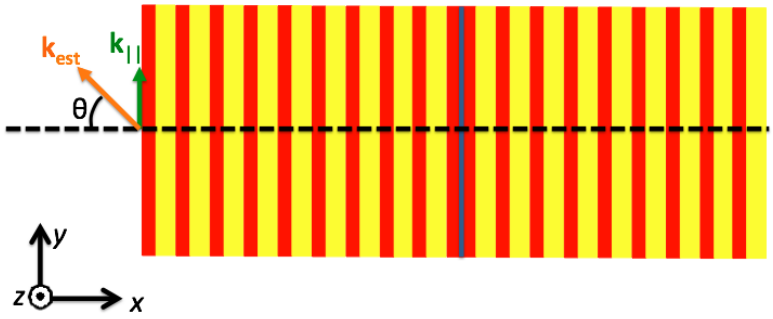

Figure 2.19: Schematic of polariton emission outside the cavity.

oscillator and its own reservoir, which causes the energy dissipation in the environment. A way to do that is to introduce the complex frequencies $\omega_C(\mathbf{k}) - i\gamma_C(\mathbf{k})$ and $\omega_X(\mathbf{k}) - i\gamma_X(\mathbf{k})$. The new eigenstates are thus complex and

$$\omega_{LP}(\mathbf{k}) = \frac{\omega_X(\mathbf{k}) + \omega_C(\mathbf{k})}{2} - i\frac{\gamma_X(\mathbf{k}) + \gamma_C(\mathbf{k})}{2} - \frac{1}{2}\sqrt{(\delta_\mathbf{k} - i(\gamma_X(\mathbf{k}) - \gamma_C(\mathbf{k}))^2 + \Omega_R^2},$$
$$\omega_{UP}(\mathbf{k}) = \frac{\omega_X(\mathbf{k}) + \omega_C(\mathbf{k})}{2} - i\frac{\gamma_X(\mathbf{k}) + \gamma_C(\mathbf{k})}{2} + \frac{1}{2}\sqrt{(\delta_\mathbf{k} - i(\gamma_X(\mathbf{k}) - \gamma_C(\mathbf{k}))^2 + \Omega_R^2}.$$

In the case of zero detuning ($\delta_\mathbf{k} = 0$ and thus $\hbar\omega_X(\mathbf{k}) = \hbar\omega_C(\mathbf{k}) = \hbar\omega_0(\mathbf{k})$) and with $g = \hbar\Omega_R/2$ they become

$$\hbar\omega_{LP}(\mathbf{k}) = \hbar\omega_0(\mathbf{k}) - i\hbar\frac{\gamma_X(\mathbf{k}) + \gamma_C(\mathbf{k})}{2} - \sqrt{g^2 - \hbar^2\frac{(\gamma_X(\mathbf{k}) - \gamma_C(\mathbf{k}))^2}{4}},$$
$$\hbar\omega_{UP}(\mathbf{k}) = \hbar\omega_0(\mathbf{k}) - i\hbar\frac{\gamma_X(\mathbf{k}) + \gamma_C(\mathbf{k})}{2} + \sqrt{g^2 - \hbar^2\frac{(\gamma_X(\mathbf{k}) - \gamma_C(\mathbf{k}))^2}{4}}.$$

When the interaction between the two oscillators is higher than the combined relaxation term, i.e. $g > \hbar\left|\gamma_X(\mathbf{k}) - \gamma_C(\mathbf{k})\right|/2$, the real parts of $\hbar\omega_{LP}$ and $\hbar\omega_{UP}$ are different the system is in the *strong coupling* regime. Indeed the real parts of the eigenvalues defines their energies and in that case the anticrossing behavior shown in Fig. 2.17 is still verified as well as the all the above discussed arguments are still valid.

However, this is not true if $g < \hbar\left|\gamma_X(\mathbf{k}) - \gamma_C(\mathbf{k})\right|/2$ and the system enters in the so called *weak coupling* regime. The two eigenvalues are now degenerate in energy and the spontaneous emission rate of the emitter X interacting with the optical mode C is

modified. In that case the emitter relaxation by spontaneous emission is characterized by an exponential decay and its spontaneous emission rate is given by [57]:

$$\frac{1}{\tau_{cav}} = \frac{4g^2 Q}{\hbar\omega_0}. \tag{2.22}$$

In order to define a figure of merit to quantitatively evaluate how the cavity acts on the spontaneous emission, the value given by eq.(2.22) should be compared to the free space emission rate of the emitter in a transparent homogeneous medium with refractive index n [57]:

$$\frac{1}{\tau_{free}} = \frac{|\mathbf{d}|^2 \omega^3 n}{3\pi\epsilon_0 \hbar c^3}, \tag{2.23}$$

where $\mathbf{d}$ is the electric dipole of the emitter and ϵ_0 and c the dielectric constant and the speed of light in the vacuum, respectively.

The ratio between τ_{cav} and τ_{free} gives a factor, also called *Purcell factor* F, which is a measure of how much the cavity modify the emission rate of the emitter. F is related to the cavity Q-factor (defined in eq.(2.10)) through the equation [56, 57]

$$F = \frac{3}{4\pi^2} Q \left|\mathbf{a}(\mathbf{r_X})\right|^2 \left(\frac{\lambda}{n}\right)^3, \tag{2.24}$$

where $\mathbf{a}(\mathbf{r})$ is the normalized mode function, $\mathbf{r_X}$ the position of the emitter, n the refractive index of the medium and λ the wavelength of the cavity mode. When F is greater than 1, the emitter radiates faster in the cavity than in free space and the emission is enhanced, otherwise it is quenched. When the emitter is placed in the maximum of the electric field, the Purcell factor can be expressed as a function of the modal volume, i.e. $1/V = max_{\mathbf{r}} \left\{|\mathbf{a}(\mathbf{r})|^2\right\}$, thus resulting [56, 57]

$$F = \frac{3}{4\pi^2} \frac{Q}{V} \left(\frac{\lambda}{n}\right)^3, \tag{2.25}$$

with V that can be also written as

$$V = \frac{1}{\max_r \left\{\varepsilon(\mathbf{r}) \left|\mathbf{E}(\mathbf{r})\right|^2\right\}} \int_V \varepsilon(\mathbf{r}) \left|\mathbf{E}(\mathbf{r})\right|^2 d\mathbf{r}, \tag{2.26}$$

where $\mathbf{E}$ is the localized electric field and ε the dielectric constant of the material composing the cavity.

Chapter 3

Single photon sources based on single nanoemitters

Contents

In past centuries researchers tried for a while to understand the nature of the electromagnetic radiation, and in the early 1900s they began to understand that Maxwell's formalism, introduced in 1861 [58], was not able to describe completely its behavior. The first corpuscular theory was elaborated by Albert Einstein in 1905, who predicted that the electromagnetic radiation is composed by wave packets, called *photons*, each of which with an energy of $h\nu$ [59]. The first experimental evidence of that is considered to be the photoelectric effect (discovered by Hertz in 1886), in which a material emits electrons when irradiated by an UV light. In 1914 Robert A. Millikan re-built Hertz's

experiment and observed several phenomena not explainable by means of classical theory, which where instead confirmed by Einstein's predictions.

In the last decade single photon generation has been an intense research topic due to its potential application in cutting edge research fields such as quantum communication, quantum information and quantum cryptography. In this chapter, after a brief introduction on single photon generation and characterization, a new type of single photon source based on asymmetric core/shell colloidal nanocrystals is proposed and described.

3.1 How to generate single photon beams

3.1.1 Attenuated coherent beams

The simplest way to obtain an approximate single photon flux is to attenuate a pulsed laser beam. In a laser beam the arrival times of the photons follow a Poisson distribution, i.e. the probability to have n photons in a pulse can be written as

$$P(n,\mu) = \frac{\mu^n}{n!} e^{-\mu}, \tag{3.1}$$

where the parameter μ represents the source rate. From the Bayes' theorem, the probability to have more than one photon in a laser pulse is thus [60]:

$$P_{2+} = P(n>1|n>0,\mu) = \frac{P(\{n>1\}\cap\{n>0\},\mu)}{P(n>0,\mu)} = \tag{3.2}$$

$$= \frac{1-P(1,\mu)-P(0,\mu)}{1-P(0,\mu)} = \frac{1-(1+\mu)\,e^{-\mu}}{1-e^{-\mu}} \overset{\mu\to 0}{\simeq} \mu/2. \tag{3.3}$$

For an ideal single photon source one wants to have one photon in each pulse, and the quantity reported in eq.(3.2) should thus be zero. However P_{2+}, also called *fractional information leakage* in the contest of quantum cryptography [60], can be minimized only by bringing μ towards zero. It is thus evident that the attenuation of coherent laser pulses does not allow to obtain efficient single photon generation, because $\mu \to 0$ would means a photon rate of ~ 0.

3.1.2 Fluorescence of a single emitter

An efficient way to generate a single photon flux consists in using the fluorescence of a two level system [61]. Such system, initially in its ground state $|0\rangle$, can be brought in its excited stated ($|1\rangle$) by a continuous wave or a pulsed laser beam. In a simple picture, the system remains in the state $|1\rangle$ up to the spontaneous relaxation toward the state $|0\rangle$ loosing the exceeding energy by emitting a photon.

Let us suppose that:

- the duration of the excitation pulse is shorter than the lifetime of the excited level ($\tau_{|1\rangle \to |0\rangle}$) in order to have a single cycle of absorption and re-emission,
- the period of the laser pulses is longer than $\tau_{|1\rangle \to |0\rangle}$,
- the excitation pulse intensity is high enough to stimulate the transition $|0\rangle \to |1\rangle$,
- the relaxation $|1\rangle \to |0\rangle$ is purely radiative.

Under these hypotheses, in a single transition $|1\rangle \to |0\rangle$ there is no way to have the emission of more then one photon, and its probability $P_{2+} = P(n > 1|n > 0)$ goes automatically to zero. Moreover, in the case of a pulsed laser beam, if each exciting pulse generates a transition $|0\rangle \to |1\rangle$, the photons are emitted *on-demand*, i.e. triggered by the excitation pulse.

The fluorescence of a single emitter acting as a two-level system represents thus an efficient way to generate fluxes of triggered single photons, as also demonstrated by the first experiments with Sodium and Manganese atoms, performed in 1977 and 1985, respectively [62, 63].

The excitation and the radiative relaxation of a two-level system are well described by the *Fermi's golden rule*, for which the transitions $|0\rangle \to |1\rangle$ and $|1\rangle \to |0\rangle$ follow an exponential statistics with parameters k_p and k_{rad}, respectively. The emission statistics can be fully characterized by the time distribution of the absorption-emission cycle $d(\tau)$ (also called *delay function*). In the case under examination, $d(\tau)$ is the convolution

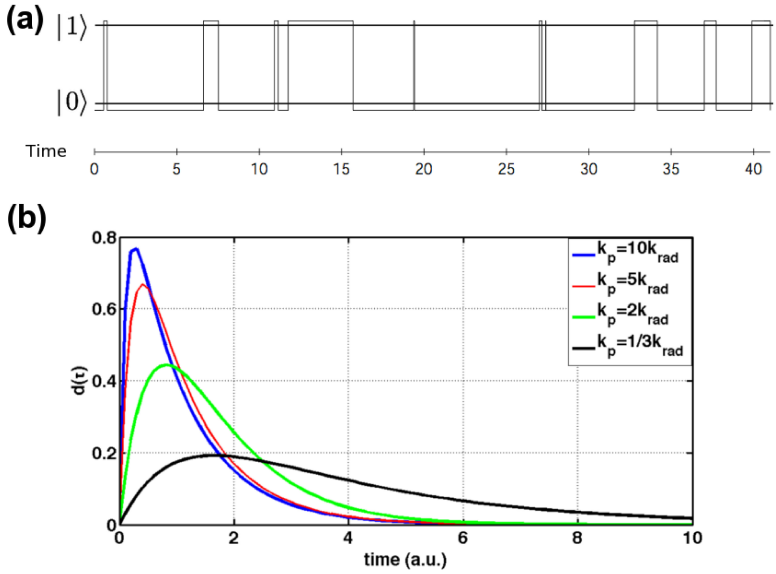

Figure 3.1: **(a)** Schematic representation of the transitions between $|0\rangle$ and $|1\rangle$ for $k_p = 3k_{rad}$. **(b)** $d(\tau)$ behavior for several values of the ratio k_p/k_{rad}.

between the time distributions given by the Fermi's golden rule, i.e. [64–67]

$$d(\tau) = \frac{k_p k_{rad}}{k_p - k_{rad}} \left[e^{-k_{rad}\tau} - e^{-k_p\tau} \right]. \tag{3.4}$$

A typical events flux is shown in Fig. 3.1(a), while the characteristic behavior of $d(\tau)$ is reported in Fig. 3.1(b). If $k_p \gg k_{rad}$ the delay function become

$$d(\tau) = k_{rad} e^{-k_{rad}\tau}. \tag{3.5}$$

3.2 Single photon sources characterization

3.2.1 The second order autocorrelation function

The characterization of a single photon beam is usually performed monitoring the photons detected at two different time instants t_1 and t_2. This can be done by measuring the *second order autocorrelation function* of the electric field intensity associated to the beam, defined as [68]

$$g^{(2)}(t_0,t)=\frac{\langle E^*(t_1)E^*(t_2)E(t_1)E(t_2)\rangle}{\left\langle|E(t_1)|^2\right\rangle\left\langle|E(t_2)|^2\right\rangle}=\frac{\langle I_i(t_1)I_i(t_2)\rangle}{\langle I_i(t_1)\rangle\langle I_i(t_2)\rangle}, \tag{3.6}$$

where $\langle\cdot\rangle$ represents the statistic average.

3.2.1.1 Classical radiation

In the case of classical light beams, $I_i(t)$ should respect the Cauchy-Schwartz inequality, i.e.

$$\langle I_i(t_1)I_i(t_2)\rangle^2\leq\left\langle I_i^2(t_1)\right\rangle\left\langle I_i^2(t_2)\right\rangle \tag{3.7}$$

Moreover, in the case of stationary stochastic processes (i.e. statistical averages do not depend on the initial time instant $t_1=t$ but only on the difference between $t_1=t$ and the current time $t_2=t+\tau$) it is possible to write:

$$\begin{cases} g^{(2)}(t_1,t_2)=g^{(2)}(\tau) \\ \\ \langle I_i^2(t_1)\rangle=\langle I_i^2(t_2)\rangle \end{cases} \Rightarrow\quad \langle I_i(t)I_i(t+\tau)\rangle^2<\langle I_i^2(t)\rangle^2\quad\Rightarrow \tag{3.8}$$

$$\Rightarrow\langle I_i(t)I_i(t+\tau)\rangle<\langle I_i^2(t)\rangle\Rightarrow\frac{\langle I_i(t)I_i(t+\tau)\rangle}{\langle I_i(t)\rangle^2}<\frac{\langle I_i^2(t)\rangle}{\langle I_i(t)\rangle^2}\Rightarrow g^2(\tau)<g^2(0), \tag{3.9}$$

with $\tau=t_2-t_1$. In the same way, it is possible to show that $\langle I_i^2(t)\rangle\leq\langle I_i(t)\rangle^2$, thus meaning $1\leq g^{(2)}(0)$ [68]. $g^{(2)}(0)=1$ means that there is no correlation between two simultaneous photodetections, i.e. a source can not emit a beam able to produce single detections and thus, for the classical theory, single photon sources do not exist.

3.2.1.2 Corpuscular light beams

In a more general picture, one should take into account the quantum nature of the light. In a quantum description of the electromagnetic field, the electric field can be written as:

$$E(t)=E^{(+)}(t)+E^{(-)}(t), \tag{3.10}$$

where $E^{(-)}(t)$ is the Hermitian conjugate of $E^{(+)}(t)$. The second order autocorrelation function is thus:

$$g^{(2)}(t_1,t_2)=\frac{\left\langle E^{(-)}(t_1)E^{(-)}(t_2)E^{(+)}(t_2)E^{(+)}(t_1)\right\rangle}{\left\langle E^{(-)}(t_1)E^{(+)}(t_1)\right\rangle\left\langle E^{(-)}(t_2)E^{(+)}(t_2)\right\rangle}=\frac{\langle I_i(t_1)I_i(t_2)\rangle}{\langle I_i(t_1)\rangle\langle I_i(t_2)\rangle}, \tag{3.11}$$

The main difference is that now $E^{(+)}(t_1)$ and $E^{(+)}(t_2)$ do not commutate and the Cauchy-Schwartz inequality cannot be exploited and then values of $g^{(2)}(0)<1$ are allowed.

The second order autocorrelation function corresponds to the correlations between two events detected at the time instants $t_1=t$ and $t_2=t+\tau$, and the photon detection event corresponds to the application of the annihilation operator $E^{(+)}$. If η is the detection efficiency (supposed to be equal at the two time instants) the probability to detect a photon at the time instant t_1 and another one at the time instant t_2 can be written as:

$$P(t_1,t_2)=\eta^2\left|E^{(+)}(t_2)E^{(+)}(t_1)\,|i\rangle\right|^2=$$
$$=\eta^2\,\langle i|\,E^{(-)}(t_1)E^{(-)}(t_2)E^{(+)}(t_2)E^{(+)}(t_1)\,|i\rangle\ .$$

Equation (3.11) thus became

$$g^{(2)}(\tau)=\frac{P(t,t+\tau)}{P(t)P(t+\tau)}=\frac{P(t+\tau|t)}{P(t+\tau)}. \tag{3.12}$$

$g^{(2)}(\tau)$ is thus proportional to the probability to detect a photon at the time instant $t+\tau$ when another one has been received at t, while the normalizing factor is the probability to detect a photon at the generic instant t. The following situations are thus possible:

if $g^{(2)}(0)>1$ packets of photons are generated by the source and the flux is called *super-poissonian*. Examples of this situation, also called *photon bunching*, are the black body radiation and the stimulated emission, which allows the generation of photons in the same state, thus leading to an excess of correlation.

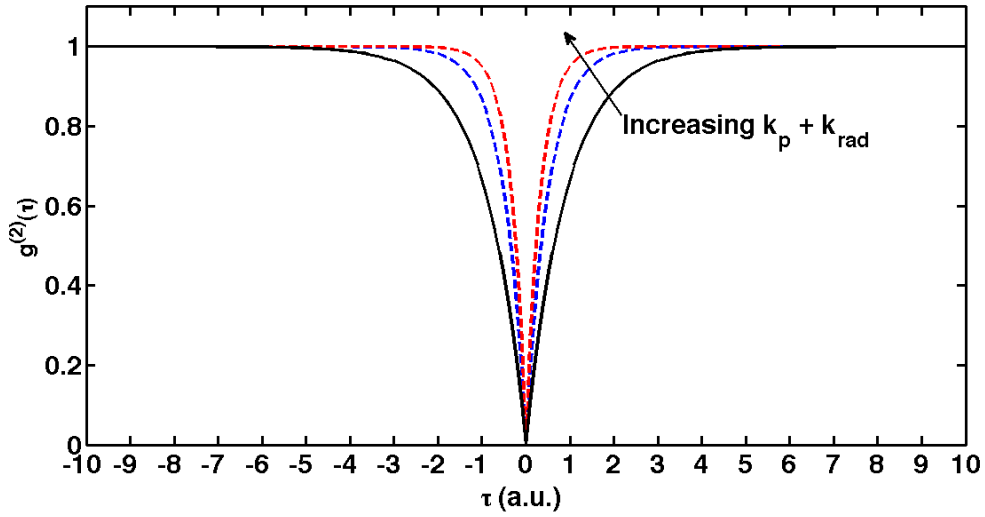

Figure 3.2: $g^{(2)}(\tau)$ function behavior for several values of $k_p + k_{rad}$.

if $g^{(2)}(0) = 1$ the probability to detect a second photon at the time instant t does not depend on what is happened at t (i.e. $P(t|t) = P(t)$). All detection events are thus independent and the source is called *poissonian*.

if $g^{(2)}(0) < 1$ the photon flux is *antibunched*, the beam is called *sub-poissonian* and the photons come from a non classical system. That is the case of an ideal single photon source, for which two photons are never emitted at the same time, i.e. $P(t + 0|t) = 0 \Rightarrow g^{(2)}(0) = 0$.

3.2.1.3 Continuous excitation of a two level system

In the case of a continuous wave excitation beam the second order autocorrelation function of the light emitted by a two level system can be theoretically calculated from the distribution $d(\tau)$ obtaining [68]

$$g^{(2)}(\tau) = 1 - e^{-(k_p + k_{rad})|\tau|}, \tag{3.13}$$

with k_p and k_{rad} defined in section 3.1.2. The behavior of $g^{(2)}(\tau)$ for several values of the rates k_p and k_{rad} is reported in Fig. 3.2, evidencing that, since $g^{(2)}(0) = 0$, the source is sub-poissonian.

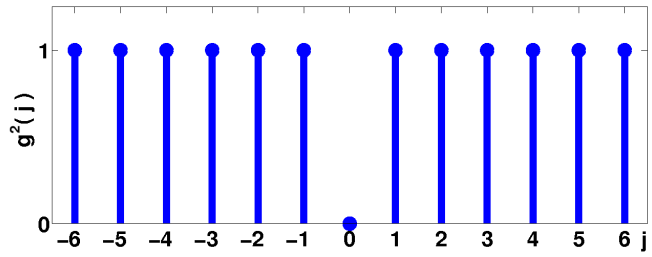

Figure 3.3: Theoretical representation of $g^{(2)}(j)$ for a single photon source obtained with purely radiative transition of a two level system.

3.2.1.4 Pulsed excitation of a two level system

In the case of a pulsed excitation, $g^{(2)}(i,j)$ (the time variables are now discretized) is given directly by eq.(3.12): it is the conditional probability to detect a photon at the $j-th$ time instant when another photon has been received at the $i-th$ instant normalized to the probability to detect a photon at the generic time instant i.

Let us consider a single photon source based on a two level system which emits one photon by exploiting the transition $|1\rangle \rightarrow |0\rangle$ and that this photon can be detected with probability P_1. In the ideal case the single transition does not lead to any pair of photons, thus resulting in $P_{2+} = 0$. As a consequence

$$P(j=0|i=0) = 0, P(j=1|i=0) = P_1, \ldots, P(j=k|i=0) = P_1 \quad \forall \quad k>0, \quad (3.14)$$

while

$$P(j=0) = P_1, P(j=1) = P_1, \ldots, P(j=k) = P_1 \quad \forall \quad k>0. \quad (3.15)$$

As a consequence:

$$g^{(2)}(j) = \begin{cases} 0 & if \quad j=0 \\ 1 & if \quad j \geq 1 \end{cases} \quad (3.16)$$

In summary, in the case of single photon source based on a two level system and excited by a pulsed laser, the autocorrelation function is a discretized Dirac comb with a missed pulse at the time $j=0$ (see figure Fig. 3.3).

3.2.1.5 About the pulse duration

The previous paragraph supposes that the excitation is constituted by ideal Dirac's pulses and that the relaxation $|1\rangle \rightarrow |0\rangle$ happens instantaneously. However the duration of the excitation pulses is finite and the relaxation dynamic of the two level system depends on both k_p and k_{rad} (see paragraph 3.1.2 for definitions). First of all, the excitation pulse duration τ_p should be shorter than the lifetime of the excited state (i.e. $\tau_p \ll 1/k_{rad} = \tau_{rad}$), in order to avoid multiple excitation of the system within the same pulse. Under this hypothesis, the probability P_σ to excite the system from $|0\rangle$ to $|1\rangle$ is [69]

$$P_{\sigma(k_p)} = \frac{k_p}{k_p + k_{rad}} \left(1 - e^{-\tau_p(k_p+k_r)}\right) \overset{\tau_p \ll \tau_{rad}}{\approx} 1 - e^{-\tau_p k_p}. \tag{3.17}$$

It is thus evident that in order to obtain $P_{\sigma(k_p)} \rightarrow 1$ and to fulfill at the same time the condition of short pulse the following relation should be true:

$$k_{rad} \ll 1/\tau_p \ll k_p. \tag{3.18}$$

3.2.1.6 About the finite lifetime

The photon auto-correlation function shown in Fig. 3.3 supposes that the transition $|1\rangle \rightarrow |0\rangle$ takes place instantaneously (i.e. the lifetime of the excited state is very short). However, as already mentioned, the transition time follows an exponential distribution with characteristic time $1/k_{rad}$ and the autocorrelation function assumes the behavior reported in Fig. 3.4. The absence of the peak at $\tau = 0$ still evidences the single photon regime of the beam, and each peak follows a decreasing exponential function of parameter k_{rad}.

3.2.2 Experimental characterization

In order to measure the autocorrelation function of an antibunched photon flux it is necessary to use detectors able to distinguish single photon events, such as photomultiplier tubes or single photon Avalanche PhotoDiodes (APDs). However these detectors

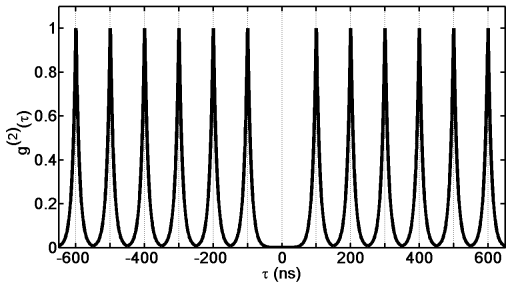

Figure 3.4: Theoretical representation of $g^{(2)}(\tau)$ for a two level system excited by a pulsed laser beam taking into account the finite lifetime of the transition $|1\rangle \rightarrow |0\rangle$, with $\tau_{rad} < T_p$. The transition $|1\rangle \rightarrow |0\rangle$ is considered purely radiative, while the transition $|0\rangle \rightarrow |1\rangle$ is induced each $T_p = 100ns$.

often suffer of important drawbacks that do not allow them to distinguish between bunched and antibunched photon fluxes. One of the most important is the so-called *dark time*, typic of APDs: when a photon is detected by an APD, a finite time τ_{dark} is needed to repopulate the p-n junction. This means that for a time interval τ_{dark} the photodiode cannot detect any other photon and several simultaneous detection events can be interpreted as a single photon event. It is thus evident that, in the case of a two level system, if the photon antibunching is observed on characteristic times $\tau_r < \tau_{dark}$, a single APD is not suitable to measure the autocorrelation function.

This problem can be overtaken by using a method developed in 1956 by Robert Hanbury Brown and Richard Q. Twiss [70] with the aim to measure the second order autocorrelation function of the light emitted by the star Sirius. In its quantum revisitation this technique foresees to measure the second order autocorrelation function for single photon events using two detectors.

3.2.2.1 The Hanbury Brown and Twiss (HBT) detection scheme

In the HBT detection scheme, sketched in Fig. 3.5, photons impinging on a 50%/50% beam splitter are split towards two fast detectors (for example two APDs), one defined as "Start" and the other as "Stop" detector. When a photon is received by the start

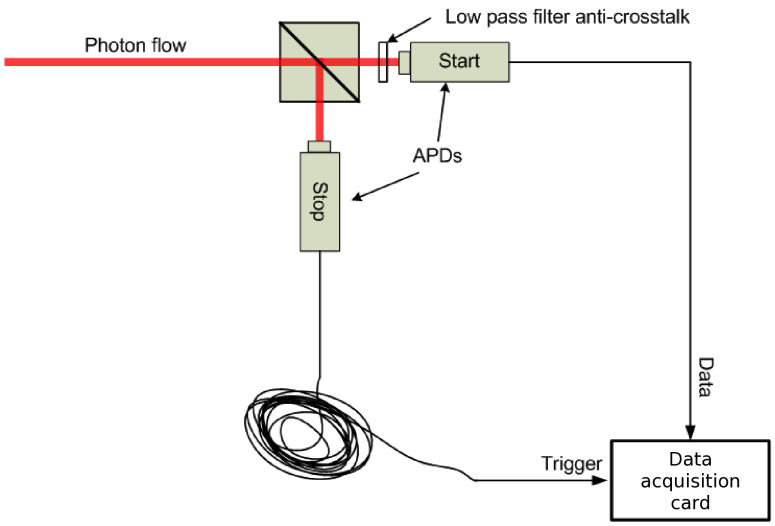

Figure 3.5: Schematic representation of an HBT detection based on two APDs.

detector, the delays between this event and all the photons received by the stop detector in a time window of a fixed duration T_w can be measured and stored. Repeating the process for a number of start photons N_{start}, the coincidence histogram $h(\tau)$ of the delays between the received photons on the start and stop detectors can be extrapolated. $h(\tau)$ represents a non-normalized stochastic estimation, on a given number of time windows, of the probability $P(t+\tau|t)$ to detect a photon at the time $t+\tau$ (which is the time at which the stop events have been recorded) when a photon has been already received at the time instant t (the time at which the corresponding start event has been recorded). As described by equation (3.12), $P(t+\tau|t)$ is proportional to the autocorrelation function, and $h(\tau)$ can be thus considered a direct estimation of $g^{(2)}(\tau)$.

3.3 Single emitters for single photon generation

In past years several materials have been suggested to be single photon emitters. For instance, across 1977 and 1986 isolated mercury, sodium and barium atoms were demonstrated to be able to emit antibunched photon fluxes [62,63,71]. With the development

of novel and flexible techniques to optically probe and study single atoms [72] and the rising up interest in cavity quantum electrodynamic (cQED), the attention of scientific community in this field focused on weak and strongly coupled systems [73–75].

An alternative to single atoms are single molecules, and several works have been carried out in past years [42, 76–79]. An important result with these emitters has been obtained in January 2011 [14]: K. G. Lee and collaborators embedded a *terrylene* molecule in a layered structure in order to modify its radiation diagram and to re-address all photons in the collection cone of the microscope objective, reaching a photon rate of $\sim 50 \cdot 10^6$photons/second [14] together with a collection efficiency of $\sim 94\%$.

Another robust system to emit single photons on demand at room temperature is provided by individual nitrogen-vacancies (NVs) in bulk diamond and diamond nanocrystals (NCs) [80–84]. NV in diamond NCs can be considered as punctual non-classical light sources [80–82] and can be coupled with photonic crystals nanocavities [85, 86] or manipulated by properly developed nanotechnologies [87]. Moreover, a new technological approach proposed by Babinec and collaborators [12], allows to embed a single NV vacancy in a diamond nanowire, leading to extremely high photon extraction efficiency and detected rates of $\sim 2.5 \cdot 10^5$ photons/second in continuous wave pumping regime. The ability to readily fabricate these single defect centers has resulted in the commercialization of the first SPS based on the NV defect in diamond [88] and their application to quantum cryptography [83, 89, 90].

Also epitaxial semiconductor quantum dots (QDs) are promising nanostuctures for the realization of real single photon devices. As mentioned in section 2.1.3, the Stransky-Krastanov (SK) growth method is one of the most common procedure to realize QDs, while droplet epitaxy or situ-defined procedures do not reach the same versatility. In the matter of single photon generation, in last years the scientific community focused its activity on two aspects: the operation temperature and the single photon efficiency. The SK procedure exploits the lattice constant mismatch between two crystalline materials in order to create the nucleation of quantum dots on a flat

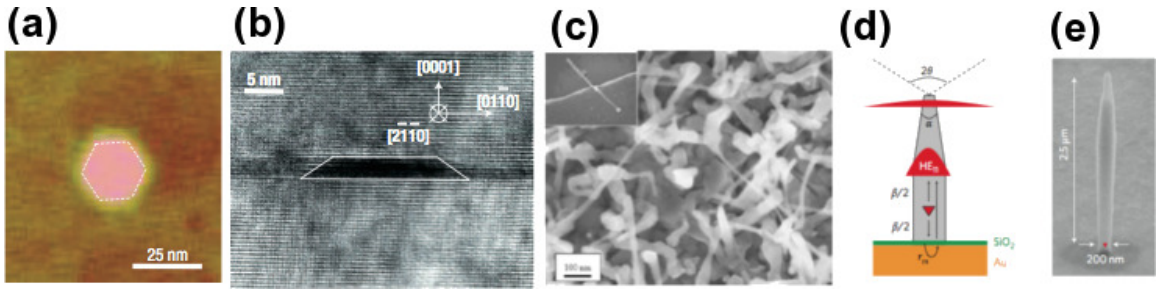

Figure 3.6: In plane atomic force microscope **(a)** and cross-section **(b)** scanning electron microscope (SEM) of the a GaN/AlN QD [Images reproduces from ref. [41]]. **(c)** SEM image of a CdSe dot in a ZnSe wire [Image reproduced from ref. [91]]. **(d)** Sketch and SEM image of QD in nanowire structures [Images reproduces from ref. [13]]

crystalline substrate [36]. These self-assembled structures are usually pyramidal or lens shaped, with a lateral size in the range $10 \div 20nm$ and vertical dimensions of few nanometers (see for instance the structures reported in Fig.s 3.6(a) and (b)). These dimensions and the irregular shape do not allow SK QDs to be single photon emitters at room-temperature, due to the low distance between the confined energy states. However, it is well known that they are able to generate stable flux of single photons at cryogenic temperatures of $T \sim 4K$. The two highest operation temperatures of single SK QDs as single photon emitter have been reported in 2006 and 2008, with GaAN/AlN QDs ($T \sim 200K$) [41] and CdSe QDs in ZnSe nanowires ($T \sim 220K$) [91], respectively (see Fig.s 3.6(a), (b) and (c)).

An epitaxial QD is usually embedded in a semiconductor matrix, which has a refraction index higher than the surrounding air, from which the QD luminescence is usually collected. This configuration leads to poor collection efficiency, also at very low temperature. A solution to this problem has been proposed in 2010 by J. Caludon and coworkers [13], who recently showed that encapsulating a single InAs QD in a GaAs photonic nanowire (PNW) it is possible to reach collection efficiencies of $\sim 72\%$, reaching a single photon flux of $\sim 55 \cdot 10^6$ photons/second in the first lens of the collection setup in the case of pulsed excitation at a rate of ~ 80MHz.

Another suitable way to tailor and enhance the emission of single photon sources is to embed the single quantum emitter in a micro or nanocavity. Both weak and strong coupling regime, discussed in section 2.3, can lead to single photon generation. Weak coupling enhances the spontaneous emission, and the final emission rate Γ_{X-C} is related to the rate of the uncoupled emitter Γ_X via the relation $\Gamma_{X-C} = \Gamma_X F_p$, where F_p is the Purcell factor, already defined in eq.(2.25). Several single dot-cavity coupled systems have been proposed in past years, including photonic crystals cavities [92], microdisk resonators [93], pillar microcavities [94, 95] and micropillar photon molecules [96].

The way to obtain single photon generation in strongly coupled systems is based on the equivalent for photons of the Coulomb blockade, also called *photon quantum blockade*. It is a phenomenon preventing the resonant injection of more than one photon into a mode of a non-linear cavity, leading to photon antibunching in photon-autocorrelation measurements. If a two level system is strongly coupled to a cavity, the mechanism underlying photon blockade is the anharmonicity of the Jaynes-Cummings ladder of eigenstates. In that case the eigenstates are grouped into two-level manifolds denoted $|n, \pm\rangle$ with energies $\hbar\omega_{n,\pm} = \hbar\left(n\omega_0 \pm g\sqrt{n}\right)$, where n is the number of energy quanta in the system and ω_0 is the bare-cavity frequency. If the system is pumped at energy $\hbar\omega_{pump} = \hbar\left(\omega_0 + g\right)$, this pump is resonant with the first-order manifold, but detuned from transitions to the second manifold which has an energy $\hbar\omega_{1\to 2} = \hbar\left[\omega_0 + g\left(\sqrt{2} - 1\right)\right]$, thus giving rising to the photon blockade phenomenon (see Fig.3.7 for a sketch of eigenstates structure). This operation regime has been reached with both single atoms trapped in optical cavities and single quantum dots in photonic crystals nanocavities in 2005 and in 2008 [97, 98] and with two different spectroscopic methods, i.e. transmission and reflection spectroscopy, respectively (see Fig.s 3.7(b) and (c) for an optical sketch of the proposed configurations).

Moreover, other theoretical works proposed the realization of the *polariton quantum blockade* and of the photon blockade through quantum interferences in photonic molecules [29, 99, 100]. In the case of polariton blockade [29], the strong polariton-

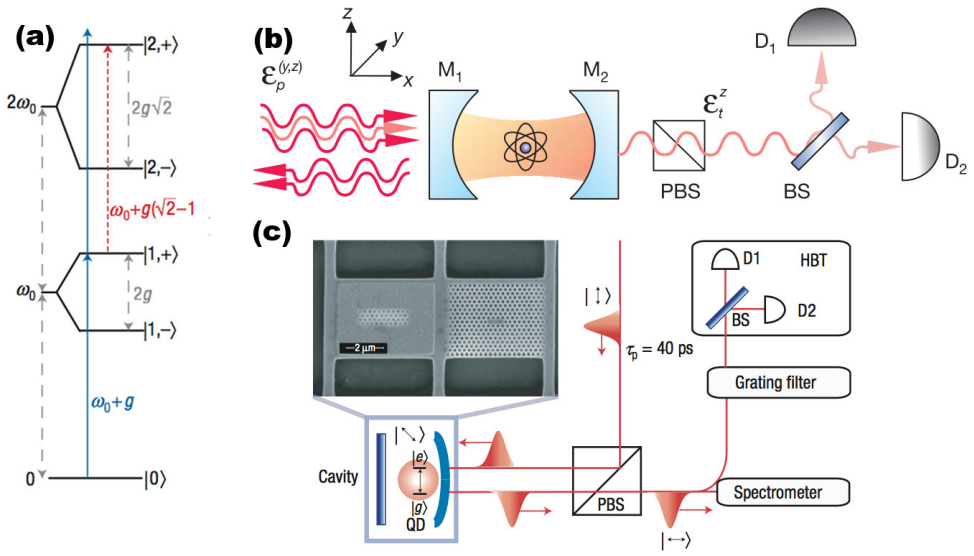

Figure 3.7: **(a)** Sketch of eigenstates structure of a anharmonic. [Figure reproduced form ref. [97]] **(b)** Optical setup used by Birnbaum and coworkers to realize the photon blockade experiment with a single atom trapped in an optical cavity [Figure reproduced form ref. [98]]. **(c)** Optical setup used by Faraon and coworkers to realize the photon blockade experiment with a single QD in a photon crystal cavity [Figure reproduced form ref. [97]].

polariton repulsive interaction forbid two polaritons to coexist in the same cavity if the modal volume of the localized electromagnetic field is sufficiently small: if only one polariton is excited in the cavity, it can re-emits only a single photon.

3.4 Single photon generation with semiconductor colloidal nanocrystals

As already mentioned, Stransky–Krastanov grown QDs are catching the attention of scientific community, but are still limited by the operating temperature, far from 300 K [41,91]. On the other hand, wet-chemically synthesized colloidal core/shell nanocrystals (NCs), sketched in Fig. 3.8(A), are promising single photon emitters for room temperature applications [11], due to the well separated quantum energy states, the low cost synthesis, the broad tunable emission range, and the compatibility with planar

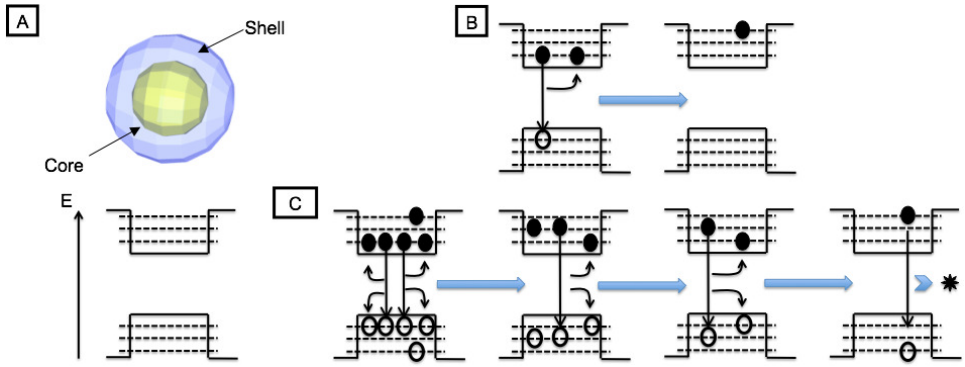

Figure 3.8: **(A)** Schematic representation of a colloidal nanocrystal and its bandstructure. **(B)** Non-radiative Auger recombination in the case of a charged nanocrystal. **(C)** Non-radiative Auger recombination when more then one e-h pair is excited in the nanocrystal.

nanofabrication technology [101–104].

Carrier-carrier interactions in colloidal NCs are enhanced by virtue of the high confinement induced by the small dimensions. The efficiency of the non-radiative Auger recombination process is therefore strongly enhanced and becomes efficient at room temperature. Auger effect is the cause of blinking and single photon emission, and thus represents one of the most interesting phenomena in these nanoparticles. It relies in the energy transfer from an electron-hole (e-h) pair recombination to other carriers present in the NC [69, 105, 106]. Two important situations in which it takes place are schematized in Fig.3.8(B) and (C). If a NC is initially ionized (for example because of thermal- or photo-ionization) and an e-h pair is excited in the nanoparticle, the Auger process constrains the e-h pair to recombine in a non-radiative way by transferring its energy to the localized charge (Fig.3.8(B)). The NC remains thus ionized and the photon emission is forbidden until the charge neutrality is recovered. Instead, if more than one e-h pair are excited in the NC (Fig.3.8(C)) and if the NC is not ionized, the carrier pairs recombine through the Auger process and transfer their energy to each other. When just one pair remains in the NC, it rapidly relaxes and then recombine emitting a photon.

The picture that can be deduced from these considerations is the following. If the

Auger recombination is efficient, a charged NC cannot emit, thus leading to the PL fluctuations known as blinking. If the NC is initially neutral and more than one e-h pair are excited in the structure, they have a very high probability to recombine non-radiatively through the Auger mechanism until a single e-h pair remains in the NC, that can recombine through the emission of a single photon.

Auger process is also responsible for the emission intensity saturation usually observed in colloidal nanocrystals. Let suppose that the NC is excited by a pulsed laser beam and let call N the number of e-h pairs excited in the NC in a laser pulse. If the non-radiative Auger energy transfer between e-h pairs is not efficient, multi excitonic states (mX) are allowed to bind. If Q_{mX} is the quantum yield of the m-th multiexcitonic state (i.e. the radiative recombination probability of m e-h pairs in the nanocrystal per laser pulse), the time integrated photoluminescence intensity of a colloidal NC as a function of the average number of e-h pair excited in the nanocrystal for each laser pulse can be modeled as follows [107]:

$$I\left(\langle N\rangle\right) = \sum_{N=1}^{\infty}\left[P\left(N,\langle N\rangle\right)\sum_{m=1}^{N} Q_{mX}\right]. \tag{3.19}$$

where $P\left(N,\langle N\rangle\right)$ is the Poisson's distribution of average $\langle N\rangle$. If the Auger process forbids multiexciton binding (i.e. $Q_{mX} = 0 \quad \forall m > 1$), eq. (3.19) become [107]

$$I\left(\langle N\rangle\right) = 1 - e^{-\langle N\rangle}, \tag{3.20}$$

and $I\left(\langle N\rangle\right)$ follows the saturation behavior displayed in Fig. 3.9. On the contrary, if the Auger process is not taken into account, all quantum yields are equal to unity (i.e. $Q_{mX} = 1 \quad \forall m > 0$) and $I\left(\langle N\rangle\right)$ is proportional to $\langle N\rangle$, as shown by the dashed line in Fig. 3.9, and each e-h pair injected in the NC is allowed to radiatively recombine.

It is thus evident that the Auger recombination takes an important role in the charge dynamics of colloidal nanocrystals and it is, at the same time, the cause of drawbacks (for instance blinking and spectral diffusion) and the physical phenomenon at the basis of the room-temperature operation of these nanoparticles as single photon emitters. Recently, several techniques have been proposed to tailor the efficiency of

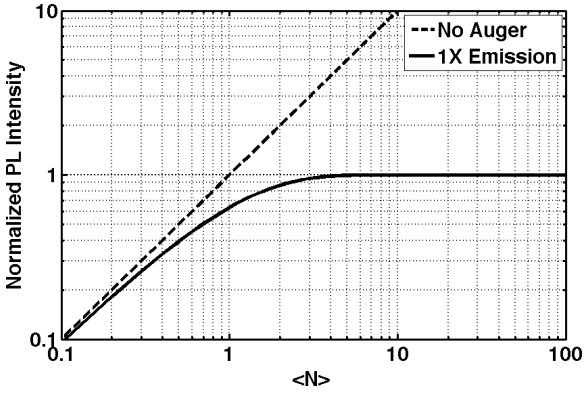

Figure 3.9: The **black continuous line** is a typical behavior of the normalized PL intensity I of a colloidal nanocrystal as a function on the average number of e-h pairs injected in the NC for each laser pulse. If Auger process is efficient, the quantum yields of multiexcitonic states Q_{mX} is negligible, and $I(\langle N\rangle) = 1 - e^{-\langle N\rangle}$. If this does not happen, full PL intensity saturation is not expected, up to the limit of $Q_{mX} = 1 \quad \forall m > 0$, for which $I(\langle N\rangle)$ is proportional to $\langle N\rangle$, as shown by the **black dashed line**.

the Auger effect in order to engineer NCs spontaneous emission and to reduce blinking [16, 17, 103, 106–109]. These strategies can be substantially divided in two types; one relies in tailoring nanocrystals shape and size in order to engineer electrons and holes wavefunctions [16, 17, 106, 107], while the other one foresees the coupling of NCs with photonic nanostructures [103, 108]. The first one is investigated in this chapter, while the second one will be the subject of chapter 4.

3.4.1 Semiconductor colloidal nanocrystals in nanocavities

The insertion of an ensemble of colloidal quantum dots in vertical microcavities with distributed Bragg reflectors has been demonstrated using different techniques [110,111], and among them, the ones which rely on a post processing of the structure by using focused ion beam (FIB) [112] or by imprint lithography [111] to obtain micropillars have raised a broad interest. However, very few papers in the literature report on single NC embedded in microcavities and efficiently emitting triggered single photons at room

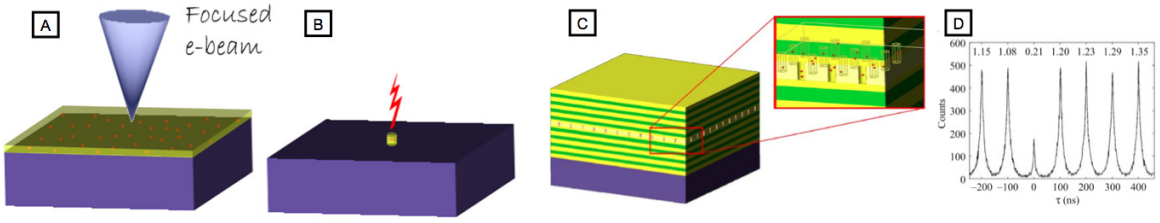

Figure 3.10: **(A)** Schematic representation of the localization of single colloidal quantum dots by direct electron beam lithography of a resist/NCs blend. **(B)** By a careful control of the molar density of the NCs dispersed in the resist and pillar volume it is possible to isolate single QDs. **(C)** Schematic of single colloidal quantum dots microcavity array obtained by direct electron beam lithography and SiO2/TiO2 DBR deposition. **(D)** Histogram of coincidence counts of fluorescence from a single QD in microcavity.

temperature. A single CdSe/ZnS colloidal QD has been successfully coupled to whispering gallery modes generated on the surface of glass and polymer microspheres by Artemyev and collaborators [113], who reported a Purcell factor $F_p \sim 10$. The same group also obtained strong coupling using anisotropically-shaped CdSe nano-crystal coupled to a single photon mode of a polymer microsphere, showing a vacuum Rabi splitting between 30 and $45\mu eV$ [114]. Recently, a new approach has made possible the pinpointing of single colloidal quantum dots by direct electron beam lithography. The controlled localization of ordered arrays of single colloidal nanocrystals has been demonstrated in ref. [115] by dispersing a specific concentration of nanocrystals inside a negative high-resolution electron-beam resist. In this way, ensembles of nanocrystals embedded in electronic resists can be easily patterned by means of traditional lithographic processes, since the presence of semiconductor clusters in the matrix does not significantly affect the sensitivity of the polymeric host and, at the same time, the emission properties of the nanocrystals are not influenced by the interaction with the electron beam [101, 102, 104, 115]. Through a careful control of molar density of the dispersed NCs and of the patterning of nanosized pillars in the NC/resist blend with well tuned diameters, it is possible to obtain a very high probability of having single

colloidal NCs localized in a single nanopillar (Fig.s 3.10(A) and 3.10(B)). An approach to localize a single NC in a photonic cavity, proposed by A. Qualtieri and collaborators [103], relies in the exploitation of the above-described localization technique on top of a SiO2/TiO2 Bragg mirror. Covering the array of localized single quantum emitters by a second DBR (Fig. 3.10(C)), they obtained a non-classical emission from single nanocrystals in microcavity at room temperature (Fig. 3.10(D)). As shown in ref. [103], this method allows to obtain a Purcell factor of 2.4, approaching the theoretical predictions [116].

3.5 Colloidal dots in rod: an engineered structure for a novel source of single photons

One of the limiting feature of spherical colloidal nanocrystals is that their light emission is not linearly polarized [117, 118]. For this purpose, since 2000 the attention of scientific community in the field of colloidal NCs focused on the realization of asymmetric structures to obtain polarized light emitters [119]. The first synthesis procedure to realize such structures was developed by Peng and co-workes [119], whose work showed that it is possible to realize elongated nanocrystals, called *nanorods* (NRs). This result opened a new research line, in particular after the experimental verification of the linear polarization of the radiation emitted by a single NR [120,121]. Up to now, several asymmetric nanocrystals (summarized in Fig. 3.11) have been proposed in the literature, and among them of remarkable importance are nanorods [119], core/shell nanorods [122], thetrapods [123], dot-in-rod [124], dot-in-thetrapod [125], and rod in rod [126], each of which with interesting emission properties obtained by tailoring the electrons and holes wavefunctions.

In particular, CdSe/CdS dots-in-rods (DRs), obtained by surrounding a spherical CdSe core with an elongated CdS shell, turn out to be very promising quantum emitters by virtue of their interesting ensemble polarization properties [127] and of their dipole-

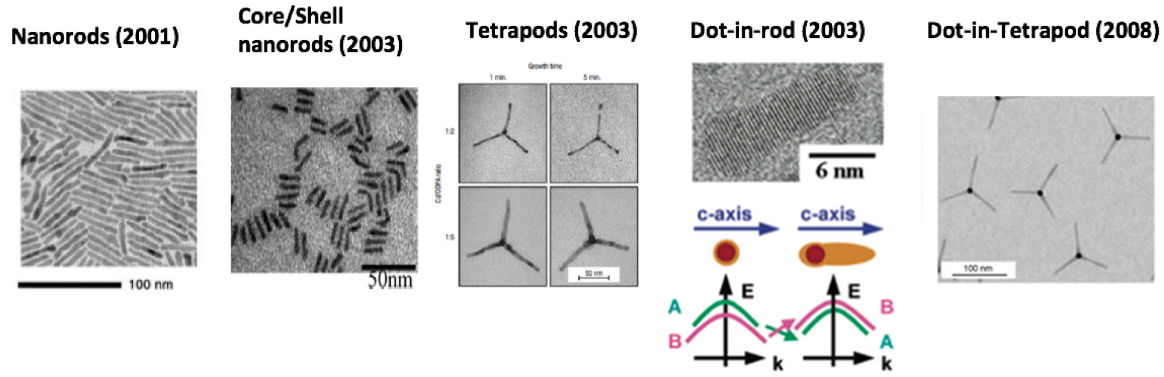

Figure 3.11: **(a)** Nanorods. Reproduced from ref. [119]. **(b)** Core/Shell Nanorods. Reproduced from ref. [122]. **(c)** Tetrapods. Reproduced from ref. [123]. **(d)** Dot-in-rods. Reproduced from ref. [124]. **(e)** Dot-in-tetrapods. Reproduced from ref. [125].

like emission. In addition, they exhibit short lifetime [128] and quantum efficiency of 75%, which can be further improved by surrounding the CdSe/CdS nanocluster with additional ZnS shell layers [129], thus obtaining a CdSe/CdS/ZnS structure.

Compared to core NRs and CdSe/ZnS core/shell NRs, the use of a CdS shell, having low lattice mismatch with the CdSe core, minimizes the influence of surface traps between core and shell on the radiative recombination process, which occur in the low band gap core. This therefore avoids the well-known increase of the average radiative lifetime of the system due to the interaction of excitons with surface traps at the core/shell interface [130].

After a brief review of an innovative synthesis procedure to realize high aspect-ratio DRs, this section describes the experimental results of a deep spectroscopic investigation on these nanoparticles, showing their suitability as room-temperature, polarized and stable sources of single photons with extremely reduced blinking.

3.5.1 A seeded-growth approach

The *seeded-growth* (SG) approach has been proposed by L. Carbone and co-workers in 2007 and allows to synthesize asymmetric nanocrystals starting the shell growth from a preformed seed (a sketch of the synthesis procedure is reported in Fig. 3.12(a)). When compared to other techniques based on the classical synthesis of core/shell nanocrystals, it presents several advantages. In particular, in the case of DRs

- the range of the rods aspect ratio (rod length/rod diameter) achievable with the SG synthesis (up to 30:1) is much wider than the one achievable with other synthesis schemes (for which the maximum reported aspect ratio was 4:1),
- because of the high growth temperature, large aspect ratio rods can be synthesized preserving regular shapes and the obtained nanoparticles show no tendency to aggregate,
- the original seed is preserved in the final rod structure as well as the location of the seed along the rod. This can be partly elucidated by carrying out geometric phase analysis, which is a quantitative high-resolution transmission electron microscopy (HRTEM) technique (described below).

The CdSe/CdS DRs used in this work were synthesized using the procedure reported in Ref. [127] and summarized in appendix C.1.

A typical output of the synthesis procedure is reported in Fig. 3.12(b), obtained by a Transmission Electron Microscope (TEM). The structural parameters of a single DR have been evaluated by high-resolution (HR) TEM and a result of this measurement on a single nanoparticle is reported in Fig. 3.12(c). It is useful to graphically elaborate the HRTEM image to obtain more information on the structural parameters of the DR, performing the above mentioned geometric phase analysis. In particular in Fig. 3.12(d) a color scale has been used to display the variations on the periodicity of the HRTEM contrast: areas of the same color are regions with the same lattice constant.

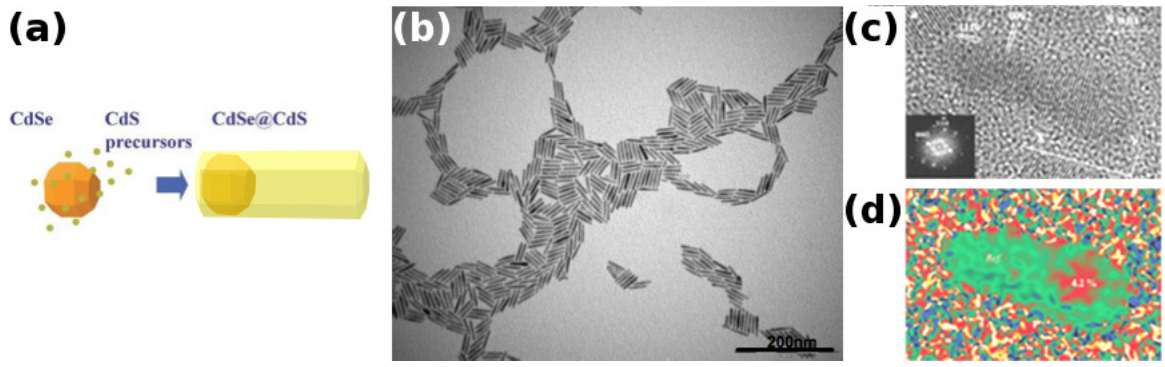

Figure 3.12: **(a)** Sketch of the synthesis procedure. **(b)** TEM image of the obtained DRs. **(c)** High-resolution TEM image of a single DR. **(d)** False color image of the lattice mismatch between core and shell materials. (c) and (d) have been reproduced from ref. [127].

The red circular zone shows a structural alteration of 4.2% with respect to the reference area (reported in green), which is almost the mismatch between bulk CdS and CdSe reticular constant ($\sim 4\%$).

Typical emission and absorption spectra of the synthesized nanoparticles are displayed in Fig.3.13 for several values of core diameter and shell length. The high absorption at short wavelengths is due to the quasi continuum of high-energy levels of both core and shell, while the absorption local maximum at longer wavelengths can be assigned to the transition between valence and conduction band in the CdSe core [127]. The non-resonant stoke shift (i.e. the energy difference between the emission peak and the lowest energy peak in the absorption) ranges from 35meV to 49meV. Also if the core size play the most important role in the spectral position of both emission and absorption peaks, a not negligible contribution is also brought by the shell size. As one can see by comparing Fig.3.13(b) and (c), for a longer shell the quantum confinement is enhanced, and the PL peak shifts toward higher energies (i.e. shorter wavelengths).

3.5.2 The electronic structure

Since the development of the seeded growth synthesis procedure, the scientific community has investigated the electronic structure of CdSe/CdS dot-in-rod, and several

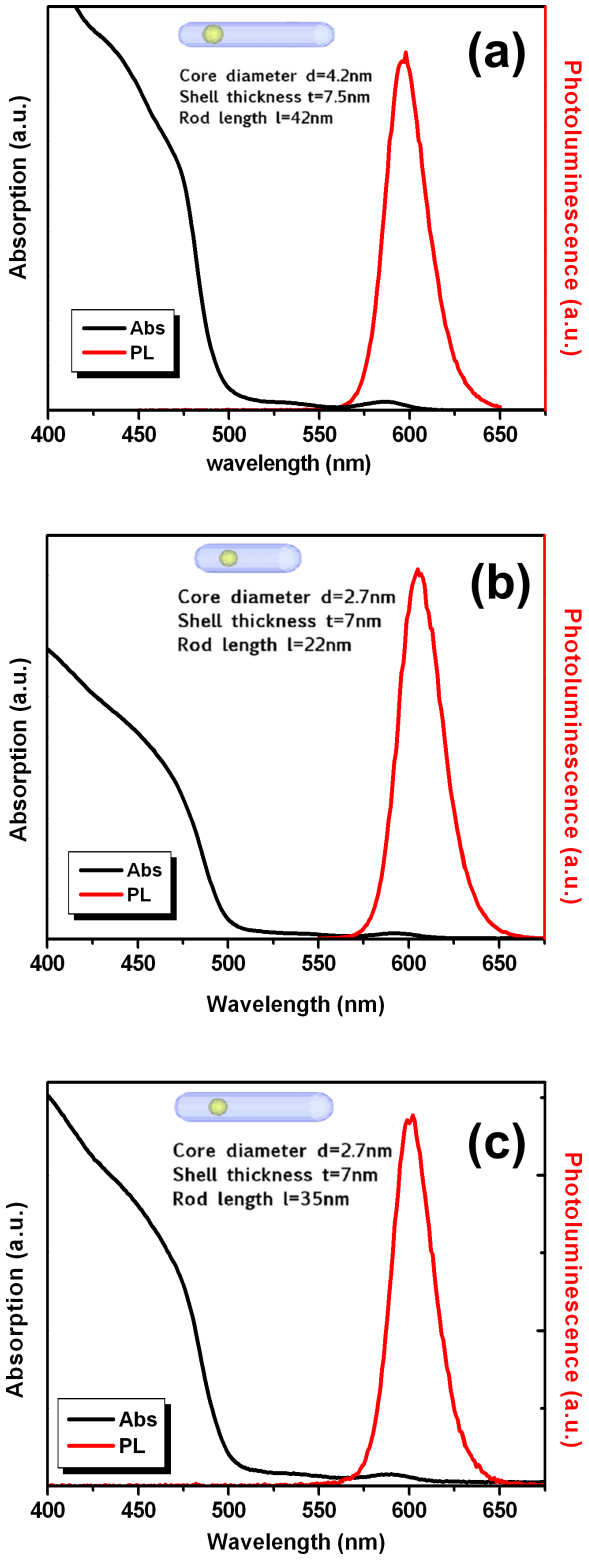

Figure 3.13: Absorption (black lines) and emission (red lines) spectra for three different dot-in-rod configuration.

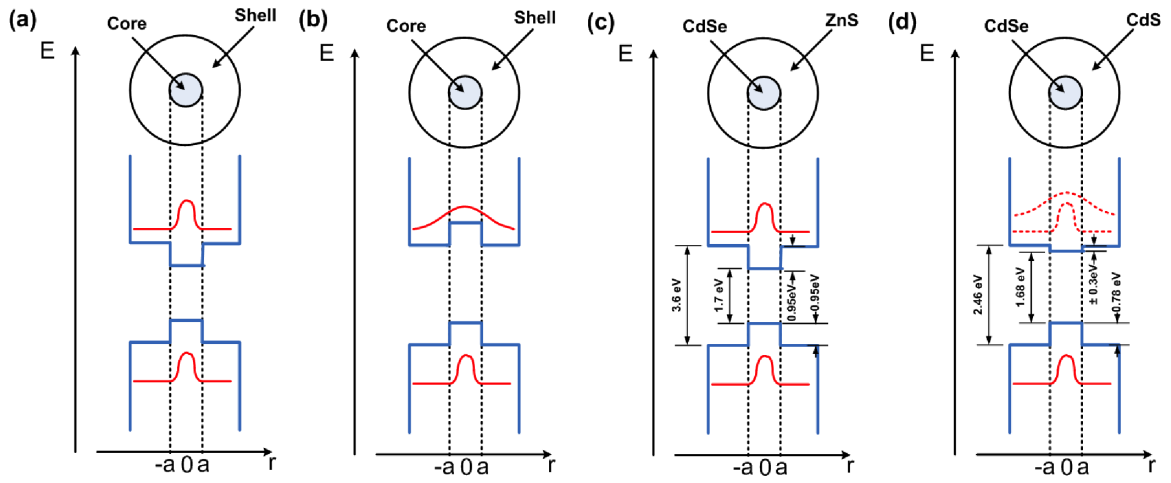

Figure 3.14: **(a)** Sketch of a type-I NC bandstructure. **(b)** Sketch of a type-II NC bandstructure. **(c)** Sketch of the bandstructure of a spherical CdSe/ZnS nanocrystal. **(d)** Sketch of the bandstructure of a spherical CdSe/CdS nanocrystal.

works have appeared in literature addressing this topic [128, 131–136].

On the basis of charge carriers confinement, colloidal nanocyrstals are divided in two categories, sketched in Fig. 3.14 (a) and (b). In *type-I* NCs (Fig. 3.14(a)) electrons and holes are strongly confined inside the core of the structure and their wavefunctions are localized in this zone, while in *type-II* NCs (Fig. 3.14(b)) one of the two carriers is delocalized in the whole NC. In the spherical core/shell configuration CdSe/ZnS the band offsets between the two materials lead to the electronic structure reported in Fig. 3.14(c), that shows a confinement for both electrons and holes wavefunctions.

Due to a valence band offset of $0.78eV$ between CdSe and CdS, also CdSe/CdS spherical nanocrystals strongly confine holes. However, while the band gaps of CdSe and CdS are well-known (1.68 and 2.46 eV, respectively [137]), the conduction band offset Δ_c values reported so far in literature are controversial (Δ_c is usually reported to be in the interval $[-0.3, 0.3]\,eV$ [137–139]) and the situation of the electrons is not clear. A standard way to probe the carriers confinement relies on measuring the lifetime of the excited state for several shell sizes. In particular, in 2008 Malher [16] and co-workers have shown that, for core a diameter of $2.5nm$, by increasing the shell

size from 1 to 9 atomic layers, the radiative lifetime increases from $25ns$ up to $60ns$. Indeed, in the case of *type-II* nanoparticles, increasing the shell thickness the electrons wavefuction spread increases, thus reducing the spatial overlap between electrons and holes wavefunctions. When this happens the probability to find an electron and a hole at the same time in the core decreases, as well as their recombination probability, thus increasing the average carriers lifetime in the nanocrystal.

These inhomogeneous values of Δ_c in bulk materials are reflected also in the evaluation of conduction band offset of CdSe/CdS DRs. Literature contributions disagree on the confinement nature, and independent experiments have suggested CdSe/CdS DRs to be type-I or type-II structures [128, 131–136]. Indeed, while both theory and experiments assessed the band-offset to be type-I like [128, 133], all the measurements devoted to direct probe the carriers localization suggested that the electron wavefunction is spread on the whole CdS rod [131–134, 136]. By studying multiexciton binding in DRs with several core and shell sizes, in 2009 Sitt and co-workers [135] suggested that the electrons confinement is strongly dependent on core diameter. In particular their work shows a transition in the biexciton (BX) energy shift ($\Delta_{BX} = E_{BX} - E_X$, where E_{BX} and E_X are the biexction and exciton binding energies) as a function of core diameter d: for d lower than $\sim 2.8nm$, they measured a positive Δ_{BX} and a strong reduction of triexciton (TX) emission, while for core diameter larger than 2.8nm they observed negative Δ_{BX} and the TX intensity become higher. According to ref. [135], for type-II systems the biexction is characterized by repulsive interactions leading to $\Delta_{BX} > 0$, while for type-I nanoparticles such interaction is attractive and $\Delta_{BX} < 0$. These values clearly indicate that for $d < 2.8nm$ the nanoparticles result to be type-II, while both the carriers are localized if $d > 2.8nm$ (type-I) [135].

Another way to probe the charge carriers confinement relies on monitoring the autcorrelation function of the light emitted by the nanoparticle at zero delay time $g^{(2)}(0)$. As already discussed in section 3.4, the non-radiative Auger recombination process plays an important role in NCs carriers dynamic. In particular, its rate k_A

is directly proportional to the carriers confinement: the stronger the confinement, the higher the probability to have a non-radiative recombination of an additional e-h pair present in the nanocrystal. This means that in the case of ultra-strong confinement the Auger process is faster than the radiative recombination and dominates up to when only one e-h pair remains in the NCs (i.e. $k_A \gg k_{rad}$). As a consequence, the Auger process efficiency directly leads to a modification of $g^{(2)}(0)$: if Auger process is not efficient (i.e. k_A is comparable with k_{rad} or $k_A < k_{rad}$) the probability to emit more than one photon per excitation pulse P_{2+} should not be zero, thus resulting in $g^2(0) \neq 0$. On the contrary, if Auger process is efficient (i.e. $k_A \gg k_{rad}$) low $g^{(2)}(0)$ values are expected.

We have investigated this behavior for several geometrical configuration of DRs as a function of the intensity of a picosecond pulsed laser (pulse duration $\sim 50ps$) used to excite the carriers in the nanocrystal (see appendix B.1 for a complete description of the experimental set-up). The geometrical parameters of the analyzed DRs are displayed in the insets of Fig. 3.15. The coincidence histograms $h(\tau)$ reported in Fig. 3.15 clearly show a rising up of the correlation peak at zero delay time when the excitation pump power is increased for DRs with core diameter $d \sim 2.7nm$, while it remains almost constant for $d \sim 4.2nm$.

In order to quantify this effect in terms of $g^{(2)}(0)$, for each $h(t)$ the autocorrelation function at zero delay has been calculated as the ratio between the area subtended by the peak at $\tau = 0$ and the average of the areas subtended by the seven nearest peaks. Moreover, the average number of e-h pair per pulse injected in the dot in rod ($\langle N \rangle$) has been assessed by exploiting eq. (3.20). As shown in Fig. 3.16, the normalized and time-integrated PL intensity of a DR is well fitted by the function $I(P) = I_0 \left(1 - e^{-\alpha P}\right)$, where α is the fitting parameter, $\alpha P = \langle N \rangle$ and I_0 the saturation value of the PL intensity. This method reasonably allows to estimate $\langle N \rangle$ directly from the measured PL intensity.

Fig. 3.17 displays the value of $g^{(2)}(0)$ as a function of the average number of e-h

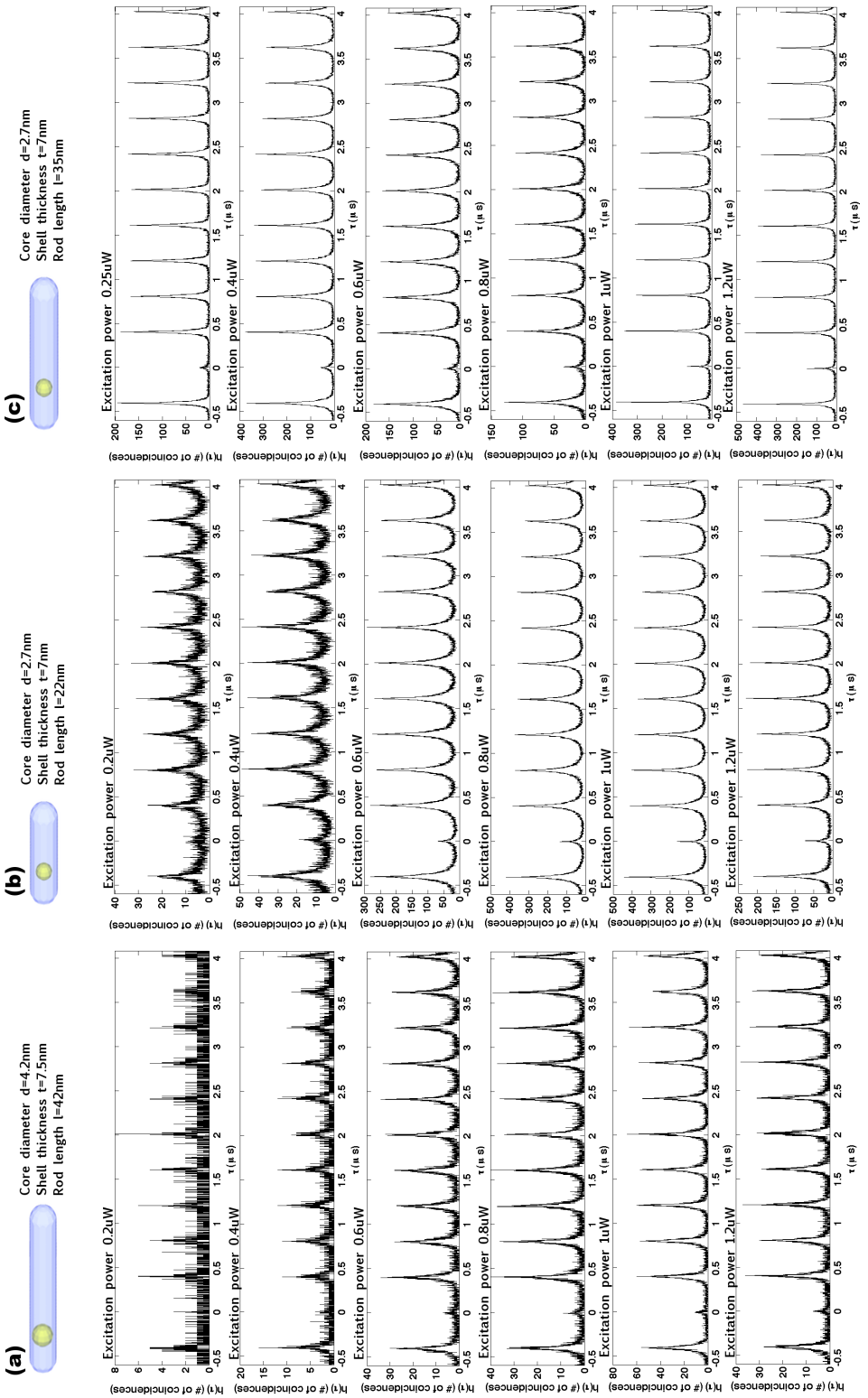

Figure 3.15: Coincidence histograms $h(\tau)$ obtained from DRs with the following geometrical parameters: **(a)** $d = 4.2nm$, $t = 7.5nm$, $l = 42nm$, **(b)** $d = 2.7nm$, $t = 7nm$, $l = 22nm$, **(c)** $d = 2.7nm$, $t = 7nm$, $l = 35nm$ and for several excitation powers.

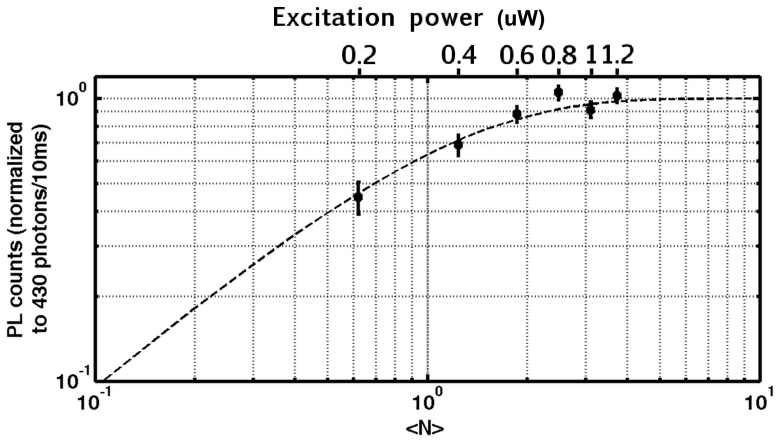

Figure 3.16: Time-integrated photoluminescence intensity as a function of average number of injected e-h pair per pulse $\langle N \rangle$ and of the excitation power. Filled circles with error bars represent experimental data, while dashed line is the function $I(\langle N \rangle) = 1 - e^{-\langle N \rangle}$.

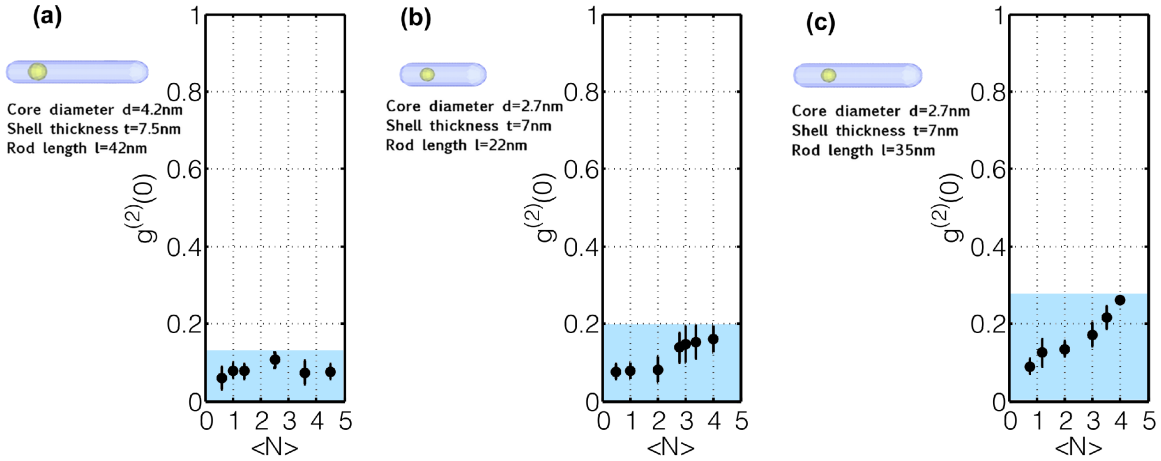

Figure 3.17: Absolute value of $g^{(2)}(0)$ as a function of the excitation power for DRs of geometrical parameters: **(a)** $d = 4.2nm$, $t = 7.5nm$, $l = 42nm$, **(b)** $d = 2.7nm$, $t = 7nm$, $l = 22nm$, **(c)** $d = 2.7nm$, $t = 7nm$, $l = 35nm$.

pairs per pulse $\langle N \rangle$ excited in the structure (see section 3.5.3 for further details on the estimation of $\langle N \rangle$). If $d \sim 4.2nm$, the excitation power does not influence the $g^2(0)$ behavior, which remains lower than 0.12, while in both DRs with $d \sim 2.7nm$ two different excitation regimes can be distinguished: one at low excitation powers, in which the probability to emit more than one photon per pulse is $P_{2+} \sim 0.06 \pm 0.02\%$ [1], and another one at higher excitation powers in which $g^{(2)}(0)$ is higher. This last behavior is typical of a type-II system, in which one of the carriers is delocalized, while the constant value of $g^{(2)}(0)$ reported in Fig. 3.17(a) evidences that, for bigger cores, DRs are type-I nanoparticles. Indeed in type-II NCs the lower k_A makes the probability of multiexciton binding to increase, which can thus recombine emitting more than one photon. It is also important to underline that for smaller cores the values of $g^{(2)}(0)$ at high excitation powers depends also on the shell length: the longest sample ($l \sim 35nm$) reaches a $g^{(2)}(0) \sim 0.27$, while for the shortest one ($l \sim 22nm$) $g^{(2)}(0) \sim 0.20$. This modification of the highest value of $g^{(2)}(0)$, of the order of $\sim 30\%$, is a further confirmation of charge carriers delocalization: by increasing the rod length the overlap between electrons and holes wavefunctions decreases, as well as the efficiency of the Auger process, thus resulting in a higher $g^{(2)}(0)$.

3.5.3 Reduced blinking

In section 2.1.4.2 it has been already discussed that one of the most limiting features of colloidal NCs from the point of view of the applications is the so called *blinking*, i.e. time-dependent fluctuations of PL intensity due to the charges localized in the nanoparticle. A figure of merit to quantify the blinking of a nanoparticle is the probability to have off-periods longer than a given value, i.e. $P_{off}(\tau_{off} > \tau)$. In the case of colloidal NCs it has been demonstrated that $P_{off}(\tau_{off} > \tau)$ follows a power law distribution [140], i.e. $P_{off}(\tau_{off} > \tau) \propto 1/\tau^{\mu}$. In particular, for standard CdSe/ZnS

[1] Let us point out that this value has been obtained directly on the collected data without any noise suppression algorithm.

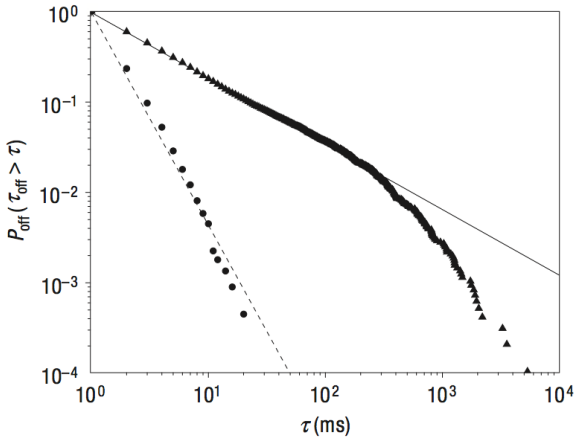

Figure 3.18: Cumulative distributions of off times in a logarithmic scale. Circles (respectively triangles) correspond to the fluorescence intermittency of the CdSe/CdS (respectively CdSe/ZnS) nanocrystal. The solid line is a power-law distribution of parameter $\mu = 0.73$ and the dashed line a power-law distribution of parameter $\mu = 2.4$. Figure and caption reproduced from ref. [16].

nanocrystals $\mu \approx 0.5$ for short τ [140], while for longer times $P_{off}(\tau_{off} > \tau)$ falls down faster due to the finite duration of the experiment. This situation is well summarized by the cumulative distribution of the off-times reported Fig. 3.18 by the filled triangles. This curve follows well a power-law distribution with $\mu = 0.73$ for $\tau < 2 \cdot 10^2 ms$. It is important to underline that the fitting factor μ plays an important role from the statistical point of view: the higher the parameter μ, the lower the probability to have long blinking periods. In particular:

- If $\mu < 1$ all the momenta of the distribution $1/\tau^\mu$ diverge, and in particular its average value and its variance are not defined,
- If $1 < \mu < 2$ the blinking statistics changes and the mean value converges,
- If $\mu > 2$ the mean value and the variance converge and the law fulfills the central limit theorem.

Recently, it has been demonstrated that by surrounding a CdSe core by a giant CdS shell the behavior of $P_{off}(\tau_{off} > \tau)$ can be modified [16]. In this work, Mahler and co-workers show that the μ-index can become higher than 2, strongly reducing the long off-periods distinctive of CdSe/ZnS NCs. A typical behavior of the cumulative distribution of off-times obtained from giant CdSe/CdS nanocrystals is reported by filled circles in Fig. 3.18. By analyzing the behavior of $P_{off}(\tau_{off} > \tau)$ as a function of τ for CdSe/CdS dot-in-rods, we show that also these nanoparticles present a strongly reduced blinking related to carriers delocalization and to shell thickness around the core.

As a support for the reader, the behavior of the normalized time-integrated PL intensity as a function of $\langle N \rangle$ has been reported in Fig. 3.19(a). The average saturation value, above the excitation power of $0.8\mu W$, results to be ~ 50000 photons per second (the PL intensity is considered saturated when the emission intensity reaches 85% of the final saturation value). Taking into account the collection efficiency of our experimental setup (which is $\sim 2.8\%$, see appendix B.1 for a detailed descriptions) we find that the DR emits about $1.79 \cdot 10^6$ photons per second at excitation rates of 2.5MHz, thus corresponding to a total single photon efficiency of $\sim 70\%$ at room temperature.

Typical PL time traces obtained from a single DR with geometrical parameters $d = 2.7nm$, $t = 7nm$ and $l = 22nm$ are reported in Fig. 3.19(b): for all the excitation densities, long blinking periods seem to be avoided, in particular for $\langle N \rangle > 1$. This is confirmed by the cumulative distribution of the off-period durations displayed in Fig. 3.20 and relative to the traces reported in Fig. 3.19(b). Below saturation (i.e. excitation power lower than $0.6\mu W$) $1 < \mu < 2$, while for higher excitation regimes μ is constantly higher than 2. This behavior can be interpreted in conjunction with that reported in Fig. 3.19.

For low carrier density, the system is in the monoexcitonic regime, i.e. in average less than a single e-h pair per pulse is excited in the NC. In such conditions the emission intensity is not saturated, its average value is close to the noise of the detection system

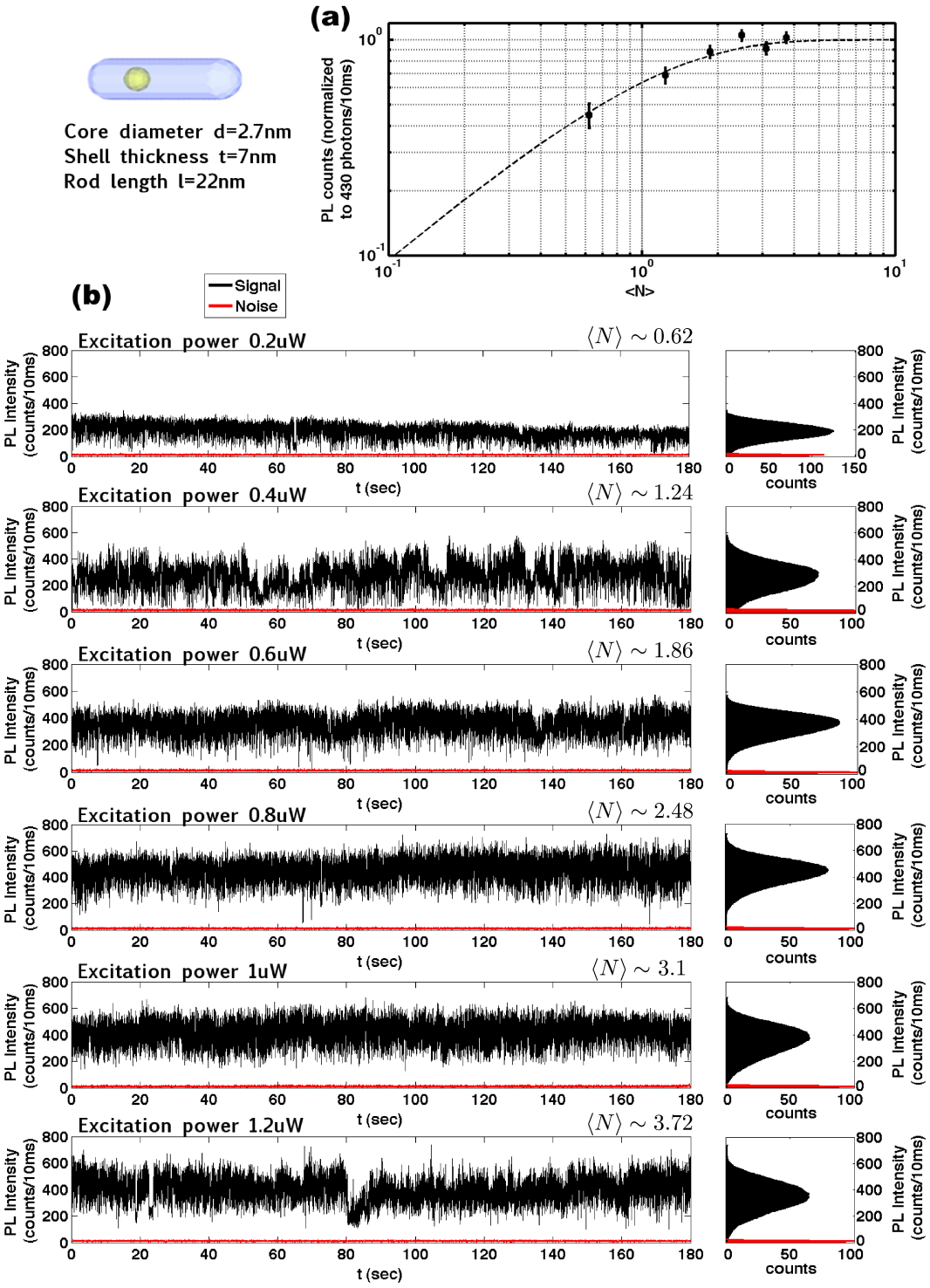

Figure 3.19: **(a)** Mean PL intensity as a function of the average number of electron-hole pairs per pulse injected in the DR. Filled squares are measured data normalized to 43000 photons/second, dashed line is the function $I = 1 - e^{-\langle N \rangle}$, where $\langle N \rangle$ is the average number of injected e-h pairs. **(b)** PL time traces (left panels) and intensity distributions (right panels) for several excitation powers. [measurements performed on DRs of geometrical parameters $d = 2.7nm$, $t = 7nm$, $l = 22nm$.]

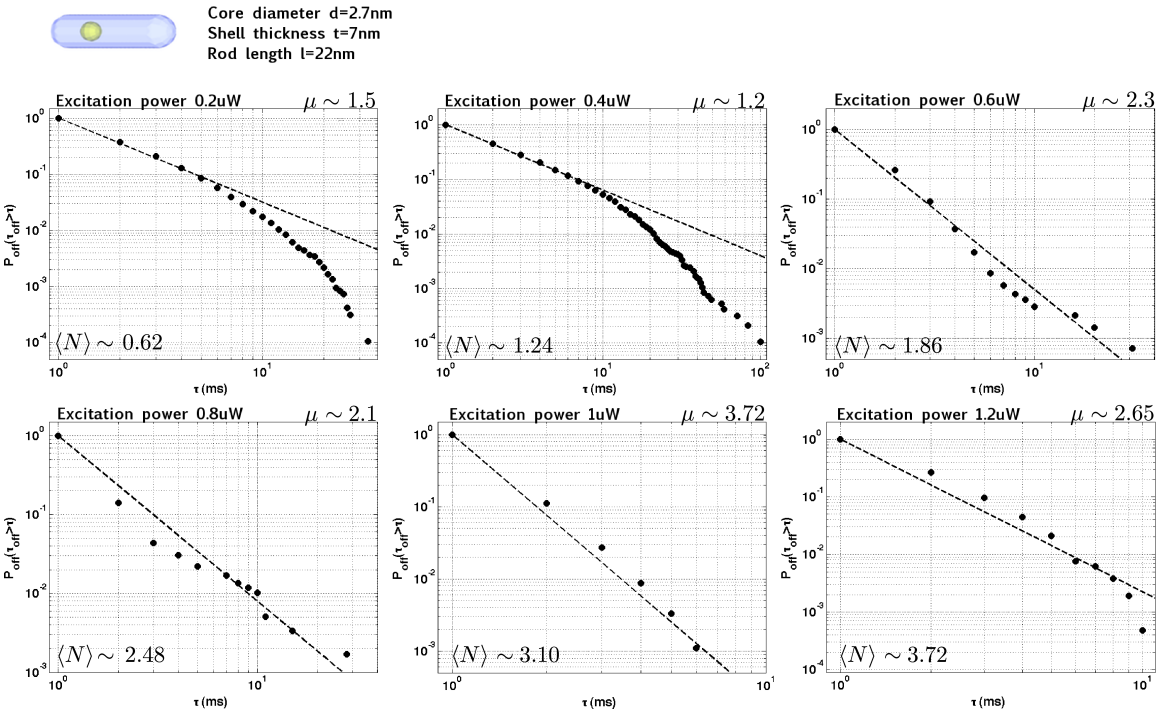

Figure 3.20: Cumulative distributions of off times in a logarithmic scale [DR of geometrical parameters $d = 2.7nm$, $t = 7nm$, $l = 22nm$]

and some counts are comparable to the noise. Since in the calculation of $P_{off}(\tau_{off} > \tau)$ all the PL counts lower than almost four times the noise level are considered as a blinking period, at weak excitation, power lower μ indexes can be expected. For high excitation power (i.e. higher than the saturation value) the PL intensity is instead well above the noise level and no long blinking periods are observed and $\mu > 2$.

The PL intensity fluctuations depend principally on the interaction between the last e-h pair in the nanocrystal and an ionization charge present in the nanocrystal, as discussed in section 3.4. As suggested in ref.s [16, 106, 141], if the ionization charge is kept away from core (for instance it is in the shell or on the shell surface) $\mu > 2$ can be achieved. The μ-index is therefore expected to depend on the geometrical configuration of DRs.

The reduced-blinking behavior shown in Fig.s 3.19 and 3.20 is confirmed for longer nanocrystals with the same shell thickness around the core ($\frac{t-d}{2} \sim 2.15nm$), with aver-

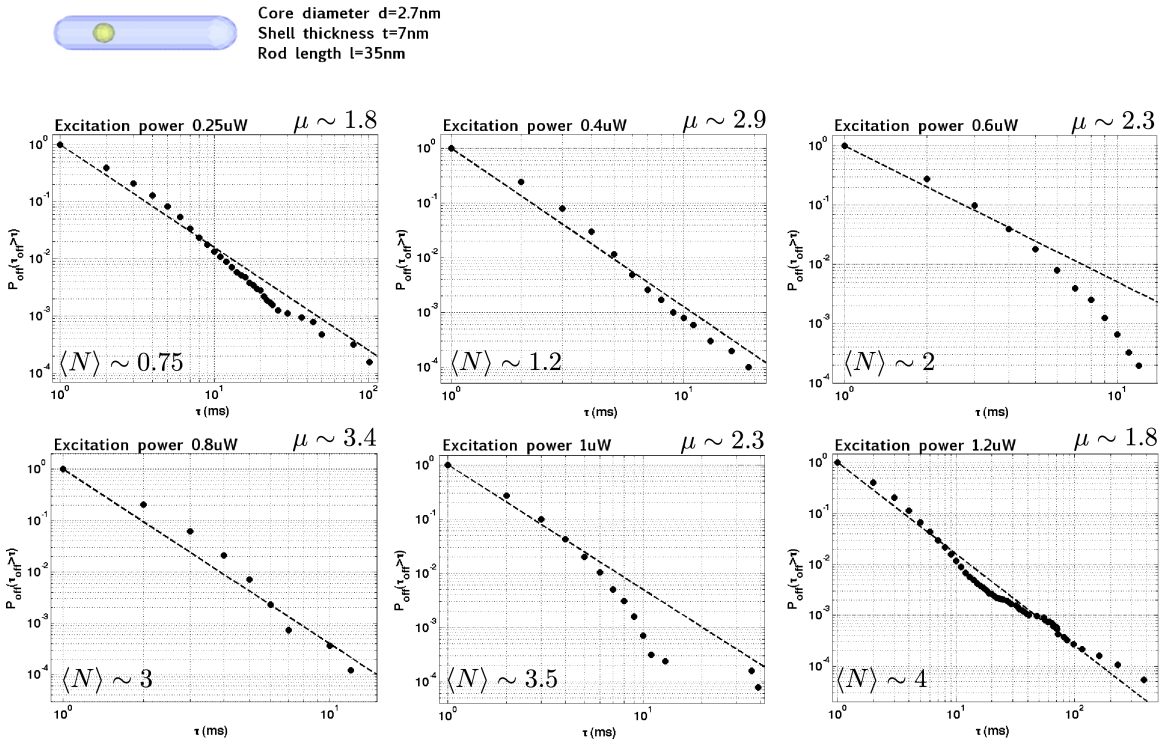

Figure 3.21: Cumulative distributions of off times in a logarithmic scale [DR of geometrical parameters $d = 2.7nm$, $t = 7nm$, $l = 35nm$]

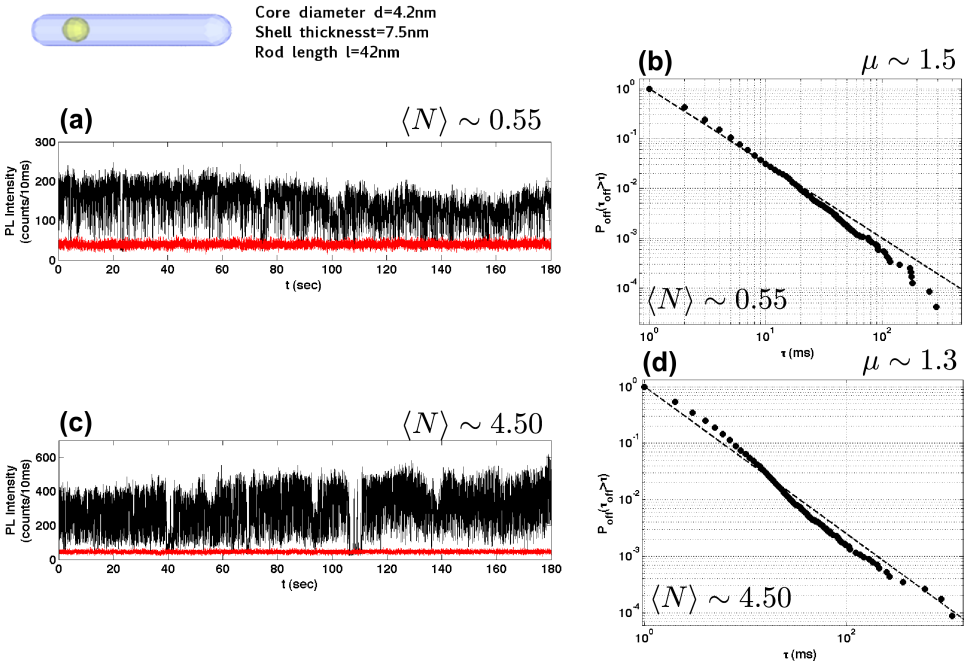

Figure 3.22: PL time traces [(a) and (c)] and cumulative distribution of off time in logarithmic scale below and above carriers saturation. [DR of geometrical parameters $d = 4.2nm$, $t = 7.5nm$, $l = 42nm$].

age μ-indexes higher than 2 (see Fig. 3.21). However, by reducing the shell thickness around the core to $\frac{t-d}{2} \sim 1.4nm$ the value of μ decreases to $\mu \sim 1.3$, and the mean duration of the off-times increases, as shown by the the PL time traces and the off time distribution displayed in Fig. 3.22. This statistical analysis therefore demonstrates a strong reduction of blinking in thick DRs independently on their length, reaching the state of the art of spherical CdSe/CdS NCs [16,106]. In the following, we propose an interpretation of this behavior based on radiative and non-radiative channel engineering and on the interactions with ionization charges localized in the nanocrystal.

3.5.4 DRs lifetime

The excited state lifetime depends on wavefunctions localization. Very recently at IMB labs in Zurich, G. Rainò and collaborators performed a systematic study on DRs emission as a function of temperature for several core sizes and total nanocrystals thickness of $\sim 4.5nm$ [142], showing that the PL intensity of an ensemble of DRs decays mono-exponentially as a function of time (i.e. $I(t) = ae^{-\tau t}$) and that the excited state lifetime increases by increasing the operating temperature [Fig. 3.23(a)]. As shown in ref. [142], the dependence reported in Fig. 3.23(a) allows to assess the degree of wavefunction delocalization: for core diameters smaller than $\sim 2.9nm$, the delocalization of electron wavefunction is evident. These deductions are coherent with our interpretations based on autocorrelation function previously detailed in section 3.5.2. Moreover, the lifetimes reported in ref.s [128, 142] for measurements performed on ensembles of DRs are similar to our results for thin DRs at the single particle level (total thickness about $t \sim 4.5nm$, core diameter $d \sim 2.7nm$ and total length $l \sim 50nm$) and reported in Fig. 3.23(b) [143].

However for thicker DRs ($t = 7nm$) we have found a different behavior. For core diameters of $d \sim 2.7nm$, when the pump intensity is chosen to have $g^2(0)$ as low as possible (black dots and red line in Fig. 3.24) a longer time constant appears with characteristic times $\tau_2 = 75ns \pm 2ns$ and the decay curve is fitted by a biexponential function $I(t) = ae^{-t/\tau_1} + be^{-t/\tau_2}$. When the pump intensity is increased above saturation (green dots and blue line in Fig. 3.24) even a biexponential function is not enough to fit the experimental data. This is due to the small multiexcitonic emission which is concentrated at short times [128]. Excluding the first $10ns$, the rest of the data are well fitted by a biexponential with almost the same parameters as for lower excitation powers ($\tau_1 = 17.5ns \pm 2ns$, $\tau_2 = 66ns \pm 2ns$). As discussed in the following paragraph, one of the time constants can be assigned to single e-h recombination, while the other one is due to a particular three charges configuration in the nanocrystal, the *trion*, that give rise to a grey emission state in the photoluminescence intensity.

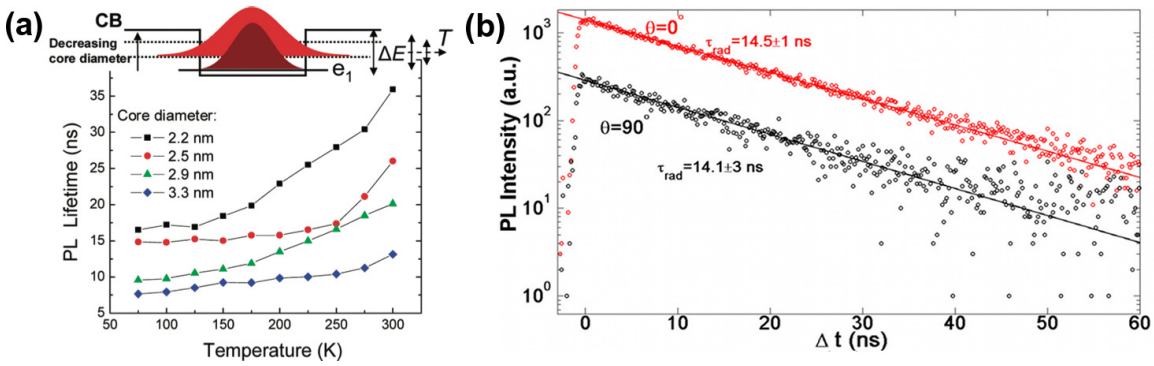

Figure 3.23: **(a)** Temperature dependence of the PL lifetime for all core diameters studied. The sketch illustrates the expected conduction band configuration, i.e., the change in the energy levels for different core diameters [Reproduced from ref. [142]]. **(b)** Radiative decay curves in logarithmic scale detected for light polarized along the rod axes ($\theta = 0°$) and perpendicular to rod axes ($\theta = 90°$). [DRs geometrical parameters: total thickness about $t \sim 4.5nm$, core diameter $d = 2.7nm$ and total length $l \sim 50nm$)]

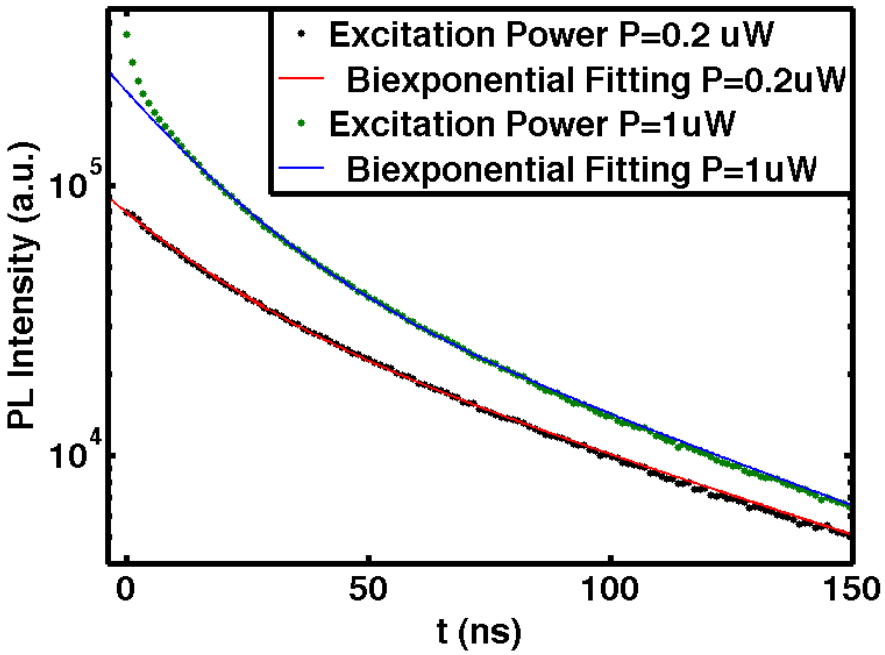

Figure 3.24: Typical decay curves for DRs of geometrical parameters $d = 2.7nm$, $t = 7nm$ and $l = 22nm$

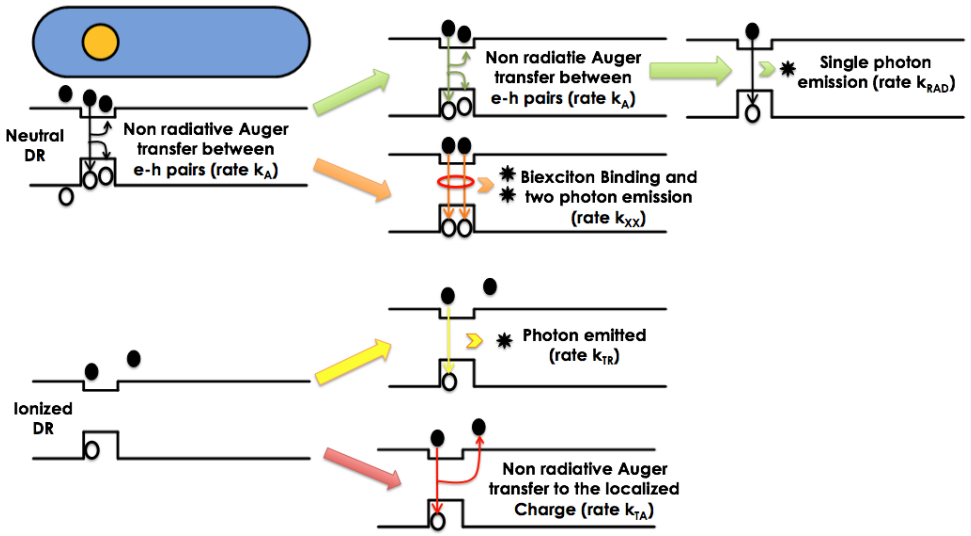

Figure 3.25: DRs recombination channels. **Green and orange paths** show the possible radiative recombination channels when the DR is in a neutral condition, while **yellow and red paths** are associated to trion charge configuration. k_A is the non-radiative Auger energy transfer rate between e-h pairs; k_{RAD} is the radiative rate of last e-h pair remaining excited in the nanocrystal; k_{XX} is the biexciton binding time; k_{TR} is the radiative rate of the trion configuration; k_{TA} is Auger non-radiative energy transfer between an e-h pair and a charge ionizing the nanocrystal.

3.5.5 Intensity distributions and grey emission state

Blinking is normally associated to localized charges in the NCs, as detailed in section 3.4. As a support for the following discussion, a scheme of the possible recombination channels in a DR is reported in Fig. 3.25. If a charge is localized in the structure, an e-h pair can recombine through an Auger mechanism and transfer its energy to this charge. When this happens, the photon emission is lost and the NC remains charged (red path in Fig. 3.25). The next e-h pair excited in the NC will be subject to the same phenomenology, and the NC cannot emit up to when the charge neutrality is recovered. By increasing the shell thickness, Mahler and co-workers [16] changed the interaction behavior of this three-charge process (also called trion, a charge plus an e-h pair): in giant CdSe/CdS NCs, the trion can lead to a photon emission with a

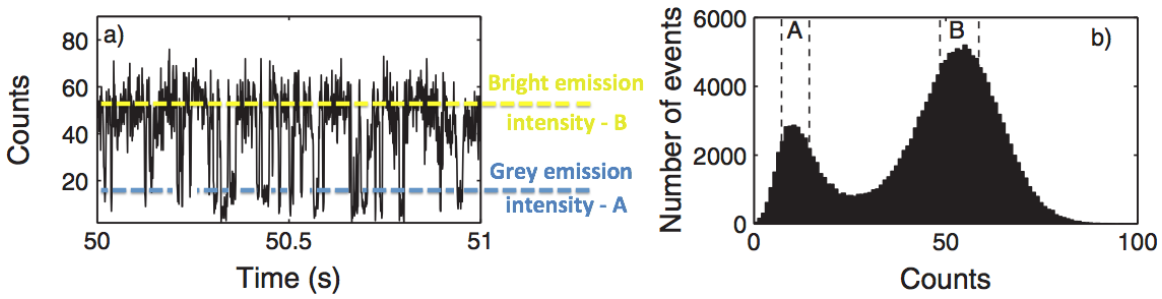

Figure 3.26: **(a)** Fluorescence intensity of a single CdSe/CdS NC with giant shell. **(b)** Intensity histogram corresponding to (a). [Reproduced from ref. [106]]

quantum efficiency of $Q_T \sim 0.19$ and a rate k_{TR} (yellow path in Fig. 3.25), while the rest of time the e-h pair recombine through an Auger mechanism. It is important to point out that this non-radiative interaction comes from the e-h interaction with a localized charge and has a rate k_{TA}, which is different from k_A, which is dependent on the interaction between e-h pairs (green and orange paths in Fig. 3.25). This process is at the origin of the *grey state* emission, which is identified by a decrease of the PL intensity. A typical time trace with its intensity cumulative distribution for giant-shell spherical NCs, reproduced from ref. [106], are reported in fig.3.26: bright and grey emission states are clearly visible in both graphs.

A typical PL time trace detected from an isolated DR with a temporal zoom are reported in Fig. 3.27. In the 180 seconds of this acquisition, just few sharp blinking deeps are observed, and the nanocrystal seems to emit always in the bright state. At the first glance, the PL intensity seems to not show any grey emission states, but this is not completely true. Figure 3.28 displays the cumulative PL intensity histograms for two different excitation powers and the correspondent time traces. If the DR was always in the bright state and never ionized, the cumulative distribution should have been symmetric around the mean intensity value. However Fig.s 3.28(b) and (d) clearly shows that this does not happen for DRs. Indeed the two time traces reported in Fig.s 3.28(a) and (c) clearly show a grey emission state oscillating in the light blue area reported on background. The PL counts coming from this grey emission influence the

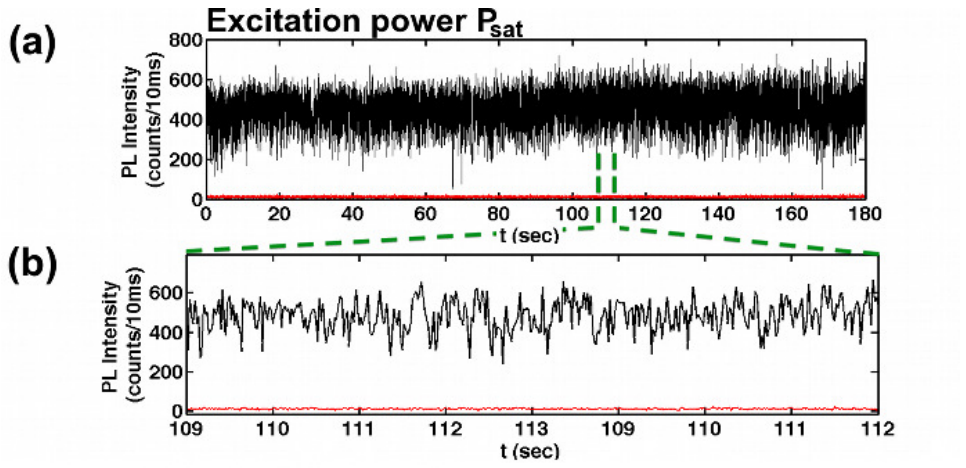

Figure 3.27: **(a)** Shows a tipical PL intensity for a DR with d 2.7nm, t 7nm, l 22nm. **(b)** Displays a temporal zoom of (a). Red lines represent the noise counts, $P_{sat} = 0.8\mu W$,$\langle N \rangle = 2.48$.

intensity histograms in the zones shown by the light blue bars in Fig.s 3.28(b) and (d).

DRs exhibit ionization and grey states, with grey state mean intensity emission near to the bright state average value. As a consequence, it is difficult to distinguish the PL counts coming between the two states, that are almost superposed one to the other, while this is straightforward for the data reported in Fig. 3.26, where the two states are well separated. The grey state should also have a different emission wavelength if compared to the bright state, but spectral resolved PL measurements are not a viable strategy to distinguish between grey and bright emission, because of the broad spectral width of the bright state ($\sim 15nm$ [128]).

In order to define the average intensity emission of the grey state, and therefore its quantum efficiency, we used the following algorithm. (i) We defined the average value of the bright state $\langle I_b \rangle$ as the PL intensity for which the maximum of the intensity distribution is reached. (ii) We then supposed that all the counts at PL intensities higher than $\langle I_b \rangle$ are not influenced by the gray state, and we calculated their standard deviation σ_b from $\langle I_b \rangle$. (iii) After that we defined the average emission intensity of the grey state $\langle I_g \rangle$ as the average of the PL counts lower than $\langle I_b \rangle - 1.5 \cdot \sigma_b$, where the factor

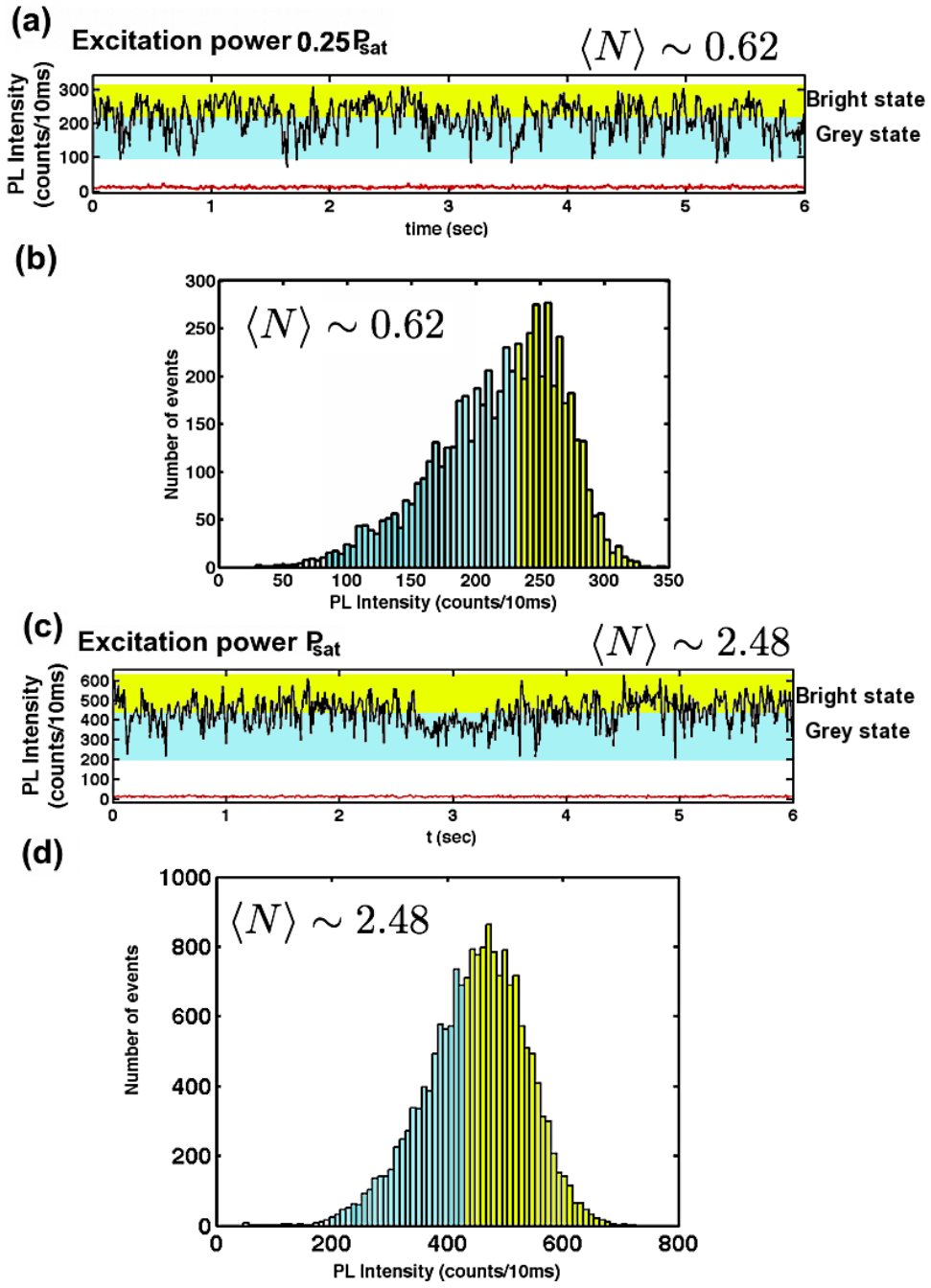

Figure 3.28: **(a), (c)** Show typical PL intensities for a DR with d $2.7nm$, t $7nm$, l $22nm$ for two excitation regimes. Light blue area indicates the PL counts interval that can be associated to the grey state. Yellow area represents counts almost not influenced by the grey state emission. **(b), (d)** displays the intensity distribution histogram of (a) and (c), respectively. The light blue bars represents the counts influenced by the grey emission, thus leading to an asymmetric distribution. Yellow bars represents counts almost not influenced by the grey state emission.

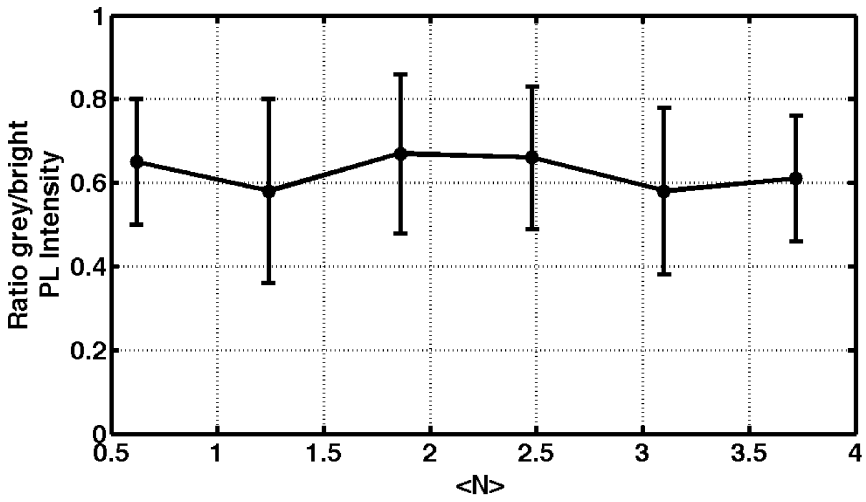

Figure 3.29: Ratio between the grey and the bright mean PL intensity as a function of the average number of e-h pairs injected in the NC $\langle N \rangle$. Error bars are due to the grey state PL counts standard deviation.

1.5 has been empirically defined in order to minimize the influence of the bright state counts on the grey state average intensity and to maximize the number of grey state counts taken into account in the computation. (iv) We supposed that all the counts with intensities lower than $\langle I_g \rangle$ are not influenced by the bright state counts, and we computed the grey state standard deviation σ_g as their standard deviation from $\langle I_g \rangle$.

With this method, the ratio between the grey and bright states PL intensity has been assessed to be $\langle I_g \rangle / \langle I_b \rangle \sim 0.6 \pm 0.2$ independently on the injected carrier density, as reported in Fig. 3.29. Supposing the quantum efficiency of bright state almost unitary [106], the quantum efficiency of the grey state can be defined as $Q_T = \langle I_g \rangle / \langle I_b \rangle \sim 0.6 \pm 0.2$, where $\langle I_g \rangle$ and $\langle I_b \rangle$ are the time averages of the bright and grey state PL intensities.

As discussed in section 3.5.4, the time decay shows a bi-exponential behavior also below saturation, while above saturation the influence of multiexcitonic states resides at short times. We already mentioned that the overlap between the emission intensity of the bright and the grey states does not allow to well distinguish between the two

states in the PL time trace. Nevertheless, a threshold between grey and bright state can be defined as $I_{th} = (\langle I_b \rangle + \langle I_g \rangle)/2$. By considering the PL counts lower than I_{th}, the weight of the faster time constant in the decay curve rise up. This reasonably allows us to associate the fast decay time to the trion configuration ($1/k_T = \tau_2 \approx 19.5ns$) and the slowest one to the radiative lifetime $\tau_1 \approx 75ns$.

Given the quantum efficiency of the grey state $Q_T \sim 0.6 = k_{TR}/(k_{TR} + k_{TA}) = k_{TR}/k_T$, it is possible to calculate the radiative lifetime of the trion $\tau_{TR} = 1/k_{TR}$ and the characteristic time of the trion Auger process $\tau_{T_A} = 1/k_{TA}$. Since $k_{TR} = Q_T k_T$, the radiative lifetime of the trion is $\tau_{TR} = 1/k_{TR} \approx 31ns$. The characteristic time of the trion Auger process is $\tau_{T_A} = 1/(k_T - k_{TR}) \approx 53ns$, and $\tau_{TR}/\tau_{TA} \sim 0.58$. Therefore, $\tau_{TA} > \tau_{TR}$ (i.e. $k_{TA} > k_{TR}$) and the probability to have a radiative recombination of the trion is higher than the probability to have a non radiative energy transfer to the third charge, explaining the presence of a grey emission with high quantum efficiency. The yellow path of Fig. 3.25 is thus the favorite relaxation channel for the trion. The role of a thicker shell is therefore to keep the ionizing charge away from the emitting core also in the direction perpendicular to the rod axis, reducing the overlap between its wavefunction and the one of the e-h pairs excited in the DR and minimizing their mutual interactions. For comparison, giant shell CdSe/CdS NCs show $\tau_{TR} \approx 45ns$ and $\tau_{TA} \approx 10ns$ together with $Q_T = 0.19$ [106].

Let us point out that k_{TA} and k_A are based on different interactions and are thus not necessary bound together: the possibility to independently tune these two parameters would allow a strong freedom in tailoring emission properties. For instance, one of the conclusions that can be extrapolated from these results is that the key to obtain non-blinking single photon emission is to force the nanocrystal toward the green and yellow radiative channels of Fig. 3.25, asking for $k_{TR} >> k_{TA}$ and $k_A >> k_{RAD}$, while if a large amount of biexciton is needed the condition $k_A >> k_{RAD}$ should not be fulfilled. We have shown that playing on DRs thickness it is possible to modify k_{TR} and k_{TA}, while rod length acts directly on multiexciton binding rate by slightly

modifying the electrons wavefuction. The possibility to tune these parameters allowed us to obtain a strong reduction of blinking [$P_{off}(\tau_{off} > 50ms) = 0.001$] together with a $g^2(0) < 0.26 \pm 0.01$, and efficiency of the $\sim 70\%$.

3.5.6 Polarized, dipole-like single photon generation

When compared with spherical nanoparticles, elongated NCs presents an higher degree of linear polarization [120,121,127]. In the case of low-dimensional nanoparticles able to emit single photon fluxes this property is appealing for the implementation of quantum cryptography algorithms. The measurements of the autocorrelation reported in section 3.5.2 have been used to asses the carrier confinement in the nanoparticle, finding a type-I behavior for core diameter $d \sim 4.2nm$ and a quasi type-II behavior for $d \sim$ 2.7. Moreover, they show that DRs emit single photons almost independently on the excitation power. In this section the suitability of DRs as source of single photons is demonstrated by showing linear polarization of the single photon flux as well as the dipole-like radiation pattern of DRs.

In order to analyze the polarization properties of a single DR the emission intensity of the bright state have been measured by introducing a half wavelength plate and a linear polarizer in the detection path in order to detect different polarization angle (θ): when $\theta = 0°$ (90°) only the light polarized along (perpendicular to) the rod axis is collected (see setup described in appendix B.1).

As shown in Fig.3.30, the PL intensity as a function of θ well fitted by the curve $\delta cos^2(\omega t)+1-\delta$, where $\delta = \frac{|I_{\parallel}-I_{\perp}|}{|I_{\parallel}+I_{\perp}|}$ is the *degree of linear polarization*. Interestingly, for type-II nanoparticles δ depends on the rod length. Reducing DR thickness to $t \sim 4.5nm$ it is possible to reach $\delta \sim 80\%$ for rods lengths of 50nm, as reported in Fig. 3.30(a). The possibility to tailor the degree of linear polarization can be reasonably ascribed to the electrons wavefunction delocalization, as in the case of nanorods. In order to confirm this interpretation, also the polarization properties a DR with bigger core ($d \sim 4.2nm$) has been investigated: in that case electrons should be more localized and

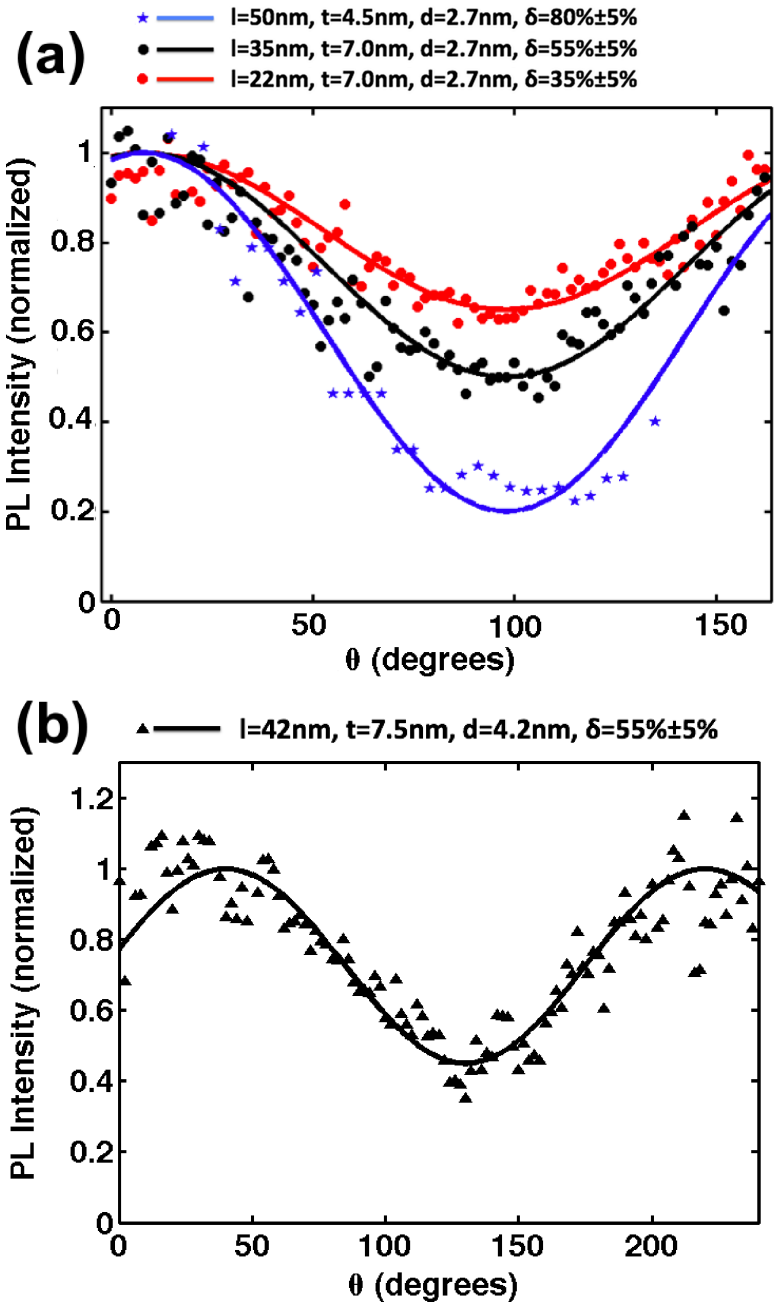

Figure 3.30: PL intensity as a function of the detection polarization angle θ. DRs geometrical parameters are mentioned above the graphs.

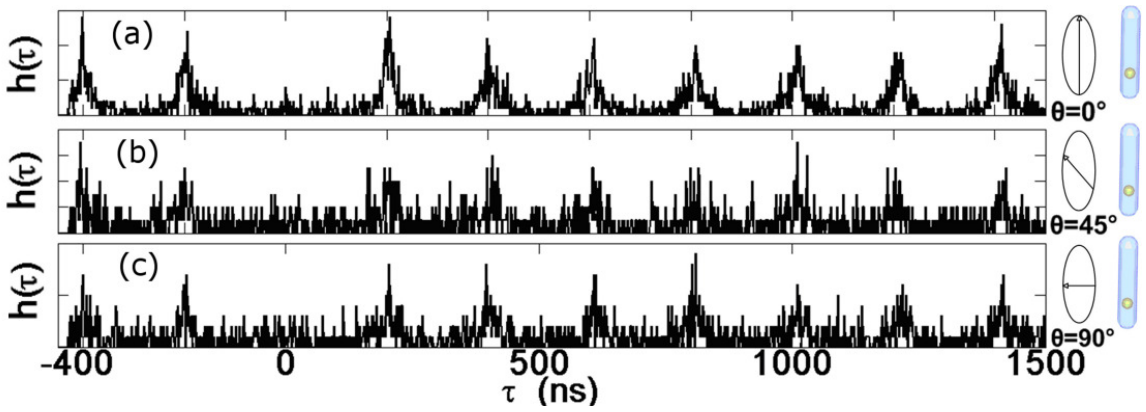

Figure 3.31: **(a)** PL intensity as a function of the detection polarization angle θ and DR geometrical parameters $d = 2.7nm$, $t = 4.5nm$, $l = 22nm$. **(b-d)** Coincidence histogram $h(\tau)$ for three different value of θ. Because of the weak signal collected for $\theta = 90°$, the integration time used for the measurement in (c) is almost five times longer than in (a).

should lead to a lower δ. Indeed, as shown by Fig. 3.30(b), for a length $l = 42nm$ we have found $\delta \sim 55\%$. With the goal to confirm that the photon flux is antibunched for each component of the polarization vector, in the case of higher δ the autocorrelation function for several values of θ has been measured. Representative results of these measurements are shown in Fig.s 3.31(a–c). Clear antibunched emission was obtained for each polarization, showing that by changing the polarization detection angle the nonclassical light flux is preserved.

In order to determine the dipole orientation in each DR, a defocused microscope technique has been adopted: when a high numerical aperture microscope objective is moved from the focal point, an omnidirectional emitter on the sample plane is identified by means of concentric defocusing lines around the original focused spot. On the contrary, when the radiation diagram is dipolelike and the dipole is perpendicular to the microscope collection axis, the circular behavior is substituted by two arcs around the position of the investigated object. Fig.s 3.32(a) and (b) display the PL images collected with a high numerical aperture oil objective (NA=1.40) for different focal points in the case of DRs with $\delta = 80\%$. The focused image (Fig. 3.32(a)) shows

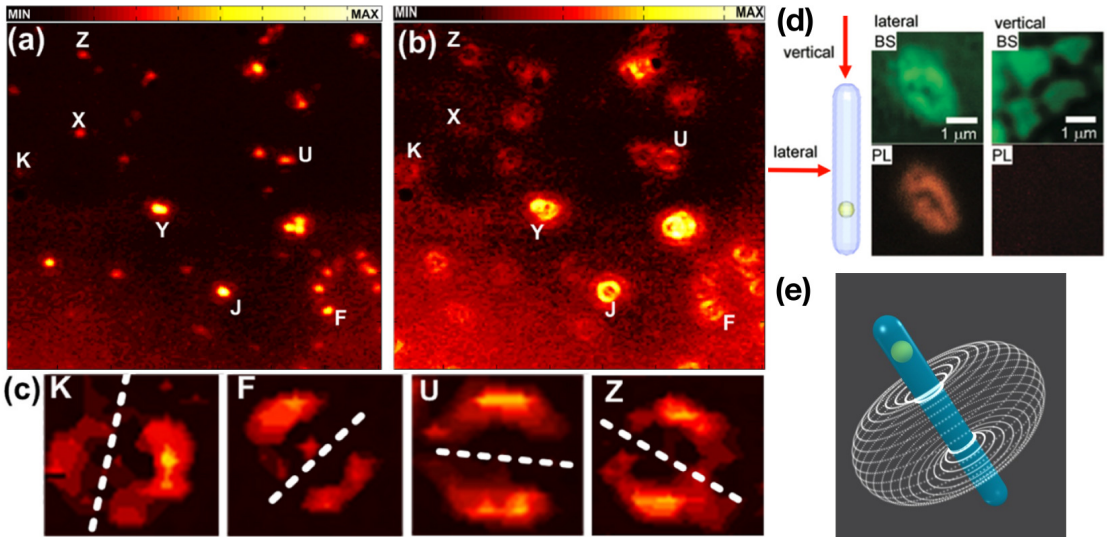

Figure 3.32: **(a)** Focused microscope images on an area of $50x50\mu m^2$. **(b)** Defocused microscope images of the same area shown in (a) when the objective is 500 nm far from the focal point. **(c)** Detail of four isolated DRs oriented along four different directions. **(d) BS panels** Excitation laser back-scattering for an horizontal (left) and vertically (right) aligned DRs. **(d) PL panels** PL intensity for an horizontal (left) and vertically (right) aligned DRs. **(e)** Sketch of the radiation pattern of a DR. Panel (d) has been reproduced from ref. [127]

the presence of several isolated DRs (for example Z, U, K, and F) and some clusters composed by more than one nanoparticle, for example Y and J, as demonstrated by the fact that their emission does not exhibit antibunching. By moving the microscope objective 500 nm far from the focal point (Fig. 3.32(b)), we detected the defocused images by means of a high quantum efficiency CCD. The single DRs Z, U, K, and F are characterized by two well defined defocusing curves. The defocused pattern can be used to identify the orientation of the DR (and therefore the orientation of the polarization vector) on the substrate by connecting the two minima of the defocusing lines as shown is Fig. 3.32(c) for K, U, F, and Z nanocrystals. This is not the case of the DR clusters Y and J in Fig. 3.32(a). Since these clusters are composed by a few DRs the resulting radiation patterns originate by a combination of dipolelike diagrams. Moreover, independent experiments [127] performed on vertically aligned DRs show

that no emission is collected coaxially to the rod axes. Fig.3.32(d) show the laser back-scattering and the photoluminescence intensity for horizontally and vertically aligned DRs: while the laser back-scattering allows to infer the presence of DRs also when exciting and collecting coaxially with them, no PL intensity is detected. These results confirm the dipole-like behavior of single photon flux, resulting in the radiation pattern reported in Fig. 3.32(e).

3.6 Conclusions and perspectives: a dot in a rod-based device for quantum cryptography

This chapter show that DRs allows a certain freedom in radiative channels engineering, making them blinking-free sources of single photons on-demand. In particular, DRs thickness permits to tailor the interaction between e-h pairs and carriers excited in the NC, the core diameter admit to modify wavefunction localization, while, in the case of quasi-type-II DRs, rod length acts directly on multiexciton binding rate by slightly modifying the electrons wavefuction. Indeed, by tuning these geometrical parameters, i.e. core diameter, shell thickness and rod length, it has been possible to obtain a strong reduction of blinking $[P_{off}(\tau_{off} > 50ms) = 0.001]$ together with a $g^2(0) < 0.26 \pm 0.013$, and efficiency of the $\sim 70\%$. By playing on both shell thickness and rod length it is also possible to induce a linear polarization of the light emitted by a single DR, reaching degrees of linear polarization as high as 80%. Moreover, a defocused microscope technique has been exploited to identify the orientation of randomly deposited DRs. Reasonably, this approach allows to choose a proper set of four well oriented DRs as a base for cryptography algorithms after a random deposition of the emitters.

Further improvements exploiting alignment techniques could also allow to control the orientation of DRs also during the deposition, thus increasing the potential of such emitters as room temperature nanosources for effective quantum cryptography systems. Indeed the use of DR single nanocrystals would make possible to emit single photons

with the desired polarization basis by orienting the nanocrystals at 0°, 90°, -45°,45° with respect to a specific axis. A defined orientation of the DRs can be achieved by different methods, such as strong electric fields, mechanical rods rotation through MEMS nanoactuators or by localizing and orienting single nanocrystals on prepatterned substrates. The use of specifically oriented polarized emitters would allow to avoid the recourse to optical components, such as linear polarizers, which would affect the source rate.

A viable strategy to achieve this goal relies in exploiting the dipole moment oriented along the rod axis of the DR, which allows for the orientation of the nanoparticles by applying an electric field during the deposition [127]. In order to do that, two types of electric contacts have been realized, and are displayed in Fig.s 3.33(a-d) and (e-h), respectively. In particular, $200nm$ thick gold electric contact on SiO_2 substrate has been deposited through a lift-off process following the geometries reported in Fig. 3.33, thus realizing tip [Fig. 3.33(a)-(d)] and planar [Fig. 3.33(e)-(h)] electrical contacts at four different angular orientations with gaps in the order of $200nm$. In order to orientate the nanocrystal on the substrate, an electric field of $\sim 2.5 \cdot 10^5 V/cm$ has been applied after the drop casting of a DRs nanomolar solution and during solvent evaporation in order to orientate the nanocrystals on the substrate. Preliminar results of nanocrystals luminescence after solvent evaporation are reported in Fig. 3.34 for both planar [Fig. 3.34(a,b)] and tip-shaped contacts [Fig. 3.34(c,d)]. DRs result to be disposed on the positive electric contact (which is at a non-zero potential difference if compared with the substrate) and within the contacts gap. Reasonably, the fluorescence between the tips shown in Fig. 3.34(d) follows the electric field lines, confirming that DRs disposes themselves exploiting an intrinsic dipole moment.

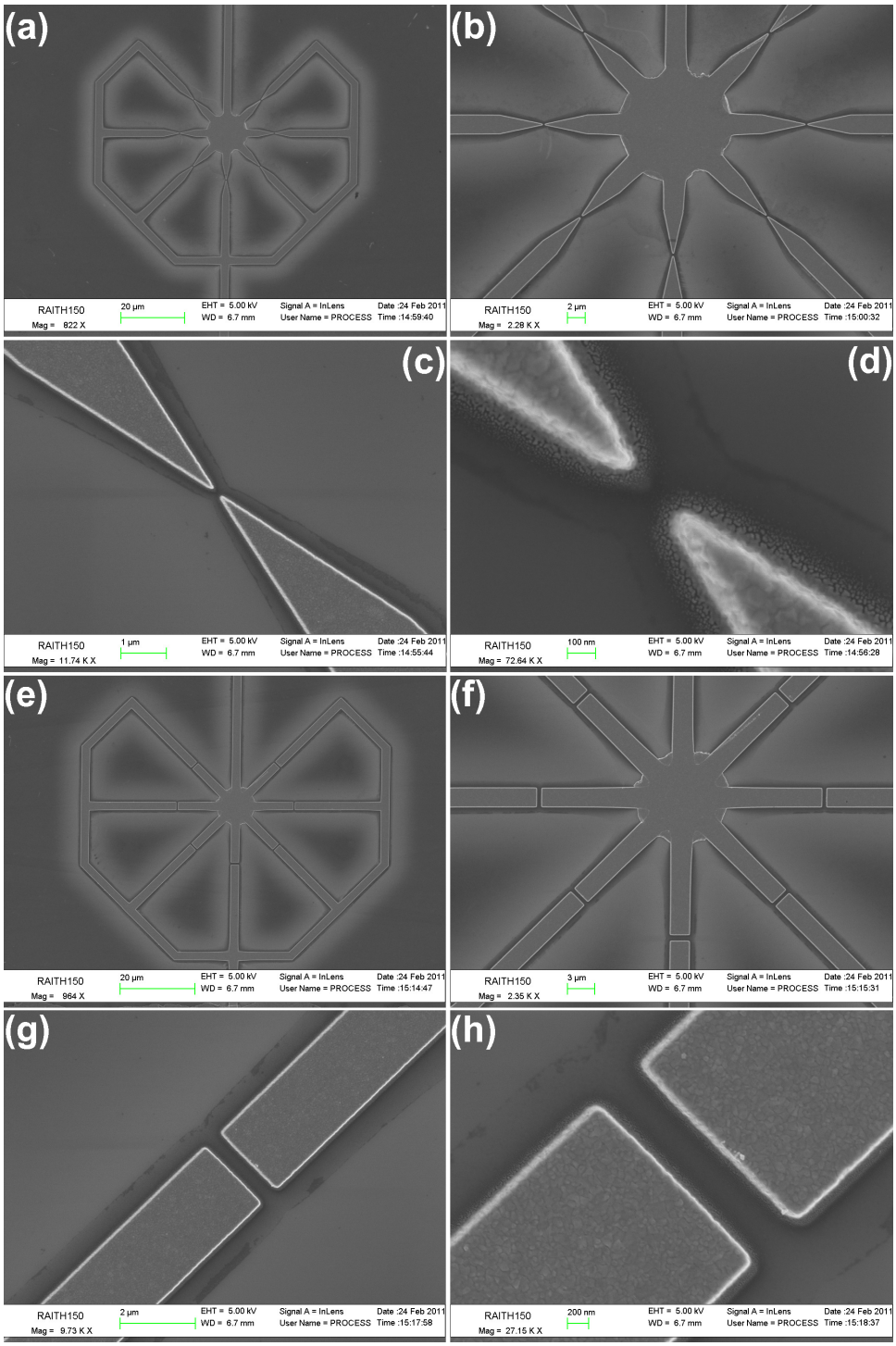

Figure 3.33: SEM micrographs of the realized electrical contacts.

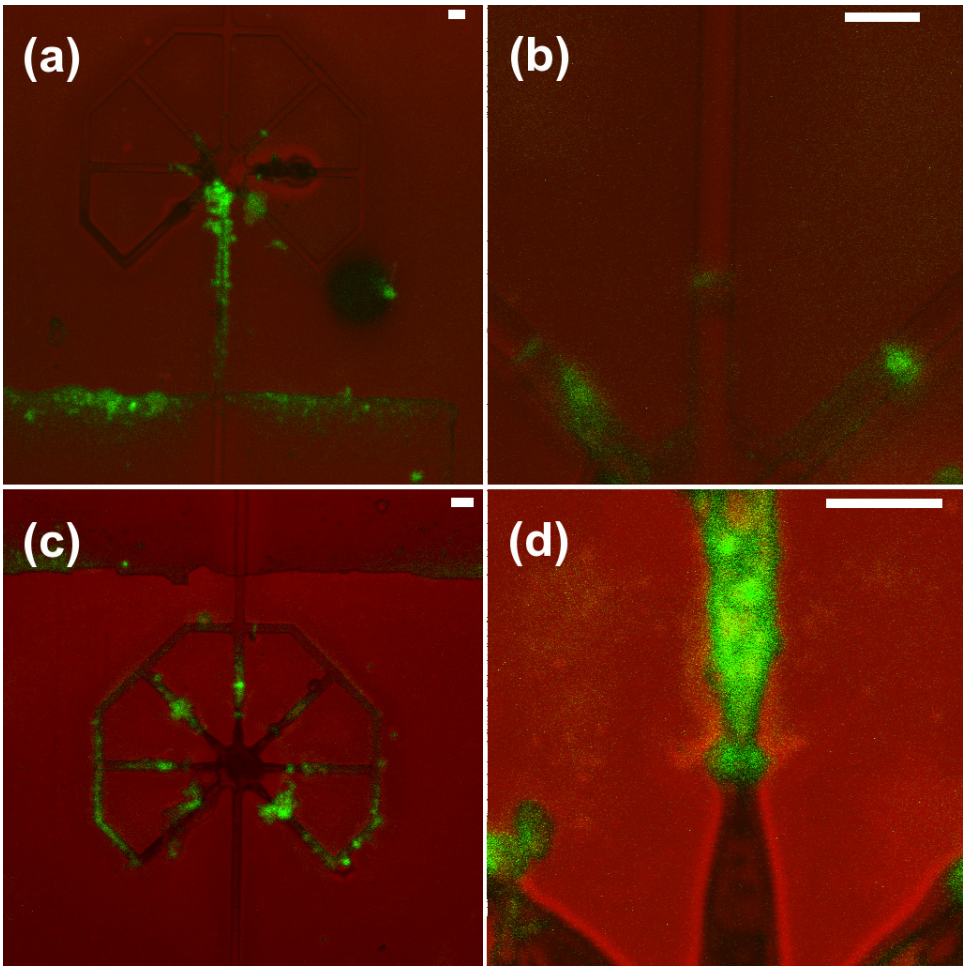

Figure 3.34: Confocal microscopy images of aligned DRs. Red and green signal are excitation laser backscattering and DR luminescence, respectively. Scale bare is $4\mu m$.

3.7 Peer-reviewed journal publications

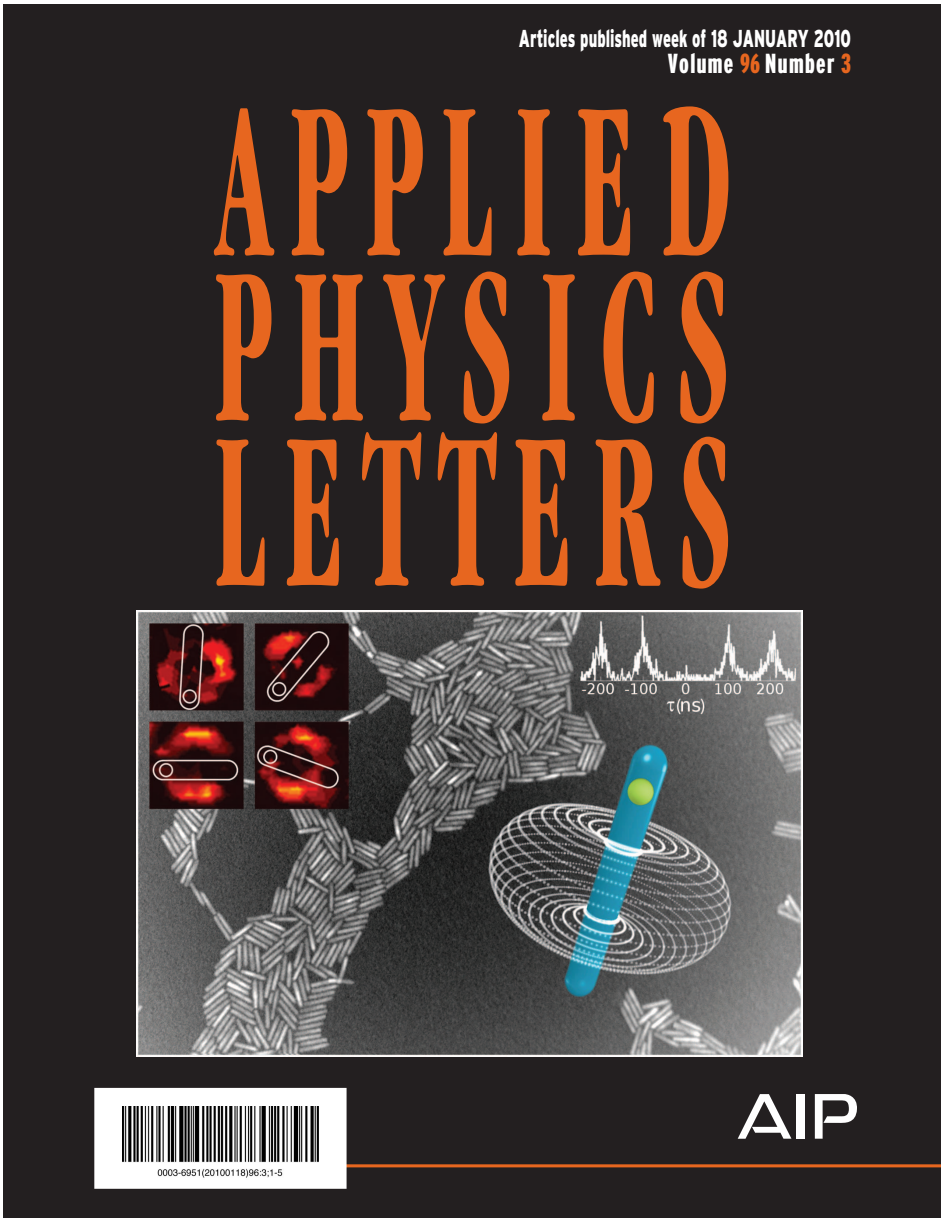

APPLIED PHYSICS LETTERS **96**, 033101 (2010)

Room temperature-dipolelike single photon source with a colloidal dot-in-rod

Ferruccio Pisanello,[1,2,a)] Luigi Martiradonna,[3] Godefroy Leménager,[1] Piernicola Spinicelli,[1] Angela Fiore,[2] Liberato Manna,[4] Jean-Pierre Hermier,[5] Roberto Cingolani,[2,3] Elisabeth Giacobino,[1] Massimo De Vittorio,[2,3] and Alberto Bramati[1]
[1]*Université Pierre et Marie Curie, Laboratoire Kastler Brossel, CNRS UMR8552, Ecole Normale Supérieure, 4 place Jussieu, 75252 Paris Cedex 05, France*
[2]*National Nanotechnology Laboratory, CNR/INFM, Scuola superiore ISUFI, Università del Salento, 16 Via Arnesano, Lecce 73100, Italy*
[3]*Center for Bio-Molecular Nanotechnology, Istituto Italiano di Tecnologia (IIT), Via Barsanti 1, Arnesano, Lecce 73010, Italy*
[4]*Central Research Lab, Istituto Italiano di Tecnologia (IIT), 30 Via Morego, Genova 16163, Italy*
[5]*Groupe d'étude de la Matière Condensée, CNRS UMR8635, Université de Versailles, Saint-Quentin-en-Yvelines, 45 avenue des Etats-Unis, 78035 Versailles Cedex, France*

(Received 5 October 2009; accepted 1 December 2009; published online 19 January 2010)

We propose colloidal CdSe/CdS dots in rods as nonclassical sources for quantum information technology. Such nanoemitters show specific properties such as strongly polarized emission of on-demand single photons at room temperature, dipolelike behavior and mono-exponential recombination rates, making us envision their suitability as sources of single photons with well defined quantum states in quantum cryptography based devices. © *2010 American Institute of Physics*. [doi:10.1063/1.3291849]

The development of efficient fully polarized single photon sources (SPSs) operating at room temperature is a cutting-edge research field.[1–3] The main application of SPSs is undoubtedly quantum information technology and in particular private keys distribution based on single photon fluxes of well defined quantum states.[4–6] Nonclassical light emission has been demonstrated from several nanometre-sized materials, such as single molecules,[7] defects in diamonds,[3] quantum dots,[8] single atoms in microcavities,[9] and more recently from elongated nanostructures such as carbon nanotubes[10] and quantum dots embedded in quantum wires.[11] Among these propositions, Stransky–Krastanov grown structures are catching the attention of scientific community[8,11] but are still limited by the operating temperature, far from 300 K. On the other hand, wet-chemically synthesized colloidal core/shell nanocrystals (NCs) are promising emitters for room temperature applications, due to the well separated allowed quantum energy states,[12,13] the low cost synthesis, the broad tunable emission range, and the compatibility with planar nanofabrication technology.[2,14–16] Although these emitters suffer from drawbacks, recent advances in fabrication succeeded in obtaining enhanced emission and almost suppressed blinking.[17,18] In 2001, elongated NCs [so called nanorods (NRs)] have been suggested as appealing room-temperature light emitters.[19] In particular, CdSe/CdS dots-in-rods (DRs), obtained by surrounding a spherical CdSe core with an elongated CdS shell[20] turn out to be very promising quantum emitters by virtue of their interesting ensemble polarization properties and therefore the expected dipolelike emission. In addition, they exhibit short lifetime and quantum efficiency of ~75% (further improved by surrounding the nanocluster with additional ZnS shell layers).[21] Compared to core NRs, the use of a CdS shell, having low lattice mismatch with the CdSe core, minimizes the influence of surface traps between core and shell on the radiative recombination process, which occurs in the low band gap core.[22] This avoids the well known increase of the average radiative lifetime of the system due to the interaction of excitons with surface traps.[23]

In this work we propose colloidal CdSe/CdS DRs as suitable fully polarized single photon sources for quantum information technology applications. We first show the nonclassical behavior of the light emitted by an isolated DR, then, by time and polarization resolved spectroscopy, we assess its polarization properties and we deduce the physical processes involved in the experiment. By exploiting their dipole nature we also measured the orientation of the DRs on the substrate by means of a defocused imaging technique, showing that DRs are suitable nanosources for quantum cryptography algorithms based on a single photon flux with a well defined quantum state, such as BB84 and B92.[4,5]

CdSe/CdS DRs were prepared by using the seeded growth approach proposed in Ref. 20 with a rod length $l \sim 50$ nm and a core diameter $c \sim 2.7$ nm. A typical output of the synthesis is reported in Fig. 1(a). A nanomolar solution of DRs in toluene was drop-casted on a glass coverslip thus obtaining a superficial DR density lower than 0.1 DR/μm^2. The sample was analyzed by a confocal microscopy system. A picosecond-pulsed excitation laser diode (wavelength 404 nm, pulse width ~50 ps) was focused on a single DR and time- and polarization-resolved spectroscopy and single photon counting measurements were performed by means of a high-sensitivity Hanbury–Brown and Twiss setup, based on a pair of avalanche photodiodes (APDs). The signals from the photodiodes were elaborated by a data acquisition card, used in two different configurations. All measurements were performed at room temperature.

In the start-stop mode, the delays between the received photons on the two APDs provide the measurement of the

a)Author to whom correspondence should be addressed. Electronic mail: pisanello@spectro.jussieu.fr. Tel.: +33144277266. FAX: +33144273845.

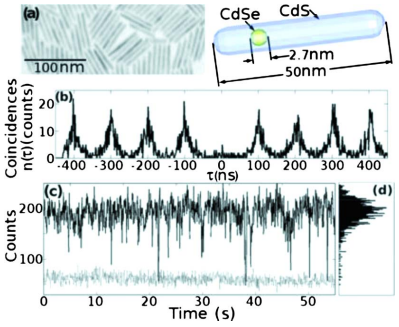

FIG. 1. (Color online) (a) Transmission electron microscope image and sketch of the synthesized DRs. (b) Autocorrelation function for unpolarized detection obtained with a laser repetition rate ν=5 MHz. (c) Example of a typical time resolved signal detected from a DR with a time binning of 100 ms. The gray dotted line represents the noise time trace. (d) Intensity distribution corresponding to (c).

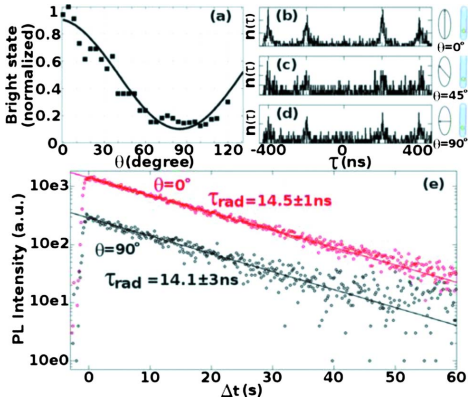

FIG. 2. (Color online) (a) Mean value of the bright state as a function of the polarization detection angle. The square dots represent experimental data, the solid line is the $\rho(\theta)$ fitting function. [(b)–(d)] Coincidence histogram n(τ) for three different value of θ. (e) Radiative decay curves in logarithmic scale detected for θ=0° and 90°.

coincidence histogram n(τ), proportional to the second order autocorrelation function $g^2(\tau)=\langle I(t)I(t-\tau)\rangle/[\langle I(t)\rangle\langle I(t-\tau)\rangle]$, where I(t) is the collected signal and τ is the delay between the received photons. $g^2(\tau)$ is a fundamental parameter to evaluate a SPS and to identify an isolated nanocristal: indeed if $g^2(0)=0$, that is no photons are detected with zero delay, we can infer that I(t) is a flux of single photons. A typical result of this measurement on a single DR is reported in Fig. 1(b). The negligible area of the $g^2(t)$ function around zero delay is the evidence that the system emits two or more photons at the same time with a negligible probability, computed to be ~0.02. Besides inferring that there are no multiple emitting DRs in the investigated area, this is the evidence that no more than one photon is emitted by each DR and that never two excitons are allowed to radiatively recombine per each excitation pulse. This finding can be assigned to the ability of Auger processes to suppress the radiative recombination of multiexcitonic states. When a laser pulse excites various electron hole pairs, they recombine nonradiatively through Auger processes until only one electron hole pair remains. Therefore, considering the coincidences histogram reported in Fig. 1(b), we can infer that multiexcitonic emissions, detrimental for the realization of advanced optical sources emitting single photons on demand, is avoided in the nanoclusters under investigation at the used pump regime (mean power ~1 μW).

Moreover, it is well known in literature that in strongly confined quantum emitters, such as colloidal NCs, two excitons localized in the same nanometer-sized core region feel a mutual interaction, thus generating a biexcitonic system.[24] Bi-excitons assume specific characteristics, such as different recombination energy, quadratic dependence from excitation power and faster decay time, with respect to the single exciton.[24] As shown in the following, besides the information inferred by the coincidences histogram, we can also have a confirmation about the single excitation pulse-single emission behavior of our DRs by measuring its radiative decay curve, where the presence of a biexcitonic system would lead to a nonmonoexponential trend.

By triggering the data acquisition card with the laser pulses (laser triggered mode), we recorded individual photon events with their absolute arrival times and their delays from the synchronization pulse. The typical time resolved photoluminescence (PL) trace of a single DR emission and the corresponding intensity distribution are displayed in Figs. 1(c) and 1(d), respectively. These curves clearly show only one emission level, identified as a bright state, in contrast to what observed in Ref. 25 in a charged CdSe/CdS NC, in which a nonradiative Auger process and a low efficient radiative process, usually referred to as gray state, are in competition. In our case, the absence of gray states, traps, and biexcitonic processes let us predict that a monoexponential decay behavior, only due to the single exciton recombination, is the dominant physical process involved in the quantum system under investigation.

In order to analyze the polarization properties of a single DR the mean emission intensity of the bright state has been measured for several detection polarization angles θ; when θ=0° (90°) only the light polarized along (perpendicular to) the rod axis is collected. As shown in Fig. 2(a) these mean values are well fitted by the curve $\rho(\theta)=d\cos^2(\theta)+(1-d)/2$, with a degree of linear polarization $d=(I_\parallel-I_\perp)/(I_\parallel+I_\perp)$ reaching ~80% ($I_\parallel$ and $I_\perp$ are the intensity at θ=0° and 90°). In order to confirm that the photon flux is antibunched for every component of the polarization vector, we measured the autocorrelation function for several values of θ. Representative results of these measurements are shown in Figs. 2(b)–2(d). Clear antibunched emission was obtained for each polarization, showing that by changing the polarization detection angle the nonclassical light flux is preserved.

The decay rate of the PL has been also measured. Two typical decay curves are reported in Fig. 2(e) for θ=0° and 90°. Both curves show a monoexponential decay function $A_r\exp\{-(t-t_0)/\tau_r\}$ with the best fit decay constant τ_r ~14.5 ns. This result, coupled to the antibunching behavior and to the time resolved PL, is a further evidence that in the investigated temporal range no secondary radiative processes such as biexcitonic emission or gray recombination processes are involved in the fluorescence of the CdSe/CdS DR.

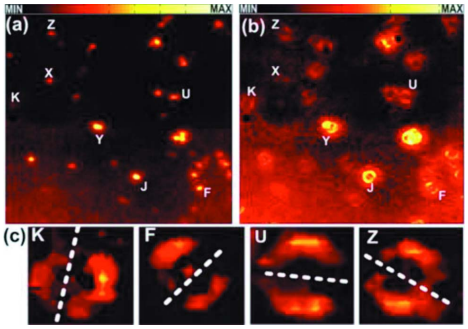

FIG. 3. (Color online) (a) Focused microscope images on an area of 50 $\times 50$ μm^2. (b) Defocused microscope images of the same area shown in (a) when the objective is 500 nm far from the focal point. (c) Detail of four isolated DRs oriented along four different directions.

In order to determine the dipole orientation in each DR, a defocused microscope technique[26] has been adopted: when a high numerical aperture microscope objective is moved from the focal point, an omnidirectional emitter on the sample plane is identified by means of concentric defocusing lines around the original focused spot. On the contrary, when the radiation diagram is dipolelike and the dipole is parallel to the microscope coverslip, the circular behavior is substituted by two arcs around the position of the investigated object. Figures 3(a) and 3(b) display the PL images collected with a high numerical aperture oil objective (NA=1.40) for different focal points. The focused image [Fig. 3(a)] shows the presence of several isolated DRs (for example Z, U, K, and F) and some clusters composed by more than one nanoparticle, for example Y and J, as demonstrated by the fact that their emission does not exhibit antibunching. By moving the microscope objective 500 nm far from the focal point [Fig. 3(b)] we detected the defocused images by means of a high quantum efficiency CCD. The single DRs Z, U, K, and F are characterized by two well defined defocusing curves. The defocused pattern can be used to identify the orientation of the DR (and therefore the orientation of the polarization vector) on the substrate by connecting the two minima of the defocusing lines as shown is Fig. 3(c) for K, U, F, and Z nanocrystals. This is not the case of the DR clusters Y and J in Fig. 3(a). Since these clusters are composed by a few DRs the resulting radiation patterns originate by a combination of dipolelike diagrams.

Here we have shown that a defocused microscope technique can be exploited to identify the orientation of randomly deposited DRs. Reasonably, this approach allows to choose a proper set of four well oriented DRs as a base for cryptography algorithms after a random deposition of the emitters. Further improvements exploiting alignment techniques[20] could also allow to control the orientation of DRs also during the deposition, thus increasing the potential of such emitters as room temperature nanosources for effective quantum cryptography systems.

In summary, we propose colloidal CdSe/Cds DRs as nonclassical emitters for quantum information technology. We assessed the absence of radiative biexcitonic recombination and gray states reporting complete and fully polarized photon antibunching, showing the suitability of these nanoemitters as dipolelike, room temperature, and polarized single photon sources. The possibility to identify the orientation of a single DR on the substrate suggests a viable strategy for the implementation of quantum information algorithms based on polarized single photon fluxes.

This work was supported by the Agence Nationale de la Recherche (Grant No. ANR-08-BLAN-0070-01). The authors thank Benedetta Antonazzo and Rosanna Mastria for their support in the synthesis of colloidal nanocrystals.

[1]S. Strauf, N. G. Stoltz, M. T. Rakher, L. A. Coldren, P. M. Petroff, and D. Bouwmeester, Nat. Photonics **1**, 704 (2007).
[2]A. Qualtieri, G. Morello, P. Spinicelli, M. T. Todaro, T. Stomeo, L. Martiradonna, M. De Giorgi, X. Quélin, S. Buil, A. Bramati, J. P. Hermier, R. Cingolani, and M. De Vittorio, New J. Phys. **11**, 033025 (2009).
[3]D. A. Simpson, E. Ampem-Lassen, B. C. Gibson, S. Trpkovski, F. M. Hossain, S. T. Huntington, A. D. Greentree, L. C. L. Hollenberg, and S. Prawer, Appl. Phys. Lett. **94**, 203107 (2009).
[4]C. H. Bennet and G. Brassard, in *Proceedings of the International Conference on Computers, Systems and Signal Processing, Bangalore, India, 1984* (IEEE, Piscataway, NJ, 1984), p. 175.
[5]C. H. Bennett, Phys. Rev. Lett. **68**, 3121 (1992).
[6]A. Beveratos, R. Brouri, T. Gacoin, A. Villing, J. P. Poizat, and P. Grangier, Phys. Rev. Lett. **89**, 187901 (2002).
[7]C. Brunel, B. Lounis, P. Tamarat, and M. Orrit, Phys. Rev. Lett. **83**, 2722 (1999).
[8]S. Kako, C. Santori, K. Hoshino, S. Götzinger, Y. Yamamoto, and Y. Arakawa, Nature Mater. **5**, 887 (2006).
[9]M. Hennrich, T. Legero, A. Kuhn, and R. Rempe, New J. Phys. **6**, 86 (2004).
[10]A. Högele, C. Galland, M. Winger, and A. Imamoğlu, Phys. Rev. Lett. **100**, 217401 (2008).
[11]A. Tribu, G. Sallen, T. Aichele, R. Andr, J.-P. Poizat, C. Bougerol, S. Tatarenko, and K. Kheng, Nano Lett. **8**, 4326 (2008).
[12]P. Michler, A. Imamoglu, M. D. Mason, P. J. Carson, G. F. Strouse, and S. K. Buratto, Nature (London) **406**, 968 (2000).
[13]B. Lounis and W. E. Moerner, Nature (London) **407**, 491 (2000).
[14]L. Martiradonna, L. Carbone, A. Tandaechanurat, M. Kitamura, S. Iwamoto, L. Manna, M. De Vittorio, R. Cingolani, and Y. Arakawa, Nano Lett. **8**, 260 (2008).
[15]A. Qualtieri, L. Martiradonna, T. Stomeo, M. T. Todaro, R. Cingolani, and M. De Vittorio, Microelectron. Eng. **86**, 1127 (2009).
[16]L. Martiradonna, T. Stomeo, M. De Giorgi, R. Cingolani, and M. De Vittorio, Microelectron. Eng. **83**, 1478 (2006).
[17]B. Mahler, P. Spinicelli, S. Buil, X. Quelin, J. P. Hermier, and B. Dubertret, Nature Mater. **7**, 659 (2008).
[18]X. Wang, X. Ren, K. Kahen, M. A. Hahn, M. Rajeswaran, S. Maccagnano-Zacher, J. Silcox, G. E. Cragg, A. L. Efros, and T. D. Krauss, Nature (London) **459**, 686 (2009).
[19]X. Peng, L. Manna, W. Yang, J. Wickham, E. Scher, A. Kadavanich, and A. P. Alivisatos, Nature (London) **404**, 59 (2000).
[20]L. Carbone, C. Nobile, M. De Giorgi, F. Della Sala, G. Morello, P. Pompa, M. Hytch, E. Snoeck, A. Fiore, I. R. Franchini, M. Nadasan, A. F. Silvestre, L. Chiodo, S. Kudera, R. Cingolani, R. Krahne, and L. Manna, Nano Lett. **7**, 2942 (2007).
[21]S. Deka, A. Quarta, M. G. Lupo, A. Falqui, S. Boninelli, C. Giannini, G. Morello, M. De Giorgi, G. Lanzani, C. Spinella, R. Cingolani, T. Pellegrino, and L. Manna, J. Am. Chem. Soc. **131**, 2948 (2009).
[22]D. Steiner, D. Dorfs, U. Banin, F. Della Sala, L. Manna, and O. Millo, Nano Lett. **8**, 2954 (2008).
[23]N. N. Hewa-Kasakarage, M. Kirsanova, A. Nemchinov, N. Schmall, P. Z. El-Khoury, A. N. Tarnovsky, and M. Zamkov, J. Am. Chem. Soc. **131**, 1328 (2009).
[24]M. Achermann, J. A. Hollingsworth, and V. I. Klimov, Phys. Rev. B **68**, 245302 (2003).
[25]P. Spinicelli, S. Buil, X. Quélin, B. Mahler, B. Dubertret, and J. P. Hermier, Phys. Rev. Lett. **102**, 136801 (2009).
[26]X. Brokmann, M.-V. Ehrensperger, J. P. Hermier, A. Triller, and M. Dahan, Chem. Phys. Lett. **406**, 210 (2005).

VERSITA

OPTO-ELECTRONICS REVIEW **18**(1), 0–0

DOI: 10.2478/s11772-009-0026-7

Recent advances on single photon sources based on single colloidal nanocrystals

INVITED PAPER

M. De VITTORIO*[1], F. PISANELLO[1,2], L. MARTIRADONNA[1], A. QUALTIERI[1], T. STOMEO[1], A. BRAMATI[2], and R. CINGOLANI[1]

[1]National Nanotechnology Laboratory of CNR-INFM, c/o Distretto Tecnologico ISUFI – Università del Salento, Via Arnesano, 73100 Lecce, Italy
[2]Université Pierre et Marie Curie, Laboratoire Kastler Brossel, CNRS UMR8552, Ecole Normale Supérieure, 4 Place Jussieu, Paris 75005, France

Single colloidal quantum dots (QDs) are increasingly exploited as triggered sources of single photons. This review reports on recent results on single photon sources (SPS) based on colloidal quantum dots, whose size, shape and optical properties can be finely tuned by wet chemistry approach. First, we address the optical properties of different colloidal nanocrystals, such as dots, rods and dot in rods and their use as single photon sources will be discussed. Then, we describe different techniques for isolation and positioning single QDs, a major issue for fabrication of single photon sources, and various approaches for the embedding single nanocrystals inside microcavities. The insertion of single colloidal QDs in quantum confined optical systems allows one to improve their overall optical properties and performances in terms of efficiency, directionality, life time, and polarization control. Finally, electrical pumping of colloidal nanocrystals light emitting devices and of NC-based single photon sources is reviewed.

Keywords: quantum dots, colloidal nanocrystals, emission efficiency, microcavity optical modes

1. Introduction

Single photon sources (SPSs) are a breakthrough in quantum information due to their possible exploitation in fields such as quantum communication, quantum computation, quantum lithography, and quantum cryptography [1–4]. In particular, quantum cryptography theorizes the secure distribution of a secret key between two partners through quantum photonic states. Also referred to as quantum key distribution (QKD) [5,6], this method is intrinsically secure since a quantum state cannot be read by an eavesdropper without being modified [7]. Since its initial proposal in 1984 [8] and its first experimental demonstration in 1992 [9], QKD has been implemented in many ways [10], exploiting different techniques for the generation of single photons. True single photon sources [11,12] have been demonstrated to outperform key distribution based on attenuated classical laser pulses [13], where multiple photon emission is hard to avoid [14]. Implementations of single photon sources based on individual molecules [15], nitrogen vacancy centres [16] or dopant atoms [17] are rather inefficient due to low emission rates and rapid saturation.

An ideal quantum light source should generate one single photon per excitation pulse, which can be accomplished by using the emission of a single quantum system, such as a single quantum dot [18]. By virtue of their unique electronic structure and quantum confinement, single quantum-dot emitters reliably generate single photons on demand when excited by short optical or electrical pulses. Since 1982, when the concept of quantum dots (QDs) was first proposed by Arakawa and Sakaki [19], their peculiar properties have been applied to a number of photonic devices, and impressive results in the synthesis and application of these powerful nanostructures have been demonstrated. Epitaxial QDs, obtained by the Stranski-Krastanov self-organized growth mode [20], have demonstrated their potential as light sources for ultrafast semiconductor lasers and optical amplifiers (SOAs) for optical communications, showing new functionalities and astonishing performances such as high gain and efficiency, ultra-low threshold current densities and temperature insensitivity [21–23]. A different approach for the fabrication of quantum dots is based on wet chemistry for the synthesis of colloidal QDs. These colloidal nanocrystals (NCs) are good candidates for QDs photonic applications in different fields such as health, energy, environment and aerospace due to their low fabrication costs, high quantum efficiency at room temperature, high versatility in the chemical synthesis, and broad tunable emission range [24]. Both epitaxy and wet chemistry have demonstrated to be effective for the fabrication of single QDs embedded in triggered non-classical sources of single photons. Epitaxial QDs exhibit single photon emission only

*e-mail: massimo.devittorio@unile.it

at cryogenic temperature [25], whereas single colloidal NCs based on II-VI compounds exhibit photon antibunching at room temperature and above [26,27], by virtue of their peculiar electronic properties. In order to tailor and enhance the emission of SPSs, single quantum emitters should be embedded inside micro and nanocavities. The insertion of QDs in quantum confined optical systems, such as high quality factor resonators, allows us to improve the overall performances in terms of efficiency and directionality, together with a better control on the polarization characteristics of the emitted photons. Among the above discussed species for single photon generation, self-assembled epitaxial and colloidal QDs can be straightforwardly incorporated into cavities by using standard micro and nanotechnological processing techniques.

In this work recent advances on single photon sources based on single colloidal quantum dots are reviewed. We first recall basic concepts related to the optical properties of colloidal nanocrystals, with special emphasis on their photon antibunching, blinking and spectral diffusion phenomena. We then discuss the technological approaches for isolating and positioning single colloidal quantum dots, an essential requirement for practical realization of single nanocrystal SPSs. The third section reports on the approaches to significantly enhance the emission efficiency of SPSs by coupling the emission of single nanocrystals to microcavity optical modes. The successful achievement of this challenging technological target leads to devices with enhanced performances in terms of extraction efficiency, low divergence and improved emission efficiency in both weak and strong coupling regimes. Finally, possible approaches for the electrical pumping of single colloidal nanocrystal SPS devices are discussed. Electrically driven triggered sources of single photons are highly attractive since they would bring compact SPSs to practical application, without requiring expensive and sizeable light excitation sources.

2. Single colloidal quantum dots as sources of single photons

Semiconductor colloidal nanocrystals synthesized by wet chemical approaches as sources of single photons have been extensively studied in the last years because of their low fabrication costs, high quantum efficiency and photostability also at room temperature [28]. Broad tunability of their emission wavelength from the visible to the infrared has been readily achieved by virtue of the high versatility in the chemical synthesis, which allows for excellent control over NCs size, shape and composition [29–32].

Typical nanocrystals are nanometer-sized spherical core--shell structures. The role of the shell is to engineer the band structure of the nanostructure and to passivate the core surface, thus reducing surface defects, such as dangling bonds, which dramatically affect their efficiency and photostability. Due to their absorption continuum at energies above the exciton transition they can be excited by a variety of light sources. Recombination from higher excited states, multi--exciton and charged excitons in careful experimental conditions is typically negligible because of strong Auger processes [33], and the emission of single photons can be made highly probable only from single exciton recombination.

In spite of their excellent quantum efficiency and photostability, colloidal nanocrystals, when observed at the single particle level, exhibit fluorescence blinking and spectral diffusion. The first effect consists in the random switching of fluorescence between bright ("on") and dark ("off") states [34]. Such a fluctuation of the luminescence over time has been attributed to charge transfer or charge escape from the dot, which leads to a free charge in the NC, preventing any possible radiative recombination for times in the order of milliseconds. A strategy to control and completely prevent blinking has been recently proposed by Mahler and coworkers [35], who show that a thicker shell in CdSe-CdS NCs allows one to control the blinking behaviour, suggesting that well-designed shells are the key parameters for obtaining non-blinking QDs. Non blinking behaviour has been also obtained in ternary CdZnSe/ZnSe NCs, designed as a radial graded alloy of CdZnSe into ZnSe [36].

Spectral diffusion consists of random spectral jumps ascribed to charge movements or, more generally, to instability in the nanoscale environment of the nanocrystals, which cause strong fluctuations of local electric fields [37,38]. The resulting linewidth of single nanocrystals is broadened by the time integration of NCs emission at slightly shifted wavelengths. High temporal resolution is necessary to observe, in a single quantum dot, the evolution of spectral diffusion [39]. In CdSe/ZnS single colloidal nanocrystals, a spectral diffusion of 4 μeV over a time scale of 200 μs was observed for an emission peak having a linewidth as narrow as 6.5 μeV [40].

The good emission efficiency at room temperature, good stability and advances in high spatial resolution spectroscopic techniques has allowed in the last years a deeper understanding of the peculiar optical properties of QDs, by probing NCs at single particle level [34,37].

Evidence of efficient single photon emission at room temperature corroborates the potential of these nanostructures as active medium of single photon sources. A Hanbury Brown and Twiss setup is normally used to confirm the non-classical nature of the single QD emission through the second-order correlation function,

$$g^{(2)}(\tau) = \frac{< I(t+\tau)I(t) >}{< I(t+\tau) >< I(t) >}$$

i.e., an intensity-intensity correlation function, having information on both photon statistics and dynamics of the light generated from the nanocrystals. Figure 1(a) shows the scheme of a Hanbury Brown and Twiss setup. Single photons impinging on a beam splitter are split towards two fast avalanche photodiodes (APDs), which allow to measure directly $g^{(2)}(\tau)$, by detecting the delay between the arrival events. The absence of coincident detection events on the two detectors is the fingerprint of a one-by-one photon

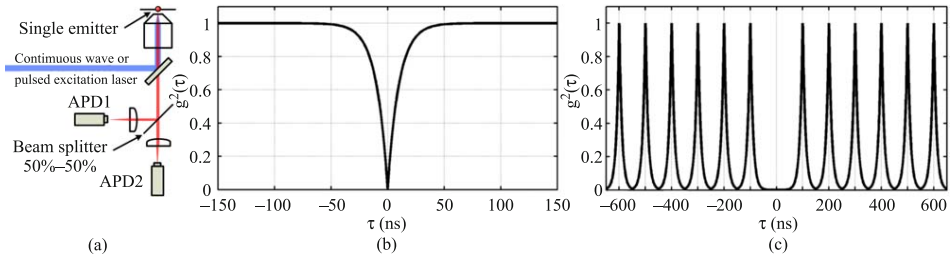

Fig. 1. Schematic representation of the Hanbury Brown and Twiss setup (a), typical behaviour of the second order autocorrelation function for continuous (b) and pulsed excitation (c).

emission, i.e., photon antibunching. In most single photon sources at room temperature, this behaviour is manifested by a dip around zero time delay ($\tau = 0$) in the second-order correlation function [Fig. 1(b)]. When using a pulsed excitation, the second-order correlation function consists of an array of short peaks with the period of the pumping sources and the evidence of single photon emission is the absence of the peak at zero time delay [Fig. 1(c)].

Most of the photon antibunching reports in the literature are based on II-VI NCs constituted by a CdSe spherical core embedded in either ZnS or CdS shells. In CdSe/CdS NCs, by virtue of a low lattice mismatch, the influence of defects on the radiative recombination process is reduced, as well as the influence of surface traps on single excitons, which usually tend to increase the average radiative lifetime of the system. The full control on the growth parameters in the wet chemical synthesis process was exploited to synthesize different NCs such as rods, dot in rods, tetrapods and also dimers [29,31,32,41,42]. Most of these nanocrystals demonstrated to be effective sources of single photons. In particular nanorods, i.e., elongated NCs, and CdSe/CdS dot-in--rods (DR), obtained by surrounding a spherical CdSe core with an elongated CdS shell [31,43] appear to be very promising quantum emitters, by virtue of their relatively short lifetime [44,45] and electrical dipole-moment oriented along the rod axis [29,43] which leads to a higher degree of linear polarization [29,43,45].

This feature, invaluable for a SPS device, allows a deterministic photon polarization to be achieved, as required in BB84 and B92 cryptographic algorithms [8,46], without recurring to polarizers to encode information. In Ref. 47, it is shown that the polarization control of single photons can be achieved by using dot-in-rods rotated at different angles, envisioning a strategy to develop polarization controlled, low cost and highly efficient room temperature single photon sources.

3. Localization of single quantum dots

Both epitaxial self-organized quantum dot and colloidal nanocrystals have been used as active media of single photon sources. Both being based on self organization, one of the most challenging tasks is the control over the QD position, in order to align the nanoemitter to a microcavity or to fabricate arrays of SPS devices in specific locations.

The typical way to realize a single photon source based on self organized QDs is to inspect the sample, purposely fabricated with low-density of quantum dots ($<10^9$ cm^{-2}), and after having localized an isolated area with a single nanostructure inside, to build a device using very high resolution fabrication techniques [48–50]. The nucleation sites, and therefore the surface density of epitaxial QDs, are usually controlled by carefully tuning the Stranski Krastanov growth parameters. Colloidal NCs are typically diluted to nanomolar concentrations and dropcasted on glass cover slides, obtaining, after evaporation of solvents, isolated nanocrystals with an average distance among them in the order of microns.

These approaches, though well-suited for the characterization through confocal microscopy of photon antibunching behaviour in single nanostructures, are not appropriate for the realization of controlled arrays of SPS to be embedded in QKD commercial systems.

In order to localize epitaxial QDs, fabrication of site--controlled pre-patterned recesses in the substrate and regrowth has been successfully exploited [51] to embed single QDs inside micropillar vertical cavities [52] and 2D photonic crystal membranes [53], but poor control over emission wavelength and lack of single photon emission up to room temperature prevent their practical use.

Recently, a new approach has made possible the pinpointing of single colloidal quantum dots by direct electron beam lithography. The controlled localization of ordered arrays of single colloidal nanocrystals was demonstrated in Ref. 54 by dispersing a specific concentration of nanocrystals inside a negative high-resolution electron-beam resist after precipitation and re-dilution in methyl-isobutyl-ketone (MIBK) solvent. Ensembles of nanocrystals embedded in electronic resists can be easily patterned by means of traditional lithographic processes, since the presence of semiconductor clusters in the matrix does not significantly affect the sensitivity of the polymeric host and, at the same time, the emission properties of the nanocrystals are not influenced by the interaction with the electron beam [55]. To obtain on average one nanocrystal inside a nanosized pillar of the NC/resist blend, direct e-beam patterning is employed

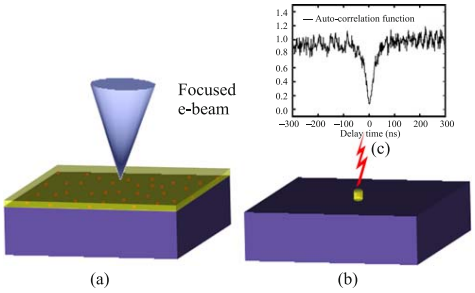

Fig. 2. Schematic representation of the localization of single colloidal quantum dots by direct electron beam lithography of a resist/NCs blend (a). By a careful control of molar density of the NCs dispersed in the resist and pillar volume it is possible to isolate single QDs (b). Autocorrelation function of an isolated CdSe/ZnS QD of coincidence counts of fluorescence from a single QD in microcavity (c).

[Figs. 2(a) and 2(b)]. Through a careful control of molar density of the NCs dispersed in the resist and pillar volume, i.e., blend layer thickness and pillar diameter, it is possible to obtain a very high probability of having localized single colloidal NCs, whose photon antibunching behaviour was confirmed through a confocal microscope and Hanbury--Brown and Twiss setup [Fig. 2(c)].

It is worth mentioning a few more methods for trapping single colloidal nanocrystals which rely on electrostatic trapping in nanogaps [56] or by electrostatic biological self--aligned placement [57]. In the latter case, the self-aligned positioning of a nanocrystal in the cage-shaped negatively charged protein is followed by the trapping of the protein on specific positively charged ultra small positions. Electrostatic trapping is very attractive remarkably for nanocrystals exhibiting a high dipole moment, such as asymmetric dot-in-rods.

4. Coupling of colloidal QDs to microcavities

The presence of a cavity strongly affects the density of available photon states (PDOS) of the environment. When an emitter is placed inside a cavity, many properties of its light emission can be strongly modified. Spontaneous emission rate and radiative decay can be engineered and enhanced, radiative pattern and divergence angles can be modified to improve collection efficiency and optical matching with optical fibers, spectral emission can be narrowed or filtered and the emission polarization can be controlled.

Micro and nanocavities embedding nanoemitters are the subject of intense studies for the realization of ultra-low threshold microlasers, or cavity quantum electrodynamics (CQED). CQED systems allow us fundamental studies of coherent interactions of confined electromagnetic fields (cavity photons) and microscopic dipoles (single nanoemitters) [58–61].

The task of aligning a single nanoemitter to a cavity is very challenging since its single exciton transition must be coupled to a resonant mode of a high quality factor (Q-factor) microcavity. When this is achieved, the efficiency and emission properties of a single colloidal NC are significantly improved. The coupling between the nanoemitter and the cavity can be either strong or weak depending on the coupling parameter,

$$g = \frac{\mu_{dm}}{\hbar}\sqrt{\frac{\hbar\omega}{2\varepsilon_0 V}}$$

where V is the cavity mode volume, ε_0 is the vacuum dielectric constant, and μ_{dm} is the dipole moment of the transition. Asymmetric NCs, such as nanorods and dot-in-rods, are particularly suitable for the achievement of strong coupling regime since they show a strong dipole moment and increased dipole oscillator strength [62].

Weak coupling enhances the spontaneous emission, whose rate is given by the Purcell factor

$$F_p = \frac{3}{4\pi^2}\frac{Q}{V}\left(\frac{\lambda}{n}\right)^3.$$

When a nanocrystal is inserted into the microcavity and its eigenfrequency ω_{QD} is resonant with the high-Q cavity mode ω_{cav} and $g^2 > (\gamma_{cav} - \gamma_0)^2/16$, being γ_0 and γ_{cav}, the field decay rate in free space and inside the cavity, respectively, the confined photonic and electronic states interact by coherently exchanging energy. This leads to a new strongly coupled quantum-mechanical system which evolves with a coupling strength defined by the vacuum Rabi splitting [63–68].

In both strong and weak coupling, the target is to reduce the modal volume of cavity and to carefully tune its Q-factor as it is typically possible in photonic crystal nanocavities. When F_p is greater than 1, the emitter radiates faster in the cavity than in free space and the emission is enhanced only as long as the system remains in the weak coupling regime.

The coupling is maximized when the emitter is placed in the maximum of the electric field intensity; however, this is hard to be fulfilled for point-like emitters, since it requires a high accuracy in nanocrystals positioning inside an ultra--small volume.

Doping of vertical microcavities with an ensemble of NCs has been demonstrated by different techniques, by embedding the nanocrystals in two distributed Bragg reflectors (DBRs) [69] and by focused ion beam (FIB) post-milling to obtain micropillars [70] or by imprint lithography [71].

However, very few papers in the literature report on single colloidal nanocrystals embedded in microcavities and efficiently emitting triggered single photons at room temperature.

Coupling of a single colloidal quantum dot with photonic cavities has been achieved by exploiting whispering gallery modes generated on the surface of glass and polymer microspheres [72]. Artemyev *et al.* report on the coupling of

a single CdSe/ZnS NCs chemically bound to the surface of a single glass microsphere, reporting the Purcell factor F_p ~10. The same group reported on a strongly coupled CQED system consisting of an anisotropically-shaped CdSe nanocrystal coupled to a single photon mode of a polymer microsphere, showing a vacuum Rabi splitting between 30 and 45 μeV in a microsphere cavity, slightly deformed to remove mode degeneracy [61].

Although glass spherical cavities localize very high quality factor modes, their use as SPS is hindered due to their relatively large mode volume and their poorly collimated photon emission.

In this respect, photonic-crystal structures [73,74] are promising candidates for the trapping of light in ultrasmall volumes with high Q-factor [75–77]. Two- and three-dimensional photonic crystal microcavity architectures were also exploited by Wu *et al.* [78], who coupled PbSe nanocrystals to a silicon PC membrane, and by Lodhal *et al.* [79] who used a titania inverse opal as host photonic crystal lattice.

Photonic crystal cavities, providing a well collimated emission, are more suited for the realization of SPS, but the crucial step for their fabrication, i.e., the positioning of single colloidal nanocrystals in the resonant path of the cavity modes, is difficult to be achieved.

While the demonstration at low temperature of single photon emission from a single epitaxial quantum dot coupled to cavity modes has been reported both in micro/nanopillars vertical cavity resonators [80] and in two-dimensional photonic crystal resonators [48], the localization of single colloidal NCs inside a microcavity resulted to be more complex, due to the more difficult handling of these nanoemitters. Recently, the experimental observation of fluorescence from single colloidal nanocrystals in microcavities by both doping of a chiral liquid-crystal microcavity and also by a microcavity fabricated by spin coating of several polymeric layers and dispersing a nanomolar concentration of NC in the waveguiding layer was reported [81]. A further step toward the practical realization of single NC based SPS was reported in Ref. 82. Qualtieri *et al.* showed for the first time the occurrence of photon antibunching at room temperature from single colloidal CdSe/ZnS nanocrystals inserted in an ordered array of vertical microcavities. The approach relies on the single NC localization technique obtained by direct electron beam lithography on top of a SiO_2/TiO_2 Bragg mirror [82]. Subsequently, the array of localized single quantum emitters was clad by a second DBR consisting of four alternating quarter-wavelength thick layers of TiO_2/SiO_2.

Figure 3 shows the schematic of the fabricated microcavity and the antibunching demonstration [Fig. 3(c)] from single nanocrystals in microcavity at room temperature.

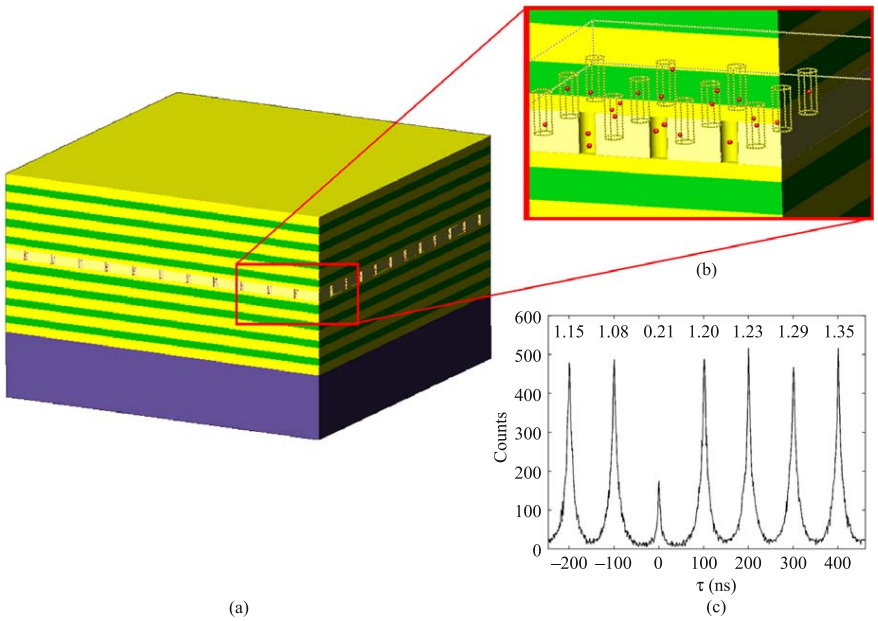

Fig. 3. Schematic of single colloidal quantum dots microcavity array obtained by direct electron beam lithography and SiO_2/TiO_2 DBR deposition (a,b). Histogram of coincidence counts of fluorescence from a single QD in microcavity (reproduced with permission from Ref. 82) (c).

5. Electrical pumping of single photon sources based on colloidal nanocrystals

Colloidal NCs have demonstrated their potential in many applications due to their aforementioned peculiar properties. Most experimental results on photon antibunching are based on optical pumping of NCs, but recently different approaches for electrical pumping/driving of colloidal nanocrystals embedded in light emitting devices or solar cells are being pursued. Injection of carriers in colloidal NCs is not as straightforward as for epitaxial QDs, where these nanostructures can be directly embedded in p-n junctions.

Direct injection of charge carriers in colloidal nanocrystals is typically limited due to the presence of an insulating organic capping layer on the nanocrystals. An indirect approach for the electrical pumping is based on the insertion of NCs inside a device which transfers either radiatively or non-radiatively the accumulated electrical energy to colloidal nanocrystals. The latter mechanism, called Förster resonant energy transfer (FRET), is based on a donor-acceptor non-radiative coupling and is governed by the spectral overlap between the emission spectrum of the donor species with the absorption spectrum of an acceptor and by the distance between them. In this process of non-radiative transfer, described for the first time by Theodor Förster in 1948 [83,84], the excess energy of the donor is transferred to the acceptor by a dipole-dipole interaction in a purely non-radiative process whose rate is given by the formula

$$R_{ET} = \frac{9c^4\kappa^2}{8\pi n^4 \tau_r}\frac{1}{d^6}\int_0^\infty \frac{f_D(\omega)\alpha_A}{\omega^4}d\omega\,, \qquad (1)$$

where c is the speed of light, n is the refractive index of the medium, κ^2 is the parameter given by the mutual orientation of the donor to acceptor dipoles (for isotropic orientation equal to 2/3), and τ_r is the radiative lifetime of the donor and the integral is the "overlap integral" which takes into account the overlap between the donor emission spectrum $f_D(\omega)$ and the absorption spectrum of the acceptor $\alpha_A(\omega)$. The most significant factor is the distance d between the acceptor and the donor, the FRET rate being proportional to the inverse of the sixth power of d.

For very short donor-acceptor distances, shorter than the extent of dipoles, higher order effects prevail, but their discussion is beyond the scope of this review.

FRET has been exploited in the last years in many demonstrations of LEDs based on hybrid technologies and embedding colloidal nanocrystals.

An approach to nanocrystal-based, electrically pumped light emitting devices exploits hybrid organic/inorganic structures, in which only a small fraction of the charge carriers is directly delivered to nanocrystals through the organic network [85,86]. Coe *et al.* demonstrated efficient electrical injection in a colloidal quantum dot LED embedding a single monolayer of QDs between two organic thin films [85]. The organic layers transport charge carriers to the vicinity of the QD monolayer. Exciton generation on QDs occurs via two parallel processes, direct charge injection and non-radiative energy transfer from excitons close to the single QD monolayer, and formed in organic molecules in grain boundaries, interstitial spaces, and voids. These excitons then undergo FRET energy transfer to the lower-energy QD sites, where they recombine radiatively. Based on the same approach, the only evidence of electroluminescence from a single colloidal quantum dot is reported in Ref. 87, where no evidence of photon antibunching is reported, however.

The performance of these hybrid devices is limited by the low carrier mobility in both the organic and nanocrystal components, and by the poor stability of the organic molecules. Moreover, single nanocrystal single photon sources, triggered by electrical pulses, are still to be demonstrated.

Most of the reports on FRET in the past years have taken into account an ensemble of NC as acceptors. When single nanocrystals are used one has to deal with the reduced transition width, which becomes narrower and narrower as the temperature is decreased. This behaviour, together with the possibility of shifting the transition in asymmetric rod-like NCs through the quantum confined Stark effect (QCSE) [88], has been exploited in Ref. 89 to switch on and off the energy transfer between a dye molecule and an asymmetric dot in rod NC [90].

Finally, it is worth mentioning the radiative energy transfer, which is a technique used in traditional colour conversion schemes based on phosphors. The emission of a photon from a semiconductor standard LED is followed by absorption and re-emission by an optically active material, which is typically a phosphor but can also be replaced

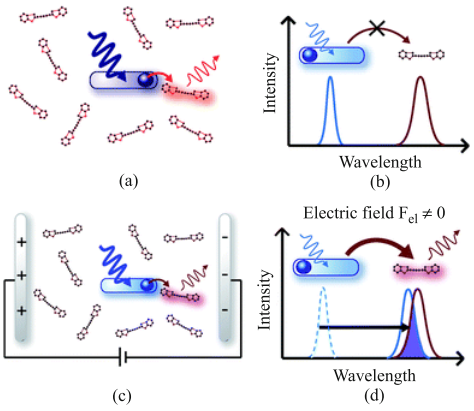

Fig. 4. Electrical control of energy transfer in a single FRET couple consisting of a dye molecule and an asymmetric dot in rod NC (a). Each NC is, in principle, adjacent to one acceptor molecule (b). At low temperatures, however, the electronic transitions of donor and acceptor are too narrow to enable a sufficient spectral overlap, required for efficient FRET (c). Application of an electric field to the NC-dye mixture can facilitate FRET by Stark-shifting the emission of the NC into resonance with the absorption of an adjacent dye molecule (reproduced with permission from Ref. 90) (d).

by nanocrystals. This approach has been already exploited for the demonstration of white light LEDs based on colloidal NCs on nitride-based quantum wells LEDs [91]. The quantum wells can be pumped electrically in the same way a common LED is pumped but the efficiency of the energy transfer is very poor, typically several orders of magnitude lower than non-radiative FRET transfer [92].

6. Conclusions

This review has discussed recent achievements and technological approaches for the realization of single photon sources based on single colloidal nanocrystals, a building block for future quantum information. Despite the body of work done so far, many issues still need to be faced and some of the technological problems to be solved. Manipulation, embedding and positioning inside the microcavities and efficient electrical pumping of single colloidal nanocrystals are technological subjects discussed in this paper, which still need to find optimal solution. However, the impressive results and astonishing performances reported in the literature in the last years make triggered sources of single photons closer and closer to their practical application in quantum communication and quantum cryptography.

References

1. D. Bouwmeester, A.K. Ekert, and A. Zeilinger, *The Physics of Quantum Information*, Springer, Berlin, 2000).
2. A.N. Boto, P. Kok, D.S. Abrams, S.L. Braunstein, C.P. Williams, and J.P. Dowling, "Quantum interferometric optical lithography: exploiting entanglement to beat the diffraction limit", *Phys. Rev. Lett.* **85**, 2733–2736 (2000).
3. E. Knill, R. Laflamme, and G.J. Milburn, "A scheme for efficient quantum computation with linear optics", *Nature* **409**, 46–52 (2001).
4. N. Gisin, G. Ribordy, W. Tittel, and H. Zbinden, "Quantum cryptography", *Rev. Mod. Phys.* **74**, 145–195 (2002).
5. P. Michler, A. Imamoglu, M.D. Mason, P.J. Carson, G.F. Strouse, and S.K. Buratto, "Quantum correlation among photons from a single quantum dot at room temperature", *Nature* **406**, 968–970 (2000).
6. M. Pelton, C. Santori, J. Vuckovic, B. Zhang, G.S. Solomon, J. Plant, and Y. Yamamoto, "Efficient source of single photons: A single quantum dot in a micropost microcavity", *Phys. Rev. Lett.* **89**, 233602–233605 (2002).
7. W.K. Wootters and W.H. Zurek, "A single quantum cannot be cloned", *Nature* **299**, 802–803 (1982).
8. C.H. Bennett and G. Brassard, *Int. Conf. on Computers, Systems and Signal Processing*, 175, Bangalore, (1984).
9. C.H. Bennett, F. Bessette, G. Brassard, L. Salvail, and J. Smolin, "Experimental quantum cryptography", *J. Cryptol.* **5**, 3–28 (1992).
10. N. Gisin, G. Ribordy, W. Tittel, and H. Zbinden, "Quantum cryptography", *Rev. Mod. Phys.* **74**, 145–195 (2002).
11. B. Lounis, and M. Orrit, "Single-photon sources", *Rep. Prog. Phys.* **68**, 1129–1179 (2005).
12. A.J. Shields, "Semiconductor quantum light sources", *Nat. Photonics* **1**, 215–223 (2007).
13. A. Beveratos, R. Brouri, T. Gacoin, A. Villing, J.P. Poizat, and P. Grangier, "Single photon quantum cryptography", *Phys. Rev. Lett.* **89**, 187901–187904 (2008).
14. E. Waks, K. Inoue, C. Santori, D. Fattal, J. Vuckovic, G.S. Solomon, and Y. Yamamoto, "Secure communication: Quantum cryptography with a photon turnstile", *Nature* **420**, 762–762 (2002).
15. T.H. Lee, P. Kumar, and A. Mehta, "Oriented semiconducting polymer nanostructures as on-demand room-temperature single-photon source", *Appl. Phys. Lett.* **85**, 100–102 (2004).
16. C. Kurtsiefer, S. Mayer, P. Zarda, and H. Weinfurter, "Stable solid-state source of single photons", *Phys. Rev. Lett.* **85**, 290–293 (2000).
17. S. Strauf, P. Michler, M. Klude, D. Hommel, G. Bacher, and A. Forchel, "Quantum optical studies on individual acceptor bound excitons in a semiconductor", *Phys. Rev. Lett.* **89**, 177403 (2002).
18. P. Michler, A. Kiraz, C. Becher, W.V. Schoenfeld, P.M. Petroff, L. Zhang, E. Hu, and A. Imamoglu, "A quantum dot single-photon turnstile device", *Science* **290**, 2282–2285 (2000).
19. Y. Arakawa and H. Sakaki, "Multidimensional quantum well laser and temperature dependence of its threshold current", *Appl. Phys. Lett.* **40**, 939–941 (1982).
20. I.N. Stranski and L. Von Krastanow, "Abhandlungen der Mathematisch-Naturwissenschaftlichen Klasse", *Akademie der Wissenschaften und der Literatur in Mainz* **146**, 797 (1939).
21. T. Akiyama, M. Sugawara, and Y. Arakawa, "Quantum-dot semiconductor optical amplifiers", *Proc. IEEE* **95**, 1757–1766 (2007).
22. N.N. Ledentsov, D. Bimberg, and Z.I. Alferov, "Progress in epitaxial growth and performance of quantum dot and quantum wire lasers", *J. Lightwave Technol.* **26**, 1540–1555 (2008).
23. A. Salhi, G. Rainò, L. Fortunato, V. Tasco, G. Visimberga, L. Martiradonna, M.T. Todaro, M. De Giorgi, R. Cingolani, A. Trampert, M. De Vittorio, and A. Passaseo, "Enhanced performances of quantum dot lasers operating at 1.3 μm", *IEEE J. Sel. Top. Quant.* **14**, 1188–1196 (2008).
24. C.B. Murray, D.J. Norris, and M.G. Bawendi, "Synthesis and characterization of nearly monodisperse CdE (E = sulfur, selenium, tellurium) semiconductor nanocrystallites", *J. Am. Chem. Soc.* **115**, 8706–8715 (1993).
25. S. Kako, C. Santori, K. Hoshino, S. Götzinger, Y. Yamamoto, and Y. Arakawa, "A gallium nitride single-photon source operating at 200 K", *Nat. Mater.* **5**, 887–892 (2006).
26. P. Michler, A. Imamoglu, M.D. Mason, P.J. Carson, G.F. Strouse, and S.K. Buratto, "Quantum correlation among photons from a single quantum dot at room temperature", *Nature* **406**, 968–970 (2000).
27. B. Lounis and W.E. Moerner, "Single photons on demand from a single molecule at room temperature", *Nature* **407**, 491–493 (2000).
28. X. Brokmann, L. Coolen, M. Dahan, and J.P. Hermier, "Measurement of the radiative and nonradiative decay rates of single CdSe nanocrystals through a controlled modification of their spontaneous emission", *Phys. Rev. Lett.* **93** 107403–107406 (2004).
29. J. Hu, L.S. Li, W. Yang, L. Manna, L.W. Wang, and A.P. Alivisatos, "Linearly polarized emission from colloidal semiconductor quantum rods", *Science* **292**, 2060–2063 (2001).

30. L. Manna, D.J. Milliron, and A. Meisel, E.C. Scher, and A.P. Alivisatos, "Controlled growth of tetrapod-branched inorganic nanocrystals", *Nat. Mater.* **2**, 382–385 (2003)
31. D.V. Talapin, R. Koeppe, S. Götzinger, A. Kornowski, J.M. Lupton, A.L. Rogach, O. Benson, J. Feldmann, and H. Weller, "Highly emissive colloidal CdSe/CdS heterostructures of mixed dimensionality", *Nano. Lett.* **3**, 1677 (2003).
32. A. Fiore, R. Mastria, M.G. Lupo, G. Lanzani, C. Giannini, E. Carlino, G. Morello, M. De Giorgi, Y. Li, R. Cingolani, and L. Manna, "Tetrapod-shaped colloidal nanocrystals of II-VI semiconductors prepared by seeded growth", *J. Am. Chem. Soc.* **131**, 2274–2282 (2009).
33. V.I. Klimov, A.A. Mikhailovsky, D.W. McBranch, C.A. Leatherdale, and M.G. Bawendi, "Quantization of multiparticle Auger rates in semiconductor quantum dots", *Science* **287**, 1011–1013 (2000).
34. M. Nirmal, B.O. Dabbousi, M.G. Bawendi, J.J. Macklin, J.K. Trautman, T.D. Harris, and L.E. Brus, "Fluorescence intermittency in single cadmium selenide nanocrystals", *Nature* **383**, 802–804 (1996).
35. B. Mahler, P. Spinicelli, S. Buil, X. Quelin, J.P. Hermier, and B. Dubertret, "Towards non-blinking colloidal quantum dots", *Nat. Mater.* **7**, 659–664 (2008).
36. X. Wang, X. Ren, K. Kahen, M.A. Hahn, M. Rajeswaran, S. Maccagnano-Zacher, J. Silcox, G.E. Cragg, A.L. Efros, and T.D. Krauss, "Non-blinking semiconductor nanocrystals", *Nature* **459**, 686–689 (2009).
37. S.A. Empedocles, D.J. Norris, and M.G. Bawendi, *Phys. Rev. Lett.* **77**, 3873–3876 (1996).
38. H.P. Lu and X.S. Xie, "Single-molecule spectral fluctuations at room temperature", *Nature* **385**, 143–146 (1997).
39. L. Biadala, Y. Louyer, P. Tamarat, and B. Lounis, "Direct observation of the two lowest exciton zero-phonon lines in single CdSe/ZnS nanocrystals", *Phys. Rev. Lett.* **103**, 037404–037407 (2009).
40. L. Coolen, X. Brokmann, P. Spinicelli, and J.P. Hermier, "Emission characterization of a single CdSe-ZnS nanocrystal with high temporal and spectral resolution by photon-correlation Fourier spectroscopy", *Phys. Rev. Lett.* **100**, 027403–027406 (2008).
41. L. Manna, E. Scher, and A.P. Alivisatos, "Synthesis of soluble and processable rod, arrow, teardrop, and tetrapod shaped CdSe nanocrystals", *J. Am. Chem. Soc.***122**, 12700–12706 (2000).
42. C.M. Liddell and C.J. Summers, "Monodispersed ZnS dimers, trimers, and tetramers for lower symmetry photonic crystal lattices", *Adv. Mater.* **15**, 1715–1719 (2003).
43. L. Carbone, C, Nobile, M.De Giorgi, F. Della Sala, G. Morello, P. Pompa, M. Hytch, E. Snoeck, A. Fiore, I.R. Franchini, M. Nadasan, A.F. Silvestre, L. Chiodo, S. Kudera, R. Cingolani, R. Krahne, and L. Manna, "Synthesis and micrometer-scale assembly of colloidal CdSe/CdS nanorods prepared by a seeded growth approach", *Nano. Lett.* **7**, 2942 (2007).
44. G. Morello, F. Della Sala, L. Carbone, L. Manna, G. Maruccio, R. Cingolani, and M. De Giorgi, "Intrinsic optical nonlinearity in colloidal seeded grown CdSe/CdS nanostructures: Photoinduced screening of the internal electric field", *Phys. Rev.* **B78**, 195313–195320 (2008).
45. F. Pisanello, L. Martiradonna, P. Spinicelli, A. Fiore, J.P. Hermier, L. Manna, R. Cingolani, E. Giacobino, M. De Vittorio, and A. Bramati, "Dots in rods as polarized single photon sources", *Superlattices Microst.* doi:10.1016/j.spmi.2009.06.009 (2009).
46. C.H. Bennet, "Quantum cryptography using any two nonorthogonal states", *Phys. Rev. Lett.* **68**, 3121–3124 (1992).
47. F. Pisanello, L. Martiradonna, P. Spinicelli; A. Fiore, J.P. Hermier, L. Manna, R. Cingolani, E. Giacobino, A. Bramati, and M. De Vittorio, "Polarized single photon emission for quantum cryptography based on colloidal nanocrystals", *IEEE Proc.* of *11th Int. Conf. on Transparent Optical Networks*, 1–4 (2009).
48. K. Hennessy, A. Badolato, M. Winger, D. Gerace, M. Atatüre, S. Gulde, S. Fält, E. L. Hu, and A. Imamolu "Quantum nature of a strongly coupled single quantum dot-cavity system", *Nature* **445**, 896–899 (2007).
49. Y. Ota,M. Nomura, N. Kumagai, K. Watanabe,S. Ishida, S. Iwamoto, and Y. Arakawa, "Enhanced photon emission and absorption of single quantum dot in resonance with two modes in photonic crystal nanocavity", *Appl. Phys. Lett.* **93**, 183114 (2008).
50. M. Toishi, D. Englund, A. Faraon, and J. Vučković, "High-brightness single photon source from a quantum dot in a directional-emission nanocavity", *Opt. Express* **17**, 14618–14626 (2009).
51. E. Pelucchi, S. Watanabe, K. Leifer, Q. Zhu, B. Dwir, P. De Los Rios, and E. Kapon, "Mechanisms of quantum dot energy engineering by metalorganic vapour phase epitaxy on patterned nonplanar substrates", *Nano. Lett.* **7**, 1282–1285 (2007), Q. Zhu, K.F. Karlsson, E. Pelucchi, and E. Kapon, "Transition from two-Dimensional to three-dimensional quantum confinement in semiconductor quantum wires/ quantum dots", *Nano. Lett.* **7**, 2227–2233 (2007).
52. C. Schneider, T. Heindel, A. Huggenberger, P. Weinmann, C. Kistner, M. Kamp, S. Reitzenstein, S. Höfling, and A. Forchel, "Single photon emission from a site-controlled quantum dot-micropillar cavity system", *Appl. Phys. Lett.* **94**, 111111 (2009).
53. P. Gallo, M. Felici, B. Dwir, K.A. Atlasov, K.F. Karlsson, A. Rudra, A. Mohan, G. Biasiol, L. Sorba, and E. Kapon, "Integration of site-controlled pyramidal quantum dots and photonic crystal membrane cavities", *Appl. Phys. Lett.* **92**, 263101 (2008).
54. A. Qualtieri, G. Morello, P. Spinicelli, M.T. Todaro, T. Stomeo, L. Martiradonna, M. De Giornia, X. Quélinc, S. Builc, A. Bramati, J.P. Hermier, R. Cingolani, and M. De Vittorio, "Room temperature single-photon sources based on single colloidal nanocrystals in microcavities", *Superlattices Microst*. doi:10.1016/j.spmi.2009.05.004 (2009).
55. A. Qualtieri, L. Martiradonna, T. Stomeo, M.T. Todaro, R. Cingolani, and M. De Vittorio, "Multicoloured devices fabricated by direct lithography of colloidal nanocrystals", *Microelectron. Eng.* **86**, 1127–1130 (2009).
56. R. Krahne, T. Dadosh, Y. Gordin, A. Yacoby, H. Shtrikman, D. Mahalu, J. Sperling, and I. Bar-Joseph, "Nanoparticles and nanogaps: controlled positioning and fabrication", *Physica* **E17**, 498–502 (2003)
57. S. Yoshii, S. Kumagai, K. Nishio, A. Kadotani, and I. Yamashita, "Electrostatic self-aligned placement of single nanodots by protein supramolecules", *Appl. Phys. Lett.* **95**, 133702 (2009).
58. P.R. Berman, *Cavity Quantum Electrodynamics*, Academic Press, San Diego, CA, 1994, T. Mokari and U. Banin, "Syn-

thesis and properties of CdSe/ZnS core/shell nanorods", *Chem. Mater.* **15**, 3955–3960 (2003).
59. I.I. Rabi, "Space quantization in a gyrating magnetic field", *Phys. Rev.* **51**, 652–654 (1937).
60. L. Allen and J.H. Eberly, *Optical Resonances and Two-Level Atoms*, Wiley, New York, 1975.
61. N. Le Thomas, U. Woggon, and O. Schöps, "Cavity QED with semiconductor nanocrystals", *Nano. Lett.* **6**, 557–561 (2006).
62. A. Shabaev and A.L. Efros, "1D exciton spectroscopy of semiconductor nanorods", *Nano. Lett.* **4**, 1821–1825 (2004).
63. C. Weisbuch, M. Nishioka, A. Ishikawa, and Y. Arakawa, "Observation of the coupled exciton-photon mode splitting in a semiconductor quantum microcavity", *Phys. Rev. Lett.* **69**, 3314–3317 (1992).
64. M. Brune, F. Schmidt-Kaler, A. Maali, J. Dreyer, E. Hagley, J.M. Raimond, and S. Haroche, "Quantum Rabi oscillation: A direct test of field quantization in a cavity", *Phys. Rev. Lett.* **76**, 1800 (19960.
65. R.J. Thompson, G. Rempe, and H.J. Kimble "Observation of normal-mode splitting for an atom in an optical cavity", *Phys. Rev. Lett.* **68**, 1132 (1992).
66. R.K. Chang, and A.J. Chamillo, "Optical processes in microcavities", *Advanced Series in Applied Physics* **3**, World Scientific, Singapore, 1996.
67. H. Benisty, J.M. Gerard, R. Houdre, J. Rarity, and C. Weisbuch, "Confined photon systems", *Lecture Notes in Physics* **531**, Springer-Verlag, Berlin, 1999.
68. Y. Yamamoto, F. Tassone, and H Cao, "Semiconductor cavity quantum electrodynamics", *Springer Tracts in Modern Physics* **169**, Springer-Verlag, Berlin 2000.
69. M. Poitras, C.B. Lipson, H. Du, M.A. Hahn, and T.D. Krauss, "Photoluminescence enhancement of colloidal quantum dots embedded in a monolithic microcavity", *Appl. Phys. Lett.* **82**, 4032–4034 (2003).
70. M. Kahl, T. Thomay, V. Kohnle, K. Beha, J. Merlein,, M. Hagner, A. Halm, J. Ziegler, T. Nann, Y. Fedutik, U. Woggon, M. Artemyev, F. Pérez-Willard, A. Leitenstorfer, and R. Bratschitsch, "Colloidal quantum dots in all-dielectric high-Q pillar microcavities", *Nano. Lett.* **7**, 2897–2900 (2007).
71. L. Martidadonna, L. Carbone, M. De Giorgi, L. Manna, G. Gigli, R. Cingolani, and M. De Vittorio, "High Q-factor colloidal nanocrystal-based vertical microcavity by hot embossing technology", *Appl. Phys. Lett.* **88**, 181108 (2006).
72. M.V. Artemyev, U. Woggon, R. Wannemacher, H. Jaschinski, and W. Langbein, "Light trapped in a photonic dot: Microspheres act as a cavity for quantum dot emission", *Nano. Lett.* **1**, 309–314 (2001).
73. E. Yablonovitch, "Inhibited spontaneous emission in solid--state physics and electronics", *Phys. Rev. Lett.* **58**, 2059–2062 (1987).
74. S. John, "Strong localization of photons in certain disordered dielectric superlattices", *Phys. Rev. Lett.* **58**, 2486–2489 (1987).
75. O. Painter, R.K. Lee, A. Scherer, A. Yariv, J.D. O'Brien, P.D. Dapkus, and I. Kim, "Two-dimensional photonic band--gap defect mode laser", *Science* **284**, 1819–1821 (1999).
76. B.S. Song, S. Noda, T. Asano, and Y. Akahane, "Ultra--high-Q photonic double-heterostructure nanocavity", *Nat. Mater.* **4**, 207–210 (2004).
77. T. Tanabe, M. Notomi, E. Kuramochi, A. Shinya, and H. Taniyama, "Trapping and delaying photons for one nanosecond in an ultrasmall high-Q photonic-crystal nanocavity", *Nat. Photonics* **1**, 49–52 (2007).
78. Z. Wu, Z. Mi, P. Bhattacharya, T. Zhu, and J. Xu, "Enhanced spontaneous emission at 1.55 μm from colloidal PbSe quantum dots in an Si photonic crystal microcavity", *Appl. Phys. Lett.* **90**, 171105 (2007).
79. P. Lodahl, A.F. van Driel, I.S. Nikolaev, A. Irman, K. Overgaag, D. Vanmaekelbergh, and W.L. Vos, "Controlling the dynamics of spontaneous emission from quantum dots by photonic crystals", *Nature* **430**, 654–657 (2004).
80. J.M. Gérard , B. Sermage, B. Gayral, B. Legrand, E. Costard, and V. Thierry-Mieg, "Enhanced spontaneous emission by quantum boxes in a monolithic optical microcavity", *Phys. Rev. Lett.* **81**, 1110–1113 (1998).
81. S.G. Lukishova, L.J. Bissell, V.M. Menon, N. Valappil, M.A. Hahn, C.M. Evans, B. Zimmerman, T.D. Krauss, C.R. Stroud Jr, and R.W. Boyd, "Organic photonic bandgap microcavities doped with semiconductor nanocrystals for room-temperature on-demand single-photon sources", *J. Mod. Opt.* **56**, 167–174 (2009).
82. A. Qualtieri, G. Morello, P. Spinicelli, M.T. Todaro, T. Stomeo, L. Martiradonna, M. De Giornia, X. Quélinc, S. Builc, A. Bramati, J.P. Hermier, R. Cingolani, and M. De Vittorio, "Nonclassical emission from single colloidal nanocrystals in a microcavity: a route towards room temperature single photon sources", *New J. Phys.* **11**, 033025 (2009).
83. T. Förster, "Intermolecular energy transference and fluorescence", *Ann. Phys. Leipzig* **2**, 55–75 (1948).
84. T. Förster, "Experimentelle und theoretische untersuchung des zwischenmolekularen ubergangs von elektronenanregungsenergie", *Z. Naturforsch.* **4a**, 321–327 (1949).
85. S. Coe, W.K. Woo, M. Bawendi, and V. Bulović, "Electroluminescence from single monolayers of nanocrystals in molecular organic devices", *Nature* **420**, 800–803 (2002).
86. V.L. Colvin, M.C. Schlamp, and A.P. Alivisatos, "Light-emitting diodes made from cadmium selenide nanocrystals and a semiconducting polymer", *Nature* **370**, 354–357 (1994).
87. H. Huang, A. Dorn, V. Bulovic, and M. Bawendi, "Electrically driven light emission from single colloidal quantum dots at room temperature", *Appl. Phys. Lett.* **90**, 023110 (2007).
88. J. Müller, J.M. Lupton, P.G. Lagoudakis, F. Schindler, R. Koeppe, A.L. Rogach, J. Feldmann, D.V. Talapin, and H. Weller, "Wave function engineering in elongated semiconductor nanocrystals with heterogeneous carrier confinement", *Nano. Lett.* **5**, 2044–2049 (2005).
89. K. Becker, J.M. Lupton, J. Müller, A.L. Rogach, D.V. Talapin, H. Weller, and J. Feldmann, "Electrical control of Förster energy transfer", *Nat. Mater.* **5**, 777–781 (2006).
90. A.L. Rogach, T.A. Klar, J.M. Lupton, A. Meijerinkd, and J. Feldmann, "Energy transfer with semiconductor nanocrystals", *J. Mater. Chem.* **19**, 1208–1221 (2009).
91. M. Achermann, M.A. Petruska, S. Kos, D.L. Smith, D.D. Koleske, and V.I. Klimov, "Energy-transfer pumping of semiconductor nanocrystals using an epitaxial quantum well", *Nature* **429**, 642–646 (2004).
92. S. Nizamoglu, E. Sari, B. Jong-Hyeob, L. In-Hwan, and H. Volkan Demir, "Green/yellow solid-state lighting via radiative and nonradiative energy transfer involving colloidal semiconductor nanocrystals", *IEEE J. Sel. Top. Quant.* **15**, 1163–1170 (2009).

Chapter 4

Silicon nitride photonic crystals nanocavities as versatile platform for visible spectral range nanophotonics

Contents

Two-dimensional (2D) photonic crystal (PhC) technology is well established at telecommunication bands, and materials such as Silicon (Si), Gallium Arsenide (GaAs) or Indium Phospide (InP) represent a common solution for applications at these wavelengths [144–147]. However the interest of scientific community on structures operating in other spectral regions, such as the visible one, is growing up for both linear and nonlinear applications [19–21]. Indeed, 2D-PhC cavities resonant in the visible spectral

range are considered a promising tool to boost photonic device performances in several fields, such as biosensing, integrated optics, quantum communications, solar energy, etc. As a consequence of this wide area of interest, a photonic platform able to answer to the needs of all these fields would be attractive for scientific and technical communities.

Trying to develop such technological platform, the first problem one should face is the material choice. In principle it should be transparent in the whole visible spectral range with a refractive index (n) relatively high, low cost, compatible with silicon (Si) based technologies, robust, biocompatible and simply functionalizable with several biological species.

In past years several materials have been proposed with this purpose; among them, of remarkable interest are Gallium Nitride (GaN) [148], Gallium Phospide (GaP) [149], polymers [102] and Silicon Dioxide (SiO_2) [150]. Another appealing material for the above-mentioned applications is Silicon Nitride (Si_3N_4), which answers to most of the above-mentioned requirements. Indeed, stoichiometric silicon nitride is transparent in the visible spectral range with a refractive index $n \sim 1.9$ (@ $\lambda = 600nm$) [1], it can be grown on Si with low cost and widely diffused growth facilities such as Plasma Enhanced Chemical Vapor Deposition (PECVD) [151], it is compatible with Si based electronics (it is used as insulator in MOSFET gates [152, 153]), it is biocompatible and allows the functionalization of several kinds of proteins [154–156].

Several Si_3N_4 2D-PhC cavities have been already proposed in past years [19, 157, 158], showing a maximum experimental quality factor (Q) of ~ 5000 in the case of a double heterostructure nanocavity [158]. Moreover, recent advances in development of nanobeam cavities have led to extremely high quality factors also in the visible range,

[1] In a general picture, the refractive index is complex, i.e. $\tilde{n} = n + i\kappa$, where n is linked to the phase speed, while κ indicates the amount of absorption loss when the electromagnetic wave propagates through the material and is called *extinction coefficient*. Si_3N_4 refractive index (n_{SiN}) and extinction coefficient (κ_{SiN}) were measured through spectrophotometric and ellipsometric methods, giving value of n=1.93 and k=0 at a wavelength $\lambda = 600nm$.

with a maximum Q of $\sim$ 55000 [159–161]. In this chapter Si_3N_4 PhC resonators are proposed as a platform to realize photonic devices based on spontaneous emission engineering of nanoemitters in the visible spectral range. The versatility of the approach is demonstrated by coupling the two dipole-like modes of a closed band gap single point defect nanocavity with organic and inorganic light emitters: (i) DNA strands marked with Cyanine 3 (Cy3) organic dyes, (ii) antibodies bounded to fluorescent proteins (TRITC) and (iii) colloidal semiconductor nanocrystals (NCs) localized in the maximum of the resonant electric field. The application of this technology to a real device and the possibility to reach the strong coupling regime between a single NC and a PhC cavity are also discussed.

4.1 Microcavity design: the closing band-gap and the modal selective tuning

4.1.1 The closing band-gap for low refractive index materials

As detailed in section 2.3, when a quantum light emitter, such as a quantum dot, is coupled to an optical resonant mode, the interaction between the two oscillators can lead to two different coupling regimes, known as strong and weak coupling. In weak coupling conditions, the resonant mode modifies the dynamic of the emitter, allowing the engineering of its spontaneous emission. Indeed, the spontaneous emission rate of an emitter weakly coupled to a photonic eigenstate is modified by the Purcell factor $F = 3/(4\pi^2)Q/V\,(\lambda/n)^3$, where Q and V are the quality factor and the modal volume of the photonic mode, respectively. If the system is instead in the strong coupling regime, the confined excitons and photons coherently exchange energy with a coupling strength inversely proportional to V, i.e. $g \propto 1/\sqrt{V}$. Therefore, in both regimes the dynamic of the coupled system is strongly dependent on the properties of the photonic mode and, notably, on the electromagnetic field confinement in both time and spatial

domains.

In order to observe these phenomena at visible wavelengths, different optical resonators have been proposed so far [103,114], but 2D-PhCs represent the most promising structures, since they give the best control on the optical properties of the confined system. At present, PhC resonators for applications in the visible spectral range are based on various geometries [19,102,158] and on higher-order modes of the widely studied single-point defect [162] (also known as H1 cavity, sketched in Fig. 4.1(a), inset)[2] . The H1 cavity consists of a missed hole in a triangular PhC lattice, which allows two orthogonally polarized resonant modes in the photonic band gap (hereafter referred to as x- and z-pole modes, on the base of the orientation of the wavector).

The H1 resonator presents several advantages with respect to other PhC configurations for applications in quantum optics. For instance, the cross polarization of x-and z-pole modes and the absence of higher-order modes can be exploited to satisfy the requirements of quantum information algorithms [163]. As compared with other PhC point defects, the H1 cavity presents the lowest V, thus enhancing QED phenomena in both strongly and weakly coupled systems. The confinement in extremely small modal volumes is more challenging for visible light, since the constraint to use low-absorption materials in this spectral range does not allow recourse to high-refractive-index semiconductor membranes, thus reducing the effectiveness in localizing the optical modes. Nevertheless, the aforementioned advantages, together with the increasing interest toward the realization of efficient emitting devices in the visible spectral range, foster theoretical and experimental studies to find alternative routes to improve light confinement in low-index H1 systems.

The structure under investigation consists of a H1 cavity obtained in a triangular lattice of air holes with period a and radius r in a silicon nitride slab having refractive index $n = 1.93$ and thickness t. The electromagnetic behavior of such a structure

[2]High order modes, such as hexapole modes, are not supported by unmodified H1 cavities, but they can be induced by modifying the radius of the first neighboring holes.

was investigated by using Plane-Wave Expansion (PWE) and 3D Finite Difference Time Domain (FDTD) algorithms [164]. All the calculations were restricted to TE-like modes, i.e. modes with non-negligible components of the electric field along x and z and a non-negligible component of the magnetic field along y.

Our approach to realize ultrasmall-volume PhC cavities while keeping high Q-factors in the visible range and preserving the dipolelike shape of the modes is based on the closing band-gap technique [165], which involves the optimization of the thickness t of the PhC slab. As shown in Fig. 4.1(a) for the x-pole mode, the Q factor is quite constant for $t < 1.2a$, and it has a maximum for $t = 1.55a$. As reported in figs.4.1(b) and 4.1(c), the Photonics Band Gap (PBG) existing for $t = 0.7a$ disappears when t is increased to $1.55a$, in agreement with the closing-bandgap principle presented in ref. [165]. This let us infer that the electromagnetic confinement in the xz plane is not due to the PBG but can be assigned to the mismatch in the momentum space between the cavity mode and the second guided mode in the PhC slab, as described by Tandaechanurat et al. [165]. The increased thickness of the slab leads to slight variations of the x- and z-pole modal profiles along y. For this reason, V continuously grows as a function of t, as shown in Fig. 4.1(a). However, because the modal extension in the xz plane is preserved, these variations of V are negligible with respect to the increase in Q, and thus the Purcell factor [Fig. 4.1(d)] follows the Q-factor behavior: for $t = 1.55a$, F is maximized to $F \sim 78$ with $V \sim 0.68\,(\lambda/n)^3$ and $Q \sim 700$. A similar trend has been found for the z-pole mode.

4.1.2 Modal selective tuning

The engineering of x- and z-pole modes would foster many applications based on H1 nanocavities operating at visible wavelengths. For instance, the degeneracy of x- and z-pole modes may be useful for entangled photon generation [166]. Other applications, such as single-photon sources or PhC-based optical read out of lab-on-chip devices [167], require well-defined and linearly polarized non-degenerate resonances. Several solutions

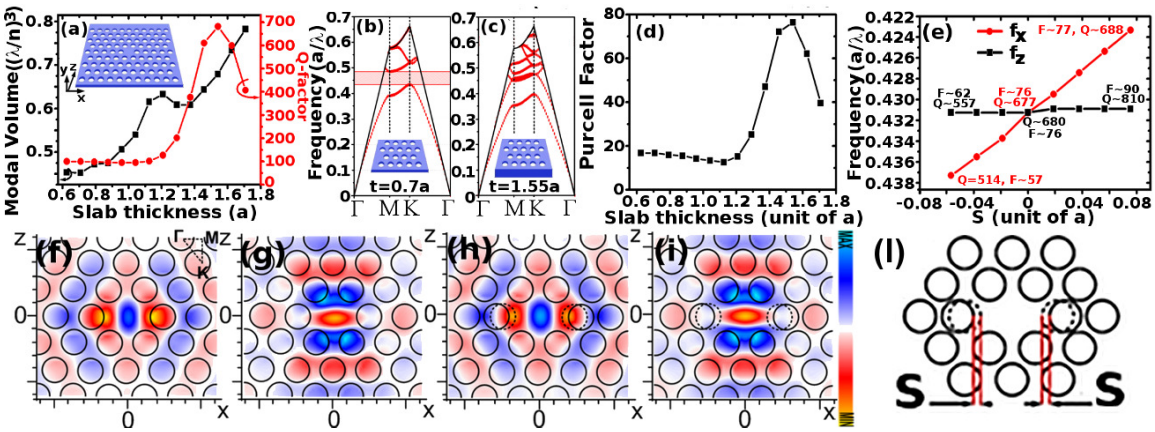

Figure 4.1: **(a)** Dependence of modal volume and Q factor on the thickness of the slab t. Inset, photonic crystal H1 cavity. **(a), (c)** Photonic band structure of the structure for $t = 0.7a$ and $t = 1.55a$, respectively. **(d)** Dependence of the Purcell factor on t (for $S = 0$). (e) Modification of the resonant frequencies and of the Q factor of the degenerated modes when two cavity neighboring holes are moved, as shown in the inset. The holes are moved closer to (farther from) the center for $S < 0$ ($S > 0$). **(f)** E_z for the x-pole mode in an unmodified H1 cavity. **(g)** E_x for the z-pole mode in an unmodified H1 cavity. **(h)** E_z for the x-pole mode in a H1 cavity with S=0.2a. **(i)** E_x for the z-pole mode in a H1 cavity with $S = 0.2a$. **(l)** Definition of S.

have been reported in past years to break the energy degeneracy of the optical modes or to recover it [162,168–170]. A versatile strategy to break the degeneracy is displayed in Fig. 4.1(e): by moving two cavity neighboring holes, it is possible to change the resonant frequency of the x-pole mode (f_x) significantly without affecting the z-pole mode. This finding is due to the selective modification of the wavevector $\mathbf{k} = (k_x, k_y, k_z)$ along a specific direction. Indeed x- and z-pole modes have the strongest component of $\mathbf{k}$ oriented along the x and z axes, respectively. When two holes are moved closer to the center of the cavity along the x axis (S<0, see Fig. 4.1(l) for definition), thus changing k_x while keeping k_z constant, f_x increases and f_z is unchanged. In the same way f_x decreases for $S > 0$, while keeping f_z constant. Figures 4.1(f-i) show the x- and z-pole modal profiles for an unmodified H1 cavity and for a cavity with $S = 0.2a$. The

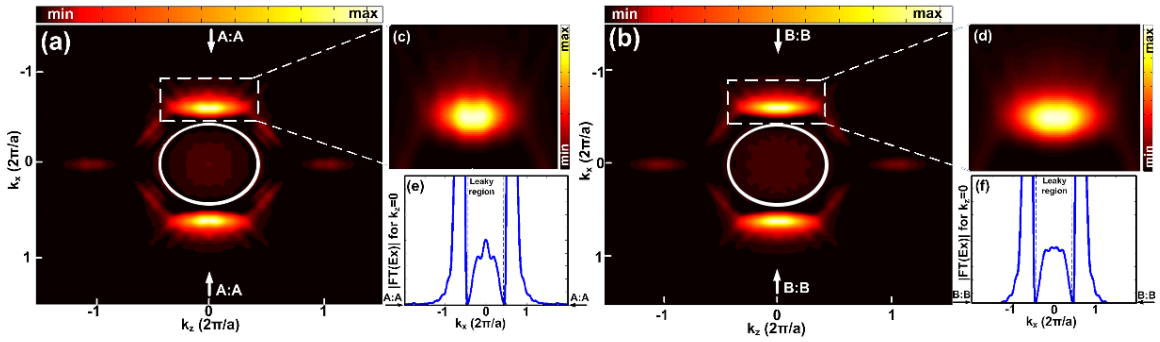

Figure 4.2: E_x field-distribution in momentum space for the z-pole mode. The white circle represents the lightcone. **(a)** $|2DFT(E_x)|$ for $S = -0.1a$; **(b)** $|2DFT(E_x)|$ for a $S = 0.2a$; **(c)** Zoom to a specific area of (a). **(d)** Zoom to a specific area of (b). **(e)** Momentum function extracted from (a) for $k_z = 0$. (f) Momentum function extracted from (b) for $k_z = 0$.

electric field component along x (E_x) of the z-pole mode profile remains unchanged when the holes are moved far from the center [Figs.4.1(g) and 4.1(i)]. The shift instead results in the elongation of the x-pole modal function along x [Figs. 4.1(f) and 4.1(h)], thus modifying its resonant frequency.

Such modifications of the field distributions also lead to variations of the Q factors of the modes [Fig.4.1(e)]. If $S < 0$, abrupt changes are introduced near the maximum of the electric field [171] of the z-pole mode function, resulting in an increase in radiation losses and in a smaller Q factor ($Q \sim 557$ for $S = -0.057a$). In contrast, if $S > 0$ these abrupt variations in the modal profile are avoided, the radiative energy in the light-cone minimized, and the Q factor of the z-pole mode enhanced with a V and f_z almost unchanged. The optimized Q-factor turns out to be $Q \sim 810$ for $S = 0.075a$, and the Purcell factor is assessed as $F \sim 90$.

These findings are confirmed by the analysis in the z-pole momentum space, obtained by using a 2D Fourier Transform (2DFT), reported in Fig.s 4.2(a) and (b) for shifts $S = -0.1a$ and $S = 0.2a$, respectively. The region inside the white circle of Fig.s 4.2 (a) and (b) represents the leaky region, defined by the light cone [171–173]: the stronger the components in this region, the higher the radiation losses in the direction

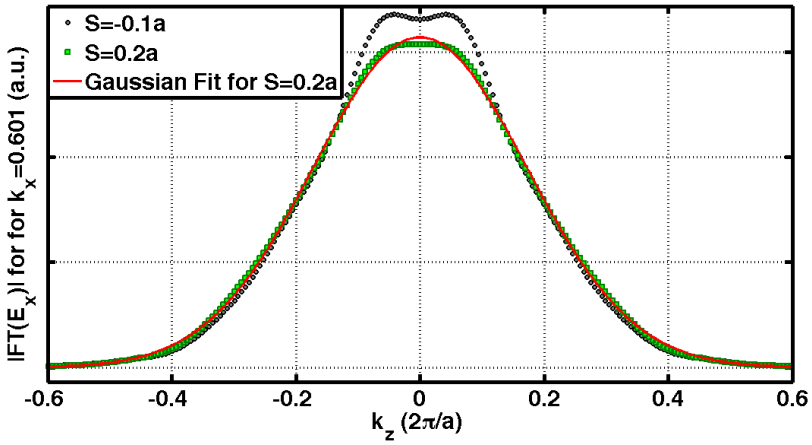

Figure 4.3: Cross section of the lobe for $S = -0.1a$ shown in Fig. 4.2(c) (black circles) and of the lobe $S = 0.2a$ displayed in Fig. 4.2(d) (green squares). Red continuous line represents a gaussian fit of the case $S = 0.2a$.

perpendicular to the slab. For $S = -0.1a$ (Fig.4.2(a) and (e)) a sharp peak is present at the center of the leaky region, affecting the value of Q; instead if $S = 0.2a$ (Fig.s 4.2(b) and (f)), the 2DFT is almost constant inside the light cone. As demonstrated in [171], the Q-factor depends also on the shape of the two peaks outside the light cone. A Gaussian shape typically leads to higher Q-factor, giving a direct measure of the energy not coupled with the radiation mode. Fig.s 4.2(c) and (d) show a zoom of Fig. 4(a) and (b), respectively: the behavior for $S = -0.1a$ is far from a 2D Gaussian function. For $S = 0.2a$ (Fig.4.2(d)), it is instead clear that by moving two holes far from the center, a 2D Gaussian function for these peaks is obtained, as also confirmed by the 1D gaussian fitting of the cross section of these lobes reported in Fig. 4.3. Therefore, by increasing the z-pole Q-factor, a positive S does not substantially affect the position, modal volume and resonant frequency of the z-pole electric field main lobe, leading to a straightforward increase of the Purcell factor of microresonators.

This therefore verify that momentum space engineering, a strategy exploited to improve the confinement of defect states localized within the PBG [102, 171], can also be efficient for cavity resonances without PBG.

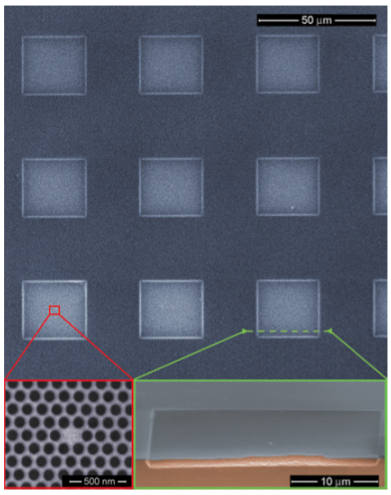

Figure 4.4: Top and bird's eyes view of the realized nanocavities.

4.2 Fabrication of Si_3N_4 PhC nanocavities

The 2D-PhC nanocavities were fabricated into a 400-nm-thick Si_3N_4 layer deposited on a silicon substrate by means of Plasma Enhanced Chemical Vapor Deposition (PECVD) technique. Si_3N_4 refractive index was measured through spectrophotometric methods (performed with a Varian Cary 5000 spectrophotometer), giving a value of $n_{SiN} = 1.93@\lambda = 600nm$.

The PhC geometry was defined using a Raith150 e-beam lithography tool. A thickness of 400 nm of ZEP520-A resist was chosen to ensure sufficient durability as a mask for pattern transfer into the underlying Si_3N_4 and, at the same time, to ensure a good resolution of the e-beam writing. The patterns defined in the ZEP were then transferred into the Si_3N_4 layer using inductive coupled plasma reactive ion etching (ICP-RIE) in fluorine chemistry until the silicon substrate surface was reached. The membrane structure was released by wet etching of the underlying Si substrate in a TetraMethylAmmonium Hydroxide (TMAH) solution. Each sample consisted of an array of H1 nanocavities, whose dimensions were scaled according to the lattice period a (in the range $a = 257nm - 277nm$) thus allowing spectral shifting of the resonant wavelength. Figure 4.4 and 4.5(a) show a Scanning Electron Microscope (SEM) image

of the realized resonators.

4.3 Coupling of H1 nanocavity with organics and inorganics emitters

The theoretical findings described in section 4.1 have been experimentally demonstrated by coupling to the nanocavities both cyanine 3 (Cy3) fluorophore and core/shell CdSe/CdS colloidal dot-in-rod nanocrystals. Room temperature microphotoluminescence (μPL) characterization was therefore performed to investigate the properties of the coupled system (see appendix B.2 for a detailed description of the experimental setup).

4.3.1 Nanoemitters deposited on top of the cavity

A micro-molar solution ($10^{-6} mol/l$) of DRs in toluene was prepared by using the synthesis procedure described in section 3.5.1 and drop-casted on the realized microcavities. Figure 4.5(b) shows three resonances for three different values of a. The resonant peaks are well approximated by a Lorentzian function [Fig.4.5(b), inset]. For $a \sim 265nm$, a $Q \sim 620$ is observed for an unmodified H1 cavity.

To explore the mode shifting over a wide spectral range, an organic fluorophore (Cy3) with broad emission spectrum was immobilized on the device. Figures 4.5(c-f) report the (μPL) spectra for different values of S. The z-pole mode is almost unaffected by the shift of the holes, whereas the x-pole mode becomes broadly tunable by changing S. The two modes were identified by performing polarization-resolved measurements, and their resonant wavelengths (λ_x and λ_z, respectively) are displayed in Fig.4.5(g) for several values of S. In agreement with the theoretical results of Fig.4.4(e), the x-pole mode is tunable over a range $\Delta\lambda_x \sim 40nm$. Small discrepancies between experimental results and theoretical calculations have been observed in terms of slight variations of λ_z and weak nonlinearity of λ_x; since these variations do not show a clear dependence on

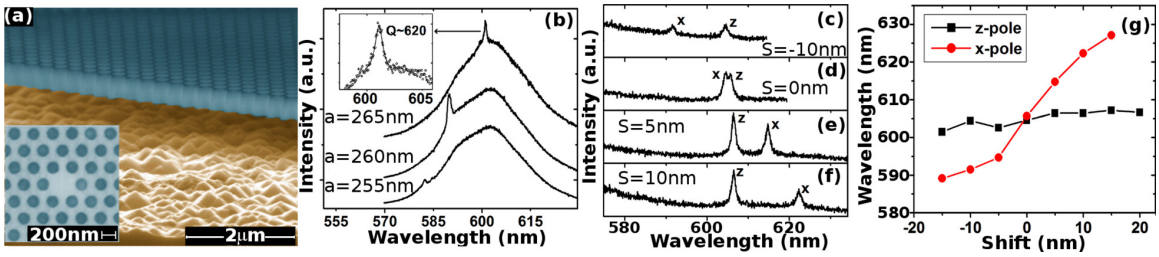

Figure 4.5: **(a)** Bird's eye view of the realized air-bridge structure and (inset) its in-plane view. **(b)** Resonances obtained by drop casting colloidal nanocrystals on the structure for three different values of a and $r = 0.308a$. The inset shows the Lorentzian fitting of the resonant peak for $a = 265nm$. **(c)-(f)** Resonance of x- and z-pole modes for different values of the hole shift and $a = 270nm$. **(g)** Resonant frequencies of x- and z-pole modes as a function of the hole shift.

S, they could be reasonably attributed to unavoidable fabrication imperfections. The theoretical findings about the influence of the holes position on the z-pole Q-factor have been confirmed by the experiments. For $S = 15nm$ $Q \sim 750$ has been measured, while for $S = -20nm$ the z-pole Q-factor falls down to a value of ~ 200.

4.3.2 Colloidal nanocrystals localized in the maximum of the electric field distribution

It is well known that in 2D-PhC slabs the in-plane confinement (xz) is due to the photonic band gap produced by the PhC periodicity, while in the out-of-plane direction (y) the confinement is due to the total internal reflection. As already mentioned, in the xz plane the electromagnetic field is localized in the center of the cavity (see figures 4.1(f-i)); FDTD simulations show also that along y the main lobe of the confined radiation is in the center of the slab (see Fig. 4.6). The coupling reported in section 4.3.1 is thus not optimized, as the nanocrystals and the organic molecules are deposited on top of the cavities.

A viable strategy to approach the maximum allowed Purcell factor is to localize the

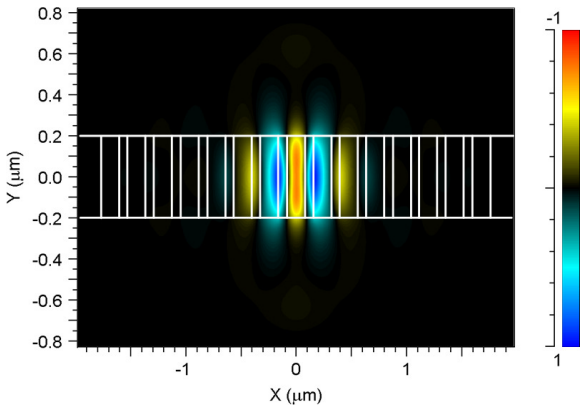

Figure 4.6: Cross view of the electric field x-component with the superposition of the slab cross-section at z = 0.

nanoemitters in the center of the slab. This has been done with colloidal dot-in-rod nanocrystals using the same fabrication process described in section 4.2 and splitting the growth procedure of the Si_3N_4 slab in two steps. Figure 4.7(a) shows a sketch of the fabrication procedure. First of all, a $200nm$ thick Si_3N_4 slab was grown on a silicon (Si) substrate. A thin layer of colloidal DRs, with a molar concentration of $\sim 10^{-6}mol/l$ was then deposited by spin-coating with a rotating speed of $500rpm$, thus obtaining a thickness lower than 10 nm, as assessed by SEM inspection. The same morphological characterization, together with photoluminescence maps collected by a confocal microscope, were used to verify the uniformity of the deposited layer. Finally, a second $200nm$ thick layer of Si_3N_4 was grown on top (see the SEM cross-section of the final structure in Fig.4.7(b)). The μPL spectra, recorded at room temperature, confirm the optical quality of the sample with an emission spectrum centered at a wavelength $\lambda_{emission} \sim 585nm$, $FWHM \sim 30nm$ (inset of Fig. 4.7(b)). The rest of the fabrication procedure follows exactly the description reported in paragraph 4.2.

Also in this case, in order to investigate the optical properties of the nanocavities, photoluminescence spectra were collected at room temperature on the structures by means of the OLYMPUS FluoView 1000 confocal laser scanning microscope, with a spatial resolution of $200nm$. A CW laser diode emitting at wavelength $\lambda_{ex} = 405nm$

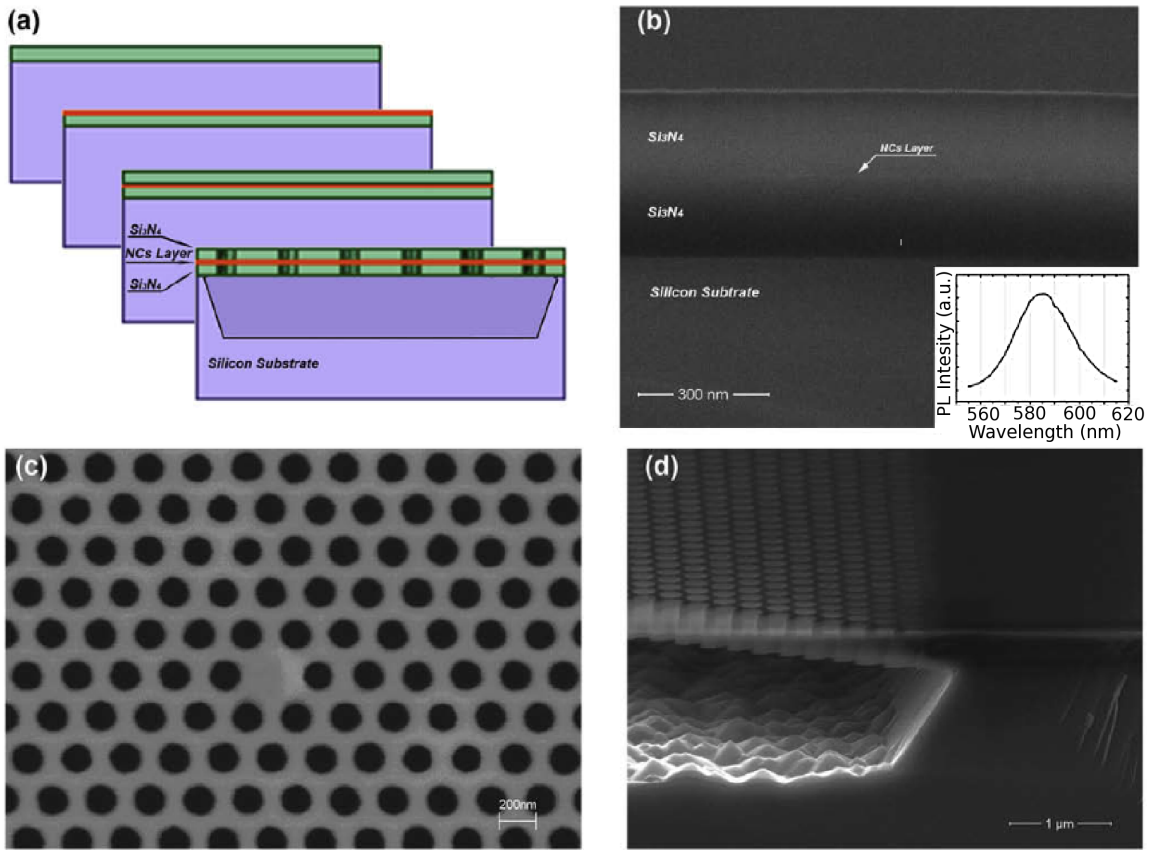

Figure 4.7: (a) Sketch of the fabrication process, (b) cross-section SEM image of the unpatterned sample; the inset represents the NCs photoluminescence after the growth of the second Silicon–Nitride layer, (c) in-plane view of the fabricated Si3N4 2D-PhC H1 nanocavity membrane and (d) its bird's eye view of the sample tilted at 30 degrees.

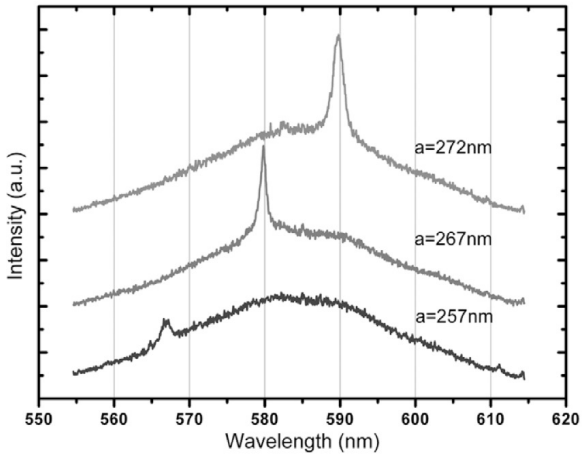

Figure 4.8: Photoluminescence spectra collected from the 2D-PhC H1 nanocavities with different lattice constants a.

was used as excitation source. The emission spectra collected from $H1$ nanocavities having different lattice constants a are reported in Fig.4.8. Superimposed to the broad emission spectrum ($FWHM \sim 30nm$) of NCs uncoupled to the cavity, sharp peaks with a quality factor of about 600 are clearly detected, assessing the modulating effects of the PhC nanocavity on the emission of NCs coupled to the optical mode localized in the defect.

Moreover, the normalized frequency a/λ of the experimental results was found to be about $a/\lambda \sim 0.46$ against the expected value of a/λ of ~ 0.431. As already suggested in case of the modal selective tuning, this slight difference can be mainly attributed to the effects of fabrication imperfections, inducing unavoidable uncontrolled variations in the optical properties of the PhCs nanocavities [174]. The efficient coupling between the semiconductor nanocrystals and the dielectric cavity is due to the fact that the nanocrystals layer can be precisely positioned in the maximum of the confined electric field in the vertical direction. Indeed, in this case the Purcell effect results optimized [56] and the spontaneous emission rate strongly increased, leading to the possibility to measure a better Q-factor [175]. At the same time it is noteworthy to point out how the introduction of a guest material, embedded in two Si_3N_4 layers, does not affect the

optical properties of the nanocavity as shown by the good match of the calculated and measured Q-factors (equal to 680 and 600, respectively).

4.4 A biosensor based on Si_3N_4 PhCs nanocavities

Recently the light molding properties of PhC have been profitably exploited to boost the performances of optical sensors and transducers for biochemical analyses [176] [177, 178]. This paragraph proposes the idea of exploiting the sharp resonances of PhC nanocavities to assign unique spectral features to fluorophore-labeled bioanalytes, thus allowing their identification through wavelength-resolved light detection. Spectral tagging of organic dyes through photonic crystal nanocavities is experimentally proved to bring important benefits to cutting edge devices for biodiagnostics, such as DNA and protein biochips, in terms of improved sensitivity, efficiency and multiplexing capability.

4.4.1 Working principle

Figure 4.9(a) reports a three-dimensional sketch of the PhC NanoCavity biochip (PhC-NC biochip) architecture. An array of 2D-PhC nanocavities, each having a different resonant wavelength, is realized on a flat substrate. The patterned surface is part of a miniaturized assay for genomic and proteomic analyses, usually referred to as DNA or protein microarray. In such devices, specific bio-molecules (probes) are immobilized through chemical surface modification or in situ synthesis and allowed to selectively bind to complementary target species, or analytes, contained in the biological solution under investigation [179]. Since fluorescent markers are typically conjugated to the target analytes, the binding events can be revealed through optical inspection of the biochip readout area, thus allowing a complete compositional analysis of the assay [180]. In inset of Fig. 4.9(a) an example of probe biomolecules immobilized on the PhC patterns is reported, showing biorecognition and capturing of specific fluorophore-labeled

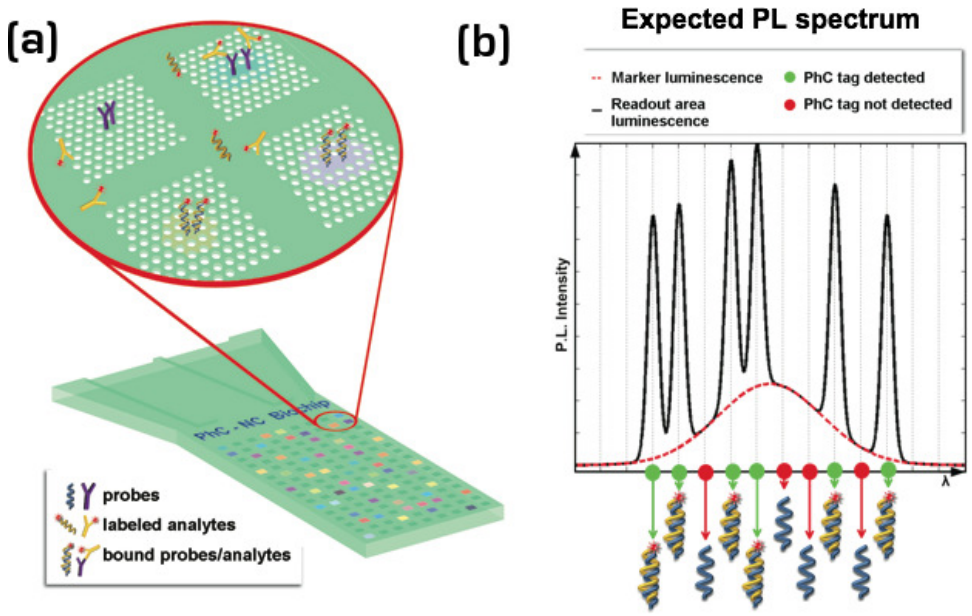

Figure 4.9: Sketch of the proposed strategy for PhC-NC biochip. **(a)** Schematic of the array of PhC nanocavities patterned on the readout area. Inset: Detail showing examples of PhC nanocavities. The cavities are functionalized with different probes molecules, that specifically interact with complementary target analytes labeled with fluorescent markers. The signal is collected from this area and spectrally discriminated in order to identify the different spectral tags univocally associated to each nanocavity and thus to each bioprobe. **(b)** Example of a possible luminescence detected from the whole readout area (black line) as compared to the unmodified broad marker luminescence (red dotted line). The presence of each peak in the spectrum reveals the presence of the corresponding analyte in the investigated assay..

target sequences. Microarray configurations, based on the localization of different probes in different regions of the readout area, permit a certain degree of parallelism in the analysis thanks to spatial discrimination [180, 181]. In this approach, different bioprobes are assigned to different resonators, thus establishing a one to one correspondence between resonant wavelengths and labeled biomolecules. In this way, although all target analytes are labeled with the same marker, upon specific binding to the complementary bioprobes, they acquire a peculiar spectral signature, thanks to the interaction of the fluorophore with the confined optical modes resonating in the cavity. A spectral scan of the signal collected from the whole readout area looks like the profile sketched in Fig.4.9(b): the broad emission spectrum of the fluorescent marker is superposed to distinct peaks, each tagging the presence of a specific target analyte in the investigated assay. Besides the spatial discrimination implemented in microarray configurations, in this case the spectral distinction contributes substantially to the parallelization of the device. Moreover, thanks to the increased radiative emission rate induced by the Purcell effect [54, 182], a significant increase in the luminescence intensity of the markers coupled to the PhC cavities is also expected, thus significantly improving the signal-to-noise ratio and the overall sensitivity of the biochip detection.

4.4.2 Experimental results

In order to verify the feasibility and wide applicability of this approach, two prototypes of PhC-NC bio-chips for the detection of different biomolecules have been realized, namely DNA and proteins. PhC nanocavities resonating in the visible spectral range were fabricated in Si_3N_4 membranes on a Si substrate, exploiting the modified single defect H1 nanocavity described in section 4.1 [108, 165, 183, 184]. Each fabricated prototype consists of arrays of optimized H1 resonators with variable lattice constant a, corresponding to different resonant wavelengths. The two samples were prepared by covalently immobilizing single-stranded DNA (ss-DNA) or antibody probes on the Si_3N_4 surface, respectively (see appendix C.3 for detailed description of the immo-

bilization procedure). Complementary DNA targets or specific secondary antibodies, labeled with cyanine 3 (Cy3) and rodhamine (TRITC) fluorophores, respectively, were then allowed to recognize the immobilized probes, thus obtaining a uniform fluorescent monolayer of the biomolecular species.

In Fig.4.10(a) four examples of the emission spectra from TRITC-labeled proteins localized onto the PhC nanocavities are displayed; the influence of the H1 resonators underneath the molecules is clearly evidenced by the presence of intense resonant peaks superposed to the broad TRITC emission lineshape. Similarly, Fig.4.10(b) shows the emission spectra collected from DNA-functionalized nanocavities (five uppermost lines), compared to the emission of Cy3- DNA strands without photonic resonators (lowest spectrum). In both cases it is evident that, by simply varying the lattice period a of the photonic crystal resonator, it is possible to assign a specific spectral feature to the emission band of the target analytes captured by the probes onto the different cavities, even though they are all labeled with the same broad emitting organic dye. The best measured Q-factor obtained in the PhC-nanocavities DNA-chip prototype is ~ 725, corresponding to a full-width at half maximum of $\sim 0.9nm$. Taking into account the spectral resolution limits, a conservative estimate suggests the possibility to distinguish up to 150 different resonant peaks within the $150nm$ bandwidth of the Cy3 emission spectrum. This means that up to 150 parallel analyses can be simultaneously performed with one single spectral scan of the readout area of the biochip, thus drastically decreasing the time required for a complete compositional identification.

Figure 4.10(c) displays the photoluminescence maps collected from an array of five different nanocavities, functionalized with ss-DNA and hybridized with Cy3-labeled complementary DNA sequences. Each map is acquired by collecting a $2nm$ wide spectral signal centered at one of the five resonating wavelengths of the nanocavities, marked from λ_1 to λ_5 in Fig.4.10(b). By comparing the different images, it is possible to distinguish a bright spot in the center of each nanocavity when the detection wavelength matches the resonant frequency.

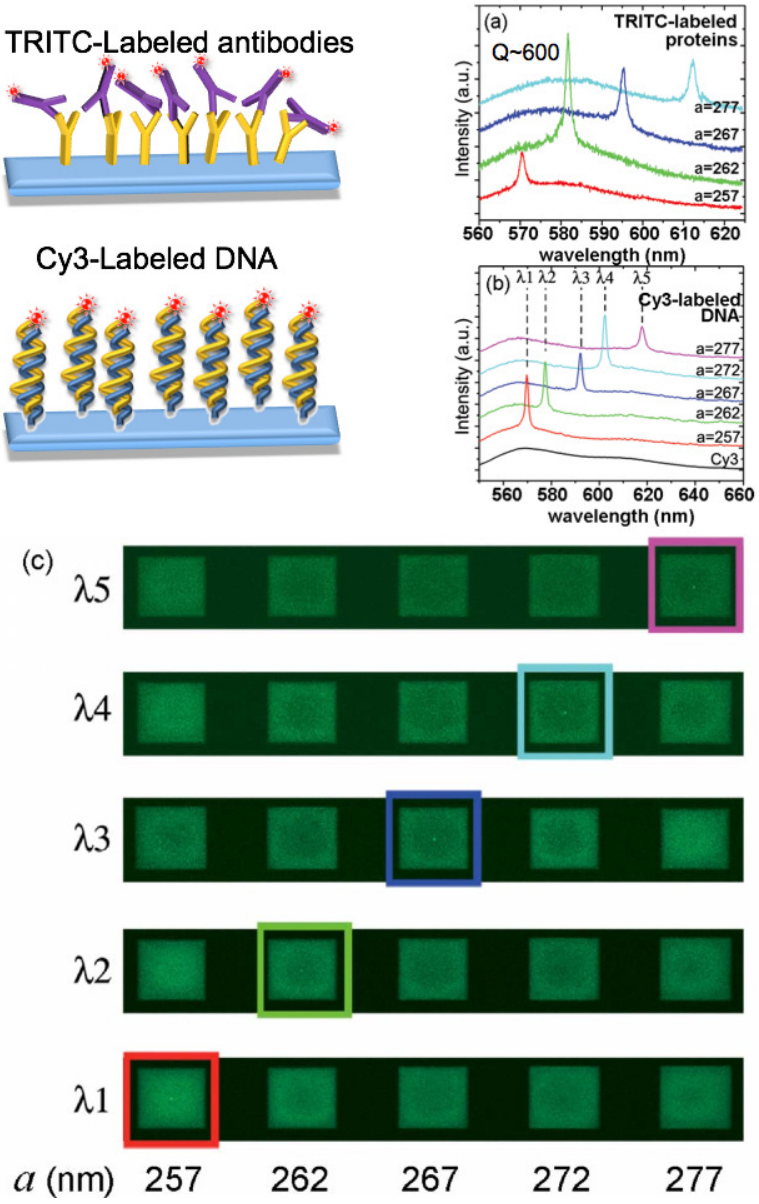

Figure 4.10: **(a)** PL spectra collected from TRITC-labeled proteins captured onto the PhC nanocavities; **(b)** PL spectra collected from Cy3–labeled DNA (colored lines) onto the PhC nanocavities as compared to Cy3 emission spectrum collected on a PhC pattern (black line); **(c)** PL maps of an array of five Cye-labeled DNA-PhC nanocavities, collected at different wavelengths [also indicated in (b)]. For each spectrum and PL map, the reported a value indicates the lattice period of the measured PhC nanocavity.

Besides the resonant effect of the H1 nanocavity, it is noteworthy that the photonic crystal pattern significantly contributes to the enhancement of the emission signal of Cy3 and TRITC. The squared areas occupied by each photonic crystal pattern are appreciably brighter than the surrounding unpatterned Si_3N_4 layer, although the immobilization and hybridization processes have been homogeneously performed on the whole sample surface. Figure 4.11 represents a 3D intensity profile collected on a H1 nanocavity upon hybridization with Cy3-labeled DNA. The profile has been taken at the resonant wavelength of the analyzed cavity. The photonic crystal pattern enhances the Cy3 luminescence up to ~ 20 times as compared to the unpatterned region. This behavior may be ascribed to the combination of two effects. First, the free standing membrane layer makes available a larger surface area to the probes immobilization (about a factor of 4 more than the unpatterned layer), resulting in a higher number of immobilized Cy3-labeled analytes in the PhC regions. Second, in 2D-PhC patterns an efficient transfer channel between externally radiated light and energy trapped in the membrane is represented by the so called leaky modes [176,185,186]. The coupling of such modes with the absorption or emission bands of neighboring emitters may lead to a significant increase of their luminescence. In our PhC-NC biochip, the leaky modes localized on the PhC pattern are responsible for the further increase of the luminescence experimentally observed. Nevertheless, at this stage our PhC pattern has been designed to improve the resonant modes localized in the H1 defect region, while a specific optimization of leaky modes effects has not been performed. Appendix C.2 describes how leaky modes act in the case of the structures under investigation.

In Fig. 4.11, the presence of a very intense resonant peak is also clear. Notably, a approximately eightfold increase with respect to the photonic crystal pattern is reached in resonant conditions, which corresponds to an overall enhancement of ~ 160 as compared to unpatterned Si_3N_4 surfaces. Together with the previously discussed enhancement mechanisms, a major role of the Purcell effect [54,182] can be envisioned, by virtue of the strong optical quantum confinement performed by the H1-shifted nanocavities.

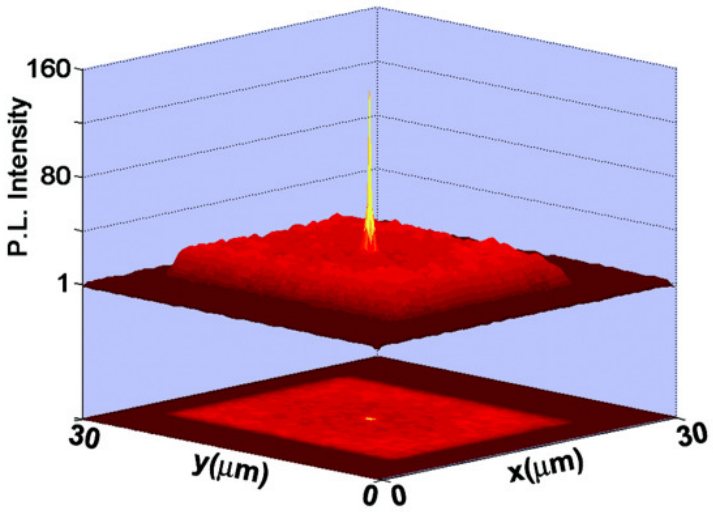

Figure 4.11: Three-dimensional intensity profile of photoluminescence collected from Cy3-labeled DNA captured by a functionalized nanocavity. Emission outside the PhC pattern has been normalized to unit. A 20-fold luminescence enhancement due to the PhC pattern, as compared to the unpatterned Si3N4 surface, has been measured. The cavity confinement further enhances Cy3 emission up to 160-fold.

The insertion of PhC cavities in classical biochip architectures leads, therefore, to a huge increase of the emission intensity of fluorescent markers, thus providing higher sensitivity, and allowing detection of very small amounts of target biomolecules in the investigated solution. In addition, the nanocavities attribute peculiar spectral features to the target analytes captured by their surface, so that the presence of specific species in the solution can be inferred by a simple spectral analysis of the optical response of the read-out region. This enables parallel detection of multiple elements, thus accelerating the analysis time. In preliminary demonstrations, emission enhancements as high as 160-fold together with high multiplexing capability and fast detection have been obtained by engineering PhC H1 resonators. Further significant improvements in sensitivity can be foreseen by combining the enhancing effects of leaky modes with resonant cavity modes. Importantly, the proposed detection system, based on the spectral identification of different analytes, can be complementarily implemented in traditional

systems based on spatial recognition to further increase the degree of parallelization.

4.5 On the possibility to reach strong coupling regime in Si_3N_4-DR system

In the previous sections of this chapter we have analyzed the weak coupling between nanoemitters and Si_3N_4 PhC nanocavities. The goal of this section is instead to evaluate if CdSe/CdS DRs are suitable quantum emitters for strongly coupled systems.

An optical emitter and a resonant cavity mode can interact in two different regimes: the weak and strong coupling. Both these types of interactions, already discussed in section 2.3, have been widely investigated in the infrared spectral region by using epitaxially grown active materials, such as quantum wells, quantum wires and quantum dots (QDs) and advanced optical resonators such as Bragg reflectors based microcavities, PhC defects and microdisks [55, 187–190]. An emerging technology, widely discussed in chapter 3, is based on the chemical synthesis of colloidal DRs, characterized by a shorter lifetime of the excited state compared to spherical nanocrystals and by an elongated shape that leads to a strong electric field inside them [128]. These two parameters are strictly linked to the so called oscillator strength, which plays a key role in the dynamic of strongly coupled systems [191]. Indeed, with elongated-core NCs, so called nanorods (NRs) [121], the strong coupling regime has been reached at cryogenic temperature by coupling them with dielectric nanospheres [114].

A system constituted by a QD (emitting at $\hbar\omega_X$) strongly coupled to an optical mode in a photonic cavity (at energy $\hbar\omega_C$) is described by the Hamiltonian [192]

$$H = \hbar\omega_C a^\dagger a + \hbar\omega_X b^\dagger b + g\left(a^\dagger b + a b^\dagger\right) \tag{4.1}$$

where a and b are the cavity and exciton operators, respectively. The last term describes the linear coupling between X and C. The coupling constant g is a fundamental parameter of a coupled system and it is linked to the properties of both X and C. By

taking into account the relaxation terms of both X and C and if the detuning between X and C is zero ($\hbar\omega_X = \hbar\omega_C = \hbar\omega_0$) the eigenenergies of a strongly coupled system are given by the following expression:

$$E_{\pm} = \hbar\omega_0 - i\frac{\gamma_X + \gamma_C}{4} \pm \sqrt{g^2 - \left(\frac{\gamma_C - \gamma_X}{4}\right)^2}, \tag{4.2}$$

where γ_c and γ_X are the linewidths (full width at half maximum) of C and X, respectively. When the $X - C$ interaction becomes larger than the combined $X - C$ decay rate (assumed as threshold t), i.e.

$$g^2 > \left(\frac{\gamma_C - \gamma_X}{4}\right)^2 = t, \tag{4.3}$$

the real part of E_+ and E_- are different $[Re(E_+) \neq Re(E_-)]$ and the two oscillators are allowed to coherently exchange energy. The coupling constant g is related to the oscillator strength of X (f) and to the modal volume (V) of C via the following equation:

$$g^2 = \frac{1}{4\epsilon_0\epsilon_r}\frac{e^2 f}{mV}, \tag{4.4}$$

where m is the free-electron mass and ϵ_0 and ϵ_r are the dielectric constant of the vacuum and of the relative dielectric constant of the medium. The photoluminescence (PL) spectrum of this system, according with Ref. [56], is:

$$S(\omega) \propto \left|\frac{E_+ - \hbar\omega_0 + \frac{\gamma_c}{2}}{\hbar\omega - E_+} - \frac{E_- - \hbar\omega_0 + i\frac{\gamma_c}{2}}{\hbar\omega - E_-}\right|. \tag{4.5}$$

From Eq.4.4 it is clear that the higher the cavity modal volume, the lower the coupling constant between X and C. The best way to obtain a low modal volume is to use a PhC based nanocavity [183]. As shown in the paragraph 4.1, in the visible spectral range these resonators present lower quality factors with respect to the infrared wavelengths because of the low refractive index of transparent materials in the wavelenght interval $500 \div 700nm$ [102]. However, V is preserved and the modal function can be confined in a volume lower than the cubic wavelength. In particular, the H1-nanocavity proposed in this chapter gives the possibility to work with resonant modes having a

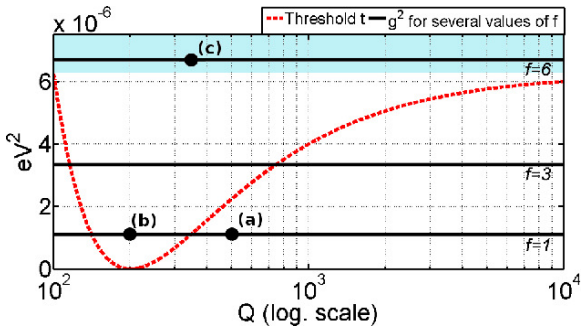

Figure 4.12: Threshold t as a function of the cavity Q-factor (red dashed line) and coupling constants g^2 for several values of f and a modal volume $V = 0.48(\lambda/n)3$. Black dots refer to the graphs of Fig.4.13.

modal volume from $V = 0.48(\lambda/n)^3$ to $V = 0.7(\lambda/n)^3$ and, importantly, a Q-factor tunable over a broad range in a simple way, with a maximum value of $Q \sim 800$. Let us suppose that a single colloidal DR emitting at $\hbar\omega_X = 2.07eV$ with a room temperature linewidth of $\gamma_X = 10meV$ [128] is localized in the center of a PhC cavity with a quality factor $Q = \hbar\omega_C/\gamma_C$. Figure 4.12 reports the behaviour of the threshold $t = (\gamma_C - \gamma_X)^2/16$ as a function of the cavity Q-factor. When the cavity linewidth γ_c approaches γ_X, the threshold t is minimized and the condition (4.3) is achieved also for lower oscillator strength. This is justifiable in a simple way: if f is not large enough to allow a coherent exchange of energy between X and C this could be compensated by approaching the two energy configurations themselves. For instance, if f does not allow to work in the light blue zone shown in Fig. 4.12, the quality factor of the cavity can be decreased in order to obtain $\gamma_C \approx \gamma_X$, thus minimizing t and obtaining the strong coupling regime. Of course, as shown by the continuous lines in Fig. 4.12, the higher f the wider the interval of Q for which $g^2 > t$. Finally t is an asymptotic threshold with respect to Q, i.e.

$$lim_{Q\to\infty} t = lim_{Q\to\infty} \left[\frac{\frac{\hbar\omega_C}{Q} - \gamma_X}{4}\right]^2 = \gamma_X^2/16, \tag{4.6}$$

and t can be overtaken also for high Q and $g > \gamma_X/4$.

An experimental evidence that the strong coupling condition regime is reached is

represented by a doublet in the PL spectrum. However, because of the relation between Eq.(4.4) and Eq.(4.2), a non-zero difference between $Re(E_+)$ and $Re(E_-)$ is not a sufficient condition for the observation of two different peaks in $S(\hbar\omega)$. Some examples of the possible situations are reported in Fig.4.13 with reference to the points evidenced in Fig.4.12. Figure 4.13 shows that below the threshold t (i.e. $Re(E_+) = Re(E_-)$) the two eigenstates are frequency-degenerate leading to a single PL peak [point (a) in Fig. 4.12]. The point (b) is instead just above threshold and the non-degeneracy of the eingen-states is clearly visible [Fig. 4.13(b)]. However, a single peak in the spectrum is still present because the vacuum Rabi splitting is significantly smaller than the spectral width of each peak. This is not the case of Fig.4.13(c), in which the PL spectrum is modified by the presence of the vacuum Rabi oscillations by virtue of a stronger oscillator strength (i.e. $g^2 \gg t$). The condition $g^2 > t$ is therefore too weak from the experimental point of view, and it would be better to referee to the widely accepted condition $g > \gamma_X; \gamma_C$, which allows to distinguish the Rabi doublet in the PL spectrum. As we will discuss in the following, the oscillator strength of colloidal NCs at room temperature is extremely low. In spite of that, for low f, the condition $Re(E_+) \neq Re(E_-)$ is fulfilled, and the strong coupling is theoretically reached. However, as in the case of Fig.4.13(b), the observation of strong coupling features would not be possible with PL measurements because the doublet state is not evident in $S(\hbar\omega)$.

Equation (4.4) and Fig.4.12 show that the emission oscillator strength f is one of the parameters defining the regime of the coupled system. f can be expressed as a function of the radiative decay rate $1/\tau_{X_r}$, i.e. [191]

$$f = \frac{6m\epsilon_0\pi c\lambda^2}{q^2 n}\frac{1}{\tau_{X_r}}, \tag{4.7}$$

where q is the electron charge. The average lifetime of the transition X (τ_X) can be estimated by fitting the decay curve obtained by the delays histogram between the laser pulses and the received photons. A typical decay behaviour measured on a single DR is reported in Fig.4.14; the experimental data are well fitted by a mono-exponential decay

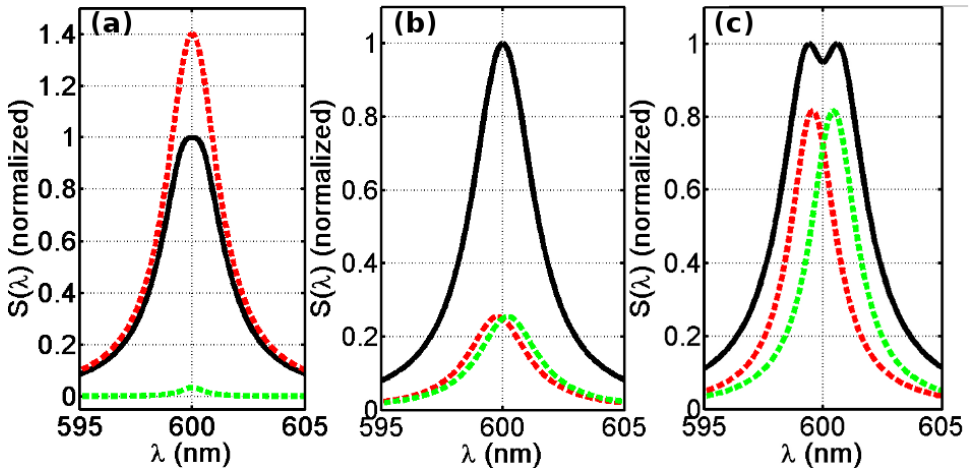

Figure 4.13: Photoluminescence spectra (black continuous lines) computed via Eq.4.5 for the points (a), (b) and (c) of Fig.4.12. Coloured dashed line represents the eigenstates.

function e^{-t/τ_X} and τ_X has been assessed to be $\sim 11ns$ for a core diameter $d \sim 2.7nm$, a shell length of $l \sim 30nm$ and a total thickness of $t_{DR} \sim 4.5nm$. This method estimates the total decay rate $(1/\tau_X)$, which is the sum of the radiative recombination rate and the non-radiative one $(1/\tau_{X_{nr}})$, i.e.

$$\frac{1}{\tau_X} = \frac{1}{\tau_{X_r}} + \frac{1}{\tau_{X_{nr}}}. \tag{4.8}$$

However it has been demonstrated that for colloidal NCs and DRs the internal quantum efficiency approaches 100% [106, 108]. As a consequence, the non-radiative rate can be considered negligible and the estimated τ_X assigned to purely radiative processes, i.e. $\tau_X \sim \tau_{X_r}$. By considering $\tau_X \sim 11ns$, the oscillator strength obtained via Eq.4.7 can be estimated to be 1.5. Lifetime measurements as a function of the intensity power were also performed. Consistently with the results reported in ref. [108], the lifetime of the excited state is almost constant at values of $11ns$.

It is thus possible to infer that, for a cavity with $V \sim 0.48(\lambda/n)^3$, a Q-factor between 150 and 400 is needed to reach the strong coupling regime with a DR characterized by an oscillator strength of $f = 1.5$. However, these parameters lead to the condition of Fig.4.13(b), in which the strong coupling is theoretically achieved but not experimentally observable. On the other hand, it has been demonstrated that at cryo-

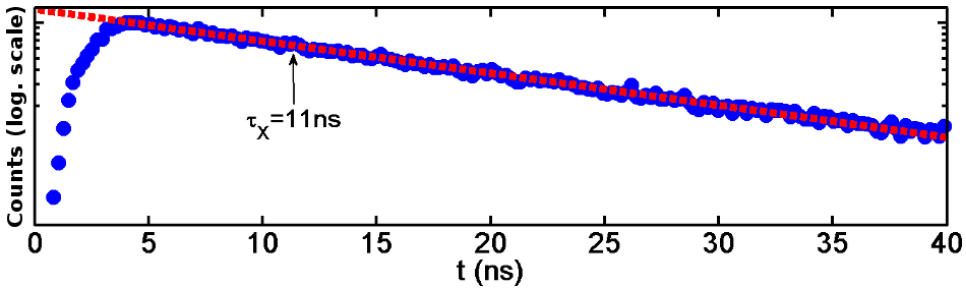

Figure 4.14: Decay curve measured on an isolated DR (blue dots) and its exponential fit (red dashed line).

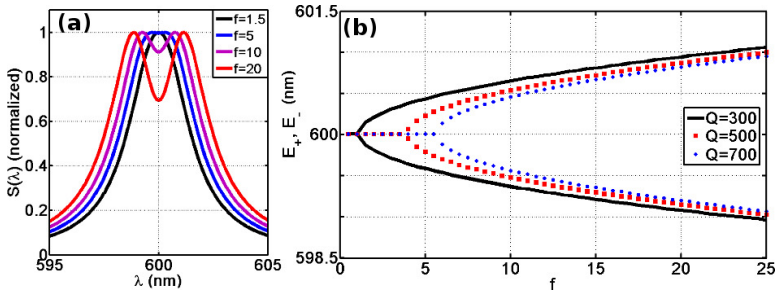

Figure 4.15: **(a)** Luminescence spectra for several values of the oscillator strength and $Q = 300$. **(b)** Spectral position of the eigenmodes for several values of Q and as a function of f.

genic temperatures, colloidal nanorods presents a lifetime of $\tau_r < 1ns$ [114] leading to a higher oscillator strength. For example $f \sim 20$ for $\tau_r = 800ps$ can be obtained via Eq.4.7. Figures 4.15(a) and (b) show that for these values of f the doublet is clearly visible in the PL spectrum and that the two eigenmodes are not degenerated, making us to envision the possibility to observe the strong coupling between a colloidal dot-in-rod and a photonic crystals cavity at cryogenic temperatures.

In summary, because of the low oscillator strength at room temeprature, analytical computations showed the theoretical possibility to achieve a strong coupling which nevertheless does not lead to a visible doublet in the PL spectrum. However, taking into account a decreasing of the DRs lifetime at cryogenic temperatures, the possibility to experimentally observe the vacuum Rabi splitting in the investigated system can be envisioned.

4.6 Conclusions and perspectives

This chapter details the use of Si_3N_4 2D-PhC cavity as flexible platform to realize photonic devices based on the engineering of spontaneous emission of nanoemitters in the visible spectral range. The versatility of the approach is demonstrated by coupling several types of emitters to the two photonic states allowed in a closed band gap single point defect nanocavity. In particular, DNA strands and antibodies marked with Cy3 and TRITC organic dyes have been immobilized on top of the nanocavities, while colloidal quantum dots emitting in the visible spectral range have been dropcasted on the devices and also positioned in the resonators at the maximum of the localized photonic mode. The optical measurements, carried out by μPL confocal microscopy, revealed maximum quality factors close to the theoretical estimations for all the emitters. Improvements in modelling and processing of PhC structures in Silicon Nitride, which is highly compatible with both biological materials and inorganic quantum emitters, let us envision a broader application of two-dimensional PhC nanocavities also in the visible spectral range. In particular, the coupling of a single colloidal dot-in-rod nanocrystal with a photonic crystal cavity would be an important milestone to reach in next years, and would allow further improvements of single photon rate and stability.

4.7 Peer-reviewed journal publications

APPLIED PHYSICS LETTERS **96**, 113702 (2010)

Spectral tagging by integrated photonic crystal resonators for highly sensitive and parallel detection in biochips

Luigi Martiradonna,[1,a)] Ferruccio Pisanello,[2,3] Tiziana Stomeo,[2] Antonio Qualtieri,[1,2] Giuseppe Vecchio,[1] Stefania Sabella,[1] Roberto Cingolani,[1] Massimo De Vittorio,[1,2] and Pier Paolo Pompa[1]

[1]*Istituto Italiano di Tecnologia (IIT), Center for Bio-Molecular Nanotechnology, Via Barsanti 1, Arnesano, Lecce 73010, Italy*

[2]*National Nanotechnology Laboratory, CNR/INFM, Scuola superiore ISUFI, Università del Salento, 16 Via Arnesano, Lecce 73100, Italy*

[3]*Laboratoire Kastler Brossel, Université Pierre et Marie Curie, CNRS UMR 8552, Ecole Normale Supérieure, 4 place Jussieu, 75252 Paris Cedex 05, France*

(Received 11 February 2010; accepted 21 February 2010; published online 17 March 2010)

We propose a technological approach aimed at improving biochips performances, based on an efficient spectral modeling and enhancement of markers fluorescence through the insertion of photonic crystal nanocavities (PhC-NCs) in the readout area of biochips. This strategy univocally associates a specific emission wavelength to a specific bioprobe immobilized on a nanocavity, therefore guaranteeing parallel detection of multiple elements and faster analysis time. Moreover, PhC-NCs significantly enhance the markers fluorescence, thus improving the detection sensitivity. © *2010 American Institute of Physics*. [doi:10.1063/1.3360810]

Biodiagnostics is a rapidly developing field, where the use of micro- and nanotechnologies enables major advancements in sensitivity and sample volume requirements.[1–5] The light molding properties of photonic crystals[6] (PhC), intended as periodic dielectric perturbations at wavelength scale, are considered a fundamental backbone for photonic applications[7–12] and, recently, have been profitably exploited for the enhancement of optical sensors and transducers for biochemical analyses.[13–15]

Here we propose the idea of exploiting the sharp resonances of PhC nanocavities to assign unique spectral features to fluorophore-labeled bioanalytes, thus allowing their identification through wavelength-resolved light detection. Spectral tagging of organic dyes through photonic crystal nanocavities is experimentally proved to bring important benefits to cutting-edge devices for biodiagnostics, such as DNA and protein biochips, in terms of improved sensitivity, efficiency and multiplexing capability.

Figure 1(a) reports a three-dimensional sketch of our PhC NanoCavity biochip (PhC-NC biochip) architecture. An array of two-dimensional PhC (2D-PhC) nanocavities, each having a different resonant wavelength, is realized on a flat substrate. The patterned surface is part of a miniaturized assay for genomic and proteomic analyses, usually referred to as DNA or protein microarray. In such devices, specific biomolecules (probes) are immobilized through chemical surface modification or *in situ* synthesis and allowed to selectively bind to complementary target species, or analytes, contained in the biological solution under investigation.[16] Since fluorescent markers are typically conjugated to the target analytes, the binding events can be revealed through optical inspection of the biochip readout area, thus allowing a complete compositional analysis of the assay.[17] In inset of Fig. 1(a), an example of probe molecules immobilized on the PhC patterns is reported, showing biorecognition and capturing of specific fluorophore-labeled target sequences. Microarray configurations, based on the localization of different probes in different regions of the readout area, permit a certain degree of parallelism in the analysis thanks to spatial discrimination.[17,18] In our approach, different bioprobes are assigned to different resonators, thus establishing a one to one correspondence between resonant wavelengths and labeled biomolecules.[19] In this way, despite all target analytes are labeled with the same marker, upon specific binding to the complementary bioprobes, they acquire a peculiar spectral signature, thanks to the interaction of the fluorophore with the confined optical modes resonating in the cavity. A

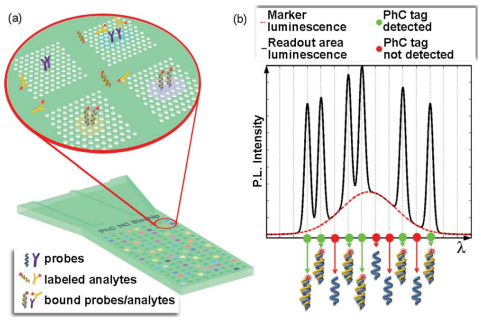

FIG. 1. (Color online) Sketch of the proposed strategy for PhC- NC biochip. (a) Schematic of the array of PhC nanocavities patterned on the readout area. Inset: Detail showing examples of PhC nanocavities. The cavities are functionalized with different probes molecules, that specifically interact with complementary target analytes labeled with fluorescent markers. The signal is collected from this area and spectrally discriminated in order to identify the different spectral tags univocally associated to each nanocavity and thus to each bioprobe. (b) Example of a possible luminescence detected from the whole readout area (black line) as compared to the unmodified broad marker luminescence (red dotted line). The presence of each peak in the spectrum reveals the presence of the corresponding analyte in the investigated assay.

[a)]Author to whom correspondence should be addressed. Electronic mail: luigi.martiradonna@iit.it. Tel.: +39832295726. FAX: +39832298386.

spectral scan of the signal collected from the whole readout area resembles the profile sketched in Fig. 1(b): The broad emission spectrum of the fluorescent marker is superimposed to distinct peaks, each tagging the presence of a specific target analyte in the investigated assay. Besides the spatial discrimination implemented in microarray configurations, in this case the spectral distinction contributes substantially to the parallelization of the device. Moreover, thanks to the increased radiative emission rate induced by the Purcell effect,[20,21] a significant increase in the luminescence intensity of the markers coupled to the PhC cavities is also expected, thus significantly improving the signal-to-noise ratio and the overall sensitivity of the biochip detection.

In order to verify the feasibility and wide applicability of this approach, we realized two prototypes of PhC-NC biochips for the detection of different biomolecules, namely DNA and proteins. PhC nanocavities resonating in the visible spectral range were fabricated in silicon nitride (Si_3N_4) membranes on a Si substrate, exploiting a modified single defect H1 nanocavity.[22,23] This consists of a triangular air-holes lattice pattern, with a local periodicity variation around a missing air hole.[24] A careful modeling of the defect geometry was performed in order to optimize the Quality factor (Q-factor) and the Purcell factor of the resonant modes, obtaining maximum theoretical values of 810 and 90, respectively.[25] Each fabricated prototype consists of arrays of optimized H1 resonators with variable lattice constant a, corresponding to different resonant wavelengths.

The two samples were prepared by covalently immobilizing single-stranded DNA (ss-DNA) or antibody probes on the Si_3N_4 surface, respectively. Complementary DNA targets or specific secondary antibodies, labeled with cyanine 3 (Cy3) and rodhamine (TRITC) fluorophores, respectively, were then allowed to recognize the immobilized probes, thus obtaining a uniform fluorescent monolayer of the biomolecular species.[25]

Spatially-resolved spectral mapping of the PhC-NC biochips surface was performed through a confocal microscope.[25] In Fig. 2(a) we display four examples of the emission spectra from TRITC-labeled proteins localized onto the PhC nanocavities; the influence of the H1 resonators underneath the molecules is clearly evidenced by the presence of intense resonant peaks superimposed to the broad TRITC emission lineshape. Similarly, Fig. 2(b) shows the emission spectra collected from DNA-functionalized nanocavities (five uppermost lines), compared to the emission of Cy3-DNA strands without photonic resonators (lowest spectrum). In both cases it is evident that, by simply varying the lattice period a of the photonic crystal resonator, it is possible to assign a specific spectral feature to the emission band of the target analytes captured by the probes onto the different cavities, even though they are all labeled with the same broad emitting organic dye. The best measured Q-factor obtained in the PhC-nanocavities DNA-chip prototype is ~725, corresponding to a full-width at half maximum of ~0.9 nm. Taking into account the spectral resolution limits, a conservative estimate suggests the possibility to distinguish up to 150 different resonant peaks within the ~150 nm bandwidth of the Cy3 emission spectrum. This means that up to 150 parallel analyses can be simultaneously performed with one single spectral scan of the readout area of the biochip, thus drastically decreasing the time required for a complete compositional identification.

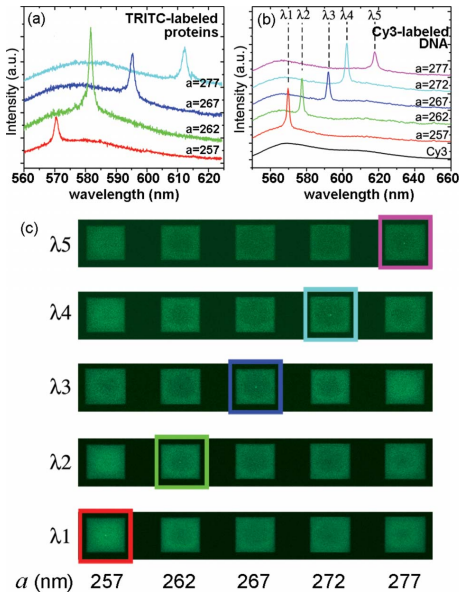

FIG. 2. (Color online) Optical characterization of a PhC-nanocavities biochip prototype. (a) PL spectra collected from TRITC-labeled proteins captured onto the PhC nanocavities; (b) PL spectra collected from Cy3–labeled DNA (colored lines) onto the PhC nanocavities as compared to Cy3 emission spectrum collected on a PhC pattern (black line); (c) PL maps of an array of five Cye-labeled DNA-PhC nanocavities, collected at different wavelengths [also indicated (b)]. For each spectrum and PL map, the reported a value indicates the lattice period of the measured PhC nanocavity (enhanced online). [URL: http://dx.doi.org/10.1063/1.3360810.1]

Figure 2(c) displays the photoluminescence maps collected from an array of five different nanocavities, functionalized with ss-DNA and hybridized with Cy3-labeled complementary DNA sequences. Each map is acquired by collecting a 2 nm wide spectral signal centered at one of the five resonating wavelengths of the nanocavities, marked from λ1 to λ5 in Fig. 2(b). By comparing the different images, it is possible to distinguish a bright spot in the center of each nanocavity when the detection wavelength matches the resonant frequency. The wavelength-dependent ON-OFF switching of the cavity regions can be better visualized in the spectral scan video provided in the Supplementary material, obtained by collecting photoluminescence maps at different wavelengths in the 552–638 nm range.

Besides the resonant effect of the H1 nanocavity, it is noteworthy that the photonic crystal pattern significantly contributes to enhancement of the emission signal of Cy3 and TRITC. The squared areas occupied by each photonic crystal pattern are appreciably brighter than the surrounding unpatterned Si_3N_4 layer, although the immobilization and hybridization processes have been homogeneously performed on the whole sample surface. Figure 3 represents a three-dimensional (3D) intensity profile collected on a H1 nanocavity upon hybridization with Cy3-labeled DNA. The profile has been taken at the resonant wavelength of the

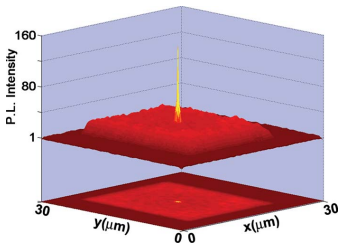

FIG. 3. (Color online) Three-dimensional intensity profile of photoluminescence collected from Cy3-labeled DNA captured by a functionalized nanocavity. Emission outside the PhC pattern has been normalized to unit. A ~20-fold luminescence enhancement due to the PhC pattern, as compared to the unpatterned Si_3N_4 surface, has been measured. The cavity confinement further enhances Cy3 emission up to ~160-fold.

analyzed cavity. The photonic crystal pattern enhances the Cy3 luminescence up to ~20 times as compared to the unpatterned region. This behavior may be ascribed to the combination of two effects. First, the free standing membrane layer makes available a larger surface area to the probes immobilization (about a factor of 4 compared to the unpatterned layer), resulting in a higher number of immobilized Cy3-labeled analytes in the PhC regions. Second, in 2D-PhC patterns an efficient transfer channel between externally radiated light and energy trapped in the membrane is represented by the so called leaky modes.[13,26,27] The coupling of such modes with the absorption or emission bands of neighboring emitters may lead to a significant increase of their luminescence.[12,13] In our PhC-NC biochip, the leaky modes localized on the PhC pattern[25] are responsible for the further increase of the luminescence experimentally observed. Nevertheless, at this stage our PhC pattern has been designed to improve the resonant modes localized in the H1 defect region, while a specific optimization of leaky modes effects has not been performed. Further theoretical and experimental efforts aimed to combine both enhancing effects will be the subject of forthcoming investigation.

In Fig. 3, the presence of a very intense resonant peak is also clear. Notably, a approximately eightfold increase with respect to the photonic crystal pattern is reached in resonant conditions, which corresponds to an overall enhancement of ~160 as compared to unpatterned Si_3N_4 surfaces. Together with the previously discussed enhancement mechanisms, a major role of the Purcell effect[20,21] is here envisioned, by virtue of the strong optical quantum confinement performed by the H1-shifted nanocavities.

The insertion of PhC cavities in classical biochip architectures leads, therefore, to a huge increase of the emission intensity of fluorescent markers, thus providing higher sensitivity, and allowing detection of very small amounts of target biomolecules in the investigated solution. In addition, the nanocavities attribute peculiar spectral features to the target analytes captured by their surface, so that the presence of specific species in the solution can be inferred by a simple spectral analysis of the optical response of the read-out region. This enables parallel detection of multiple elements, thus accelerating the analysis time. In preliminary demonstrations, emission enhancements as high as 160-fold along with high multiplexing capability and fast detection have been obtained by engineering PhC H1 resonators. Further significant improvements in sensitivity can be foreseen by combining the enhancing effects of leaky modes with resonant cavity modes. Importantly, the proposed detection system based on the spectral identification of different analytes can be complementarily implemented in traditional systems based on spatial recognition to further increase the degree of parallelization. The interesting achievements here obtained may constitute a further step toward the next generation of PhC-assisted biochips, whose potential as fast, highly sensitive devices is far from being completely expressed yet.

L.M and F.P. equally contributed to this work. The authors gratefully acknowledge Marco Grande and Virgilio Brunetti for their suggestions and input. We also thank the expert technical support of Gianmichele Epifani, Paolo Cazzato, and Vittorio Fiorelli.

[1]P.-A. Auroux, D. Iossifidis, D. R. Reyes, and A. Manz, Anal. Chem. **74**, 2637 (2002).
[2]P. P. Pompa, L. Martiradonna, A. Della Torre, F. Della Sala, L. Manna, M. De Vittorio, F. Calabi, R. Cingolani, and R. Rinaldi, Nat. Nanotechnol. **1**, 126 (2006).
[3]A. M. Armani, R. P. Kulkarni, S. E. Fraser, R. C. Flagan, and K. J. Vahala, Science **317**, 783 (2007).
[4]S.-H. Guo, S.-J. Tsai, H.-C. Kan, D.-H. Tsai, M. R. Zachariah, and R. J. Phaneuf, Adv. Mater. **20**, 1424 (2008).
[5]S. S. Shankar, L. Rizzello, R. Cingolani, R. Rinaldi, and P. P. Pompa, ACS Nano **3**, 893 (2009).
[6]E. Yablonovitch, Phys. Rev. Lett. **58**, 2059 (1987).
[7]C. Santori, D. Fattal, J. Vučković, G. S. Solomon, and Y. Yamamoto, Nature (London) **419**, 594 (2002).
[8]Y. Akahane, T. Asano, B. S. Song, and S. Noda, Nature **425**, 944 (2003).
[9]T. Baba, Nat. Photonics **2**, 465 (2008).
[10]T. Stomeo, F. Val Laere, M. Ayre, C. Cambournac, H. Benisty, D. Van Thourhout, R. Baetz, and T. F. Krauss, Opt. Lett. **33**, 884 (2008).
[11]L. Martiradonna, L. Carbone, A. Tandaechanurat, M. Kitamura, S. Iwamoto, L. Manna, M. De Vittorio, R. Cingolani, and Y. Arakawa, Nano Lett. **8**, 260 (2008).
[12]J. J. Wierer, A. David, and M. M. Megens, Nat. Photonics **3**, 163 (2009).
[13]N. Ganesh, W. Zhang, P. C. Mathias, E. Chow, J. A. N. T. Soares, V. Malyarchuk, A. D. Smith, and B. T. Cunningham, Nat. Nanotechnol. **2**, 515 (2007).
[14]N. Skivesen, A. Têtu, M. Kristensen, J. Kjems, L. H. Frandsen, and P. I. Borel, Opt. Express **15**, 3169 (2007).
[15]M. Li, Angew. Chem., Int. Ed. **47**, 7258 (2008).
[16]J.-B. Fan, M. S. Chee, and K. L. Gunderson, Nat. Rev. Genet. **7**, 632 (2006).
[17]M. Schena, D. Shalon, R. W. Davis, and P. O. Brown, Science **270**, 467 (1995).
[18]S. L. Spurgeon, R. C. Jones, and R. Ramakrishnan, PLoS ONE **3**, e1662 (2008).
[19]K. Aoki, M. De Vittorio, T. Stomeo, F. Pisanello, A. Massaro, L. Martiradonna, S. Sabella, R. Rinaldi, Y. Arakawa, R. Cingolani, and P. P. Pompa, European Patent No. EP 2154515 (A1) (pending).
[20]E. M. Purcell, Phys. Rev. **69**, 681 (1946).
[21]S. Noda, M. Fujita, and T. Asano, Nat. Photonics **1**, 449 (2007).
[22]O. Painter, R. K. Lee, A. Scherer, A. Yariv, J. D. O'Brien, P. D. Dapkus, and I. Kim, Science **284**, 1819 (1999).
[23]A. Tandaechanurat, S. Iwamoto, M. Nomura, N. Kumagai, and Y. Arakawa, Opt. Express **16**, 448 (2008).
[24]F. Pisanello, M. De Vittorio, and R. Cingolani, Superlattices Microstruct. **47**, 34 (2010).
[25]See supplementary material at http://dx.doi.org/10.1063/1.3360810 for the modeling of optical confinement and leaky modes in PhC nanocavities, for a detailed description of the experimental procedures followed for the fabrication and surface functionalization of 2D-PhC nanocavities and for the description of the optical setup.
[26]S. Fan and J. D. Joannopoulos, Phys. Rev. B **65**, 235112 (2002).
[27]K. B. Crozier, V. Lousse, O. Kilic, S. Kim, S. Fan, and O. Solgaard, Phys. Rev. B **73**, 115126 (2006).

May 15, 2010 / Vol. 35, No. 10 / OPTICS LETTERS 1509

High-Purcell-factor dipolelike modes at visible wavelengths in H1 photonic crystal cavity

Ferruccio Pisanello,[1,2,*] Antonio Qualtieri,[1,3] Tiziana Stomeo,[1] Luigi Martiradonna,[1,3] Roberto Cingolani,[1,3] Alberto Bramati,[2] and Massimo De Vittorio[1,3]

[1]*National Nanotechnology Laboratory, CNR/INFM, Scuola Superiore ISUFI, Università del Salento, 16 Via Arnesano, 73100 Lecce, Italy*

[2]*Université Pierre et Marie Curie (UPMC), Laboratoire Kastler Brossel, CNRS UMR8552, Ecole Normale Supérieure, 4 place Jussieu, 75252 Paris Cedex 05, France*

[3]*Istituto Italiano di Tecnologia (IIT), Center for Bio-Molecular Nanotechnology, Via Barsanti 1, 73010 Arnesano (Lecce), Italy*

[*]*Corresponding author: pisanello@spectro.jussieu.fr*

Received January 29, 2010; revised March 25, 2010; accepted March 29, 2010; posted April 6, 2010 (Doc. ID 123548); published May 4, 2010

The optimization of H1 photonic crystal cavities for applications in the visible spectral range is reported, with the goal to obtain a versatile photonic platform to explore strongly and weakly coupled systems. The resonators have been realized in silicon nitride and weakly coupled to both organic (fluorophores) and inorganic (colloidal nanocrystals) nanoparticles emitting in the visible spectral range. The theoretical Purcell factor of the two dipolelike modes in the defect has been increased up to ~90, and the experimental quality factor was measured to be ~750. © 2010 Optical Society of America

OCIS codes: 160.5298, 350.4238, 160.4236.

Light–matter interaction in nanometer-sized and fully confined systems is a hot research topic at infrared wavelengths and in the visible spectral range [1–4]. When a quantum light emitter, such as a quantum dot, is coupled to an optical resonant mode, the interaction between the two oscillators can lead to two different coupling regimes, known as strong and weak coupling. In weak coupling conditions, the resonant mode modifies the dynamic of the emitter, allowing the engineering of its spontaneous emission. Indeed, the spontaneous emission rate of an emitter weakly coupled to a photonic eigenstate is modified by a factor $F=3/4\ \pi^{-2}Q/V(\lambda/n)^3$, where Q and V are the quality factor and the modal volume of the photonic mode, respectively. If the system is instead in the strong coupling regime, the confined excitons and photons coherently exchange energy with a coupling strength inversely proportional to V, i.e., $g\propto 1/\sqrt{V}$. Therefore, in both regimes the dynamic of the coupled system is strongly dependent on the properties of the photonic mode and, notably, on the electromagnetic field confinement in time and spatial domains.

In order to observe these phenomena at visible wavelengths, different optical resonators have been proposed [2,4], but two-dimensional (2D) photonic crystal (PhC) cavities represent the most promising structures, since they give the best control on the optical properties of the confined system. At present, PhC resonators for applications in the visible spectral range are based on various geometries [5–7] and on higher-order modes of the widely studied single-point defect [8] [also known as an H1 cavity, sketched in Fig. 1(a), inset]. The H1 cavity consists of a missed hole in a triangular PhC lattice, which allows two orthogonally polarized resonant modes in the photonic band gap (hereafter referred to as x- and z-pole modes). The H1 resonator presents several advantages with respect to other PhC configurations for applications in quantum optics. For instance, the cross polarization of x- and z-pole modes and the absence of higher-order modes can be exploited to satisfy the requirements of quantum information algorithms [9]. As compared with other PhC point defects, the H1 cavity presents the lowest V, thus enhancing QED phenomena in both strongly and weakly coupled systems. The confinement in extremely small modal volumes is more challenging for visible light, since the constraint to use low-absorption materials in this spectral range does not allow recourse to high-refractive-index semiconductor membranes, thus reducing the effectiveness in localizing optical modes. Nevertheless, the aforementioned advantages, together with the increasing interest toward the realization of efficient emitting devices in the visible spectral range, foster theoretical and experimental studies to find alternative routes to improve light confinement in low-index H1 systems.

In this Letter, we theoretically and experimentally investigate a new design strategy to realize H1 PhC defect nanocavities in low-index materials. The confinement in the slab has been significantly improved, while the orthogonally polarized dipolelike behavior of the two photonic states allowed in the H1 defect has been preserved and no other resonant modes introduced.

An H1 cavity has been obtained in a triangular lattice of air holes with period a and radius r in a silicon nitride (Si_3N_4) slab having refractive index $n=1.93$ and thickness t. The electromagnetic behavior of such a structure was investigated by using plane-wave expansion and 3D finite difference time domain algorithms.

Our approach to realize ultrasmall-volume PhC cavities while keeping high Q factors in the visible range and preserving the dipolelike shape of the

0146-9592/10/101509-3/$15.00

1510 OPTICS LETTERS / Vol. 35, No. 10 / May 15, 2010

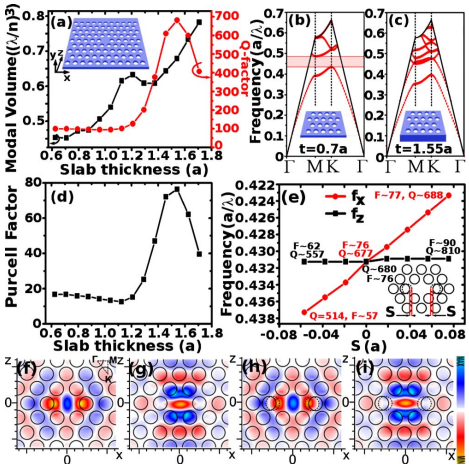

Fig. 1. (Color online) (a) Dependence of modal volume and Q factor on the thickness of the slab t. Inset, photonic crystal H1 cavity. (b), (c) Photonic band structure of the structure for $t=0.7a$ and $t=1.55a$, respectively. (d) Dependence of the Purcell factor on t (for $S=0$). (e) Modification of the resonant frequencies and of the Q factor of the degenerated modes when two cavity neighboring holes are moved, as shown in the inset. The holes are moved closer to (farther from) the center for $S<0$ ($S>0$). (f) E_z for the x-pole mode in an unmodified H1 cavity. (g) E_x for the z-pole mode in an unmodified H1 cavity. (h) E_z for the x-pole mode in an H1 cavity with $S=0.2a$. (i) E_x for the z-pole mode in an H1 cavity with $S=0.2a$.

modes first involves the optimization of the thickness of the PhC slab. As shown in Fig. 1(a) for the x-pole mode, the Q factor is quite constant for $t<1.2a$, and it has a maximum for $t=1.55a$. As reported in Figs. 1(b) and 1(c), the photonic bandgap (PBG) existing for $t=0.7a$ disappears when t is increased to $1.55a$, in agreement with the closing-bandgap principle presented in [3]. This lets us infer that the electromagnetic confinement in the xz plane is not due to the PBG but can be assigned to the mismatch in the momentum space between the cavity mode and the second guided mode in the PhC slab, as described by Tandaechanurat *et al.* [3]. The increased thickness of the slab leads to slight variations of the x- and z-pole modal profiles along y. For this reason, V grows steadily as a function of t, as shown in Fig. 1(a). However, because the modal extension in the xz plane is preserved, these variations of V are negligible with respect to the increase in Q, and thus the Purcell factor [Fig. 1(d)] follows the Q-factor behavior: for $t=1.55a$, F is maximized to $F\sim 78$ with $V\sim 0.68\ (\lambda/n)^3$ and $Q\sim 700$. A similar trend has been found for the z-pole mode.

The engineering of x- and z-pole modes would foster many applications based on H1 nanocavities operating at visible wavelengths. For instance, the degeneracy of x- and z-pole modes may be useful for entangled photon generation or quantum cryptography [9]. Other applications, such as single-photon sources or PhC-based optical read out of lab-on-chip devices [10], require well-defined and linearly polarized nondegenerate resonances. Several solutions have been reported in past years to break the degeneracy or to recover it [8,11–13]. A versatile strategy to break the degeneracy is displayed in Fig. 1(e): by moving two cavity neighboring holes, it is possible to change the resonant frequency of the x-pole mode (f_x) significantly without affecting the z-pole mode. This finding is ascribed to the selective modification of the wavevector $\mathbf{k}=[k_x,k_y,k_z]$ along a specific direction. Indeed x- and z-pole modes have the strongest component of $\mathbf{k}$ oriented along the x and z axes, respectively. When two holes are moved closer to the center of the cavity along the x axis ($S<0$, see Fig. 1(e) for definition), thus changing k_x while keeping k_z constant, f_x increases and f_z is unchanged. In the same way f_x decreases for $S>0$, while keeping f_z constant. Figures 1(f)–1(i) show the x- and z-pole modal profiles for an unmodified H1 cavity and for a cavity with $S=0.2a$. The electric field component along x (E_x) of the z-pole mode profile remains unchanged when the holes are moved far from the center [Figs. 1(g) and 1(i)]. The shift instead results in the elongation of the x-pole modal function along x [Figs. 1(f) and 1(h)], thus modifying its resonant frequency.

Such modifications of the field distributions also lead to variations of the Q factors of the modes [Fig. 1(e)]. If $S<0$, abrupt changes are introduced near the maximum of the electric field [1] of the z-pole mode function, resulting in an increase in radiation losses and in a smaller Q factor ($Q\sim 557$ for $S=-0.057a$). In contrast, if $S>0$ these abrupt variations in the modal profile are avoided, the radiative energy in the light-cone minimized, and the Q factor of the z-pole mode enhanced with a V and f_z almost unchanged. The optimized Q factor turns out to be $Q\sim 810$ for $S=0.075a$, and the Purcell factor is assessed as $F\sim 90$. We have therefore verified that momentum space engineering, a strategy exploited to improve confinement of defect states localized within the PBG [1,7], can also be effective for cavity resonances that do not need a PBG.

These theoretical findings have been experimentally demonstrated by exploiting a 2D PhC technology in a Si_3N_4–air membrane. The PhC geometry was defined in a 400-nm-thick Si_3N_4 film [see Fig. 2(a)], and both cyanine 3 (Cy3) fluorophore and core/shell CdSe/CdS colloidal dot-in-rod nanocrystals [14] have been deposited on the resonator. Room temperature microphotoluminescence characterization was therefore performed.

In order to tune the resonance of the structure, the scalability of the designed PhC was exploited, and several nanocavities, with $r=0.308a$ and different values of a, were fabricated: Fig. 2(b) shows three resonances for three different values of a. The resonant peaks are well approximated by a Lorentzian function [Fig. 2(b)]. For $a\sim 265$ nm, a $Q\sim 620$ is observed for an unmodified H1 cavity.

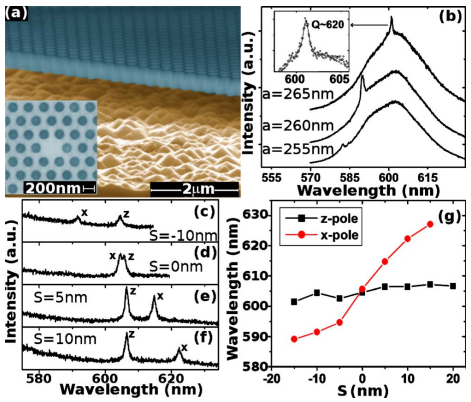

Fig. 2. (Color online) (a) Bird's eye view of the realized air-bridge structure and (inset) its in-plane view. (b) Resonances obtained by drop casting colloidal nanocrystals on the structure for three different values of a and $r=0.308a$. The inset shows the Lorentzian fitting of the resonant peak for $a=265$ nm. (c)–(f) Resonance of x- and z-pole modes for different values of the hole shift and $a=270$ nm. (g) Resonant frequencies of x- and z-pole modes as a function of the hole shift.

To explore the mode shifting over a wide spectral range, an organic fluorophore (Cy3) with broad emission spectrum was immobilized on the device. Figures 2(c)–2(f) report the microphotoluminescence spectra for different values of S. The z-pole mode is almost unaffected by the shift of the holes, whereas the x-pole mode becomes broadly tunable by changing S. The two modes were identified by performing polarization-resolved measurements, and their resonant wavelengths (λ_x and λ_z, respectively) are displayed in Fig. 2(g) for several values of S. In agreement with the theoretical results of Fig. 1(e), the x-pole mode is tunable over a range of about $\Delta\lambda_x \sim 40$ nm. Small discrepancies between experimental results and theoretical calculations have been observed in terms of slight variations of λ_z and weak nonlinearity of λ_x; since these variations do not show a clear dependence on S, they could be reasonably attributed to unavoidable fabrication imperfections. The theoretical findings about the influence of the hole's position on the z-pole Q factor have been confirmed by the experiments. For $S=15$ nm $Q\sim750$ has been measured, while for $S=-20$ nm the z-pole Q factor reduces to a value of ~200.

In summary, we have reported theoretical and experimental optimization in the visible spectral range of the H1 PhC resonator. The theoretical Purcell factor of the two degenerated modes has been increased up to ~90 without introducing high-order states or resorting to other kinds of cavities, such as an $L3$ cavity or double heterostructure, together with a maximum Q factor of ~750.

The authors acknowledge Dr. G. Vecchio, Dr. A. Fiore, M. Grande, Dr. A. Massaro, Dr. Pier P. Pompa, Dr. L. Manna, and Dr. A. Passaseo for fruitful discussions. The authors thank G. Epifani and G. De Iaco for their expert technical help.

References

1. Y. Akahane, T. Asano, B. S. Song, and S. Noda, Opt. Express **13**, 1202 (2005).
2. N. Le Thomas, U. Woggon, O. Schöps, M. V. Artemyev, M. Kazes, and U. Banin, Nano Lett. **6**, 557 (2006).
3. A. Tandaechanurat, S. Iwamoto, M. Nomura, N. Kumagai, and Y. Arakawa, Opt. Express **16**, 448 (2008).
4. A. Qualtieri, G. Morello, P. Spinicelli, M. T. Todaro, T. Stomeo, L. Martiradonna, M. De Giorgi, X. Quélin, S. Buil, A. Bramati, J. P. Hermier, R. Cingolani, and M. De Vittorio, New J. Phys. **11**, 033025 (2009).
5. M. Makarova, J. Vuckovic, H. Sanda, and Y. Nishi, Appl. Phys. Lett. **89**, 221101 (2006).
6. M. Barth, N. Nüsse, J. Stingl, B. Löchel, and O. Benson, Appl. Phys. Lett. **93**, 021112 (2008).
7. L. Martiradonna, L. Carbone, A. Tandaechanurat, M. Kitamura, S. Iwamoto, L. Manna, M. De Vittorio, R. Cingolani, and Y. Arakawa, Nano Lett. **8**, 260 (2008).
8. M. Kitamura, S. Iwamoto, and Y. Arakawa, Appl. Phys. Lett. **87**, 151119 (2005).
9. C. H. Bennett and G. Brassard, in *Proceedings of the International Conference on Computers, Systems and Signal Processing* (IEEE, 1984), p. 175.
10. L. Martiradonna, F. Pisanello, T. Stomeo, A. Qualtieri, G. Vecchio, S. Sabella, R. Cingolani, M. De Vittorio, and P. P. Pompa, Appl. Phys. Lett. **96**, 113702 (2010).
11. O. Painter, K. Srinivasan, J. D. O'Brien, A. Scherer, and P. D. Dapkus, J. Opt. A **3**, S161 (2001).
12. S. Frédérick, D. Dalacu, G. C. Aers, P. J. Poole, J. Lapointe, and R. L. Williams, Physica E (Amsterdam) **32**, 504 (2006).
13. K. Hennessy, C. Högerle, E. Hu, A. Badolato, and A. Imamoğlu, Appl. Phys. Lett. **89**, 041118 (2006).
14. F. Pisanello, L. Martiradonna, G. Lemenager, P. Spinicelli, A. Fiore, L. Manna, J.-P. Hermier, R. Cingolani, E. Giacobino, M. De Vittorio, and A. Bramati, Appl. Phys. Lett. **96**, 033101 (2010).

Phys. Status Solidi C **7**, No. 11–12, 2688–2691 (2010) / **DOI** 10.1002/pssc.200983836

physica status solidi c
www.pss-c.com
current topics in solid state physics

Evaluation of oscillator strength in colloidal CdSe/CdS dots-in-rods

Ferruccio Pisanello[*,1,2], Godefroy Leménager[1], Luigi Martiradonna[3], Piernicola Spinicelli[1], Angela Fiore[2], Alberto Amo[1], Elisabeth Giacobino[1], Roberto Cingolani[2,3], Massimo De Vittorio[2,3], and Alberto Bramati[1]

[1] Université Pierre et Marie Curie, Laboratoire Kastler Brossel, CNRS UMR8552, Ecole Normale Supérieure, 4 place Jussieu, 75005 Paris, France
[2] National Nanotechnology Laboratory of CNR/INFM, Scuola superiore ISUFI, Università del Salento, 16 Via Arnesano, 73100 Lecce, Italy
[3] Istituto Italiano di Tecnologia (IIT), Center for Bio-Molecular Nanotechnolgy, Via Barsanti 1, Arnesano, 73010 Lecce, Italy

Received 19 October 2009, accepted 20 February 2010
Published online 9 August 2010

Keywords CdSe/CdS core/shell structures, cavity electrodynamics, photonic crystals, polaritons

* Corresponding author: e-mail pisanello@spectro.jussieu.fr, Phone: +33 1 44 27 72 66, Fax: +33 1 44 27 38 45

The oscillator strength in CdSe/CdS colloidal dot-in-rods is evaluated and assessed to be of ~1.5. On the basis of this finding, the possibility to reach the strong coupling regime with photonic crystals nanocavities is discussed. In spite that carefully choosing the cavity parameters the strong coupling regime could be analytically achieved at room temperature, theoretical considerations show that the typical Rabi doublet cannot be resolved. The work draws also a viable strategy toward the observation of the strong coupling at cryogenic temperatures.

1 Introduction Light-matter coupling in nano- and micro-cavities is a fundamental research field which allows the investigation of intriguing Quantum Electro Dynamic (QED) phenomena, such as exciton-polaritons [1] and the generation of non-classical light fluxes [2]. When an optical emitter is placed in a resonant cavity and the energetic distributions of the two systems allow an interaction between the two oscillators, two different phenomena, known as *weak* and *strong coupling*, can be observed [3]. In the *weak coupling regime*, the spontaneous emission rate of an emitter X interacting with an optical mode C is modified by a factor which depends on how the energy is confined inside the cavity [4]. Instead, in the *strong coupling* condition the interaction between X and C leads to a coherent exchange of energy between them, thus resulting in vacuum Rabi oscillations [3].

Both these types of interactions have been widely investigated in the infrared spectral region by using epitaxially grown materials, such as quantum wells, quantum wires and quantum dots (QDs) and advanced optical resonators such as Bragg reflectors based microcavities photonic crystals (PhC) defects and microdisks [1, 5-8]. On the other hand, an emerging technology is based on the chemical synthesis of high luminescent QDs, so called colloidal nanocrystals (NCs). These emitters are crystalline structures with a size smaller than the Bohr radius, thus allowing discrete energy levels and the investigation of quantum mechanisms also at room temperature. Moreover, the low cost synthesis procedure and their versatility make them appealing materials for several fields, such as non classical quantum communications and biology [2, 9]. In order to rule their emission properties, several NCs compositions and shapes have been proposed in past years, allowing polarized emission and very high quantum yields [10, 11]. If colloidal NCs applications are still limited by several drawbacks, such as blinking, spectral diffusion, low oscillator strength and short coherence times, it has been recently demonstrated that by engineering the environment surrounding the quantized levels the blinking phenomenon can be overtaken [12, 13]. Among the proposed strategies to realize asymmetric core/shell structures, the dot-in-rod (DR) configuration, in which the CdSe spherical core is surrounded by an elongated CdS rod-like shell [14], presents several properties that make it very promising to reach the strong coupling regime. It has been demonstrated that such nanosystems are characterized by a shorter ex-

Contributed Article

Phys. Status Solidi C 7, No. 11–12 (2010) 2689

cited state lifetime compared to spherical nanocrystals and that the elongated shape leads to a strong electric field inside them [15]. These two parameters are strictly linked to the so called *oscillator strength*, which plays a key role in the dynamic of strongly coupled systems [16]. Indeed, with elongated-core NCs, so called nanorods (NRs) [17] the strong coupling regime has been reached at cryogenic temperature by coupling them with dielectric nanospheres [18].

The goal of this paper is to evaluate if CdSe/CdS DRs are suitable quantum emitters for strongly coupled systems. In the following, the concept of strong coupling will be introduced and the fundamental parameters which must be ruled to reach this regime will be discussed with particular attention to the strong coupling of a single colloidal NC in a PhC cavity. The oscillator strength of an isolated DR will be measured by means of time resolved spectroscopy in order to understand if these nanoclusters are suitable to reach the strong coupling regime.

2 The strong coupling regime A system constituted by a QD (emitting at $\hbar\omega_X$) strongly coupled to an optical mode in a photonic cavity (at energy $\hbar\omega_C$) is described by the Hamiltonian [19]

$$H = \hbar\omega_C a^+ a + \hbar\omega_X b^+ b + g\left(a^+ b + a b^+\right), \qquad (1)$$

where a and b are the cavity and exciton operators, respectively. The last term describes the linear coupling between X and C. The coupling constant g is a fundamental parameter to design a strongly coupled system and is bound to the properties of both X and C. By taking into account the relaxation terms of both X and C and if the detuning between X and C is zero ($\hbar\omega_X=\hbar\omega_C=\hbar\omega_0$) the eigenenergies of a strongly coupled system are given by the following expression:

$$E_\pm = \hbar\omega_0 - i\frac{\gamma_X+\gamma_C}{2} \pm \sqrt{g^2 - \left(\frac{\gamma_C-\gamma_X}{4}\right)^2} \qquad (2)$$

where γ_C and γ_X are the linewidths (full width at half maximum) of C and X, respectively. When the X-C interaction becomes larger than the combined X-C decay rate (assumed as threshold t), i.e.

$$g^2 > \frac{(\gamma_C-\gamma_X)^2}{16} = t, \qquad (3)$$

the real part of E_+ and E_- are different [$Re(E_+)\neq Re(E_-)$] and the two oscillators allowed to coherent exchange energy. In this picture the coupling constant g is related to the oscillator strength of X (f) and to the modal volume (V) of C by Eq. (3):

$$g^2 = \frac{1}{4\varepsilon_0\varepsilon_r}\frac{e^2 f}{mV}, \qquad (4)$$

where m is the free-electron mass and ε_0 and ε_r are the dielectric constant of the vacuum and of the relative dielectric constant of the medium. The photoluminescence (PL) spectrum of this system, according with Ref. [3], is:

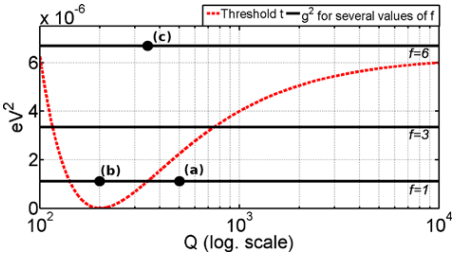

Figure 1 Threshold t as a function of the cavity Q-factor (red dashed line) and coupling constants g^2 for several values of f and a modal volume V=0.48$(\lambda/n)^3$. Black dots refer to the graphs of Fig. 2.

$$S(\hbar\omega) \propto \left| \frac{E_+ - \hbar\omega_0 + i\frac{\gamma_C}{2}}{\hbar\omega - E_+} - \frac{E_- - \hbar\omega_0 + i\frac{\gamma_C}{2}}{\hbar\omega - E_-} \right|^2 \qquad (5)$$

From Eq. (3) it is clear that the higher the cavity modal volume, the lower the coupling constant between X and C. The best way to obtain a low modal volume is to use a PhC based nanocavity [20]. In the visible spectral range these resonators present lower quality factors with respect to the infrared wavelengths because of the low refractive index of transparent materials between 500 nm and 700 nm [21]. However, V is preserved and the modal function can be confined in a volume lower than the cubic wavelength. In particular, the nanocavity proposed in Ref. [22] gives the possibility to work with resonant modes having a modal volume from $V=0.48$ $(\lambda/n)^3$ to $V=0.7$ $(\lambda/n)^3$ and, importantly, a quality-factor (Q-factor) tunable over a broad range in a simple way, with a maximum value of Q~800. Let's suppose that a single colloidal DR emitting at $\hbar\omega_X=2.072eV$ with a room temperature linewidth of $\gamma_X=10meV$ [15] is localized in the center of a PhC cavity with a quality factor $Q=(\hbar\omega_C)/\gamma_C$. Figure 1 reports the behaviour of the threshold $t=(\hbar\omega_C/Q-\gamma_X)^2/16$ as a function of the cavity Q-factor. When the cavity linewidth approaches γ_X the threshold t is minimized and the condition (3) achievable also for lower oscillator strength. For example, as shown by the continuous lines in Fig. 1, the higher f the wider the interval of Q for which $g^2>t$. However t is an asymptotic threshold in respect to Q, i.e. $\lim_{Q\to\infty} t = \gamma_X^2/16$, and t can be overtaken also for high Q and $g>\gamma_X/4$. This is justifiable in a simple way: if f is not enough to allow a coherent exchange of energy between X and C this could be compensated by approaching the two energy configurations themselves.

An experimental evidence that the strong coupling condition regime is reached is represented by a doublet in the PL spectrum. However, because of the relation between Eq. (4) and Eq. (2), a non-zero difference between $Re(E_+)$ and $Re(E_-)$ is not a sufficient condition for the observation of two different peaks in $S(\hbar\omega)$. Some examples

physica status solidi c

of the possible situations are reported in Fig. 2 with reference to the points evidenced in Fig. 1. Figure 2 shows that below the threshold t (i.e. $Re(E_+)=Re(E_-)$) the two eigenstates are frequency-degenerate leading to a single PL peak. The point (b) is instead just above the threshold t and the non-degeneracy of the eingen-states is clearly visible. However, a single peak in the spectrum is still present because the vacuum Rabi splitting is signifantly smaller than the spectral width of each peak. This is not the case of Fig. 2(c), in which the PL spectrum is modified by the presence of the vacuum Rabi oscillations by virtue of a stronger oscillator strength (i.e. $g^2 >> t$).

As we will discuss in the following, the oscillator strength of colloidal NCs at room temperature is extremely low. In spite of that, for low f, the condition $Re(E_+)\neq Re(E_-)$ is fulfilled, and the strong coupling is theoretically reached. However, as in the case of Fig. 2(b), the observation of strong coupling features would not be possible by PL measurements because the doublet state is not evident in $S(\hbar\omega)$.

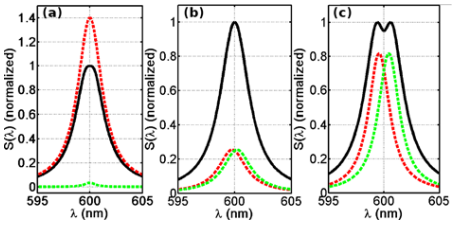

Figure 2 Photoluminescence spectra (black continuous lines) computed via Eq. (5) for the points (a), (b) and (c) of Fig. 1. Coloured dashed line represents the eigenstates.

3 Methods and techniques

3.1 Colloidal dot-in-rods synthesis The CdSe/CdS DRs were synthesized using the procedure reported in Ref. [14]. The CdSe cores were prepared by mixing TOPO (3.0g), ODPA (0.280g) and CdO (0.060g) in a 50 mL flask, heated to ca. 150 °C and exposed to vacuum for ca. 1 hour. Then, under nitrogen, the solution temperature was increased to above 300 °C to dissolve the CdO until it turns optically clear and colorless. Then 1.5 g of TOP was injected in the flask and heated to 360 °C. After that, a Se solution in TOP (0.058 g Se + 0.360 g TOP) was quickly injected in the flask and the reaction was stopped after 1 min by removing the heating mantle. CdSe seeds were precipitated with methanol, redissolved in toluene, reprecipitated with methanol, and finally dissolved in 1mL of TOP.

In order to obtain a preferred axis growth for the CdS shell, ODPA (0.290 g), HPA (0.080 g), TOPO (3.0 g) and CdO (0.060 g) were mixed in a three-neck flask, heated at 150 °C, and pumped to vacuum for ca. 1 hour. The temperature was first increased up to 300 °C and stabilized at 350 °C after the injection of 1.5 g of TOP. Then a solution of S in TOP (0.120 g S + 1.5 g TOP) containing 8×10^{-8} mol of readily prepared CdSe nanocrystals (diameter c~2.7 nm) dissolved in TOP was quickly injected in the flask. The shells were allowed to grow for about 6-8 minutes after the injection, after which the heating mantle was removed. The resulting nanocrystals (mean length 30 nm) were precipitated with methanol, washed by repeated re-dissolution in toluene and precipitation with the addition of methanol. At the end they were dissolved in toluene.

3.2 Optical characterization A nanomolar solution of DRs diluted in toluene was dropcasted on a microscope coverslip. A circularly-polarized picosecond-pulsed laser (at a wavelength of 404 nm) was focused on the sample by means of a microscope air objective. The single DR emission was collected through the same objective and sent into a Hanbury-Brown and Twiss setup based on two avalanche photodiodes. The collected signals were elaborated by means of a time-resolved data acquisition card (TimeHarp200, Picoquant). By triggering the acquisition with the laser pulses individual photon-detection events with their absolute arrival time and their delay from the laser pulse were recorded, thus allowing to analyze the PL time traces and the radiative decay behavior of the system under investigation, up to a time-resolution of *36ps*. In order to confirm that the measurements were carried out on a single nanoparticle, antibunched measurements were performed as explained in Ref. [23]. All measurements were performed at room temperature in air at the single NC level.

4 Experimental results and discussions

Equation (4) and Fig. 1 show that the emission oscillator strength f is one of the parameters which define the regime of the coupled system. f can be expressed as a function of the radiative decay rate $1/\tau_{Xr}$, i.e.

$$f = \frac{6m\varepsilon_0\pi\, c\, \lambda^2}{q^2 n}\frac{1}{\tau_{Xr}}, \qquad (6)$$

where q is the electron charge. The average lifetime of the transition X (τ_X) can be estimated by fitting the decay curve obtained by the delays histogram between the laser pulses and the received photons. A typical decay behaviour measured on a single DR is reported in Fig. 3; the experimental data are well fitted by a mono-exponential decay function $e^{-t/\tau X}$ and τ_X has been assessed to be ~11ns. It is evident that this method estimates the total decay rate ($1/\tau_X$), which is the sum of the radiative recombination rate and the non radiative one ($1/\tau_{Xnr}$), i.e.

$$\frac{1}{\tau_X} = \frac{1}{\tau_{Xr}} + \frac{1}{\tau_{Xnr}}. \qquad (7)$$

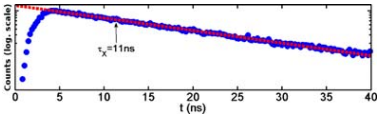

Figure 3 Decay curve measured on an isolated DR (blue dots) and its exponential fit (red dashed line).

Contributed Article

Phys. Status Solidi C **7**, No. 11–12 (2010) 2691

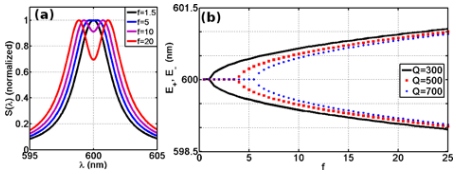

Figure 4 (a) Luminescence spectra for several values of the oscillator strength and Q=300. (b) Spectral position of the eigenmodes for several values of Q and as a function of *f*.

However it has been demonstrated that for colloidal NCs and DRs the internal quantum efficiency approaches 100% [14, 24]. As a consequence, the non radiative rate can be considered negligible and the estimated τ_X assigned to purely radiative processes, i.e. $\tau_X=\tau_{Xr}$. By considering τ_X~11 ns the oscillator strength obtained via Eq. (6) can be assessed to be 1.5. Lifetime measurements as a function of the intensity power were also performed. Consistently with the results reported in ref. [15], the lifetime of the excited state is almost constant at values of ~11 nm.

On the basis of the discussion in Section 2, we can infer that, for a cavity with $V\sim0.48(\lambda/n)^3$, a Q-factor between 150 and 400 is needed to reach the strong coupling regime with a DR characterized by an oscillator strength of $f=1.5$. However these parameters lead to the condition of Fig. 2(b), in which the strong coupling is theoretically achieved but not experimentally observable. Moreover, it has been demonstrated that colloidal nanorods presents a lifetime at cryogenic temperatures of $\tau_r<1ns$ [18] leading to a higher oscillator strength. For example $f\sim20$ for $\tau_r=800ps$ can be obtained via Eq. (6). Figures 4(a) and (b) display that for these values *f* the doublet is clearly visible in the PL spectrum and that the two eigenmode are not degenerated, making us to envision the possibility to observe the strong coupling between a colloidal dot-in-rod and a photonic crystals cavity at cryogenic temperatures.

5 Conclusions In summary, we discussed the possibility to reach the strong coupling regime with colloidal dots-in-rods. The oscillator strength of DRs has been measured by time resolved spectroscopy, assessing a value of *f*~1.5 at room temperature. Moreover, photonic crystals nanocavities have been suggested as appealing nanostructures to achieve this result because of their extremely low modal volume and the possibility to tune the quality factor of the resonant mode. Taking into account the obtained oscillator strength, analytical computations showed the possibility to achieve a strong coupling which nevertheless does not lead to a visible doublet in the PL spectrum. However, taking into account a decreasing of the DRs lifetime at cryogenic temperatures, the possibility to experimentally observe the vacuum Raby splitting in the investigated system can be envisioned.

Acknowledgements The help of Benedetta Antonazzo in the synthesis of high quality dot-in-rods is acknowledge. This work was supported by the Agence Nationale de la Recherche (reference number ANR-08-BLAN-0070-01).

References

[1] C. Weisbuch, M. Nishioka, A. Ishikawa, and Y. Arakawa, Phys. Rev. Lett. **69**, 3314 (1992).
[2] A. Qualtieri,G. Morello, P. Spinicelli, M. T. Todaro, T. Stomeo, L. Martiradonna, M. De Giorgi, X. Quélin, S. Buil, A. Bramati, J. P. Hermier, R. Cingolani, and M. De Vittorio, New J. Phys. **11**, 033025 (2009).
[3] L. C. Andreani, G. Panzarini, and J.-M. Gérard, Phys Rev. B **60**, 13276 (1999).
[4] E. M. Purcell, Phys. Rev. **69**, 681 (1946).
[5] J. P. Reithmaier, G. Sek, A. Looffler, C. Hofmann, S. Kuhn, S. Reitzenstein, L. V. Keldysh, V. D. Kulakovskii, T. L. Reinecke, and A. Forchel, Nature **432**, 197 (2004).
[6] T. Yoshie, A. Scherer, J. Hendrickson, G. Khitrova, H. M. Gibbs, G. Rupper, C. Ell, O. B. Shchekin, and D. G. Depp, Nature **432**, 200 (2004).
[7] K. Hennessy, A. Badolato, M. Winger, D. Gerace, M. Atatüre, S. Gulde, S. Fält, E. L. Hu, and A. Imamolu, Nature **445**, 896 (2007).
[8] E. Peter, P. Senellart, D. Martrou, A. Lemaître, J. Hours, J. M. Gérard, and J. Bloch, Phys. Rev. Lett. **95**, 067401 (2005).
[9] W. J. Parak, D. Gerion, T. Pellegrino, D. Zanchet, C. Micheel, S. C. Williams, R. Boudreau, M. A. Le Gros, C. A Larabell, and A. P. Alivisatos, Nanotechnology **14**, R15 (2003).
[10] X. Peng, L. Manna, W. Yang, J. Wickham, E. Scher, A. Kadavanich, and A. P. Alivisatos, Nature **404**, 59 (2000).
[11] X. Brokmann, L. Coolen, M. Dahan, and J. P. Hermier, Phys. Rev. Lett. **93**, 107403 (2004).
[12] B. Mahler, P. Spinicelli, S. Buil, X. Quelin, J. P. Hermier, and B. Dubertret, Nature Mater. **7**, 659 (2008).
[13] X. Wang, X. Ren, K. Kahen, M. A. Hahn, M. Rajeswaran, S. Maccagnano-Zacher, J. Silcox, G. E. Cragg, A. L. Efros, and T. D. Krauss, Nature **459**, 686 (2009).
[14] L. Carbone et al., Nano Lett. **7**, 2942-2950 (2008).
[15] G. Morello, F. Della Sala, L. Carbone, L. Manna, G. Maruccio, R. Cingolani, and M. De Giorgi, Phys. Rev. B **78**, 195313 (2008).
[16] M. D. Leistikow, J. Johansen, A. J. Kettelarij, P. Lodahl, and W. L. Vos, Phys. Rev. B **79**, 045301 (2009).
[17] J. T. Hu, L. S. Li, W. Yang, L. Manna, L. W. Wang, and A. P. Alivisatos, Science **292**, 2060 (2001).
[18] N. Le Thomas, U. Woggon, and O. Schöps, Nano Lett. **6**, 557 (2006).
[19] F. P. Laussy, E. del Valle, and C. Tejedor, Phys. Rev. B **79**, 235325 (2009).
[20] O. Painter, R. K. Lee, A. Scherer, A. Yariv, J. D. O'Brien, P. D. Dapkus, and I. Kim, Science **284**, 1819 (1999).
[21] L. Martiradonna, L. Carbone, A. Tandaechanurat, M. Kitamura, S. Iwamoto, L. Manna, M. De Vittorio, R. Cingolani, and Y. Arakawa, Nano Lett. **8**, 260 (2008).
[22] F. Pisanello, M. De Vittorio, and R. Cingolani, Superlattice Microstruct.; doi:10.1016/j.spmi.2009.06.003.
[23] F. Pisanello et al., Superlattices Microstruct. doi:10.1016/j.spmi.2009.06.009 (2009).
[24] S. Deka et al., J. Am. Chem. Soc. **131**, 2948 (2009).

Superlattices and Microstructures 47 (2010) 34–38

Contents lists available at ScienceDirect

Superlattices and Microstructures

journal homepage: www.elsevier.com/locate/superlattices

Modal selective tuning in a photonic crystal cavity

F. Pisanello *, M. De Vittorio, R. Cingolani

Università del Salento, Scuola Superiore ISUFI, National Nanotechnology Laboratory, CNR/INFM, 16 Via Arnesano, Lecce 73100, Italy

ARTICLE INFO

Article history:
Available online 23 June 2009

Keywords:
Photonic crystals
Single point defect
H1 cavity
Silicon nitride

ABSTRACT

We present a way to selectively tune the properties of the degenerated modes confined in a single point defect two-dimensional photonic crystal cavity based on a triangular lattice of air holes. We investigate the dependence of the modal properties of the resonator on the position of the first neighbor holes, showing that it is possible to finely tune the resonant frequency of only one of these two modes and to increase the quality factor of the mode that has no frequency shift. This is achieved by controlling the wavevector components inside the cavity. This approach is a viable strategy for the development and the optimization of several innovative devices based on bi-modal cavity arrays, such as arrays of integrated optical filters and optical read-out sections for biosensing applications.

1. Introduction

One of the most interesting properties of photonic crystal (PhC) [1,2] is the possibility to finely tune the resonance of the light trapped in a defect [3]. A careful design of the refractive index modulation in a periodic lattice results in a wavelength range where the photonic density of states is zero, called Photonic Band Gap (PBG). Among the PhC structures proposed in the past years (in one, two and three dimensions), two-dimensional (2D) PhC tiny slabs have been the subject of intense research activity. These structures allow the in-plane confinement of light by virtue of photonic crystal reflection and a classical total internal reflection (TIR) in the out-of-plane direction [4]. Light confinement in 2D-PhC slabs is obtained by simply removing some periodic elements, in order to obtain an optical resonator.

The first proposed 2D-PhC nanocavity consisted of a single point defect, referred as H1, which has been deeply studied in the last ten years. In 1999, Painter et al. [5,6] showed that this kind of

* Corresponding address: Laboratoire Kastler Brossel, CNRS UMR8552, Université Pierre et Marie Curie, Ecole normale supérieure, 4 place Jussieu, 75252 Paris Cedex 05, France. Tel.: +33 144277266; fax: +33 144273845.
E-mail address: pisanello@spectro.jussieu.fr (F. Pisanello).

0749-6036/$ – see front matter © 2009 Elsevier Ltd. All rights reserved.
doi:10.1016/j.spmi.2009.06.003

cavity exhibits a pair of doubly degenerated dipole modes, with orthogonal polarizations [6]. Refs. [6,7] also showed that by changing the symmetry of the cavity, such as by increasing the size of two of the six PhC holes around the defect, it is possible to remove the degeneracy of the modes. After Painter's studies [5–9], most of the research was aimed at optimizing two fundamental parameters of the H1 resonator, namely quality factor (Q) [27] and modal volume (V) [10], both strictly bound to QED effects [11–14] and to the enhancement of the spontaneous emission through the Purcell Factor [14]. As demonstrated by several groups [15–18], by changing the size of the first neighbor holes it is possible to generate additional modes inside an H1 cavity, with field patterns different from dipole-like ones. Following this approach, Kim et al. [15] and Shirane et al. [16] were able to induce a whispering gallery mode (with an hexapole mode function) inside an hexagonal H1 cavity, reaching the best Purcell factor [14] for a single point defect cavity of $44\,000(n/\lambda)^3$. Tandaechanurat et al. [19] showed that it is possible to increase the Q-factor in a H1 cavity by closing the photonic band gap of a PhC slab, which is obtained by just varying the thickness of the structure. Modification of resonant frequencies in a H1 cavity was also applied by Ota et al. [20] to tune the PhC H1 cavity mode and the ground state emission of a single quantum dot. They showed how to break the degeneration of the two dipole modes to couple the cavity modes with a two level system, in order to have efficient single photon sources. However, degenerate modes splitting typically leads to a shift of both resonances [5,6,15–18]. In some applications, such as for instance in the optical read-out of biosensors and lab-on-chip [21], a decoupling between a fixed optical excitation wavelength and a tunable output signal would strongly increase the signal-to-noise ratio. This tuning of only a single high Q-factor mode among two degenerate modes is not typically possible by the photonic crystal architectures proposed so far.

In this paper we propose a way to tune the properties of only one of the two degenerate modes in a H1 2D-PhC resonator, without affecting the second one. We studied three different hole shift conditions, with different symmetry centers [6,9], investigating the dependence of the resonant frequencies on the positions of the holes around the defect, checking also the variations of Q-factor. We show that by moving two holes along a specific axis on the border of the cavity, just one component of wavevector ($\mathbf{k} = [k_x, k_y, k_z]$) is modified, thus affecting the resonant frequency of only one degenerate mode. By means of the same modification of the cavity we also show that the Q-factor of the unaffected mode can be further increased. These results are explained in terms of modal profiles and wavevector $\mathbf{k}$ modifications.

2. Computational methods and PhC slab design

The proposed structure is based on triangular lattice of air holes in a silicon nitride (Si_3N_4) ($n = 2.04$ at a wavelength $\lambda = 0.5\ \mu m$) slab waveguide in air bridge configuration. Si_3N_4 is a promising material by virtue of its mechanical and optical properties; its biocompatibility and transparency in the visible spectral range can be exploited to build hybrid bio-photonic devices. The photonic band diagram was computed by using a Plane Wave Extension (PWE) [22] algorithm in order to optimize the ratio between the lattice constant a and the holes radius r. An H1 cavity was obtained by removing one hole of a triangular PhC lattice made of holes having radius $r = 0.346a$. The Finite Difference Time Domain (FDTD) simulations (carried out by using commercial software FullWave R-soft Design) have been performed by exploiting a 3D spatial discretized cell with the same dimensions along all directions and perfect matching layers [23] at the end of the spatial domain. The Q-factor computation has been performed by using the energy decay method [19] and the Fast Harmonic Analysis procedure [24], both giving consistent results. A solution convergence analysis has been performed as a function of the size of the spatial domain, in order to have an accurate Q-factor estimation. All simulations have been restricted to *transverse electric like modes* (TE-like) [3] with significant component of electric field along x- and z-directions (see Fig. 1 for axis definitions), and only one component of magnetic field along y-direction.

The computed modal profiles of the two degenerated modes in a standard H1 cavity, both at the normalized resonant frequency of $f = a/\lambda \approx 0.431$, are shown in Fig. 1(a) and (b). The z component of the electric field distribution presented in Fig. 1(a), hereafter referred to as x-pole mode, has a major component of the wavevector $\mathbf{k}$ along x axis. The mode in Fig. 1(b), hereafter referred to as z-pole

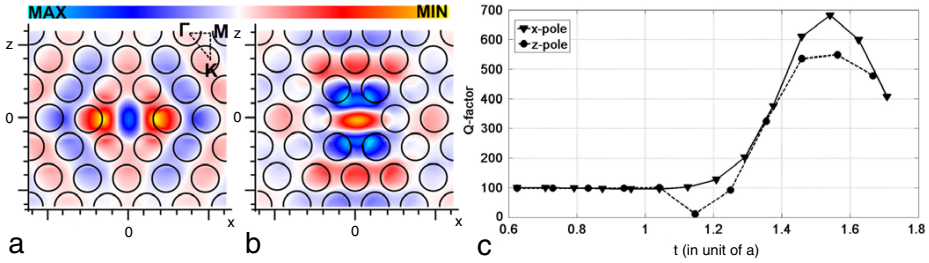

Fig. 1. (a) (b) Modal profiles in a single point defect without modifications on neighbor holes: electric field z component of the x-pole mode (a) and electric field x component of the z-pole mode (b); circular lines show the boundary of air holes. (c) Variation of Q-factor for both x-pole and z-pole modes as a function of the 2D-PhC slab thickness.

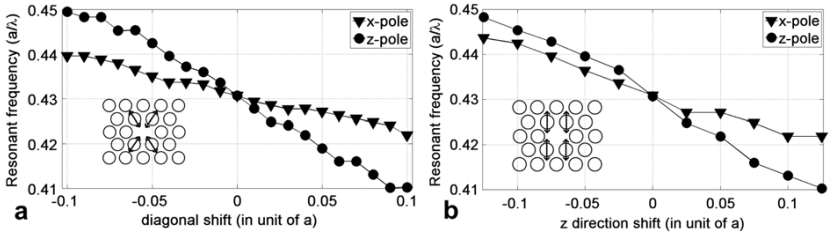

Fig. 2. Dependence of resonant frequency on two types of hole shifts. (a) *Diagonal* shift. (b) *z-direction* shift.

mode, has the strongest component of **k** along z-direction. The thickness t of the slab was optimized as a function of the Q-factor, following the closing band gap procedure explained in [19], so far not extended to low index material photonic crystals. Fig. 1(c), reporting the Q as a function of t, show that the Q-factor reaches its maximum value at $t = 1.55a$ for both modes.

3. Results and discussions

The shift of the first cavity neighbor holes leads to the splitting of the degenerate modes as reported in Figs. 2 and 3(a). When four holes are moved following Γ–K crystalline direction (as shown in inset of Fig. 2(a), see inset in Fig. 1(a) for crystal points definitions) the modification of both x and z components of **k** leads to a shift of the resonant frequencies of the two modes reported in Fig. 2(a). When the shifted holes are closer to the center of the cavity, hereafter referred to as *negative shifting*, the components of **k** are increased, as well as the resonant frequency, in both direction, whereas the opposite happens when the holes are moved far from the center (*positive shifting*). It is important to highlight that the resonance shift is higher for z-pole mode; this is due to the fact that the shape of the cavity is modified prevalently along z axis, where the z-pole mode has the strongest component of **k**. The good linearity shown in Fig. 2(a) is due to the *diagonal shift* configuration (inset of Fig. 2(a)), which, following Γ–K direction, has the center of the cavity as symmetry point [5,9]. This does not happen for the *z-direction* shift, shown in Fig. 2(b), in which the shift follows M–K direction. This configuration has no single symmetry point, and the orthogonal modes are not well distinguished because the resonant frequencies are very close.

The main result of this work is that the *x-direction* shift (see inset Fig. 3(a)) allows us to change the resonant frequency of x-pole mode without strongly affecting the resonant frequency of the z-pole mode, as reported in Fig. 3(a). In this case two holes are moved along Γ–K, so that just k_x is modified and the z-pole mode is characterized by only one constant resonant frequency. Therefore the tuning affects only the x-pole mode since the z-pole remains stable in frequency (Fig. 3(a)). x-pole and z-pole modes, for *x-direction* shift of $S_x = 0.1a$, are displayed in Fig. 3(b) and (c), respectively. We observe that

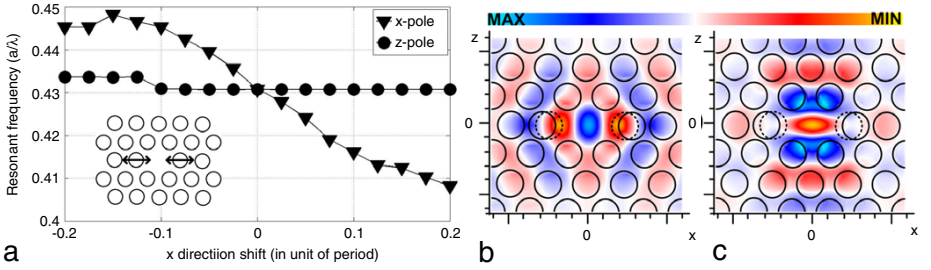

Fig. 3. Modifications on modal proprieties due to an *x-direction* shift. (a) Dependence of resonant frequency on *x-direction* shift. (b) Electric field *z* component of the *x*-pole mode. (c) Electric field *x* component of the *z*-pole mode. In both (b) and (c) the electric field modal profiles are computed for a $0.1a$ *x-direction* hole shifting; circular lines show the boundary of air holes. Dotted lines show the original hole position.

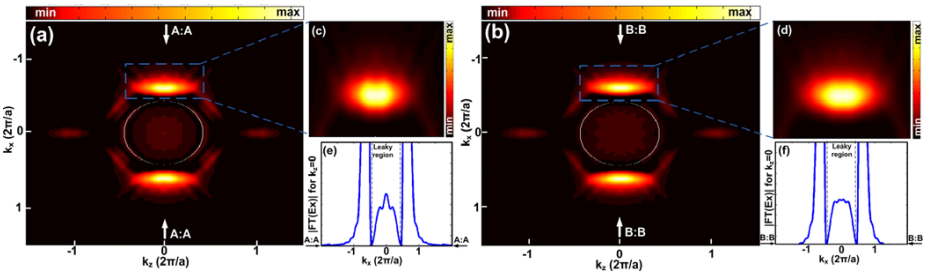

Fig. 4. E_x field-distribution in momentum space for the *z*-pole mode. The white circle represents the lightcone. (a) $|2DFT(E_x)|$ for *x-direction* shift of $Sx = -0.1a$; (b) $|2DFT(E_x)|$ for an *x-direction* shift of $Sx = 0.2a$; (c) Zoom to a specific area of (a). (d) Zoom to a specific area of (b). (e) Momentum function extracted from (a) for $k_z = 0$. (f) Momentum function extracted from (b) for $k_z = 0$.

the *z*-pole mode (Fig. 3(c)) is almost unchanged when compared with the modal profile in Fig. 1(b). The *x*-pole mode of Fig. 3(b) is instead different from Fig. 1(a) and shows a bigger main lobe due to the increased extension of the cavity along *x*. Shape modification of the cavity along *x*-direction also affects the *Q*-factor of the two modes. A hole's shift of $S_x = 0.2a$ increases the *Q*-factor value for the *z*-pole by *30%*. A negative shift along *x* leads instead to a decreased *Q*-factor of the *z*-pole mode. These variations on *Q* are due to the distance between the two shifted holes and the *z*-pole main lobe. The position of these holes affects the envelope function of the modal profile along the *x* axis. In order to increase the *Q*-factor in photonic crystal slabs it is also necessary to achieve a strong optical confinement along the *y*-direction, by avoiding abrupt changes in the electric field distribution [25]. When the holes are moved far from the center, the *z*-pole modal function behavior along *x* is smoothed; instead when they are closer to the main lobe, E_x presents sharp variations, also near its maximum value, affecting the TIR confinement. These findings are confirmed by the analysis in the *z*-pole momentum space, obtained by using a 2D Fourier Transform (2DFT), reported in Fig. 4(a) and (b) for *x-direction* shifts $Sx = -0.1a$ and $S_x = 0.2a$, respectively. The region inside the white circle of Fig. 4 represents the leaky region, defined by the lightcone [9,26,25]: the stronger the components in this region, the higher the radiation losses are in the direction perpendicular to the slab. For $S_x = -0.1a$ (Fig. 4(a) and (e)) a sharp peak is present at the center of the leaky region, affecting the value of *Q*; instead if $S_x = 0.2a$ (Fig. 4(b) and (f)), the 2DFT is almost constant inside the lightcone. As demonstrated in [25], the *Q*-factor depends also on the shape of the two peaks outside the lightcone. A Gaussian shape typically leads to higher *Q*-factor, being a direct measure of the energy not coupled with the radiation mode. Fig. 4(c) and (d) show a zoom of Fig. 4(a) and (b), respectively: the behavior for $S_x = -0.1a$ is far from a 2D Gaussian function. For $S_x = 0.2a$ (Fig. 4(d)), it is instead clear that by moving two holes

far from the center, a 2D Gaussian function for these peaks is achieved. Therefore, by increasing the z-pole Q-factor, a positive *x-direction* shift does not substantially affect the position, modal volume and resonant frequency of the z-pole electric field main lobe, leading to a straightforward increase of the Purcell factor and QED properties of microresonators.

In summary, we have proposed and numerically investigated an approach to independently tune the Q-factor and the resonance frequency of two degenerate modes in a H1 PhC resonator. We have shown that, by moving two of the holes around the cavity along the x-axis, it is possible to tune the resonant frequency of one high-Q resonant mode, without affecting the properties of the other. We found an increased Q-factor of the mode fixed in frequency, and an increase of the Purcell factor by virtue of the almost unchanged modal volume. We generalized also the closing band gap procedure and the Q behaviour as a function of the slab thickness to low refractive index PhC, showing that the best Q-factor is obtained for $t = 1.55a$.

References

[1] E. Yablonovitch, Phys. Rev. Lett. 58 (1987) 2059.
[2] S. John, Phys. Rev. Lett. 58 (1987) 2486.
[3] J.D. Joannopoulos, R.D. Meade, J.N. Winn, Photonic Crystal — Modeling the Flow of Light, Princeton University Press, 1995.
[4] P. Villeneuve, S. Fan, S. Johnson, J. Joannopoulos, Proc. IEE. Optoelectron. 145 (1998) 384.
[5] O. Painter, J. Vŭcković, A. Scherer, J. Opt. Soc. Am. B 16 (1999) 275.
[6] O. Painter, et al., J. Opt. A Pure Appl. Opt. 3 (2001) S161.
[7] O. Painter, K. Srinivasan, Opt. Lett. 27 (2003) 339.
[8] O. Painter, et al., Science 284 (1999) 1819.
[9] K. Srinivasan, O. Painter, Opt. Express 10 (2002) 670.
[10] J.S. Foresi, P.R. Villeneuve, J. Ferrera, E.R. Thoen, G. Steinmeyer, S. Fan, J.D. Joannopoulos, et al., Nature 390 (1997) 143.
[11] L.C. Andreani, G. Panzarini, J.M. Gérard, Phys. Rev. B 60 (1999) 13276.
[12] J.P. Reithmaier, et al., Nature 432 (2004) 197.
[13] T. Yoshie, et al., Nature 432 (2004) 200.
[14] E.M. Purcell, Phys. Rev. 69 (1946) 681.
[15] G.H. Kim, Y.H. LeeAkihiko, A. Shinya, Masaya Notomi, Opt. Express 12 (2004) 6624.
[16] M. Shirane, et al., J. Appl. Phys. 101 (2007) 0731071.
[17] H.Y. Ryu, et al., IEEE J. Quantum Electron. 39 (2003) 314.
[18] H.G. Park, et al., IEEE J. Quantum Electron. 38 (2002) 1353.
[19] A. Tandaechanurat, S. Iwamoto, M. Nomura, N. Kumagai, Y. Arakawa, Opt. Express 1 (2008) 448.
[20] Y. Ota, M. Nomura, N. Kumagai, K. Watanabe, S. Ishida, S. Iwamoto, Y. Arakawa, Appl. Phys. Lett. 93 (2008) 183114.
[21] K. Aoki, M. De Vittorio, T. Stomeo, F. Pisanello, A. Massaro, L. Martiradonna, et al. Italian Patent N. O2008A000614.
[22] S.G. Johnson, J.D. Joannopoulos, Opt. Express 8 (2001) 173.
[23] J.P. Berenger, J. Comput. Phys. 114 (1994) 185.
[24] V.A. Mandelshtama, H.S. Taylor, J. Chem. Phys. 107 (1997) 6756.
[25] Y. Akahane, T. Asano, B.S. Song, S. Noda, Opt. Express 13 (2005) 1202.
[26] J. Vŭcković, M. Loňcar, H. Mabuchi, A. Scherer, IEEE J. Quantum Electron. 38 (2002) 850.
[27] D. Englund, I. Fushman, J. Vŭcković, Opt. Express 12 (2005) 5961.

Chapter 5

Coherent injection of microcavity polaritons through two-photon absorption

Contents

The section 2.3 describes the strong coupling between excitons in a quantum well and confined photons in a planar microcavity. The standard excitation techniques of these type of systems consists in pumping at resonance the polariton states (i.e. upper or lower polariton branches) with a well defined energy and a well defined in plane wave vector $\mathbf{k}_{\parallel}$, or to excite the excitonic reservoir by pumping at energies higher than both polariton branches, leading in both cases to a rich phenomenology.

As in cold atoms gas, when pumped out of resonance, polaritons can condensate in the state with minimum energy, i.e. the $\mathbf{k}_{\parallel} = \mathbf{0}$ point of the lower polariton branch [193, 194]. The interesting point of this phenomenon is that by incoherently pumping the system, under certain conditions, coherent polariton emission can be recovered [27, 28, 193, 194].

When a $\mathbf{k}_{\parallel} \neq \mathbf{0}$ is instead imposed with a resonant excitation, the injected polaritons

conserve the momentum and create a quantum fluid flowing in the direction imposed by $\mathbf{k}_{\parallel}$. The polariton-polariton interactions allow this polariton quantum fluid to be generated in several regimes: it can be supersonic, subsonic or superfluid [22, 23] and it can interact with potential barriers in several ways, generating steady-states vortex singularities [24], moving vortex pairs [25] or dark solitons propagating within the fluid [26].

Strongly coupled systems are interesting also in the case of extremely weak injections, and in particular at the single polariton level. A regime of remarkable interest achievable by resonant excitation is the so called *polariton quantum blockade*, which allows strongly coupled systems to emit on-demand single photons [29]. As suggested in 2006 by Verger and co-workers [29], a sufficiently strong confinement of the cavity mode, together with a fully confined exciton, can result in strong polariton-polariton repulsions also at a single particle level, thus forbidding two polaritons to coexist in the structure. If only one polariton is excited in the cavity, it can re-emit just one photon, thus resulting in a strongly antibunched radiation. Indeed, the resonant injection of a second polariton in the system can be blocked by the presence of another polariton, because the polariton-polariton repulsion shifts the resonance frequency by an amount larger than the excitation linewidth. If a pulsed pump is used, an on-demand single-photon light source can therefore be obtained.

Obviously, resonantly pumped single photon sources should deal with the noise introduced by the excitation beam, which is usually reflected on the sample and affects the single photon detection. Indeed, the reflected photons have the same energy of the emitted ones and the high signal-to-noise ratio (SNR) needed for autocorrelation measurements is hardly achieved. A viable strategy to solve this problem has been recently proposed by researchers in Standford University [97, 195], who suggested to exploit the cross polarization of the resonant mode in a photonic crystal cavity and the excitation laser beam in order to separate the cavity-coupled signal from the pump reflection.

In this chapter we propose an alternative strategy to resonantly excite polaritons in pillars and planar microcavities without introducing any noise in the detection system. It is based in the simultaneous absorption of two photons, each of which with energy equals to one half of the excited state. Therefore, the pump laser beam results to be at a completely different energy if compared to the emitted light, and it can be easily filtered without any influence on the detectors. The high SNR achievable by this method let us envision that this two-photon absorption technique could open the way to the experimental demonstration of polariton quantum blockade in pillars microcavities.

The chapter is organized as follows: in section 5.1 the two-photon absorption (TPA) process is demonstrated for the excitation of polaritons in planar microcavities and the operation principles of this technique are discussed. After that, zero-dimensional (0D) polaritons are briefly introduced (section 5.2) and, in paragraph 5.3.2, the two-photon excitation technique is applied to the case of pillars microcavities coupled to a single quantum well. Interestingly, it has been found that TPA can lead to the macroscopic occupation of a single polariton state with emission properties similar to the ones observed in the case of polariton laser [28]. In the last section (5.3.3), an advanced pulse shaping technique is exploited to excite a single level of a pillar microcavity, showing that it is an appropriate method for the experimental demonstration of the polariton quantum blockade.

5.1 Two-photon absorption in a planar microcavity

Two-photon absorption (TPA) is defined as the simultaneous absorption of pairs of photons of the same or different energy in order to excite an electronic transition. This phenomenon was first predicted by M. Göppert-Mayer in 1931 [196] and demonstrated 30 years later by W. Kaiser and C. G. B. Garret [197] by illuminating a crystal of CaF_2 containing Eu^{2+} ions with a ruby laser beam. The energy absorbed through a TPA process is quadratically proportional to the intensity of the incident light [198] and

recently attracted significant interest in the fields of chemistry, biology, and photonics [199–201].

In order to show the suitability of TPA to excite microcavity polaritons, let us consider a planar microcavity strongly coupled to quantum well excitons with eigenstates $E_{LP}(\mathbf{k}_{\|})$ and $E_{UP}(\mathbf{k}_{\|})$ in the energy interval $[1.47eV, 1.495eV]$ with a Vacuum Rabi Splitting of $\hbar\Omega_{VRS} \sim 5.8meV$. The two-photon injection technique consists in the excitation of the polaritons at energies of $E_{Pump} = E_P/2$, with E_P the energy of the polariton state. The pump pulse (200fs, repetiton rate $\sim 76MHz$, full width at half maximum $\Delta E_{pump} \sim 13meV$, E_{Pump} tunable in the wavelength range $1580nm \div 1700nm$, i.e. $0.78eV \div 0.73eV$) is provided by an optical parametric oscillator pumped by a femtosecond pulsed Ti:S laser (see appendix B.3 for further details). It is important to point out that the linewidth of the excitation laser is $\Delta E_{Pump} \sim 13meV @ E_{Pump} = 0.751eV$. ΔE_{Pump} is thus quite larger than the Vacuum Rabi Splitting $\hbar\Omega_{VRS} \sim 5.8meV$ (i.e. $\lambda_{VRS} \sim 3.25nm$). This means that, as the splitting between upper and lower polariton branch is lower than ΔE_{Pump}, the two branches are excited at the same time.

Figure 5.1(a) displays the dispersion curve of a planar microcavity excited by laser pulses at energy

$$2 \cdot E_{Pump} \gg \frac{\min_{\mathbf{k}_{\|}}\{E_{UP}\} + \min_{\mathbf{k}_{\|}}\{E_{LP}\}}{2}, \tag{5.1}$$

for cavity-exciton detuning $\delta_{C-X} = E_C - E_X \sim 0$, where E_C and E_X are the uncoupled cavity and exciton energies, respectively. The detected photoluminescence (PL) intensity of the upper and lower polariton brach depends quadratically on the excitation power, as shown for three different values of $\mathbf{k}_{\|}$ in Fig. s 5.1(b) and (c). This quadratic dependence confirms the two photon absorption process, and it is equivalent to the linear regime observed in the same system below threshold [194].

When the excitation energy is close to the two-photon resonance condititon, i.e

$$2 \cdot E_{Pump} = \frac{\min_{\mathbf{k}_{\|}}\{E_{UP}\} + \min_{\mathbf{k}_{\|}}\{E_{LP}\}}{2} \tag{5.2}$$

and for incident momentum $\mathbf{k}_{\|}^{pump} = \mathbf{0}$, strong emission is observed at $\mathbf{k}_{\|} = \mathbf{0}$, as shown in Fig. 5.2(a). The PL intensity dependence on excitation power is still quadratic at

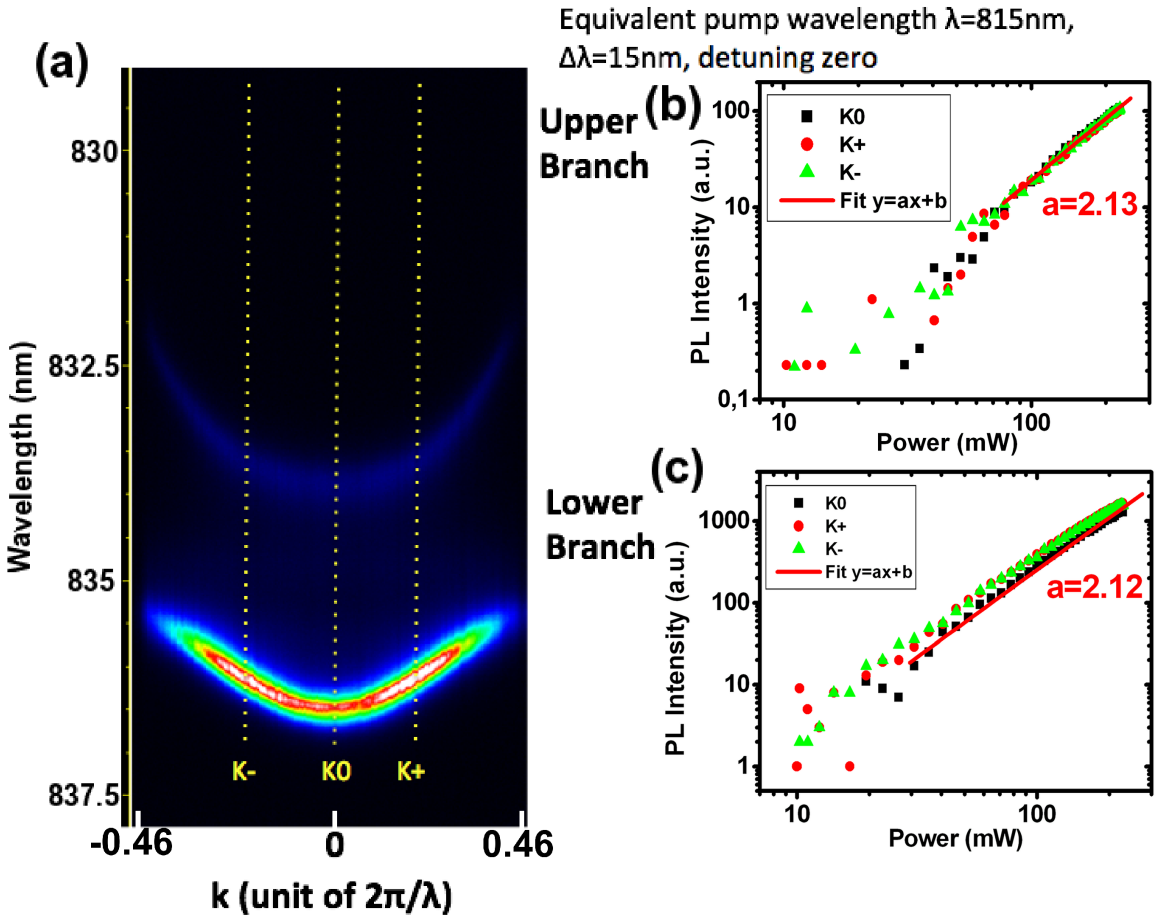

Figure 5.1: **(a)** Planar microcavity dispersion curve for femtosecond pulsed excitation at energy $2 \cdot E_{Pump} \gg \left(\min_{\mathbf{k}_\parallel}\{E_{UP}\} + \min_{\mathbf{k}_\parallel}\{E_{LP}\}\right)/2$, with $E_{pump} = 0.76eV$, which corresponds to a pump wavelength $\lambda_{pump} = 1630nm$. **(b-c)** PL intensity power dependence at points $K0$, $K-$ and $K+$ in bilogaritmic scale. Filled symbols represent measured values, while the red continuous line is a linear fit of the experimental data in bilogaritmic representation. When reported in linear scale, this fitting corresponds to the function $I = bP^a$, where I is the collected PL intensity and P the excitation power. $a \sim 2$ indicates that the PL intensity depends quadratically on the excitation power.

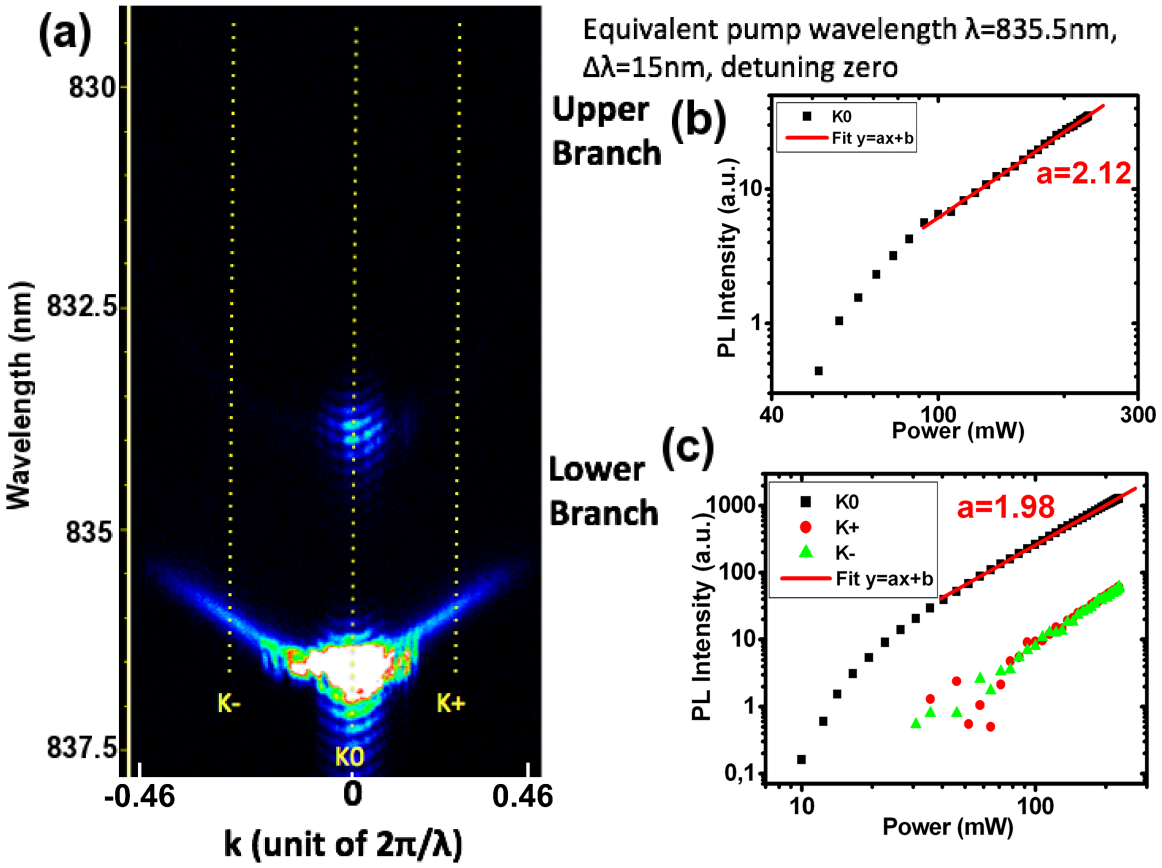

Figure 5.2: **(a)** Photoluminescence of a planar microcavity excited by femtosecond pulses at energy $2 \cdot E_{Pump} \sim \left(\min_{\mathbf{k}_\parallel}\{E_{UP}\} + \min_{\mathbf{k}_\parallel}\{E_{LP}\}\right)/2$. **(b-c)**, with $E_{pump} = 0.74eV$, which corresponds to a pump wavelength $\lambda_{pump} = 835.5nm$. PL intensity power dependence at points $K0$, $K-$ and $K+$ in bilogaritmic scale. Filled symbols represent measured values, while the red continuous line is a linear fit of the experimental data in bi-logaritmic representation. When reported in linear scale, this fitting corresponds to the function $I = bP^a$, where I is the collected PL intensity and P the excitation power. $a \sim 2$ thus means that the PL intensity depends quadratically on the excitation power.

both detection momenta $\mathbf{k}_{\parallel} = \mathbf{0}$ and $\mathbf{k}_{\parallel} \neq \mathbf{0}$ (see Fig.s 5.2(b) and (c)), and TPA thus takes place also when the condition (5.2) is fulfilled. The absence of a threshold in the PL intensity, together with the quadratic dependence on the excitation power, suggests that the bright emission at $\mathbf{k} = \mathbf{0}$ is due to a direct injection of microcavity polaritons in the emitting state.

5.2 0D polaritons in pillar microcavities

In section 5.1 we have shown that a two-photon femtosecond laser beam can be used to excite polaritons in planar microcavities. As discussed in section 2.2.2, a planar microcavity (MC) confines photons in the direction perpendicular to the Bragg reflectors and the in plane wave vector $\mathbf{k}_{\parallel}$ is not quantized. Because of that, the cavity mode extension is not suitable to induce the ultra strong polariton-polariton interactions needed for the experimental realization of the polariton quantum blockade [29], which requires a 3D confinement. With this motivation, the rest of the chapter is focused on the study of pillars MCs, which induce a three dimensional confinement of photons and that can result in strong polariton-polariton interactions [28, 202].

Several structures have been proposed so far to realize zero-dimensional polaritons, and among them of remarkable versatility and interest are photonic crystals nanocavities [187], patterned planar MCs [203] and pillar MCs [204].

Pillar microcavities are obtained by vertically etching a planar MC, thus resulting in a fully confined system that exploits the refractive index difference between the air and the materials composing the cavity in the xy plane and the cavity-induced confinement along z. Fig.5.3(a) shows a scanning electron microscope (SEM) micrograph of a pillar MC with rectangular cross section fabricated at LPN. The electromagnetic field is now confined along the three directions, as well as all the components of $\mathbf{k}$ are quantized. For a rectangular pillar of lateral sizes L_x and L_y the photon eigenstates of indexes n_x

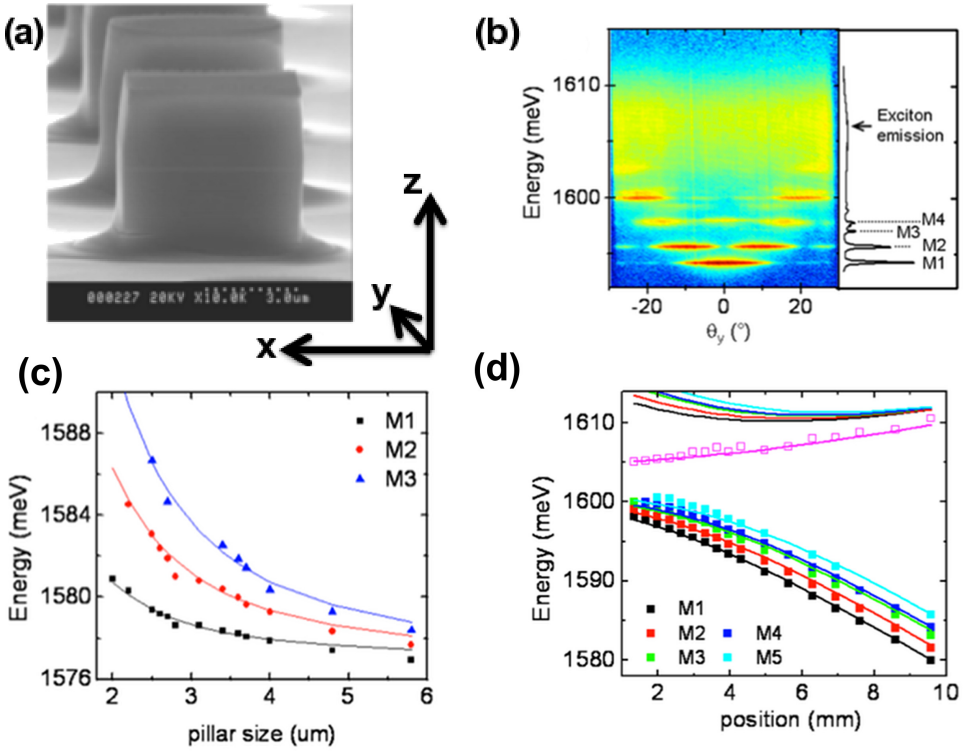

Figure 5.3: **(a)** SEM image of pillar microcavities realized at the *Laboratoire de Photonique et Nanostructure* in Marcoussis (France). **(b)** Dispersion curve of a pillar microcavity with edge sides $L_x = L_y = 3.4\mu m$ and its respective photoluminescence spectrum. θ_y is the detection angle along y. **(c)** Energies of the first three modes measured as a a function of the pillar lateral size $L_x = L_y$. **(d)** Pillars emission energies as a function of the position on the sample. If an angle is inserted between the Bragg mirrors when the planar microcavity is grown, the resonant frequency of the optical modes of the micropillars depends on the position on the sample. As a consequence, changing the position on the sample is equivalent to change the cavity-exciton detuning δ_{C_i-X}. Filled symbols are measured values, continuous lines are computed theoretical curves. Opens symbols represent exciton energy. [Images reproduced from ref. [33]]

and n_y are given by the following relation:

$$E_c^{n_x n_y} = \sqrt{(E_c^0)^2 + \left(\frac{\hbar c}{n_{cav}}\right)^2 \left[\left(\frac{\pi(n_x+1)}{L_x}\right)^2 + \left(\frac{\pi(n_y+1)}{L_y}\right)^2\right]}, \tag{5.3}$$

where E_c^0 depends on the confinement along z. The etching does not affect the exciton behavior, which remains unconfined in the xy plane, because the pillar size is larger than the exciton Bohr radius. In this picture the quantum well excitons are thus coupled to several optical modes, and, when the strong coupling condition is achieved, discretized polaritons branches appear, as shown by the dispersion curve reported in Fig. 5.3(b) for a micropillar with lateral sizes $L_x = L_y = 3.4\mu m$. As analytically described by eq.(5.3) and shown in Fig. 5.3(c), the resonant energies are inversely proportional to the pillar size and the same behavior is valid for the volume of the confined optical modes. Typical anticrossing behavior for each confined mode is usually observed, as reported in Fig. 5.3(d), thus confirming the strong coupling of each mode with quantum well excitons [28]. The cavity-exciton detuning should thus be defined for each optical mode and it becomes $\delta_{C_i-X} = E_{C_i} - E_X$, where E_{C_i} and E_X are the energy of the uncoupled i-th photonic mode and of the exciton, respectively. It is important to point out that for strong negative cavity-exciton detuning ($\delta_{C_i-X} << 0 \quad \forall i$) the upper-branch levels are extremely close to each other and usually result in a single luminescent line in the PL spectrum; this happens, for instance, for all the positions between $8mm$ and $10mm$ in Fig. 5.3(d). The specular situation takes place for strong positive detuning ($\delta_{C_i-X} >> 0 \quad \forall i$) and the levels are degenerate in the lower polariton branch.

5.3 Two-photon excitation of a pillar microcavity

The strong confinement achievable in pillars microcavities makes them promising structures for the experimental realization of the polariton quantum blockade. This section is devoted to demonstrate that polaritons can be efficiently injected in pillar microcavities by means of a TPA technique. Using the same pump beam described in section

5.1, we first show that TPA is able to excite polaritons in micropillars. Interestingly, we observed that a coherent two-photon injection can result in a macroscopic occupation of the level at the lowest energy together with emission properties similar to the one of polariton laser [28]. Next, in order to make the pulsed TPA useful for polariton quantum blockade, we describe a technique suitable for the selective excitation of a single resonant state without introducing any noise in the detection system.

5.3.1 The sample

Pillar microcavities were realized at the *Laboratoire de Photonique et Nanostructure* in Marcoussis (France) and have been obtained by etching a planar microcavity fabricated by Molecular Beam Epitaxy (MBE). The bottom Bragg mirror, composed by 30 pairs of $Ga_{0.9}Al_{0.1}As/Ga_{0.05}Al_{0.95}As$ thick $604\mathring{A}$ and $703\mathring{A}$, respectively, was grown on an undoped $GaAs$ substrate, while 26 pairs were realized for the top Bragg mirror. A single $InGaAs$ quantum well (thickness $80\mathring{A}$) and two $GaAs$ barriers thick $1.147nm$ were embedded between the two mirrors in order to obtain the final MC. With the goal to tune the cavity resonance with the exciton energy, a small angle was imposed between the two Bragg mirrors, making the energy of the resonant cavity mode dependent on the position on the sample. The microcavity PL intensity as a function of the position on the sample, reported in Fig.s 5.4(a) and (b), shows the typical anticrossing behavior, with a vacuum Rabi splitting of $\hbar\Omega_{VRS} \sim 3meV$.

In order to obtain 0D polaritons excitable by two-photon laser pulses at energies in the interval $E_{Pump} = 0.729eV \div 0.785eV$ (i.e. $\lambda_{Pump} = 1580nm \div 1700nm$), the micropillars were realized starting from a microcavity coupled with a bare exciton at energy $E_X \sim 1.477eV$ (i.e. $\lambda_X \sim 839nm$). After an electron beam lithography process, the microcavity was etched along the z direction following the mask displayed in Fig. 5.5, thus obtaining micropillars with a circular cross section and diameter ranging from $0.5\mu m$ and $5\mu m$.

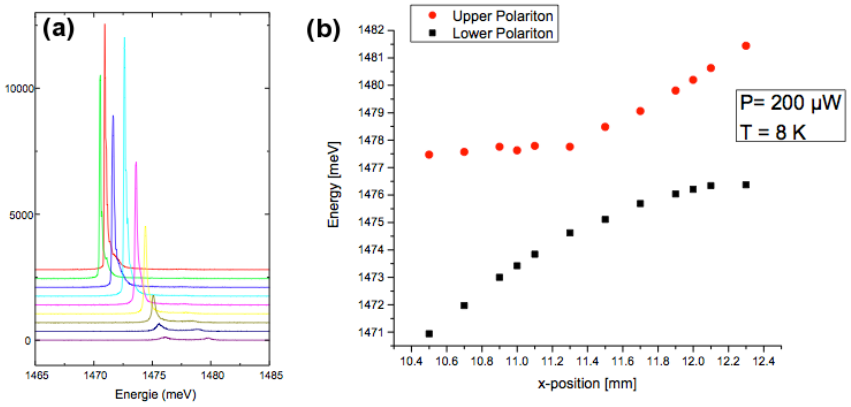

Figure 5.4: **(a)** Spectral-resolved photoluminescence of the microcavity for several positions on the sample, before the etching of the micropillars. **(b)** Energies of the polariton states as a function of the position on the sample. As described in the text, a small angle was imposed between the two Bragg reflectors in order to make the resonant energy of the cavity mode depending on the position on the sample. [These measurements were performed in the *Laboratoire de Photonique et Nanostructure* in Marcoussis (France) by using a standard out of resonance excitation technique.]

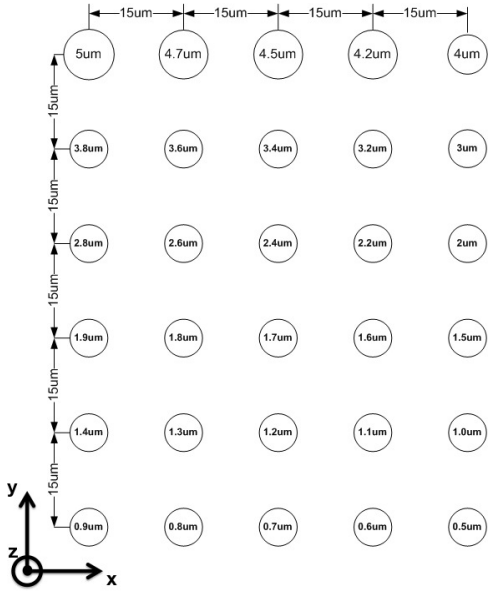

Figure 5.5: Mask used to etch the planar MC in order to obtain micropillars. Circles represent pillars cross section, the diameter is indicated inside.

5.3.2 Two photon injection of polariton laser in a pillar microcavity

A typical dispersion curve of a micropillar of diameter $D \sim 5\mu m$ excited with two-photon femtosecond pulses at energy $2 \cdot E_{Pump} \gg \left(\min_{\mathbf{k}_\parallel}\{E_{UP}\} + \min_{\mathbf{k}_\parallel}\{E_{LP}\}\right)/2$ is shown in Fig. 5.6. One can see a number of polariton states and that both energy and in-plane wavevector are quantized. Furthermore, we observe that the state at lowest energy is localized at of $\mathbf{k}_\parallel = \mathbf{0}$.

As already mentioned in the case of planar microcavities, when the pump laser fulfills the two-photon resonance condition with the lower polariton branch (i.e. $E_{Pump} = \min_{\mathbf{k}_\parallel}\{E_{LP}\}/2$), polaritons are injected coherently conserving the pumping momentum $\mathbf{k}_\parallel^{Pump}$. Let us assume that the two-photon resonant condition with the i-th state is fulfilled if $E_{pump} = E_i/2$, where E_i is the energy of the i-th polariton level.

Figure 5.7(a) reports a typical photoluminescence (PL) spectrum obtained when the two-photon resonance condition with the lowest energy polariton state at energy E_1 is fulfilled. The dependence of the PL intensity of this level as a function of the excitation power, reported in Fig.5.7(b), clearly shows the presence of a threshold (named h_1) in the emission intensity. When D decreases, h_1 moves towards lower excitation powers and a second threshold (h_2) appears for $D \leq 3\mu m$ (see red and green squares in Fig. 5.7(b)). Below h_1, the PL depends quadratically on excitation power, as shown by the fitting reported in Fig. 5.7(c), demonstrating the two-photon nature of the absorption process. Across h_1, a significant blueshift has been observed (filled circles in Fig. 5.7(d)), together with a linewidth narrowing in correspondence of h_1 ($\Delta_{h_1} = 219\mu eV - 169\mu eV = 50\mu eV$, as shown in Fig. 5.7(e)). This let us suggest that above h_1 the system enters in a different emission regime and the PL intensity grows linearly as a function of the pump power, up to a plateau for both intensity and emission energy shift just before the second threshold h_2. For excitation powers higher than $\sim 1.5 \cdot h_1$, the strong coupling is therefore lost. Moreover, both h_1 and h_2 decrease by scaling down the pillar diameter (Fig. 5.7(f)).

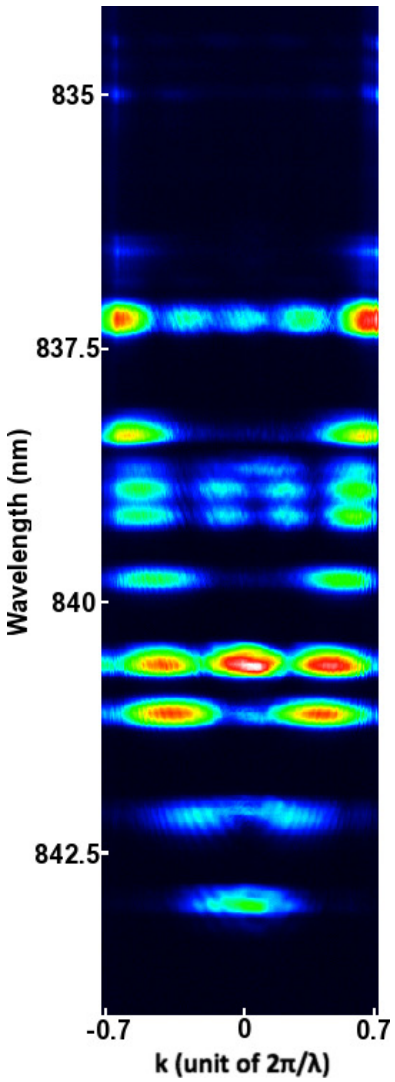

Figure 5.6: Low polariton branch dispersion curve photoluminescence from a micropillar of diameter $d = 5\mu m$ pumped at energy $2 \cdot E_{Pump} \gg \left(\min_{\mathbf{k}_\parallel}\{E_{UP}\} + \min_{\mathbf{k}_\parallel}\{E_{LP}\}\right)/2$, with $E_{pump} = 0.76eV$, which mens a pump wavelength of $\lambda_{pump} = 1630nm$.

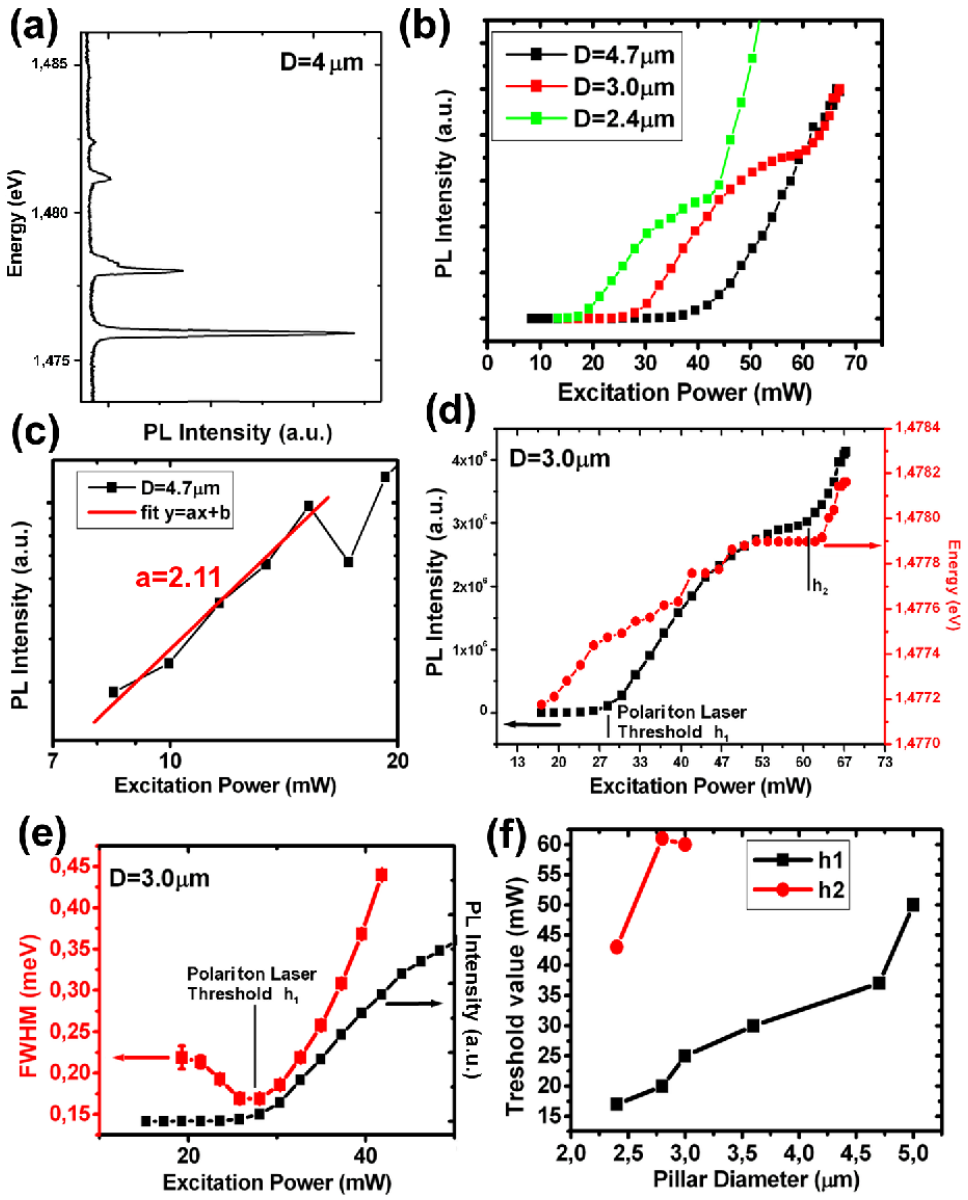

Figure 5.7: **(a)** PL spectrum of a two photon-excited micropillar of diameter $d = 4\mu m$. **(b)** Dependence of the lowest energy state PL intensity as a function of the excitation power for micropillar of diameters $d = 4.7\mu m$,$d = 3\mu m$ and $d = 2.4\mu m$. **(c)** Zoom of (b) for low excitation powers in bilogaritmic scale. Red continuous line is a linear fit of the experimental data. **(d)** Dependence of the lowest energy state PL intensity (black squares) and its energy (red circles) as a function of the excitation power for a micropillars of diameter $d = 3\mu m$. **(e)** Full width at the half maximum of the lowest energy state has a function of excitation power intensity for a micropillar of diameter $d = 3\mu m$. **(e)** Evolution of the tresholds h_1 and h_2 as a function of the pillar diameter.

These results, i.e. the presence of two thresholds, the spectral narrowing and the significant blue shift of the emission, seem to be in reasonable agreement with the ones presented in ref. [28] in the case of out-of-resonant pumping of a similar system. Indeed, in 2008 D. Bajoni and collaborators [28] showed that, by increasing the polariton density in a zero-dimensional system pumped out-of-resonance, a coherent emission from the lowest energy state of the lower branch is observed, characterized also by blue shift and strong spectral narrowing (of about $\Delta \sim 90\mu eV$). This emission, obtained without loss of the strong coupling regime, constitutes the so called *polariton laser*.

In agreement with ref. [28], in standard out-of-resonance excitation, the polariton laser regime is not induced by stimulated emission of radiation, as for photon laser, but it comes from a stimulated scattering of polaritons in the lowest energy state. Indeed the out-of-resonance excitation populates directly the excitonic reservoir, thus resulting in the coexistence of polaritons and bare excitons in the system. When the injected exciton density exceeds a saturation value the strong coupling breaks down and the normal modes of the system become the QW exciton and the cavity mode. If the injection density is further increased the electronic population inversion can be achieved and photon laser can take place. In order to move the transition between strong and weak coupling toward higher injection densities, microcavities for polariton laser usually implement several QWs in the maxima of the localized electric field. This decreases the number of excitons per QW [28, 193], thus allowing to obtain polariton laser before the transition to the weak coupling regime [193]. By exciting the system with TPA it is possible to inject directly the polaritons without the need to populate the excitonic reservoir. Polaritons are created directly in the final state and no stimulated scattering is required. A macroscopic occupation of the polariton state resonant with both excitation energy and wavevector is thus obtained, together with a low density of bare excitons in the system. In our system the saturation is reached at excitation powers $P_{excitation} > 1.5 \cdot h_1$, as represented by the plateau in the PL intensity just below h_2, shown in Fig.5.7(d). The TPA thus strongly reduces the number of bare excitons

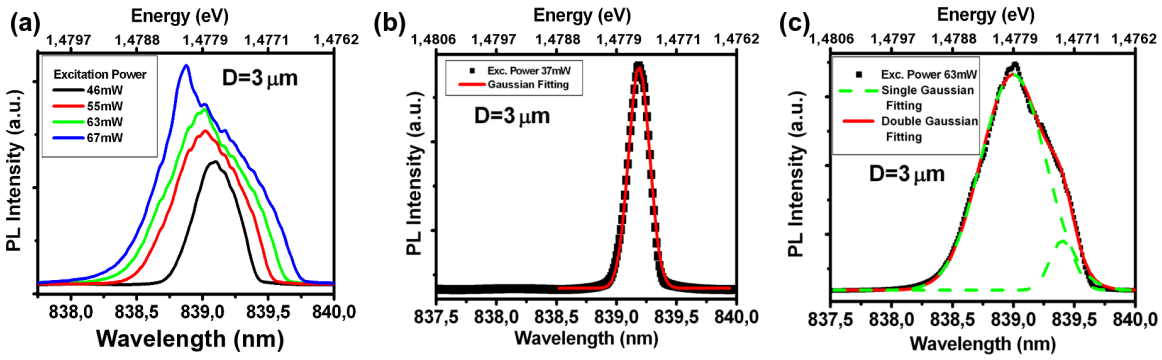

Figure 5.8: **(a)** PL spectra of the lowest energy state of micropillar of diameter $D \sim 3\mu m$ for several excitation powers above the threshold h_1. **(b)** PL spectrum for $D = 3\mu m$ in the two photon polariton laser regime well below the saturation plateau (excitation power about $1.3 \cdot h_1$). Red line is a Gaussian fitting of the experimetal data, represented by black filled squares. **(c)** PL spectrum for $D = 3\mu m$ and excitation power of about $\sim 1.1 \cdot h_2$. Dashed green lines are single Gaussians functions and the red continuous trace is their sum. Black filled squares are the experimental points.

in the system making possible to obtain polariton laser also by using a single quantum well.

It is also important to point out that for excitation powers near to h_1 the PL peak is well fitted by a single gaussian function, while when the excitation power exceeds the value $P_{excitation} \sim 2 \cdot h_1$, a second Gaussian function is needed to fit the experimental data. This behavior is the result of the conbined effect of the pulsed excitation and the time integrated detection. Due to the pulsed excitation laser, the density of the injected polaritons is not constant follows the pulse time shape. Moreover, the detection system used in the experiment has an acquisition time several orders of magnitude longer than the femtosecond temporal width of the two-photon pulse. As a consequence, when $P_{excitation} > 2 \cdot h_1$, within the same laser pulse for certain times the system is in the polariton laser regime, while in other time intervals the system is in weak coupling. As the two phenomena are characterized by resonant peaks at two different wavelengths, the resulting effect is a mixture of strong and week coupling. The need of a second

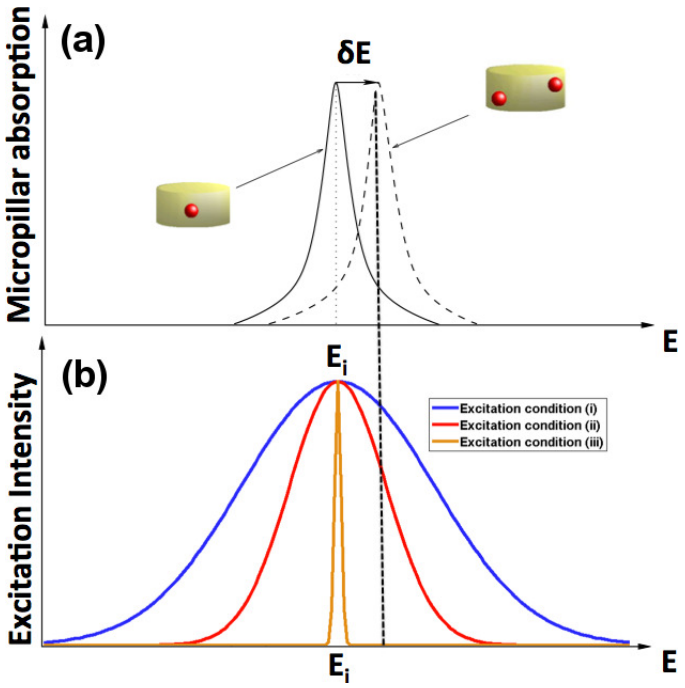

Figure 5.9: Working principle of the polariton quantum blockade: if the excitation laser is narrow enough, a second polariton cannot be injected in the system: otherwise the shifted absorption peak falls in the excitation laser spectrum and the second polariton can be injected (see table 5.1 for definition of excitation conditions (i), (ii) and (iii)).

Gaussian function to fit the PL signal can be interpreted as the coexistence of two peaks at energies nearer than their FWHM. This is confirmed by the PL spectra below and above h_1 reported in Fig.s 5.8 (b) and (c), respectively: when the micropillar is excited at powers near h_2, two peaks are evident, one at higher energy (the one in weak coupling) and one at lower energy (in strong coupling with the excitons).

5.3.3 Picosecond excitation and relaxation mechanisms

As already mentioned, the femtosecond two-photon pulse has a large spectral width, that so far has been exploited to excite a whole polariton branch or both polariton branches at the same time.

The polariton quantum blockade (PQB) is based on the resonant shift due to a two-

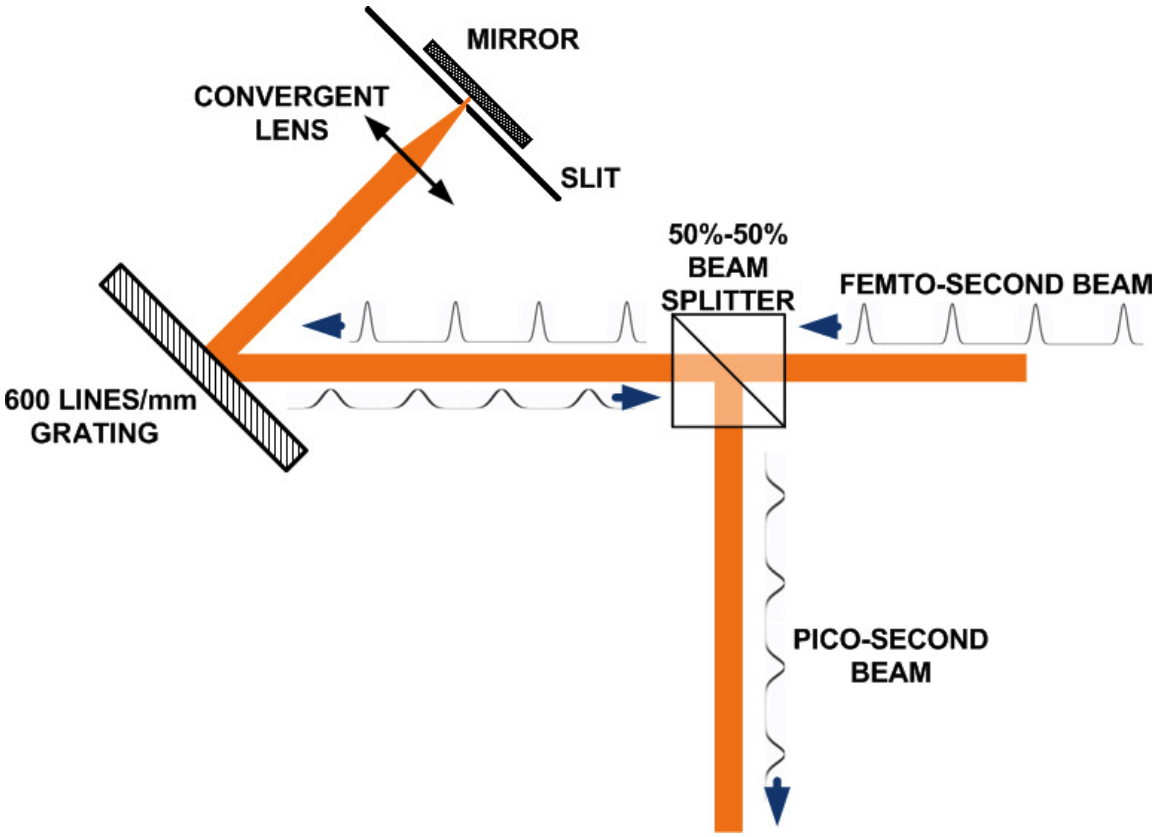

Figure 5.10: Optical setup used to modify the time-behavior of the two-photon femtosecond pulses. The femtosecond beam is dispersed by 600 lines/mm grating blazed at 1600nm and then focused on a mirror. In image focal plane of the focusing lens a system of two slits has been inserted in order to perform a spectral selection. The beam was then sent back along the same optical path and re-addressed toward the sample by a 50%-50% beam splitter. When this optical circuit is skipped, standard two-photon femtosecond pulses are used to excite the micropillars (see line (i) of table 5.1 for spectral and temporal parameters), otherwise two operation methods are possible. One consists in leaving open the slit, thus obtaining a picosecond pulsed laser without spectral selection and linewidth of $\sim 15nm$ [line (ii) of table 5.1]. The second consists in performing a spectral selection with the slit, thus obtaining a FWHM as narrow as $\sim 1nm$ (see table 5.1, line (iii)).

particle interaction, as schematically reproduced in Fig. 5.9: the resonant injection of a second polariton in the system can be blocked by the presence of another polariton, because the polariton-polariton repulsion shifts the resonant energy by an amount larger than the excitation linewidth. However, in the case of the femtosecond two-photon beam, the FWHM of the pumping laser is almost one order of magnitude larger than the single level width. As a consequence, despite to the resonance shift of the resonant energy due the two-particle interaction (δE), the new absorption peak falls well inside the excitation beam spectrum, the PQB cannot be observed because a second polariton can be injected in the system.

In order to reduce the FWHM of the laser beam, the temporal shape of the pulse has been modified through the optical path displayed in Fig. 5.10. The femtosecond two-photon beam was dispersed by a 600 line/mm grating blazed at 1600nm and the first diffraction order was focused on a mirror through a convergent lens. A slit was introduced in the focal image plane of the lens in order to perform a spectral selection of the dispersed beam. The reflection from the mirror was sent back along the incoming path and the resulting outcoming picosecond pulsed beam was redirected by using a 50%-50% beam splitter. Our setup therefore allows for three excitation modes:

(i) standard two-photon femtosecond pulses can be used to excite the sample by skipping the path reported in Fig. 5.10,

(ii) if the slit does not perform any spectral selection, two-photon picosecond pulses with $FWHM \sim 15nm$ can be used to excite the micropillars,

(iii) if a spectral selection is performed by mean of the slit, the excitation laser FWHM can be narrowed down to $\sim 1nm$.

The pulse duration and laser linewidth obtained with the three methods are summarized in table 5.1.

Next sections are devoted to demonstrate that the spectral selection (i.e. method (iii)) allows to excite a single level in a pillar microcavity. In order to do that, a

		FWHM	Pulse duration	
(i)	femtosecond	$\sim 30nm$	$\sim 150fs$	no reshaping
(ii)	picosecond	$\sim 15nm$	$\sim 2ps$	slit open
(iii)	picosecond with spectral selection	$< 1nm$	$\sim 3ps$	slit closed

Table 5.1: Summary of the different excitation techniques and the spectral and temporal parameters experimentally obtained.

micropillar of diameter $D = 3.4\mu m$ has been studied for three different cavity-exciton detuning δ_{C_i-X}. For each value of δ_{C_i-X} under investigation the experiment proceeds as follows:

1. in order to confirm the two-photon nature of the absorption process also in the case of picosecond excitation pulses, both upper and lower polariton branches are excited at the same time by using a broadband picosecond beam ($FWHM \sim 15nm$, see method (ii) defined in table 5.1),

2. the laser line is then narrowed and single polariton states in the lower and upper branch are excited one by one (method (iii)). Possible relaxations or scattering of polaritons toward other states are also probed.

As a support for the following discussion, in each photoluminescence spectrum reported in this paragraph, the levels in the upper polariton branch are superposed to a light blue background.

5.3.3.1 Negative cavity-exciton detuning

A typical PL spectrum collected from a pillar of diameter $D = 3.4\mu m$ at negative detuning and excited in two-photon resonance by picosecond broad spectrum pulses is reported in Fig. 5.11(a). The linewidth of the excitation laser beam results to be around $\Delta E_{pump} \sim 15nm$, thus still able to excite both upper and lower polariton

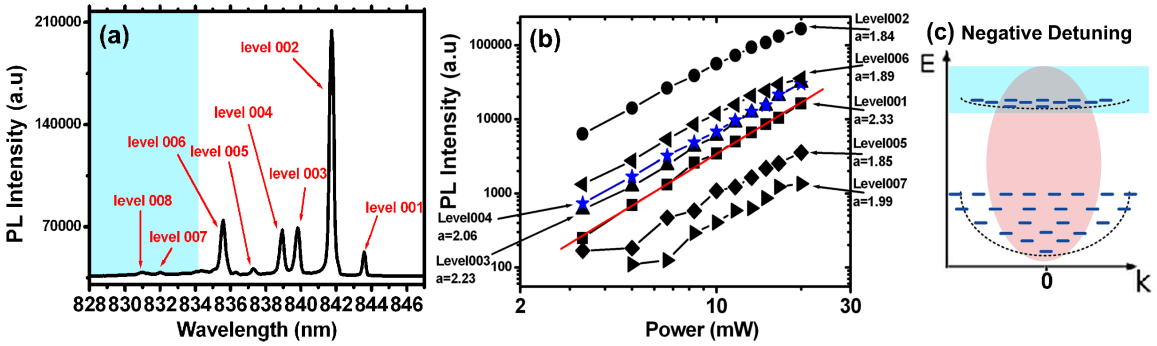

Figure 5.11: **(a)** PL spectrum of a micropillar of diameter $D = 3.4\mu m$ at negative detuning, excited with a picosecond pulse with FWHM of $\sim 15nm$. The light blue area identifies levels in the upper polariton branch. **(b)** Excitation power dependence for the spectrum reported in (a) in bi-logaritmic scale. Continuous red line represents a linear fit of slope a. **(c)** Schematic representation of the experimental conditions used to obtain (a) and (b). Light blue background identifies levels in the upper polariton branch, while the pink area identifies the energy and wavevector intervals covered by the pumping pulse. Because of the spectral with of the laser beam, both upper and lower polariton branches are excited, while the in-plane wavevector extension of the laser beam is given by the numerical aperture of the objective used to excite the sample ($N.A. \approx 0.7$).

branches at the same time. Few luminescent levels are found in the upper polariton branch (see light blue area in Fig. 5.11(a)) due to the negative detuning. Indeed, as already mentioned when Fig. 5.3(d) was discussed, at $\delta_{C_i-X} << 0$ levels in upper polariton branch are close to the exciton emission and are very close to each other, thus resulting in few luminescent peaks (see also the sketch reported in Fig. 5.11(c)). As shown by Fig. 5.11(b), the log-log excitation power dependence of the PL intensity of each level is fitted by a straight line of slope $a \sim 2$, thus confirming the quadratic behavior already verified below threshold for the femtosecond excitation.

When the FWHM of the excitation laser is narrowed down to $\Delta E_{pump} < 1nm$ (method (iii) reported in tab.5.1), it become comparable to the FWHM of PL peaks and significantly smaller than the spectral separation between the levels. With this technique it is thus possible to fulfill the two-photon resonant condition only for a single polariton level, i.e. $E_{pump} = E_i/2$. Figure 5.12 reports some PL spectra collected

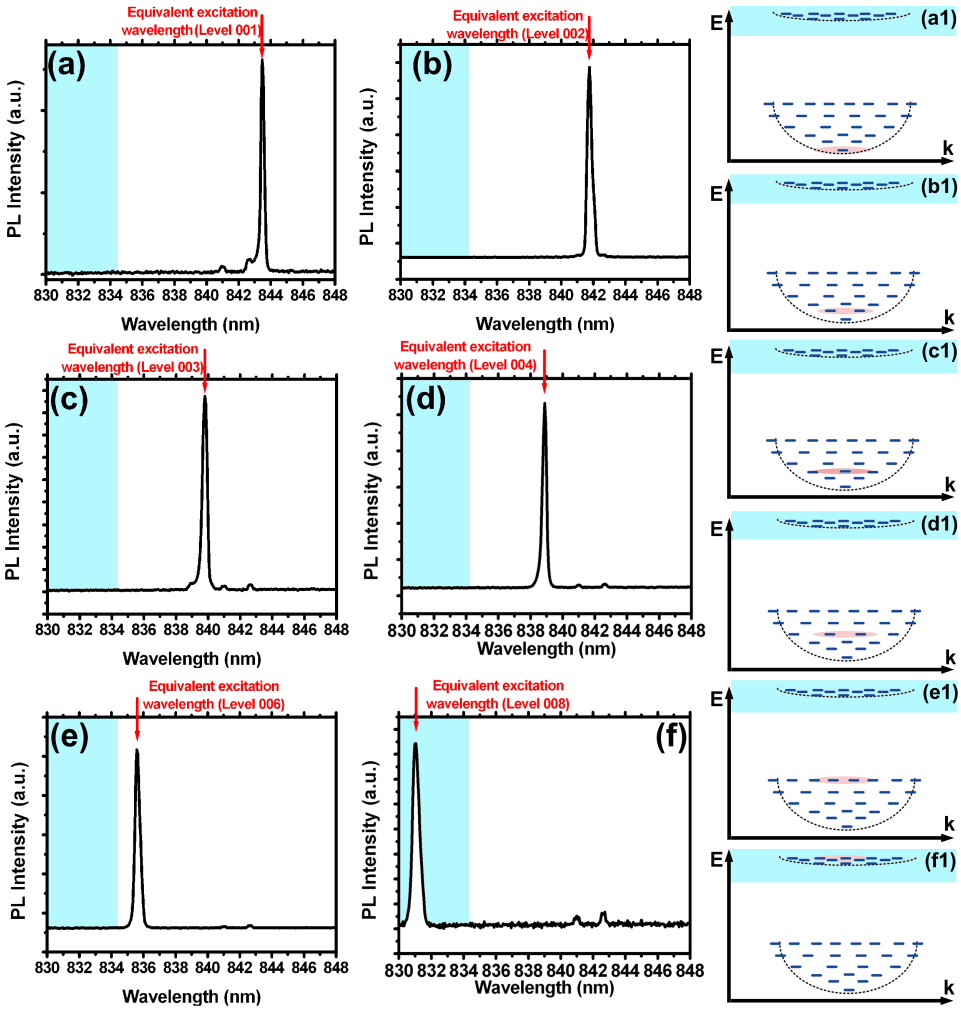

Figure 5.12: **(a)-(f)** PL spectra when single levels of a negative-detuned micropillar of diameter $D = 3.4\mu m$ are excited. The light blue area identifies the upper polariton branch. In all measurements no polariton relaxation or polariton scattering is observed. The two small peaks present in each graph come from environmental noise and are present also when the sample is not excited. **(a1)-(f1)** Schematic representation of the experimental conditions used to obtain (a)-(f), respectively. Light blue background covers the upper polariton branch, while the pink area identifies the energy and wavevector intervals covered by the pumping pulse. The laser FWHM has been narrowed by means of the slit and it is smaller than the energy separation between two levels, allowing to excite a single level. The in-plane wavevector extension of the laser beam is given by the numerical aperture of the objective used to excite the sample ($N.A. \approx 0.7$).

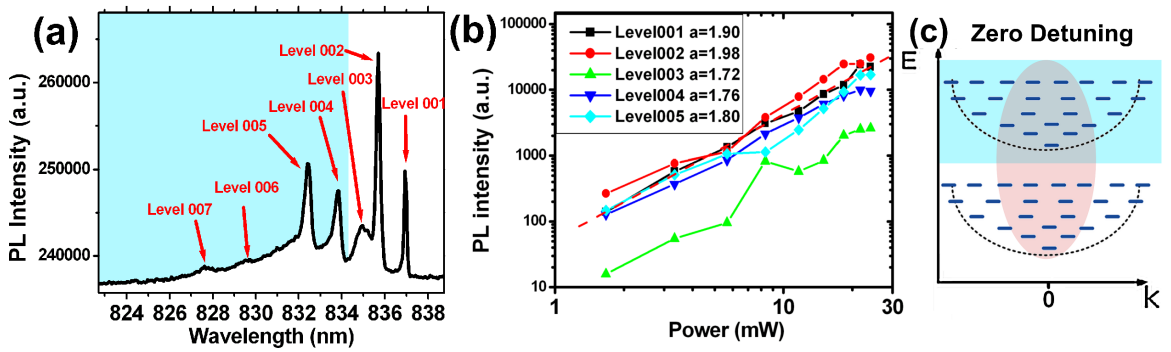

Figure 5.13: **(a)** PL spectrum of a picosecond two-photon excited micropillar of diameter $D = 3.4\mu m$ almost at zero detuning, excited with a picosecond pulse with FWHM of $\sim 15nm$. The light blue area identifies levels in the upper polariton branch. **(b)** Bi-logaritmic excitation power dependence for the spectrum reported in (a) and linear fit of slope a (red dashed line). **(c)** Schematic representation of the experimental conditions used to obtain (a) and (b). Light blue background identifies levels in the upper polariton branch, while the pink area identifies the energy and wavevector intervals covered by the pumping pulse. Because of the spectral with of the laser beam, both upper and lower polariton branches are excited, while the in-plane wavevector extension of the laser beam is given by the numerical aperture of the objective used to excite the sample ($N.A. \approx 0.7$).

exciting at two-photon resonance a single level of a micropillar of diameter $D = 3.4\mu m$ at $\delta_{X-C_i} < 0$. For resonant states in both upper and lower polariton branches (levels from 001 to 006 are in the lower branch, while levels 007 and 008 are in the upper branch) only the photoluminescence from the excited level is collected. These measurements seem to indicate that the injected polaritons are not allowed to relax or scatter in any other state.

5.3.3.2 Zero cavity-exciton detuning

Figure 5.13 displays the PL emission spectra of a pillar MC of diameter $D = 3.4\mu m$ at almost zero cavity-exciton detuning and the PL intensity of each level as a function of the excitation power for a picosecond laser beam of $FWHM \sim 15nm$ [excitation technique (ii) reported in tab.5.1]. Although such dependence remains almost quadratic as shown in Fig. 5.13(b), the relaxation behavior, probed by a narrowed picosecond

laser line, is different if compared to the case of negative detuning, as discussed below.

Figure 5.14 shows the PL spectra when a single level of the micropillar is excited with a picosecond-pulsed laser beam with $FWHM \sim 1nm$ [method (iii) in tab.5.1]. If the excited level is in the lower polariton branch (i.e. levels 001, 002 and 003) only the photoluminesce of that level is collected, as shown by Fig.s 5.14(a) and (b). On the contrary, when a level on the upper polariton branch is excited (levels from 004 to 007 are in the upper branch) also all the states in the lower polariton branch are allowed to emit (see Fig.s 5.14(c-f)). This relaxation dynamic could be assigned to two different processes: (i) an interaction with phonons that leads to a population of the excitonic reservoir, thus allowing a subsequent polariton relaxation in lower branch, and (ii) direct relaxations conserving the excitation momentum . However this second process is forbidden, since an optical dipole operator cannot directly couple the polariton states formed by the same exciton state [205].

These measurements thus suggest that in the system under investigation polariton relaxation is forbidden inside the same polariton branch, but it is allowed between upper and lower branch due to interactions with the phonon bath that indirectly populates the lower polariton branch.

5.3.3.3 Positive cavity-exciton detuning

The possibility to have polariton relaxation between the two branches is confirmed also by the experiments at positive detuning. The PL spectrum when a positive detuned micropillar of diameter $D = 3.4\mu m$ is excited by a picosecond laser pulse of spectral width $\Delta E_{pump} \sim 15nm$ is shown in Fig. 5.15(a), and its dependence on excitation power is displayed Fig. 5.15(b). In this situation all the levels of the lower polariton branch are close to the uncoupled exciton line, as sketched in Fig. 5.15(c) and deducible from Fig. 5.3(d), and they result on a single PL peak (i.e. the level 001). By exciting only this luminescent peak by the spectrally narrowed picosecond-pulsed beam, only its emission is detected (Fig. 5.16(a)), while exciting one of the levels in the upper

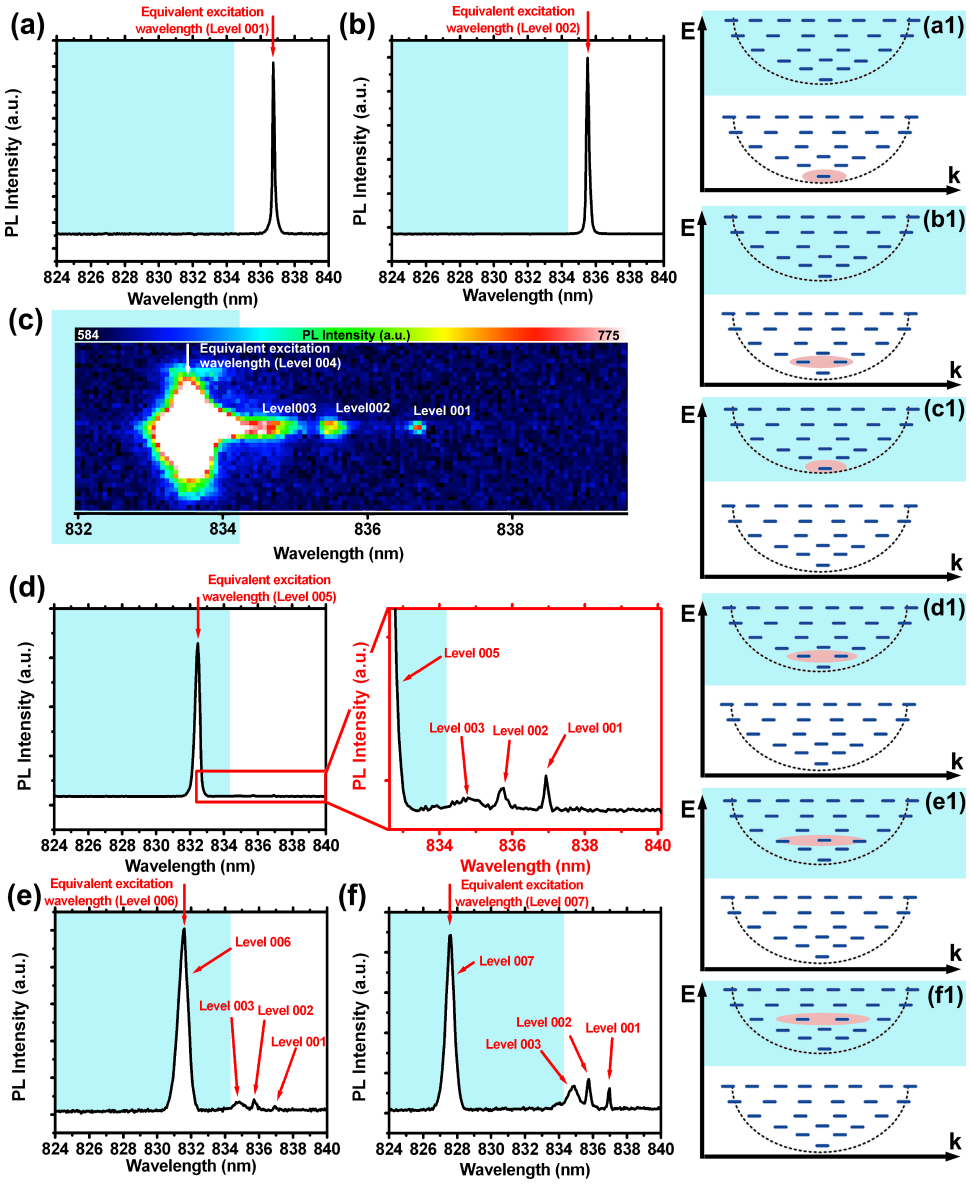

Figure 5.14: PL spectra when single levels of a micropillar at $\delta_{C_i-X} \sim 0$ are excited (pillar diameter $D = 3.4\mu m$). Light blue area indicates the upper polariton branch. When levels in the lower polariton branch are excited only the excited level luminescence is collected [**(a)** and **(b)**], while for excited levels in upper polariton branch the lower polariton branch emits [**(c)**, **(d)**, **(e)** and **(f)**]. The excited level is indicated above each graph. In (c) the rough experimental data are reported: color scale indicates the PL intensity, the horizontal axis the detection wavelength and the vertical axis is the real space on the sample. Emission intensity from level 004 has been saturated in order to make the photoluminescence coming from levels 001, 002 and 003 visible. In (d) also a zoom of the lower polariton branch is reported. **(a1)**-**(f1)** Schematic representation of the experimental conditions used to obtain (a)-(f), respectively. Light blue background covers the upper polariton branch, while the pink area identifies the energy and wavevector intervals covered by the pumping pulse. The laser FWHM has been narrowed by means of the slit and it is smaller than the energy separation between two levels, allowing to excite a single level. The in-plane wavevector extension of the laser beam is given by the numerical aperture of the objective used to excite the sample ($N.A. \approx 0.7$).

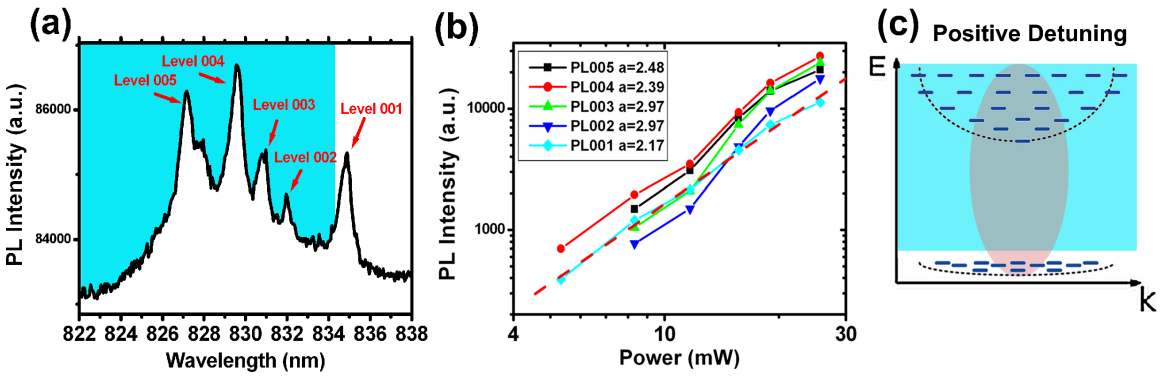

Figure 5.15: **(a)** PL spectrum of a picosecond two-photon excited micropillar of diameter $D = 3.4\mu m$, excited with a picosecond pulse with FWHM of $\sim 15nm$. The light blue area identifies levels in the upper polariton branch. **(b)** Photoluminescence intensity of the resonant states reported in (a) as a function of the excitation power. Red dashed line is a linear fit of slop a. **(c)** Schematic representation of the experimental conditions used to obtain (a) and (b). Light blue background identifies levels in the upper polariton branch, while the pink area identifies the energy and wavevector intervals covered by the pumping pulse. Because of the spectral with of the laser beam, both upper and lower polariton branches are excited, while the in-plane wavevector extension of the laser beam is given by the numerical aperture of the objective used to excite the sample ($N.A. \approx 0.7$). Levels in the lower polariton branch are close one to each other and they result in a single luminescent peak.

branch (from level 002 to level 005) the luminescence from the excited level is collected together with an emission of level 001 (Fig.s 5.16(b-d)), but no luminescence from other states in the upper branch is observed.

5.3.3.4 Discussions

The above described findings can be summarized as follows:

- for positive detuning we observe relaxations from each level of the upper polariton branch toward the degenerate levels in the lower polariton branch, but relaxation or scattering among levels in the upper branch seem to be forbidden;
- when cavity-exciton detuning is almost zero, only the relaxation from the upper branch to all the levels in lower branch is observed, while no intra-band relaxations are observed;

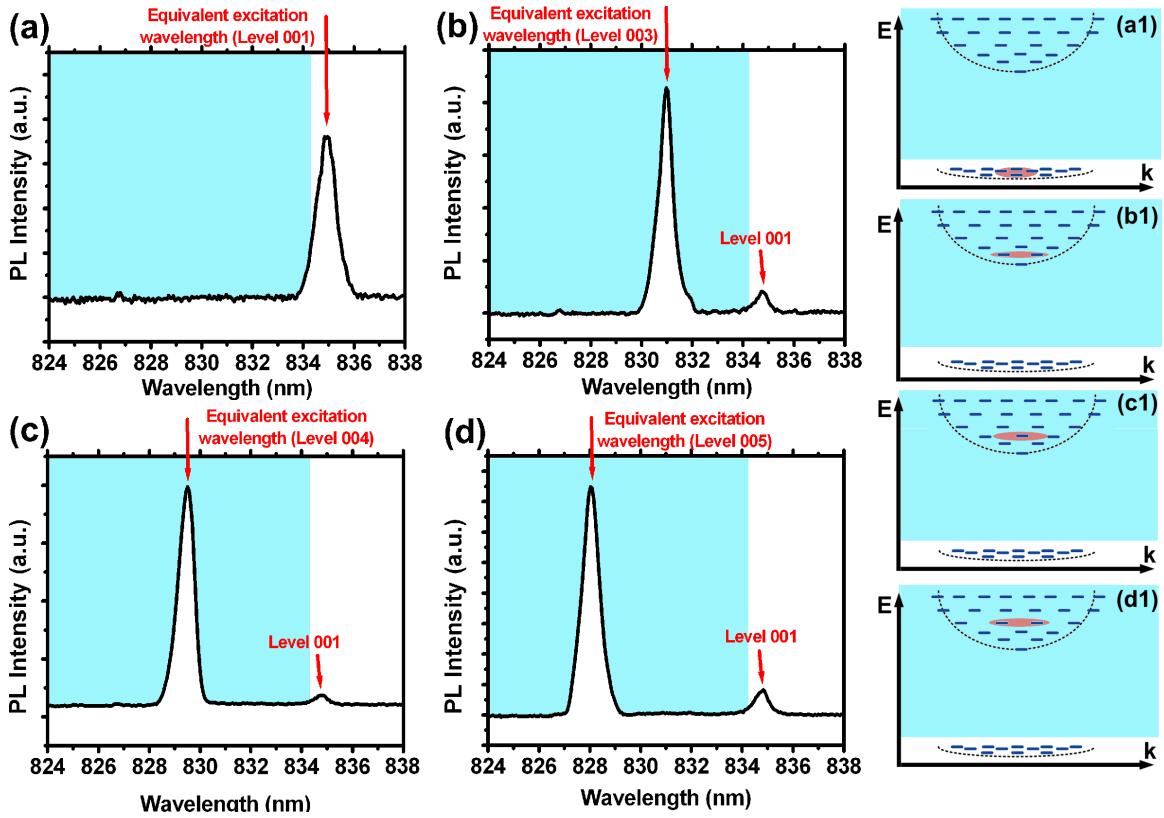

Figure 5.16: **(a)-(d)** PL spectra when single levels of a micropillar at positive detuning are excited [pillar diameter $D = 3.4\mu m$]. Light blue area indicates the upper polariton branch. The energies of the levels are now one close to each other and results in a single luminescent peak (level 001). The excited level is reported above each graph. **(a1)-(d1)** Schematic representation of the experimental conditions used to obtain (a)-(d), respectively. Light blue background covers the upper polariton branch, while the pink area identifies the energy and wavevector intervals covered by the pumping pulse. The laser FWHM has been narrowed by means of the slit and it is smaller than the energy separation between two levels, allowing to excite a single level. The in-plane wavevector extension of the laser beam is given by the numerical aperture of the objective used to excite the sample ($N.A. \approx 0.7$).

- at negative detuning, no relaxations are detected.

A reasonable explanation for the relaxation from the upper to the lower polariton branch are polaritons-phonons interactions, which allow for an indirect population of the excitonic resevoir, thus populating the whole lower branch. Although no other relaxations are observed in our system, other experimental findings in fully confined polaritons systems are in contrast with our observations [206]. For instance, Paraïso and collaborators [206] observed also intra band relaxations in both upper and lower polariton branches, which is not our case. However, literature contributions agree that relaxation behavior strongly depends on the confinement nature and efficiency.

Indeed, in past years the possibility to engineer polariton scattering toward certain levels led to interesting results, such as parametric oscillations [202, 207], spontaneous non ground state condensation [208] and enhanced thermal redistribution of polaritons injected in a well defined state [206]. However, as suggested in ref.s [202, 206, 208] these effects strongly depend on the confinement efficiency and polariton lifetime. For instance, the efficiency of the polariton-phonon interaction (that we suggested to take place in the conditions detailed in sections 5.3.3.2 and 5.3.3.3), depends on the difference between the polaritons lifetime τ_r and the polariton-phonon scattering average time τ_{ph}. The interaction with phonons is possible if $\tau_r \gtrsim \tau_{ph}$. Due to the ultra short lifetime of fully confined polaritons (of the order of tens of picoseconds [206, 208]), that moreover is not defined by only the cavity lifetime [208], time resolved analysis is an essential tool to confirm our hypothesis. Although the probing of polaritons relaxation dynamic is a suitable application for the two-photon absorption technique presented in this chapter, a full description of these phenomena needs more detailed investigations, that will be performed in next months.

Let us underline that, due to the size of the investigated micropillars, it has been not possible to observe the polariton quantum blockade. Indeed, the confinement needed to reach a sufficiently strong polariton-polariton interaction can be achieved only with very small micropillars [29]. However, the possibility to resonantly excite a single

polariton level without the introduction of noise in the detection system let us envision that the two-photon absorption technique is a viable strategy for the experimental realization of single photon sources based on polariton quantum blockade.

5.4 Conclusions and perspectives

In summary, this chapter proposes an original and flexible technique to excite microcavity polaritons with the final purpose to obtain the polariton quantum blockade. It is based on a non-linear two-photon absorption process and allows to coherently inject polaritons in a planar or pillar microcavity in resonance with the polariton branches without introducing any noise in the detection system. By virtue of the two-photon resonant conditions, that makes the majority of polaritons to be injected in the same energy state, the TPA process allows to enter in an operation regime that we called *two-photon polariton laser regime*, presenting several analogies to the standard *polariton laser* and that can be reached also in pillar microcavities coupled with a single quantum well. Moreover, by narrowing the laser spectral width, TPA is shown to be useful to excite only a single polariton level in a pillar microcavity, thus opening the way towards the experimental realization of polariton quantum blockade. Indeed, when dealing with low intensity phenomena, standard resonant excitation techniques are usually limited by the noise introduced by the pump laser reflected on the sample. A strong advantage of TPA is that it allows to resonantly pump polaritons filtering out any back reflection of the excitation laser, which is at a completely different wavelength.

Chapter 6

Conclusions

This work analyzed different aspects of fully confined systems, from the single photon generation based on single nanoparticles, to weakly and strongly coupled systems.

First, we have shown that the fine tailoring of charge carriers confinement in colloidal core/shell CdSe/CdS dot-in-rods (DRs) can be achieved by a fine control of their geometrical parameters. Indeed, by careful designing the geometrical structure of DRs, the electrons wavefunction can be strongly localized in the core or spread along the whole shell. This behavior, usually analyzed by lifetime measurements, has been monitored by means of the second order autocorrelation function $g^{(2)}(\tau)$, that is directly bound to carrier-carrier interactions and thus to carriers confinement. Moreover, our experimental results suggest that the tailoring of carriers confinement leads to the possibility to control radiative and non-radiative recombination channels in these nanoparticles. The possibility to act on wavefunctions in dot-in-rods allows one to induce several interesting features, such as polarized and dipole-like single photon emission and a blinking-free photoluminescence intensity. In our case we demonstrate a strong reduction of the photoluminescence blinking (the probability to have blinking periods longer than $50ms$ has been assessed to be as low as ~ 0.001) preserving an antibunched emission together with a total efficiency of the source of $\sim 70\%$ (i.e. $\sim 1.7 Mphotons/sec$ emitted directly by the nanoparticle excited at $2.5MHz$).

The above-mentioned properties together with the compatibility of these nanoparticles with standard nanofabrication technologies, make us envision the suitability of dot-in-rod nanostructures as sources of single photons for quantum information.

The work also discusses the possibility to realize Si_3N_4 photonic crystals nanocav-

ities for applications in the visible spectral range. These resonators, based on a two-dimensional photonic crystal realized in air suspended membranes, were explited to modify the spontaneous emission of organic and inorganic light emitters. In particular, colloidal dot-in-rods have been weakly coupled to the confined optical modes and localized in the maximum of the confined electric field in order to maximize the Purcell effect. Organic light emitters (Cyanine 3 and TRICT florescent molecules) were immobilized on top of the cavities trough surface functionalization of single DNA strains and antibodies receptors, showing the suitality of these structures for the realization of advanced and versatile building blocks for integrated photonic devices for several fields, from quantum communication to biosensing applications.

The last part of the manuscript studied a semiconductor system in which the strong coupling between a quantum well and a cavity mode gives rise to quasi-particles called *polaritons*. In particular, a two-photon excitation technique has been demonstrated to be effective to obtain an operation regime called *two-photon polariton laser*, which presents several similarities with polariton laser. Interestingly, *the two photon polariton laser* has been obtained in pillars microcavities coupled with only one quantum well. Moreover, two-photon excitation is proposed as a technique to excite systems designed with the purpose to experimentally obtain the *polariton quantum blockade*. We have show that a picosecond two-photon pulse can be used to excite a single level in a micropillar without introducing any noise in the detection system from the laser reflected on the sample. This strategy thus paves the road toward the realization of the *polariton quantum blockade* and of single photon sources based on microcavity polaritons.

Appendix A

Turbulences in quantum fluids

During this PhD thesis, I was also involved in experiments concerning the generation of polariton quantum fluids in semiconductor microcavities. This appendix includes two papers on this subject: the first one concerns the observation of a rich variety of quantum hydrodynamic effects, and in particular the observation of dark oblique solitons in a polariton superfluid.

The second one is focused in the generation of topological excitations (and in particular vortex pairs) in a quantum fluid flowing a potential barrier optically generated by using a laser beam.

REPORTS

Polariton Superfluids Reveal Quantum Hydrodynamic Solitons

A. Amo,[1,2*] S. Pigeon,[3] D. Sanvitto,[4] V. G. Sala,[1] R. Hivet,[1] I. Carusotto,[5] F. Pisanello,[1,4,6] G. Leménager,[1] R. Houdré,[7] E Giacobino,[1] C. Ciuti,[3] A. Bramati[1*]

A quantum fluid passing an obstacle behaves differently from a classical one. When the flow is slow enough, the quantum gas enters a superfluid regime, and neither whirlpools nor waves form around the obstacle. For higher flow velocities, it has been predicted that the perturbation induced by the defect gives rise to the turbulent emission of quantized vortices and to the nucleation of solitons. Using an interacting Bose gas of exciton-polaritons in a semiconductor microcavity, we report the transition from superfluidity to the hydrodynamic formation of oblique dark solitons and vortex streets in the wake of a potential barrier. The direct observation of these topological excitations provides key information on the mechanisms of superflow and shows the potential of polariton condensates for quantum turbulence studies.

Superfluidity is the remarkable property of flow without friction (*1*). It is characterized by the absence of excitations when the fluid hits a localized static obstacle at flow speeds v_{flow} below some critical velocity v_c. For small potential barriers, the critical velocity is given by the Landau criterion as the minimum of $\omega(k)/k$, with $\omega(k)$ being the dispersion of elementary excitations in the fluid. In the case of dilute Bose-Einstein condensates (BECs), v_c corresponds to c_s, the speed of sound of the quantum gas. For supersonic flows ($v_{flow} > c_s$), small obstacles induce dissipation (drag) via the emission of sound waves (*2*, *3*).

When the barrier is big, larger than the fluid's healing length—the minimum distance induced by particle interactions for changes in the density of the condensate—the density modulations caused by the barrier can generate topological excitations, such as vortices and solitons. These quantum hydrodynamic effects have been predicted to reduce the critical velocity (*4*, *5*).

Despite the amount of theoretical work (*4*–*6*), few experimental studies have addressed hydrodynamic features in atomic condensates through the observation of the break-up of superfluidity at fluid velocities lower than the speed of sound (*7*, *8*). Solitons in a quasi–one-dimensional (1D) geometry (*9*) and the nucleation of vortex pairs in an oblate BEC have been reported (*10*, *11*). Far from the hydrodynamic regime, formation of vortices and solitons has been shown by engineering the density and phase profile of the atomic condensate (*12*, *13*), or by the collision of two condensates (*14*).

Polariton superfluids appear promising in view of quantitative studies of quantum hydrodynamics. Polaritons are 2D composite bosons arising from the strong coupling between quantum well excitons and photons confined in a monolithic semiconductor microcavity. They possess an extremely small mass m_{pol} on the order of 10^{-8} that of hydrogen, which allows for their Bose-Einstein condensation at temperatures ranging from a few kelvins (*15*) up to room temperature (*16*). All parameters of the system, such as the flow velocity, density, and shape and strength of the potential barriers, can be finely tuned with the use of just one (*3*) or two (*17*) resonant lasers, and by sample (*18*) or light-induced engineering (*19*). A crucial advantage with respect to atomic condensates is the possibility of fully reconstructing both the density and the phase pattern of the polariton condensate from the properties of the emitted light (*20*). This has been exploited in the recent observations of macroscopic coherence and long-range order (*15*, *18*, *21*), quantized vortices (*20*), superfluid flow past an obstacle (*3*, *17*, *22*), and persistent superfluid currents (*23*).

Here we use a polariton condensate to reveal quantum hydrodynamic features, whereby dark solitons and vortices are generated in the wake of a potential barrier. Following a recent theoretical proposal (*24*), we investigate different regimes at different flow speeds and densities, ranging from superfluidity to the turbulent emission of trains of vortices, and the formation of pairs of oblique dark solitons of high stability. For spatially large enough barriers, soliton quadruplets are also observed.

Our experiments are performed in an InGaAs-GaAs-AlGaAs microcavity at 10 K (*25*). We excite the system with a continuous-wave (cw) single-mode laser quasi-resonant with the lower polariton branch at an angle of incidence θ, resulting in the injection of a polariton fluid with a well-defined in-plane wave vector (*3*) ($k = k_0 \sin\theta$, where k_0 is the wave vector of the excitation laser field) and velocity $v_{flow} = k\hbar/m_{pol}$. The speed of sound of the fluid c_s is related to the polariton density $|\psi|^2$ via the relation (*22*) $c_s = \sqrt{\hbar g|\psi|^2/m_{pol}}$, where g is the polariton-polariton interaction constant.

Figure 1A shows the image of a polariton fluid with $k = 0.73\ \mu m^{-1}$ and $v_{flow} = 1.7\ \mu m/ps$, created with a Gaussian excitation spot 30 μm in diameter. The resonant pump is centered slightly upstream from a photonic defect of 4.5 μm present in the microcavity, in order not to lock the phase of the flowing condensate past the defect. Two oblique dark solitons with a width of 3 to 5 μm (Fig. 1B) are spontaneously generated in the wake of the barrier created by the defect and propagate within the polariton fluid in a straight line.

An unambiguous characteristic of solitons in BECs is the phase jump across the soliton (*12*, *13*, *26*). To reveal the phase variations in the polariton quantum fluid, we make the emission from the condensate interfere with a reference beam of homogeneous phase, with a given angle between the two beams (*20*). The result (Fig. 1C) shows a phase jump of up to π (half an interference period) as a discontinuity in the interference maxima along the soliton.

The 1D soliton relationships obtained from the solution of the Gross-Pitaevskii equation (*13*, *26*) can be extended to two dimensions to relate the soliton velocity v_s in the reference frame of the fluid, the phase jump δ, and depth n_s with respect to the polariton density n away from the soliton:

$$\cos\left(\frac{\delta}{2}\right) = \left(1 - \frac{n_s}{n}\right)^{1/2} = \frac{v_s}{c_s} \qquad (1)$$

In our geometry, a soliton standing in a straight line in the laboratory frame implies a constant $v_s = v_{flow} \sin\alpha$, where α is defined in Fig. 1A. As the soliton becomes darker (n_s approaching n), the phase jump saturates at $\delta = \pi$. Indeed, the solitons remain quite deep up to the first 40 μm of trajectory (Fig. 1, B and D), with a corresponding phase jump close to, but smaller than, π. At longer distances, the depth decreases along with the phase jump. Open triangles in Fig. 1D show the ratio n_s/n as obtained from the measured phase jump and Eq. 1. This confirms that the soliton relationships, which were derived for condensates without dissipation (*26*), are applicable locally to the case of polaritons under cw pumping, where the polariton density is stationary in time. The polariton density continuously decreases downstream from the barrier due to the finite polariton

[1]Laboratoire Kastler Brossel, Université Pierre et Marie Curie-Paris 6, École Normale Supérieure et CNRS, UPMC Case 74, 4 place Jussieu, 75005 Paris, France. [2]CNRS–Laboratoire de Photonique et Nanostructures, Route de Nozay, 91460 Marcoussis, France. [3]Laboratoire Matériaux et Phénomènes Quantiques, UMR 7162, Université Paris Diderot-Paris 7 et CNRS, 75013 Paris, France. [4]NNL, Istituto Nanoscienze–CNR, Via Arnesano, 73100 Lecce, Italy. [5]INO-CNR BEC Center and Dipartimento di Fisica, Università di Trento, via Sommarive 14, I-38123 Povo, Italy. [6]Scuola Superiore ISUFI, Università del Salento, Via Arnesano, 73100 Lecce, Italy. [7]Institut de Physique de la Matière Condensée, Faculté des Sciences de Base, bâtiment de Physique, Station 3, EPFL, CH-1015 Lausanne, Switzerland.

*To whom correspondence should be addressed. E-mail: alberto.amo@lpn.cnrs.fr (A.A.); bramati@spectro.jussieu.fr (A.B.)

lifetime. This results in a decrease in the speed of sound (from $c_s = 3.5 \pm 1$ μm/ps at $\Delta y = 14$ μm, to $c_s = 1.2 \pm 0.5$ μm/ps at $\Delta y = 50$ μm [see (*25*) for the estimation of c_s], which compensates the expected acceleration of the soliton when it becomes less deep (smaller n_s/n in Eq. 1). Consequently, the solitons present an almost rectilinear shape.

Simulations based on the Gross-Pitaevskii equation, with pumping and decay (*25*) according to the model described in (*24*) for the experimental parameters of Fig. 1, show the nucleation of a pair of solitons (Fig. 2A) with its associated phase jump (Fig. 2B). The model confirms that dark solitons nucleate hydrodynamically due to the gradient of flow speeds occurring around the potential barrier, which result in density variations on the order of the healing length. Once the soliton is formed, the repulsive interparticle interactions stabilize its shape as it propagates (*6*, *27*–*29*). By contrast, no stable soliton was observed at low excitation density when polariton-polariton interactions are negligible (see fig. S3).

Other hydrodynamic regimes can be explored by varying the mean polariton density (i.e., the speed of sound) for a fixed flow speed (Fig. 3). Here, polaritons move slower than in Fig. 1 ($v_{flow} = 0.79$ μm/ps, $k = 0.34$ μm^{-1}), and due to their limited lifetime, they cannot propagate far away from the excitation spot. Hence, we have designed an excitation spot with the shape of half a Gaussian, with an abrupt intensity cut-off (fig. S1). Below the red line in Fig. 3, A to C, only polaritons propagating away from the pumped area are present, and their phase is not imposed by the resonant pump beam.

Figure 3A shows the polariton flow at subsonic speeds ($v_{flow} = 0.25\bar{c}_s$, where the bar indicates the mean speed of sound), at high excitation density. The condensate is in the superfluid regime, as evidenced by the absence of density modulations in the fluid hitting the barrier and from the homogeneous phase (Fig. 3D), showing a high value of the zero time first-order coherence (*25*), $g^{(1)}$ (Fig. 3G). When the excitation density and, correspondingly, the sound speed is decreased to $v_{flow} = 0.4\bar{c}_s$ (Fig. 3B), the fluid enters into a regime of turbulence characterized by the appearance of two low-density channels in the wake created by the barrier, with extended phase dislocations (Fig. 3E). We interpret this regime as corresponding to the continuous emission of pairs of quantized vortices and antivortices moving through those channels (*4*–*6*, *24*). Although a direct observation of the phase singularity of the emitted vortices is not possible under time-integrated cw experiments, the effects of the vortex flow are clearly seen when looking at $g^{(1)}$. Figure 3H shows a trace of low degree of coherence along each channel, due to the continuous passage of individual vortices. Finally, if the density is further decreased, we observe the formation of oblique dark solitons (Fig. 3C; $v_{flow} = 0.6\bar{c}_s$), with the characteristic phase jump along their trajectory (Fig. 3F), and a constant value of $g^{(1)}$ close to 1 (Fig. 3I).

The three regimes depicted in Fig. 3 have been anticipated by the nonequilibrium Gross-Pitaevskii model (*24*). We report a break-up of the superfluid regime at $v_{flow} \sim 0.4\bar{c}_s$, a value consistent with predictions for the onset of drag in the presence of large circular barriers (*4*, *5*). Our

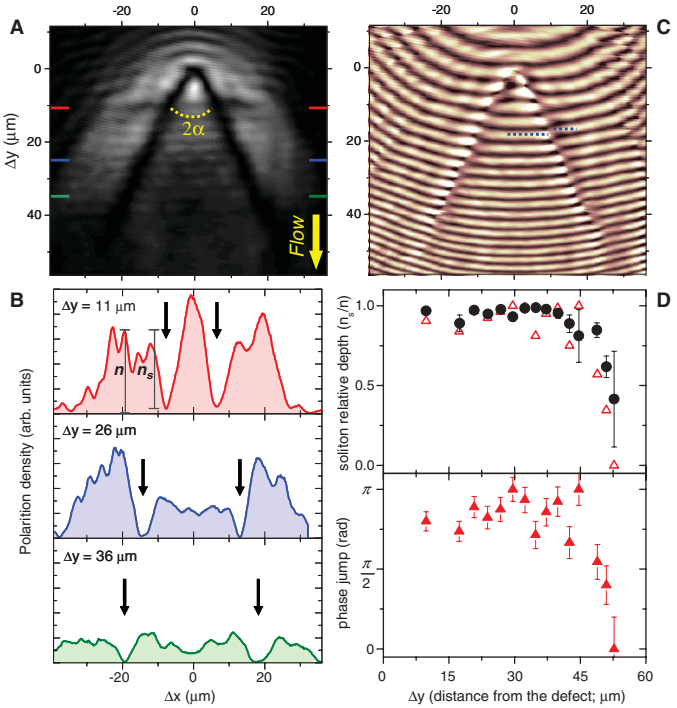

Fig. 1. (**A**) Real-space emission showing a soliton doublet nucleated in the wake of a photonic defect located at the origin. (**B**) Horizontal profiles at different downflow distances from the defect Δy. Arrows indicate the soliton position. (**C**) Interference between the emitted intensity and a constant-phase reference beam, showing phase jumps along the solitons (dashed lines). The curved shaped of the fringes and the decreasing interfringe distance arise from the geometry of the reference beam. (**D**) Soliton depth (black circles) and phase jump obtained from (C) (filled triangles; see fig. S4), showing a strong correlation. Open triangles: soliton depth obtained from the measured phase jump and Eq. 1.

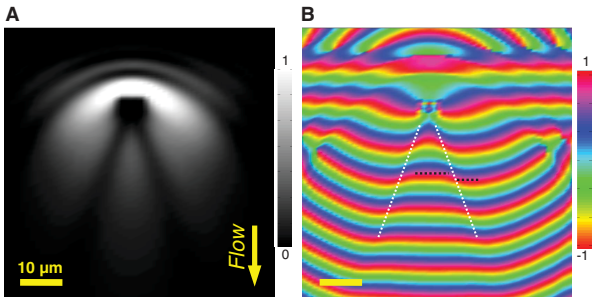

Fig. 2. (**A**) Real-space emission obtained from the solution of the nonequilibrium Gross-Pitaevskii equation for the parameters of the experiment depicted in Fig. 1. (**B**) Normalized real part of the polariton wave function, showing a phase jump (dark dashed lines) along the solitons (white dotted lines).

observations show that solitons in the polariton fluid can be stable down to subsonic speeds. This is in contrast to calculations for atomic condensates, in which oblique dark solitons are predicted to be stable only at supersonic speeds (*6*, *27*). Because our nonequilibrium simulations (Fig. 2) reproduce the observed nucleation at subsonic speeds, we infer that the additional damping in the polariton system arising from the finite lifetime is responsible for the stabilization of the soliton at subsonic speeds.

Finally, we have explored the possibility of going beyond the generation of soliton doublets by using a large circular potential barrier (*6*). Figure 4A shows a polariton flow at low momentum (k = 0.2 μm^{-1}) injected in a Gaussian spot slightly above the obstacle, which nucleates a soliton doublet. If the momentum of the flow is increased above a certain value, the strong density mismatch before and after the defect can generate a soliton quadruplet (Fig. 4B, k = 1.1 μm^{-1}). In principle, it should be possible to access even higher-order solitons by increasing both the obstacle size and the ratio v_{flow}/c_s.

Our results demonstrate the potential of polariton superfluids for experimental studies of quantum hydrodynamics. Both the velocity and the density of the quantum fluid can be finely controlled by optical means, and simultaneous access to the condensate density, phase, and coherence is available from the emitted light. These features have been essential in the reported observation of hydrodynamic generation of oblique solitons in the wake of potential barriers, and offer the opportunity to probe more complex phenomena like Andreev reflections (*30*), nucleation and trapping of vortex lattices (*24*), and quantum turbulence (*31*).

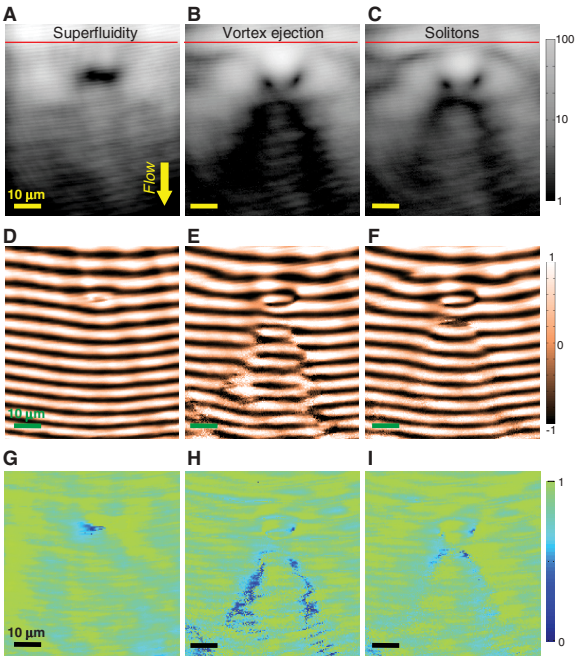

Fig. 3. (**A** to **C**) Real-space images of the polariton gas flowing downward at different excitation densities in the presence of a double defect (total width: 15 μm). The gas is injected above the red line (*25*). At high density (A) (117 mW), the fluid is subsonic (v_{flow} = 0.25$\bar{c}_s$) and flows in a superfluid fashion around the defect. At lower densities (B) (36 mW; v_{flow} = 0.4$\bar{c}_s$), a turbulent pattern appears in the wake of the defect, eventually giving rise to the formation of two oblique dark solitons (C) (v_{flow} = 0.6$\bar{c}_s$; 27 mW). (**D** to **F**) Interferograms corresponding to (A) to (C), respectively. (**G**) to (**I**) show the corresponding degree of first-order coherence [$g^{(1)}$, see (*25*)]. Saturated values of $g^{(1)}$ are due to the uncertainty in the measurements.

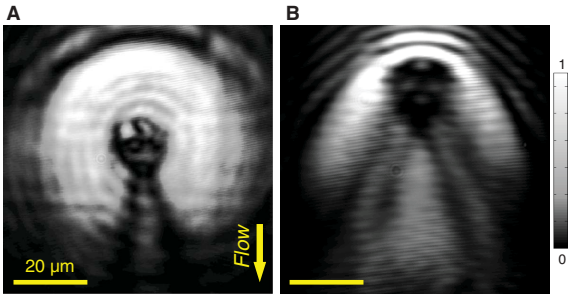

Fig. 4. Real-space images of the polariton flow around a large defect (17 μm in diameter) at low (**A**) (k = 0.2 μm^{-1}) and high (**B**) (k = 1.1 μm^{-1}) injected wave vectors showing, respectively, the formation of a soliton doublet and quadruplet.

References and Notes

1. A. J. Leggett, *Rev. Mod. Phys.* **71**, S318 (1999).
2. I. Carusotto, S. X. Hu, L. A. Collins, A. Smerzi, *Phys. Rev. Lett.* **97**, 260403 (2006).
3. A. Amo *et al.*, *Nat. Phys.* **5**, 805 (2009).
4. T. Frisch, Y. Pomeau, S. Rica, *Phys. Rev. Lett.* **69**, 1644 (1992).
5. T. Winiecki, B. Jackson, J. F. McCann, C. S. Adams, *J. Phys. At. Mol. Opt. Phys.* **33**, 4069 (2000).
6. G. A. El, A. Gammal, A. M. Kamchatnov, *Phys. Rev. Lett.* **97**, 180405 (2006).
7. C. Raman *et al.*, *Phys. Rev. Lett.* **83**, 2502 (1999).
8. R. Onofrio *et al.*, *Phys. Rev. Lett.* **85**, 2228 (2000).
9. P. Engels, C. Atherton, *Phys. Rev. Lett.* **99**, 160405 (2007).
10. S. Inouye *et al.*, *Phys. Rev. Lett.* **87**, 080402 (2001).
11. T. W. Neely, E. C. Samson, A. S. Bradley, M. J. Davis, B. P. Anderson, *Phys. Rev. Lett.* **104**, 160401 (2010).
12. S. Burger, K. Bongs, S. Dettmer, W. Ertmer, K. Sengstock, *Phys. Rev. Lett.* **83**, 5198 (1999).
13. J. Denschlag *et al.*, *Science* **287**, 97 (2000).
14. J. J. Chang, P. Engels, M. A. Hoefer, *Phys. Rev. Lett.* **101**, 170404 (2008).
15. J. Kasprzak *et al.*, *Nature* **443**, 409 (2006).
16. S. Christopoulos *et al.*, *Phys. Rev. Lett.* **98**, 126405 (2007).
17. A. Amo *et al.*, *Nature* **457**, 291 (2009).
18. E. Wertz *et al.*, *Nat. Phys.* **6**, 860 (2010).
19. A. Amo *et al.*, *Phys. Rev. B* **82**, 081301 (2010).
20. K. G. Lagoudakis *et al.*, *Nat. Phys.* **4**, 706 (2008).
21. C. W. Lai *et al.*, *Nature* **450**, 529 (2007).
22. I. Carusotto, C. Ciuti, *Phys. Rev. Lett.* **93**, 166401 (2004).
23. D. Sanvitto *et al.*, *Nat. Phys.* **6**, 527 (2010).
24. S. Pigeon, I. Carusotto, C. Ciuti, *Phys. Rev. B* **83**, 144513 (2011).
25. Materials and methods are available on *Science* Online.
26. A. D. Jackson, G. M. Kavoulakis, C. J. Pethick, *Phys. Rev. A* **58**, 2417 (1998).
27. A. M. Kamchatnov, L. P. Pitaevskii, *Phys. Rev. Lett.* **100**, 160402 (2008).
28. A. V. Yulin, O. A. Egorov, F. Lederer, D. V. Skryabin, *Phys. Rev. A* **78**, 061801 (2008).

29. Y. Larionova, W. Stolz, C. O. Weiss, *Opt. Lett.* **33**, 321 (2008).
30. A. J. Daley, P. Zoller, B. Trauzettel, *Phys. Rev. Lett.* **100**, 110404 (2008).
31. N. G. Berloff, Turbulence in exciton-polariton condensates. Preprint available at http://arxiv.org/abs/1010.5225 (2010).

Acknowledgments: We thank S. Barbay, J. Bloch, R. Kuszelewicz, W. D. Phillips, L. P. Pitaevskii, and M. Wouters for useful discussions, and L. Martiradonna for the confocal masks. This work was supported by the IFRAF, CLERMONT4, and the Agence Nationale de la Recherche. A.B. and C.C. are members of the Institut Universitaire de France.

Supporting Online Material
www.sciencemag.org/cgi/content/full/332/6034/1167/DC1
Materials and Methods
Figs. S1 to S4

28 December 2010; accepted 11 April 2011
10.1126/science.1202307

Auxiliary Material

Hydrodynamic solitons in polariton superfluids

A. Amo[1,2], S. Pigeon[3], D. Sanvitto[4], V. G. Sala[1], R. Hivet[1], I. Carusotto[5], F. Pisanello[1,4], G. Lemenager[1], R. Houdré[6], E Giacobino[1], C. Ciuti[3], A. Bramati[1]

[1]*Laboratoire Kastler Brossel, Université Pierre et Marie Curie-Paris 6, École Normale Supérieure et CNRS, UPMC Case 74, 4 place Jussieu, 75005 Paris, France*
[2]*CNRS-Laboratoire de Photonique et Nanostructures, Route de Nozay, 91460 Marcoussis, France*
[3]*Laboratoire Matériaux et Phénomènes Quantiques, UMR 7162, Université Paris Diderot-Paris 7 et CNRS, 75013 Paris, France*
[4]*NNL, Istituto Nanoscienze - CNR, Via Arnesano, 73100 Lecce, Italy*
[5]*INO-CNR BEC Center and Dipartimento di Fisica, Università di Trento, via Sommarive 14, I-38123 Povo, Italy*
[6]*Institut de Physique de la Matière Condensée, Faculté des Sciences de Base, bâtiment de Physique, Station 3, EPFL, CH-1015 Lausanne, Switzerland*

A Confocal excitation scheme

The data reported in Fig. 3 have been taken making use of a confocal excitation scheme, as shown in Suppl. Fig. 1. The laser is focalised in an intermediate plane where a mask is placed in order to hide the upper part of the Gaussian spot on that plane. Then, an image of the intermediate plane is done on the sample, producing a spot with the shape of a half Gaussian (the profile is depicted in the inset of Suppl. Fig. 1). Polaritons are resonantly injected in the microcavity with a well defined wavevector, in the region above the red line in the figure. In this configuration scheme, polaritons are free to move out of the excitation spot with a free phase, not imposed by the pump beam. This is essential for the observation of hydrodynamic effects, which involve topological excitations with phase discontinuities.

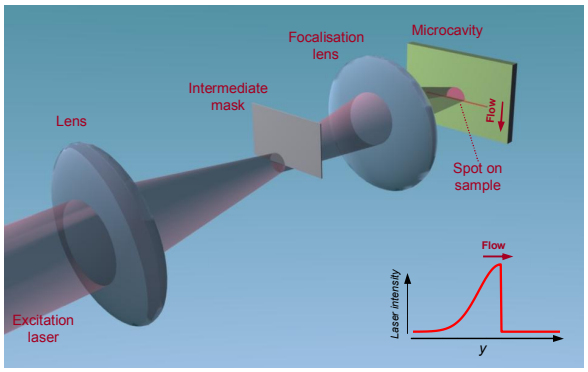

Suppl. Fig. 1. **Excitation setup for the observations of Fig. 3**. Reconstruction of the spot on the sample with the shape of half a Gaussian (a *y* cross-section is shown in the inset).

B Sound speed: density and phase jump estimations

The average sound speeds reported in the main manuscript, have been obtained from the measured soliton speed v_s and phase jump δ, with the use of Eq. 1 ($\cos(\delta/2) = v_s/c_s$). In Fig 3, the soliton regime is observed in panels c, f, i, and a sound speed can be extracted from the phase jump. In order to obtain the sound speed for other two excitation densities (panels a,b,d,e,g,h), we use the measured polariton density relative to the soliton case and the sound speed relation $c_s = \sqrt{\hbar g |\psi|^2 / m_{pol}}$. Note that the sound speed is proportional to the square root of the density $|\psi|^2$.

In order to confirm that this relationship is consistent with our results, we proceed in the same way for the data plotted in Fig. 1. In this case we take the sound speed obtained from the phase jump of the right soliton along its trajectory. The sound speed decays as the fluid is further away from the excitation area. The result is shown in black dots in Suppl. Fig. 2. Additionally, we measure the decay of the density on the edges of the soliton along its trajectory. In Suppl. Fig. 2 we plot in green triangles the magnitude $c_s = A\sqrt{I}$, where I is the emitted intensity (proportional to the polariton density) and A is a fitting constant. Remarkably, in both cases, the decay of the sound speed follows the same trend.

These results justify our method to obtain the sound speed in the superfluid and vortex emission regimes (Fig. 3a,b) from the measured sound speed in the soliton regime (Fig. 3c, obtained from the phase jump) and the relative polariton density in the other regimes.

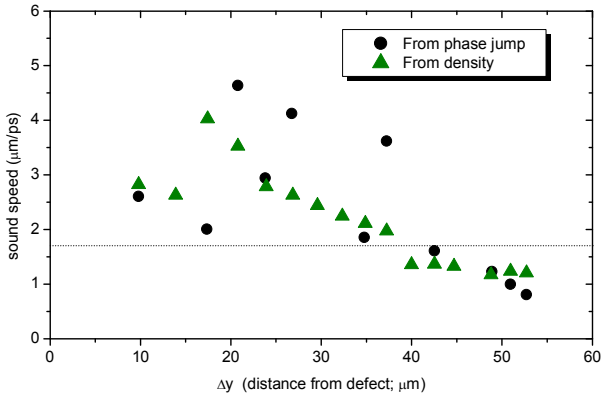

Suppl. Fig. 1. **Sound speed estimation for the data of Fig. 1**. Black dots show the sound speed obtained from the phase jump and Eq. 1 along the soliton trajectory. Green triangles show the fit from the measured square root of the emitted intensity (proportional to the polariton density). The dashed line shows the fluid speed.

All-optical control of the quantum flow of a polariton condensate

D. Sanvitto[1], S. Pigeon[2], A. Amo[3,4], D. Ballarini[5], M. De Giorgi[1], I. Carusotto[6], R. Hivet[3], F. Pisanello[3], V. G. Sala[3], P. S. Soares-Guimaraes[7], R. Houdré[8], E. Giacobino[3], C. Ciuti[2], A. Bramati[3], G. Gigli[1,5]

[1]*NNL, Istituto Nanoscienze - CNR, Via Arnesano, 73100 Lecce, Italy*

[2]*Laboratoire Matériaux et Phénomènes Quantiques, UMR 7162, Université Paris Diderot-Paris 7 et CNRS, 75013 Paris, France*

[3]*Laboratoire Kastler Brossel, Université Pierre et Marie Curie-Paris 6, École Normale Supérieure et CNRS, UPMC Case 74, 4 place Jussieu, 75005 Paris, France*

[4]*CNRS-Laboratoire de Photonique et Nanostructures, Route de Nozay, 91460 Marcoussis, France*

[5] *Istituto Italiano di Tecnologia, IIT-Lecce, Via Barsanti, 73010 Lecce, Italy*

[6] *INO-CNR BEC Center and Dipartimento di Fisica, Università di Trento, I-38123 Povo, Italy*

[7]*Departamento de Física, Universidade Federal de Minas Gerais, Belo Horizonte MG, Brazil*

[8]*Institut de Physique de la Matière Condensée, Faculté des Sciences de Base, bâtiment de Physique, Station 3, EPFL, CH-1015 Lausanne, Switzerland*

While photons in vacuum are massless particles that do not interact with each other, significant photon-photon interactions appear in suitable nonlinear media, leading to novel hydrodynamic behaviors typical of quantum fluids [1- 9]. Here we show the generation and manipulation of vortex-antivortex pairs in a Bose-Einstein condensate of exciton-polaritons – a coherent gas of strongly dressed photons– flowing against an artificial potential barrier created and controlled by a light beam in a planar semiconductor microcavity. The all optical control of the polariton quantum flow allows us to reveal new hydrodynamical phenomenologies such as the formation of vortex pairs upstream from the optical barrier, a

case of ultrashort time excitation of the quantum flow and the generation of vortices with counterflow trajectories. Additionally, we demonstrate how to permanently trap and store the quantum vortices that are hydrodynamically generated in the wake of a defect. These observations are borne out by time-dependent theoretical simulations based on the non-equilibrium Gross-Pitaevskii equation [10].

The recent advances in the optical generation, manipulation and diagnostics of quantum gases of exciton-polaritons in planar semiconductor microcavities [11] have paved the way to the study of quantum fluid phenomena in photon gases. Exciton-polaritons are bosonic quasi-particles that emerge in a semiconductor microcavity from the strong coupling of confined photons and quantum well excitons [12]. The exciton component provides efficient polariton-polariton interactions which result in strong optical nonlinearities; the photonic component allows for easily generation, manipulation and observation of polariton gases with optical techniques. As compared to standard quantum fluids such as liquid Helium or ultracold atomic gases, polariton fluids are expected to show new interesting non-equilibrium effects [13-15] that originate from the finite lifetime of the constituent particles and the driven-dissipative nature of the optical fluid.

As bosonic particles, polaritons have recently demonstrated to undergo a phase transition to a Bose-condensed state [16,17]. This has triggered the search for superfluid behaviours in polariton gases opening up new exciting possibilities as polaritons provide a unique access and control on all the relevant quantities of the fluid by simple optical means. In particular, one is able to follow in real time the evolution of the density and current profile, as well as of the quantum fluid coherence simply by observing the photonic state leaking out the cavity. These features have allowed for the study of non-linear flow phenomena in polariton gases, such as superfluidity [18-20], persistent flows lasting for very long times [21] and the hydrodynamic nucleation of dark solitons [10,22]. While the observation of these phenomena, have been out of reach in standard non-linear optical systems [6-8], photon-based polariton fluids appear as the most promising candidates for the study of quantum hydrodynamic effects. In particular this regime is characterised by the appearance of topological excitations: vortices of quantised angular momentum. These quantum of circulation lie in a multi-dimensional Hilbert space, hence they are extremely interesting for the possibility of using them, for instance, as qudits [29]—qubit in a higher dimensional system— as proposed for the case of purely photonic vortices [30,31]. In this context polariton condensates may have the advantage of having intrinsic non-linearities and being already integrated in semiconductor chips.

The present paper investigates the topological excitation of a quantum fluid encountering different kinds of obstacles capable of breaking its superfluid regime. Similar experiments were carried out using a condensate of ultracold atoms [23,24], and in polaritons, resonantly generated on a natural defect of the sample [9]. Here, we take advantage of the strong polariton non-linearities to optically create and tailor obstacle potentials of tuneable shape and intensity. We follow, in time, the vortex pairs, and show that their nucleation point and trajectory are determined by the shape and height of the barrier, as well as by the density of the quantum fluid, demonstrating the possibility to fully control by optical means the vortex appearance and motion. Moreover, using a trapping optical potential, we also show the

possibility of permanently storing the vortex pairs that are produced at the surface of a randomly chosen natural defect of the sample. This is a crucial advance with respect to the first experiments showing optical vortices in planar microcavity lasers [25] and in polariton condensates, where pinned vortices spontaneously appears in the disorder potential of the cavity [26,27] or in the minima of the excitation laser field [28]. Our results demonstrate advanced manipulation of a photon fluid by optical means, in particular for the generation and control of quantised vortices.

In the present experiment, polaritons are coherently created in a planar semiconductor microcavity by resonantly exciting the sample with a pulsed Ti-Sapphire laser. The sample is described in detail in [32] and in the method section. Time resolved real space images of the polariton field are obtained in transmission geometry with the use of a synchroscan streak camera. The real-space phase pattern of the polariton field is inferred from interferograms resulting from the interference of the cavity emission with a reference beam of constant phase coming from the pulsed laser itself.

Figure 1 shows the typical lower polariton dispersion of a microcavity under strong photon-exciton coupling. The polariton condensate is excited by a resonant laser with linear vertical polarization and a finite in-plane wavevector as indicated by the red arrow in the figure. The in-plane wavevector results in a finite flow velocity of the polariton fluid. We use the excitation scheme proposed in [10]: half of the laser spot (almost flat inside the cavity, due to saturation of polariton excitation) is masked with a sharp metallic edge so to restrict excitation of polaritons to the upstream region and let them spontaneously flow against a localized potential barrier that we create with a second laser (see below). In our configuration, out of the masked region, the phase of the superfluid is not locked to that of the laser, and therefore free to evolve in space and time. Note that if this mask is absent, as in Ref. [9], any inhomogeneity of the pumping laser, close to the obstacle, could strongly influence the fluid dynamics and the appearance of topological vortices [28].

The artificial potential barrier is created by a CW laser with linear polarization (horizontal) opposite to that of the pumping pulsed laser. This CW beam is normally incident to the sample and its frequency is resonant with the bottom of the polariton dispersion at $k_{//}$=0. Its purpose is to introduce in the spot region a steady population of exciton-polaritons large enough to locally result in a significant blueshift of the polariton states under the effect of interparticle interactions. This has demonstrated to give rise to two populations which behaves independently in case of resonant CW excitation [33], however it has never been implemented and proved to act as a potential obstacle in a non-steady state system where polaritons are truly flowing, independently from the exciting laser beams. By varying the CW intensity, blue shifts ranging from 0.1 meV to 0.8 meV are obtained. The size and shape of the potential obstacle is simply controlled by the size and the shape of the CW laser spot. Figure 1 shows a scheme of such a potential landscape. In the images shown in Figures 2-3, we isolate the emission, coming from the flowing polaritons injected by the pulsed laser, by means of suitable polarizers and using time resolved experiments.

Figure 2 shows five temporal snapshots of the real space density and phase profile of a polariton condensate injected in the cavity with a rightward velocity v_f = 1.1 µm/ps. In our

case, the polaritons are in fact flowing against the obstacle at a supersonic speed (see supplementary information) ($c_s<v_f$). The shape of the barrier is Gaussian (~10 μm in diameter, 0.4 meV of mean height) and its position is indicated by a blue circle. The successive snapshots show the formation of a pair of vortices with opposite circulation in the center of the fluid 10 ps after the arrival of the pulse and upstream from the position of the defect. Vortices are revealed as density minima corresponding to their core in Fig. 2b-e, and as fork-like dislocations in the interferograms shown in Fig. 2g-m. In the subsequent 10 ps the vortex and the antivortex are pushed away from the center of the potential barrier towards its sides at a velocity of ~ 0.9 μm/ps. However, after the vortices have reached the equator of the obstacle [34], there is a clear deceleration of their motion and a small excursion along the vertical axis orthogonal to the flow direction. After most of the polariton pulse has gone past the defect, the vortices keep wandering at a distance of a few tenths of microns from the defect, their motion being mostly oriented in the direction orthogonal to the original injected flow. The good visibility of the fringes in the interference pattern shows that the polariton fluid preserves its coherence during the whole evolution.

Remarkably, unlike what observed in Refs. [23-24,9], the formation of vortices takes place at a position right upstream of the defect and not in its wake as it is usually expected [35-37]. These works, however considered a flow hitting a strong and spatially abrupt potential. In contrast, in the present experiments we optically generate a potential with a smooth profile and relatively shallow depth, therefore allowing a small fraction of the condensate to penetrate the obstacle. Furthermore, we inject polaritons using a temporally short and spatially localized laser pulse, creating a dynamic density profile which first increases and then swiftly decreases in time after the polariton wave has passed the obstacle. A vortex pair starts to form, when the sound velocity first equals the local fluid velocity [9]. Differently from previous works vortices are observed to nucleate exactly at the spatial position where this condition is satisfied, which happens upstreams of our obstacle. This is confirmed by the solution of the time-dependent non-equilibrium Gross-Pitaevskii equations with the actual experimental excitation conditions (see Fig. 2 third row and the supplementary material).

A more detailed analysis of the vortex trajectories for different conditions of the optical barrier and the density of injected polaritons is shown in Figure 3. Increasing the CW power (Fig. 3a-c) results in the increase of both the height and the effective width of the potential experienced by the moving polaritons. A larger diameter of the potential would tend to push the vortex-antivortex nucleation point upstream, closer to the pulse injection area, where the density is higher, giving a higher sound speed c_s. At the same time, nucleation tends to occur further away from the obstacle axis, at positions where the local flow velocity tangential to the obstacle is higher, and the condition $v_f=c_s$ is satisfied. These features are well reproduced by the solution of the Gross-Pitaevskii equation for polaritons, as shown in Fig. 2S of the supplementary material. To further assess the effect of the change in polariton density on the interaction with the defect, we have repeated the experiment with a higher power of the pulsed laser (Fig. 3d), so to inject a higher density of polaritons at a similar value of the barrier height and size of Figs. 3b. The higher injected polariton density (39.8 μm^{-2} compared to 12.4 μm^{-2} for lower excitation power) corresponds to an increase of the sound speed from c_s = 0.4 μm/ps (Fig. 3b) to 0.8 μm/ps (Fig. 3d). On the other hand, the highest flow velocity takes

place at the equator of the barrier [35-37] and as a result, the nucleation point shifts laterally towards the edge of the defect, where the flow velocity is higher. Even though the increase of the density is slightly compensated by a higher fluid velocity of the injected polaritons (v_f = 1.4 μm/ps), still the dominating effect is in the variation of the speed of sound, giving an increase of 25% in c_s/v_f respect to the experiment in Fig. 3 c. This can also be seen in Figs. 3a,b and 3c, where for different values of the CW power equal to 6 mW (Fig. 3a), 26 mW (Fig. 3b) and 52 mW (Fig. 3c), the estimated speed of sound (as discussed in the supplementary material) at the vortex pair nucleation points are 0.3 μm/ps, 0.4 μm/ps and 0.5 μm/ps, respectively, consistent with nucleation points approaching the equator of the barrier

Another interesting outcome is observed for very small defect size (see Fig. 3e). Here the vortex-antivortex pair follows the contour of the obstacle and then recombines right downstream from the defect. In this case, due to the reduced dimension of the defect, the polariton density is not strongly reduced in the wake of the potential, allowing for the observation of vortex/antivortex annihilation once the flow has recovered its unperturbed pathway. This remarkable result shows the ultrashort lifetime of a topological excitation created on the quantum fluid. To some extent the fluid before and after the defect shows the same unperturbed behavior. This could be considered the quantum counterpart of the classical laminar flow (see video in the supplementary online material).

Finally in Fig. 3f we have changed the shape of the obstacle into a rectangular extended barrier with a channel of about 20 μm to allow for the polariton to flow through. Interestingly we observe the formation of a vortex pair at the boundary of the optical barrier which is first scattered back, reflected by the barrier itself, and subsequently pushed forward by the polariton condensate flowing towards the channel for the vortex, and along the barrier for the antivortex. This shows the extraordinary variety of the phenomenology and dynamics of vortex pairs obtained by simple manipulation of the optical defect.

So far we have shown that an artificial, optically induced, potential barrier is able to produce the hydrodynamic nucleation of vortices in a flowing polariton fluid. However, these vortices can only last for as long as the polariton fluid survives in the cavity. An alternative strategy to make vortices last for times much longer than the polariton lifetime is to work under a CW excitation and to use a suitably tailored mask to nucleate and then trap vortex pairs, as theoretically suggested in [10].

This proposal is experimentally demonstrated in Figure 4. Polaritons with a well-defined momentum are injected by a single CW laser and sent against a potential barrier (here formed by a natural defect present in the microcavity). In the absence of the mask (Fig. 4a), the phase of the polariton fluid is locked to that of the pump laser, so that vortices are prevented from nucleating even at supersonic speeds, as shown by the homogeneity of the interferogram in Fig. 4g. On the other hand, when a dark region is placed right downstream of the defect (dark triangle in Fig. 4b), pairs of vortices that are hydrodynamically nucleated in the proximity of the defect, can freely penetrate in the dark area where the polariton phase is not locked by the incident laser (note the phase dislocations in Fig. 4h). As the phase of the fluid is homogeneous outside the triangle, vortices cannot diffuse out and they get permanently trapped within the triangular borders. Moving the dark region slightly away from the defect, we can still observe the presence of some trapped vortices within this area (Fig. 4c-

d,i-j). On the other hand, if the dark trap is moved away from the cone set by the shock waves, (appreciable in Fig. 4a) vortices cannot get trapped inside the triangle and their appearance remains frustrated by the homogeneous phase imprinted by the pump laser (Fig. 4e,k). In Fig. 4e and 4k we have shifted the triangle of ~ 50 μm downwards so to keep it away from the ~ 60^o cone generated by a flow with a velocity of 0.9 μm/ps (k=0.38 μm^{-1}) against the defect. As a result, no vortex is present in the triangular dark region.

The capacity of storage (number of vortices per unit area) is strongly determined by the strength of the laser field inside the triangular region, as predicted in [10]. Indeed, for sufficiently high intensities of the resonant CW laser, the amount of light diffracted by the edges of the metallic mask is sufficient to partially fix the laser phase in a part of the inner region, as is the case of Fig. 4b, 4c, 4d where only a pair of vortices is present. However, reducing the total laser power, the light field inside the triangle becomes negligible and the number of vortices trapped by the masked region proliferate, as shown in Fig. 4f, mainly along the edges of the triangle. This observation demonstrates the possibility of storing a controlled number of vortices. Note that in principle the vortex pairs could be retained inside the triangle for as long as the CW laser is on.

Our experiments show the potential of optical methods for the study, generation and manipulation of quantized vortices in a quantum fluid. We show that we can fully control, via laser-induced artificial potentials, the obstacle parameters, allowing to inspect the physics of the vortex nucleation process in novel regimes and revealing unprecedented effects such as the formation upstream of the defect and the ultrashort reversible excitation of a quantum fluid. We further demonstrate the possibility of trapping and storing vortices in an all-optical way by using a triangular optically-induced potential. Our observations confirm that polariton condensates are an alternative to ultracold atoms [38] for the study of quantum fluid effects [39] in new regimes, and using solid state samples that are operational up to room temperature [40,41]. The all-optical control and trapping of vortices set the premises to study optical vortex lattices and their excitations.

Acknowledgements

This work was partially supported by the Agence Nationale pour la Recherche (GEMINI 07NANO 07043), the IFRAF (Institut Francilien pour les atomes froids) and the project MIUR FIRB ItalNanoNet. I.C. acknowledges financial support from ERC through the QGBE grant. A.B. and C.C. are members of Institut Universitaire de France (IUF). We would like to thank for a travel grant the support of the POLATOM ESF Research Networking Program. We are grateful to G. Martiradonna in helping for the realisation of the laser mask and to P. Cazzato for the technical support.

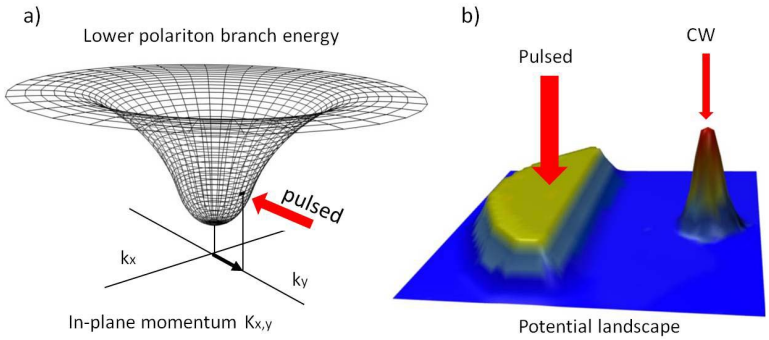

Figure 1. Schematic description of the experiment. (a) lower polariton dispersion with a red arrow indicating the pulsed laser wavevector. (b) Drawings of potential landscape, with the flat potential of the bare polariton state modified by both the pulsed laser injecting the polariton flow and by the CW laser giving origin to the artificial potential barrier.

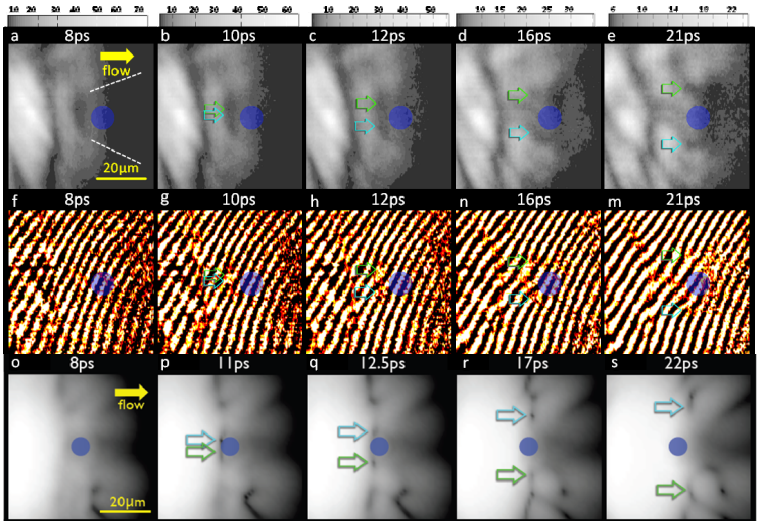

Fig.2: Upper row (a-e): snapshots of the real space emission pattern of the polariton fluid (power of the pulsed laser, P_{pulsed}=4mW) hitting an optical defect (blue circle, power of the continuous wave laser, P_{cw}=26mW) at different times (8ps, 10ps, 12ps, 16ps and 21ps after the maximum intensity of the pulse). The dark vertical contour originates from the red-shifted region created by the sharp edge of the masked laser spot. The dotted white lines show the angle of the shock waves. Medium row (f-m): corresponding interferograms giving the spatial profile of the condensate phase. These images are obtained by mixing the real space emission of the condensate with a reference beam of constant phase. An integration time of 1 s has been used for each snapshot. Lower row (o-s): theoretical simulations using the parameters of the experimental images (a-e). The agreement in the location of the nucleation process and in the following trajectory is quite good. The arrows in (b), (g) and (p) indicate the position of the vortex pair nucleation. In (c-e), (h-m) and (q-s) the arrows follow the positions of the vortex-antivortex pair as these are dragged by the polariton fluid on either side of the obstacle. Real space images are in logarithmic color scales.

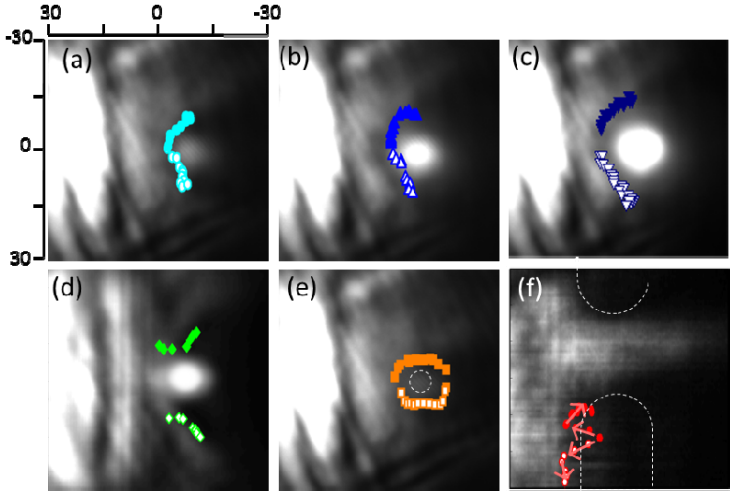

Figure 3. Time-integrated real space emission patterns and corresponding vortex trajectories (obtained from successive time shots) for different parameters of the CW laser, injection density and shape of the barrier. The vortex trajectories start from left to right. Panels (a-c, e) refer to a fixed pulse power, P_{pulsed}=4mW, and different CW powers, P_{cw}=6mW, 26mW and 52mW and 2mW respectively. Panel (d) refers to the same potential barrier as in panel (b), P_{cw}=26mW, but with higher pump intensity, P_{pulsed}=14mW. In panel (f) the optical defect is shaped into an infinitely long barrier with a ~20 μm channel where the boundary are shown with dotted white lines. Here the vortex trajectory shows an opposite behaviour going from right to left (pushed back by the barrier) and then following the flow as indicated by the arrows. The background images are time-integrated for the all duration of the experiment. The bright spot, for the strong CW powers, is due to the weak but non-zero transmission of the CW beam through the polarizer in the CCD camera, and indicates the position and shape of the defect.

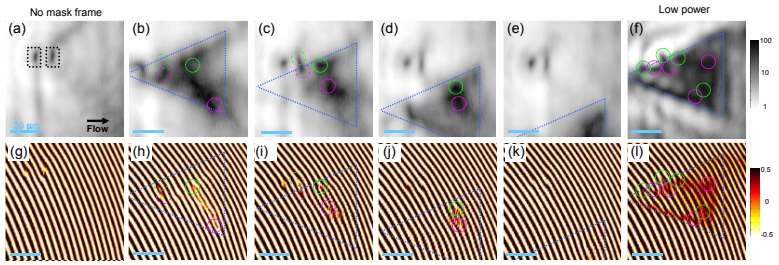

Figure 4: Real space images (a-f) and corresponding interferograms (g-l) for polaritons injected by a CW laser beam and flowing against a double natural photonic defect in the microcavity [marked by rectangular dotted contours in (a)]. In (a,g), no mask is applied to the Gaussian spot, the size of which is larger than the field of view, so that the density is almost uniform behind the defect and the phase is pinned. In (b), a dark region within the excitation spot is created, with a triangular mask, behind the defect and a pair of vortices (green and magenta solid circles) nucleates and gets trapped inside the triangular area, as evidenced by the phase dislocations shown in the interferogram (h). A second pair of vortices (dashed lines) is trapped in the right minima of the double defect. In (c-e) and (i-k), the triangular mask is laterally shifted with respect to the optical defect. In (c,d,l,j), the lateral shift is small enough for vortices to still nucleate and be visible inside the triangular trap. In (e, k), the mask has been shifted too far away from the defect and vortex nucleation is frustrated due to the homogeneous phase imprinted by the pump laser. In (f,l) the pumping power of the laser is lowered to allow for many vortex pairs to get trapped. The images are obtained by 1s integration time in the CCD camera.

References

1 Carusotto, I. & Ciuti, C. Swimming in a sea of superfluid light. *Europhys. Lett.* **41**, 5 (2010).
2 Coullet, P., Gil, L. & Rocca, F. Optical Vortices. *Optics Communications* **73**, 403-408 (1989).
3 Brambilla, M. *et al.* Transverse laser patterns .1. Phase singularity crystals. *Phys. Rev. A* **43**, 5090-5113 (1991).
4 Staliunas, K. Laser Ginzburg-Landau equation and laser hydrodynamics. *Phys. Rev. A* **48**, 1573-1581 (1993).
5 Wan, W., Jia, S. & Fleischer, J. W. Dispersive superfluid-like shock waves in nonlinear optics. *Nature Phys.* **3**, 46-51 (2007).
6 Chiao, R. Y. & Boyce, J. Bogoliubov dispersion relation and the possibility of superfluidity for weakly interacting photons in a two-dimensional photon fluid. *Phys. Rev. A* **60**, 4114 - 4121 (1999).
7 Bolda, E. L., Chiao, R. Y. & Zurek, W. H. Dissipative Optical Flow in a Nonlinear Fabry-Perot Cavity. *Phys. Rev. Lett.* **86**, 416 - 419 (2001).
8 Tanzini, A. & Sorella, S. P. Bose-Einstein condensation and superfluidity of a weakly-interacting photon gas in a nonlinear Fabry-Perot cavity. *Phys. Lett. A* **263**, 43-47 (1999).
9 Nardin, G., Grosso, G., Léger, Y., Pi tka, B., Morier-Genoud, F. & Deveaud-Plédran, B. Hydrodynamic nucleation of quantized vortex pairs in a polariton quantum fluid. *Nature Physics doi:10.1038/nphys1959* (2011).
10 Pigeon, S., Carusotto, I. & Ciuti, C. Hydrodynamic nucleation of vortices and solitons in a resonantly excited polariton superfluid. *Phys. Rev. B* **83**, 144513 (2011).
11 Deveaud, B. The Physics of Semiconductor Microcavities (WILEY-VCH Verlag, Weinheim, 2007).
12 Kavokin, A., Baumberg, J. J., Malpuech, G. & Laussy, F. P. *Microcavities*. (Oxford University Press Inc., 2007).
13 Szymanska, M. H., Keeling, J. & Littlewood, P. B. Nonequilibrium Quantum Condensation in an Incoherently Pumped Dissipative System. *Phys. Rev. Lett.* **96**, 230602 (2006).
14 Wouters, M., Carusotto, I. & Ciuti, C. Spatial and spectral shape of inhomogeneous nonequilibrium exciton-polariton condensates. *Phys. Rev. B* **77**, 115340 (2008).
15 Wouters, M. & Carusotto, I. Superfluidity and Critical Velocities in Nonequilibrium Bose-Einstein Condensates. *Phys. Rev. Lett.* **105**, 020602 (2010).
16 Kasprzak, J. *et al.* Bose-Einstein condensation of exciton polaritons. *Nature* **443**, 409-414 (2006).
17 Balili, R., Hartwell, V., Snoke, D., Pfeiffer, L. & West, K. Bose-Einstein Condensation of Microcavity Polaritons in a Trap. *Science* **316**, 1007-1010 (2007).
18 Amo, A. *et al.* Collective fluid dynamics of a polariton condensate in a semiconductor microcavity. *Nature* **457**, 291-295 (2009).
19 Carusotto, I. & Ciuti, C. Probing Microcavity Polariton Superfluidity through Resonant Rayleigh Scattering. *Phys. Rev. Lett.* **93**, 166401 (2004).
20 Amo, A. *et al.* Superfluidity of Polaritons in Semiconductor Microcavities. *Nature Phys.* **5**, 805-810 (2009).
21 Sanvitto, D. *et al.* Persistent currents and quantized vortices in a polariton superfluid. *Nature Phys.* **6**, 527-533 (2010).

22 Amo, A. *et al.* Hydrodynamic solitons in polariton superfluids. to be publishd in *Science preprint available at arXiv:1101.2530* (2011).

23 Inouye, S. *et al.* Observation of Vortex Phase Singularities in Bose-Einstein Condensates. *Phys. Rev. Lett.* **87**, 080402 (2001).

24 Neely, T. W., Samson, E. C., Bradley, A. S., Davis, M. J. & Anderson, B. P. Observation of Vortex Dipoles in an Oblate Bose-Einstein Condensate. *Phys. Rev. Lett.* **104**, 160401 (2010).

25 Scheuer, J. & Orenstein, M. Optical Vortices Crystals: Spontaneous Generation in Nonlinear Semiconductor Microcavities. *Science* **285**, 230-233 (1999).

26 Lagoudakis, K. G. *et al.* Quantized vortices in an exciton-polariton condensate. *Nature Phys.* **4**, 706-710 (2008).

27 Lagoudakis, K. G. *et al.* Observation of Half-Quantum Vortices in an Exciton-Polariton Condensate. *Science* **326**, 974-976 (2009).

28 Roumpos, G. *et al.* Single vortex-antivortex pair in an exciton-polariton condensate. *Nature Physics* **7**, 129-133, doi:10.1038/nphys1841 (2011).

29 Cerf, N. J., Bourennane, M., Karlsson, A. & Gisin, N. Security of quantum key distribution using d-level systems. *Phys. Rev. Lett.* 88, 127902 (2002).

30 Molina-Terriza, G., Torres, J. P. & Torner, L. Twisted photons. *Nature Phys.* 3, 305–310 (2007).

31 Mair, A., Vaziri, A., Weihs, G. & Zeilinger, A. Entanglement of the orbital angular momentum states of photons. *Nature* 412, 313–316 (2001).

32 Leyder, C. *et al.* Interference of Coherent Polariton Beams in Microcavities: Polarization-Controlled Optical Gates. *Phys. Rev. Lett.* **99**, 196402 (2007).

33 Amo, A. *et al.* Light engineering of the polariton landscape in semiconductor microcavities. *Phys. Rev. B* **82**, 081301 (2010).

34 the equator axis being defined to be perpendicular to the flow direction

35 Frisch, T., Pomeau, Y. & Rica, S. Transition to dissipation in a model of superflow. *Phys. Rev. Lett.* **69**, 1644-1647 (1992).

36 Jackson, B., McCann, J. F. & Adams, C. S. Vortex Formation in Dilute Inhomogeneous Bose-Einstein Condensates. *Phys. Rev. Lett.* **80**, 3903 (1998).

37 Winiecki, T., Jackson, B., McCann, J. F. & Adams, C. S. Vortex shedding and drag in dilute Bose-Einstein condensates. *J. Phys. B: At. Mol. Opt. Phys.* **33**, 4069 (2000).

38 Henn, E. A. L. *et al.* Emergence of Turbulence in an Oscillating Bose-Einstein Condensate. *Phys. Rev. Lett.* **103**, 045301 (2009).

39 Berloff, N. G. Turbulence in exciton-polariton condensates. *preprint avalilable at arXiv:1010.5225* (2010).

40 Tawara, T., Gotoh, H., Akasaka, T., Kobayashi, N. & Saitoh, T. Cavity Polaritons in InGaN Microcavities at Room Temperature. *Phys. Rev. Lett.* **92**, 256402-256404 (2004).

41 Christopoulos, S. *et al.* Room-Temperature Polariton Lasing in Semiconductor Microcavities. *Phys. Rev. Lett.* **98**, 126405 (2007).

Appendix B

Optical setups

Contents

B.1 Polarization- and time-resolved confocal setup for photon correlation measurements

The sample was analyzed by the confocal microscopy setup sketched in Fig. B.1. A picosecond-pulsed excitation laser diode (wavelength 404 nm, pulse width $\sim 50ps$) was focused on a single DR and time- and polarization-resolved spectroscopy and single photon counting measurements were performed by means of a high-sensitivity Hanbury–Brown and Twiss setup, based on a pair of avalanche photodiodes (APDs). The signals from the photodiodes were elaborated by a data acquisition card, used in two different configurations. All measurements were performed at room temperature. In the start-stop mode, the delays between the received photons on the two APDs provide the measurement of the coincidence histogram $h(\tau)$, proportional to the second order autocorrelation function $g^{(2)}(\tau)$. By triggering the data acquisition card with the laser pulses (*laser triggered mode*), it is possible to record individual photon events with

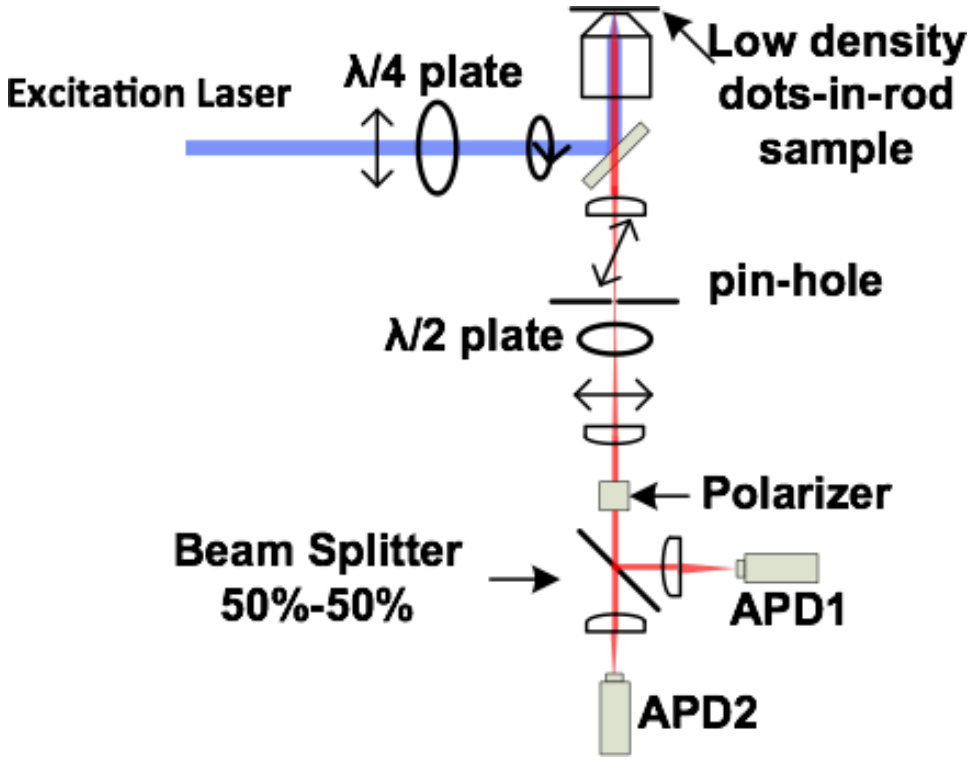

Figure B.1: Sketch of the μPL optical setup used for single photon detection.

their absolute arrival times and their delays from the synchronization pulse in order to measure the photoluminescence time traces and decay curves.

In order to evaluate optical losses in the setup, the transmission of each element has been evaluated by using an HeNe CW laser and the collection efficiency of the objective in presence of a dipole-like emitter estimated by an FDTD electromagnetic solver (see Fig.s B.2, B.3 and B.4). The total collection efficiency has been assessed to be $\sim 2.8\%$ (see Fig. B.5).

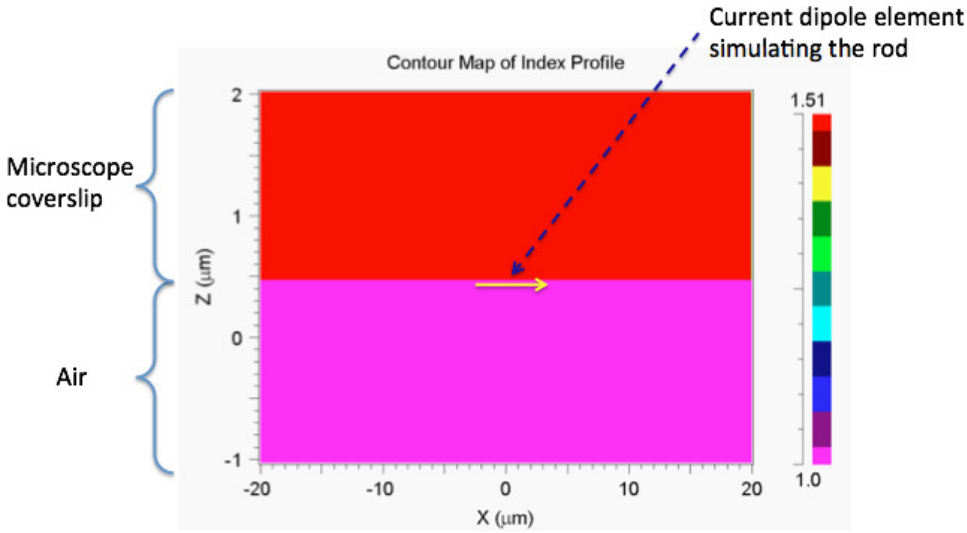

Figure B.2: Electromagnetic structure simulated to probe objective collection efficiency.

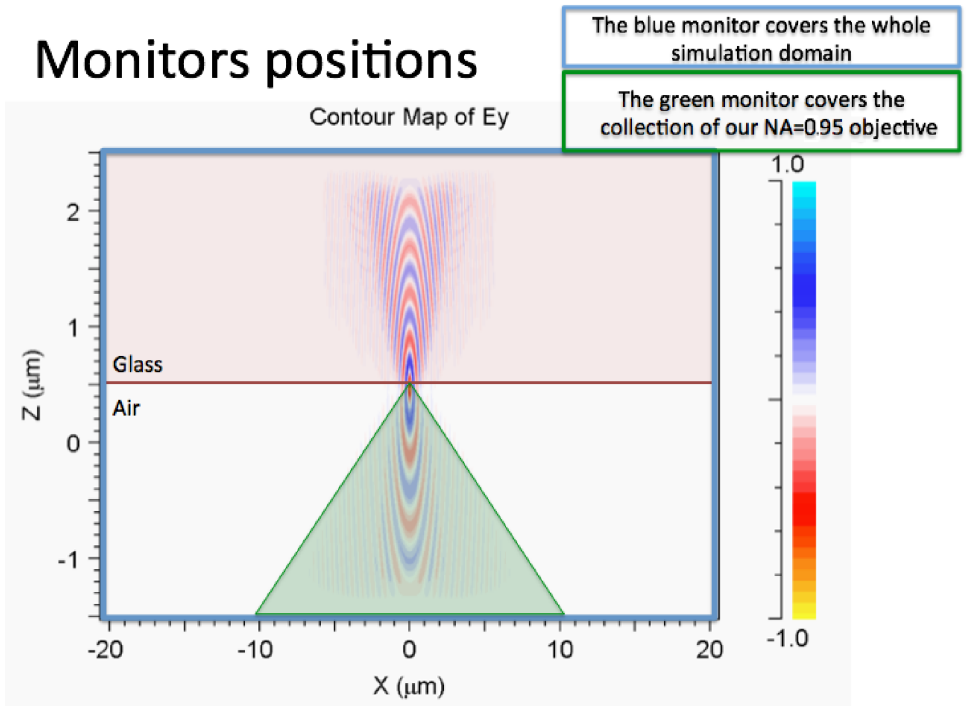

Figure B.3: Energy monitors disposition and time snap-shot of the electric field distribution.

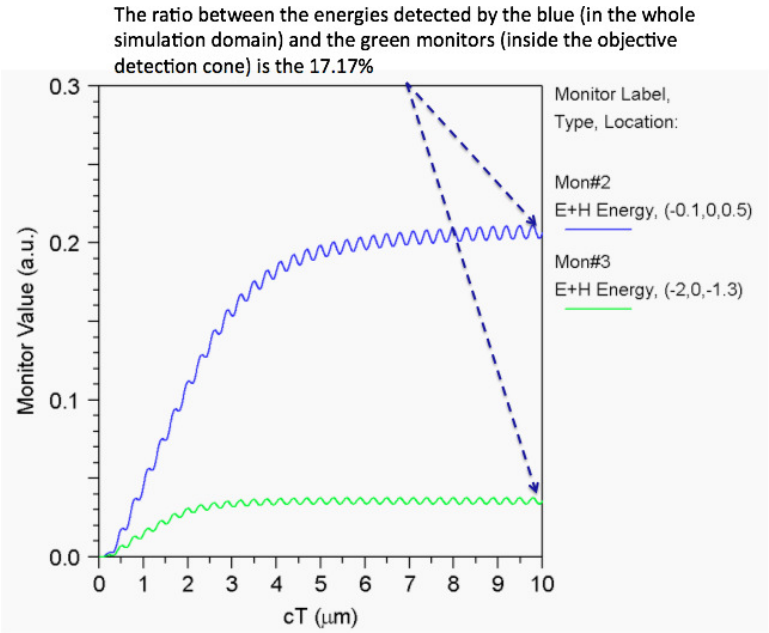

Figure B.4: Signal detected by the energy monitors a function of the FDTD time steps.

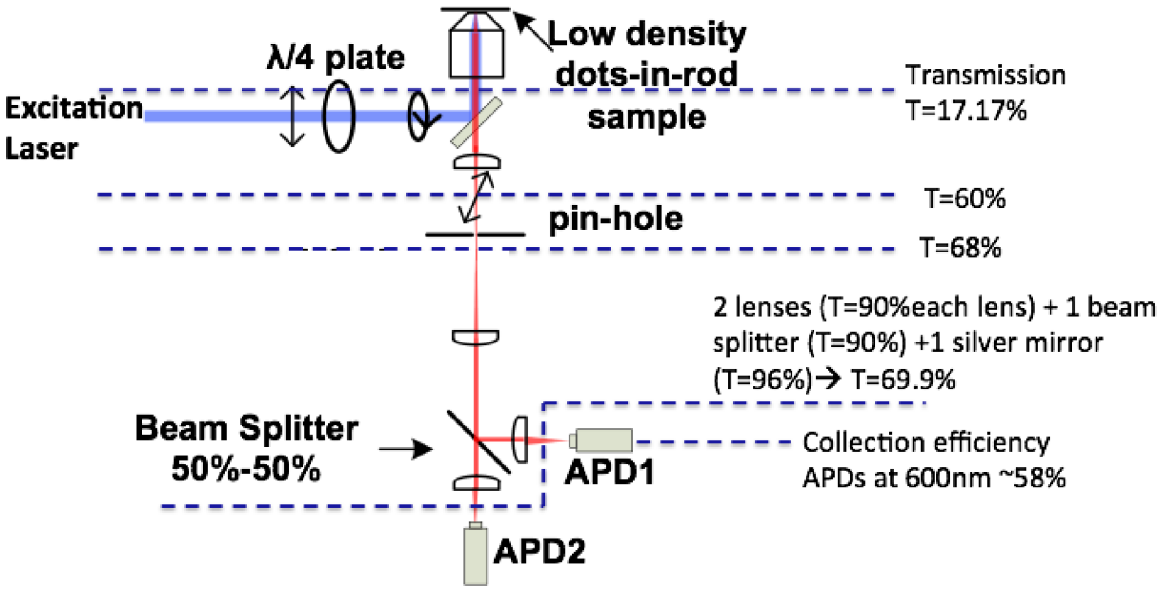

Figure B.5: Evaluation of the transmission of each optical element present in the setup.

B.2 μPL mesurements on PhC cavities

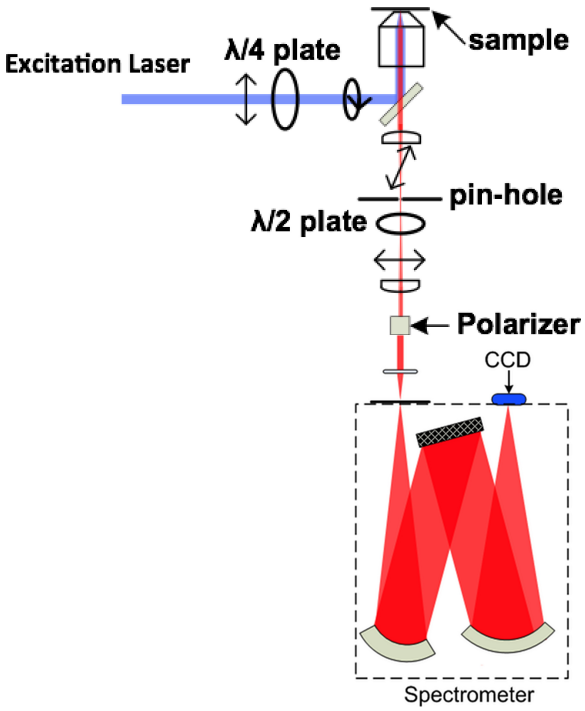

Figure B.6: Sketch of the μPL optical setup used for PhC cavity characterization.

The microphotoluminescence (μPL) measurements were performed by means of a confocal microscope (Olympus Fluoview 1000). A continuous wave excitation laser (emitting at 515 nm or 405 nm for Cy3 and NC, respectively) was focused on the sample by using an air objective with numerical aperture N.A.=0.85; the light emitted by the device was collected through the same objective, dispersed in a 300mm long spectrometer and sent to a liquid nitrogen cooled CCD. A polarizing cube and an half wavelength plate was introduced in the optical path to perform polarization resolved measurements and to identify x- and z-pole modes (see Fig. B.6 for the detailed optical path). All measurements were performed at room temperature in air.

B.3 Two photon absorption optical setup

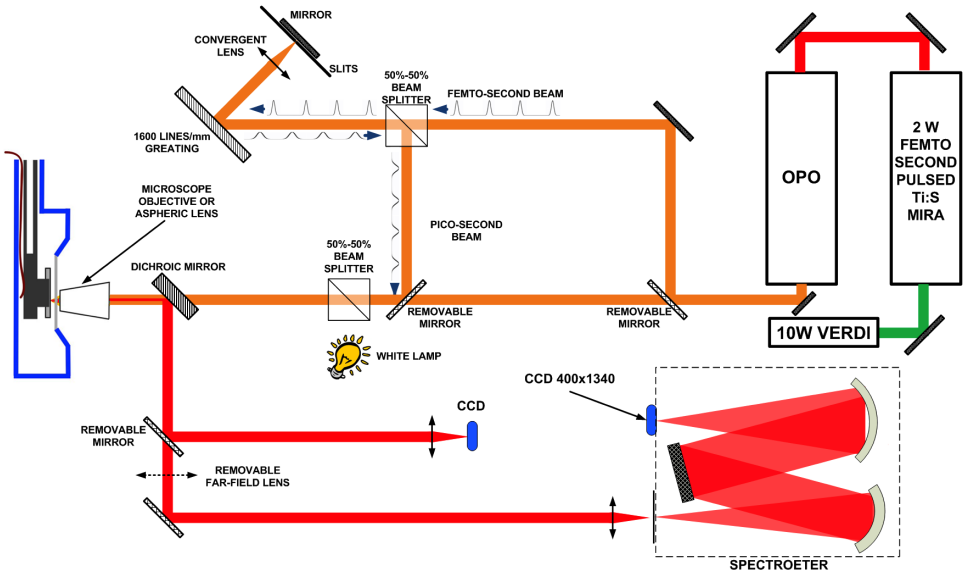

Figure B.7: Sketch of the TPA optical path.

The two photon beam is provided by an optical parametric oscillator pumped by a Ti:S femtosecond pulsed laser. The sample is placed in a He-cooled cryostat and the obtained femtosecond pulses are focused on the sample by an objective with numerical aperture N.A.=0.7 (see path sketched in Fig. B.7). The polariton emission, collected by the same excitation objective, is reflected by a dichroic mirror in order to filter the reflected laser and dispersed in a $500mm$ long spectrometer equipped by a high sensitivity CCD.

In order to reduce the full width at half maximum of the laser beam, the optical path reported in Fig. B.7 allows to modify the temporal shape of the laser pulses. The femtosecond two-photon beam was dispersed by a 600 line/mm grating and the first diffraction order was focused on a mirror through a convergent lens. A system of two slits has been introduced in the focal image plane of that lens in order to perform a spectral selection of the dispersed beam. The reflection from the mirror was sent back along the incoming path and the resulting outcoming picosecond pulsed beam was redirected toward the sample by using a 50%-50% beam splitter toward the sample.

As summarized in tab.5.1, the system allows us to excite the sample by means of three different type of pulsed beams.

Appendix C

Other procedures

C.1 Synthesis of colloidal DRs

The CdSe/CdS DRs used in this work were synthesized using the procedure reported in Ref. [127]. The CdSe cores were prepared by mixing trioctylphosphineoxide (TOPO, 3.0g), 4,4'-oxydiphthalic anhydride (ODPA, 0.280g) and CdO (0.060g) in a 50 mL flask, heated to about 150 °C and exposed to vacuum for ca. 1 hour. Then, under nitrogen, the solution temperature was increased to above 300 °C to dissolve the CdO until it turns optically clear and colorless. Then 1.5 g of trioctylphosphine (TOP) was injected in the flask and heated to 360 °C. After that, a Se solution in TOP (0.058 g Se + 0.360 g TOP) was quickly injected in the flask and the reaction was stopped after 1 min by removing the heating mantle. CdSe seeds were precipitated with methanol, redissolved in toluene, reprecipitated with methanol, and finally dissolved in 1mL of TOP. In order to obtain a preferred axis growth for the CdS shell, ODPA (0.290 g), HPA (0.080 g), TOPO (3.0 g) and CdO (0.060 g) were mixed in a three-neck flask, heated at 150 °C, and pumped to vacuum for ca. 1 hour. The temperature was first increased up to 300 °C and stabilized at 350 °C after the injection of 1.5 g of TOP. Then a solution of S in TOP (0.120 g S + 1.5 g TOP) containing $8 \cdot 10^8 mol/l$ of readily prepared CdSe nanocrystals (diameter $d \sim 2.7nm$) dissolved in TOP was quickly injected in the flask. The shells were allowed to grow for about 6-8 minutes after the injection, after which the heating mantle was removed. The resulting nanocrystals were precipitated with methanol, washed by repeated redissolution in toluene and precipitation with the addition of methanol. At the end they were dissolved in toluene.

C.2 Leaky mode characterization

The angular and spectral dependence of leaky eigenstates localized on the PhC pattern was quantified by evaluating the diffraction efficiency of the structure. This was accomplished by using a Rigorous Coupled Wave Analysis (RCWA) technique. The reflectivity maps computed for the PhC used in this work are reported in Fig. C.1; these maps have been calculated for two different polarizations of the electric field wavevector (hereafter referred to a S and P, as defined by the vectors E_s and E_p in Fig. C.1(a)) and for the crystalline directions $\Gamma - M$ and $\Gamma - K$. The typical behavior of a PhC slab reflection is clearly visible in Fig.s C.1(b-e): narrow sharp peaks are superimposed to a smooth background. As described in the main text, Cy3 and TRITC fluorophores emitting in the spectral ranges 550nm-660nm and 540nm-620nm, respectively, have been deposited on the patterned surfaces. It can be seen that a limited influence of leaky modes on the excitation light (equal to 514 nm, in our case) is expected for incident angles higher than 40 degrees, while no interaction at all is observed in the emission spectral ranges of both Cy3 and TRITC. Moreover, being the laser focused by means of an high numerical aperture objective, which corresponds to a continuous of incident beams in an angular range of $\sim 58°$ (see inset of Fig.C.1), the diffraction efficiency in the case of our setup is more realistically described by averaging the scattered light in the interval $[0°, 58°]$.

As a consequence of these numerical and theoretical results it is possible to conclude that excitation efficiency enhancement due to leaky modes has been observed but it results to be almost two order of magnitude lower than the one reported in ref. [176].

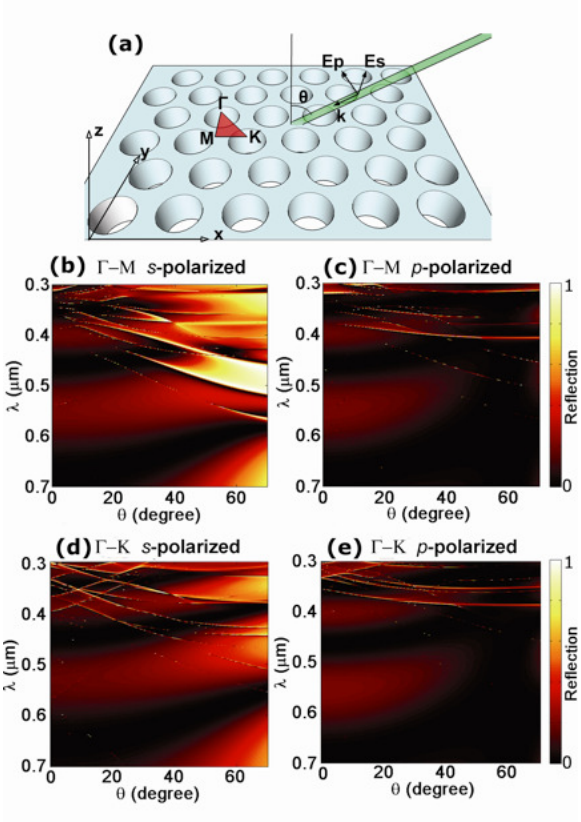

Figure C.1: Simulations of angular and spectral dependences of leaky modes in the modeled PhC pattern. **(a)**: sketch of the excitation and collection conditions of our experiment; **(b-c)**: reflectivity maps for s-and p-polarized incident light along $\Gamma - M$ direction; **(c-d)**: reflectivity maps for s- and p-polarized incident light along $\Gamma - K$ direction.

C.3 Functionalization of biomolecules on Si_3N_4 surface

Si_3N_4 surfaces containing 2D-PhC nanocavities were chemically modified by means of a solid state bioconjugation chemistry yielding primary amino-groups on the surface to link biomolecules. Before reacting with appropriate solutions, samples were thoroughly washed with acetone, isopropanol, MilliQ water for 10 min each and then cleaned for 30 min by UV/Ozone (UV-tip Cleaner, BioForce Nanosciences, Inc.). Afterwards, by reacting the surface with a freshly prepared aqueous solution of APTES (0.5%

v/v for 5 min) (Sigma–Aldrich), a layer of primary amino groups was introduced. Substrates were then abundantly rinsed with MilliQ water and stored overnight in a vacuum desiccator to evaporate physisorbed APTES aggregates. Subsequently, the amino modified layer was linked with glutaraldehyde (GTA), an homo-functional linker suitable to anchor onto the surface aminated probes, such as ssDNA or antibodies. Hence, solutions of GTA at a concentration of 2.5 % (v/v) in 100 mM phosphate buffer were incubated onto the layer and reactions were carried out at 4 °C in the dark for 2 h. Afterward, substrates were abundantly washed with MilliQ water and dried in air. GTA functionalized 2D-PhC nanocavities were then covalently linked with two class of probe biomolecules, namely aminated-ssDNA and antibodies. Specifically, the DNA probes (Thermo Fischer) (1 ?M in 1X TE buffer) were amino modified at 5' end (5' – NH2 – CGC AGG ATG GCA TGG GGG AG – 3') and spotted for 2 h onto the surface at 25 °C. After washing procedures (TE solutions at a concentration of 1X for 3 min), the hybridization experiments were carried out using complementary target DNA sequences (match: 5' – Cy3 – CTC CCC CAT GCC ATC CTG CG – 3'). DNA targets (10 μM in 1X PCR buffer) were left to hybridize with probes for 10 min at 37 °C. A single mismatch sequence (5' – Cy3 – CTC CCC CAT ACC ATC CTG CG – 3') was also tested giving a significantly lower fluorescence signal (15-20% with respect to the reference complementary sequence).

Similarly, antibody solutions (mouse monoclonal Anti-Vinculin, Clone hVIN-1, purchased from Sigma Aldrich) at the concentration of 1 μg/mL in 100 mM phosphate buffer were spotted for 1h onto the glutaraldehyde-activated substrates. The immunomodified surfaces were then thoroughly rinsed with 0.02 % of Tween20 and 1X PBS buffer, and incubated for 1h with a solution of Rhodamine (TRITC)-conjugated AffiniPure F(ab')2 Fragment Goat Anti-Mouse IgG (H+L) at a concentration of 1:200 in 1X PBS (purchased from Jackson ImmunoResearch Laboratories, INC.). Finally, substrates were abundantly washed in 1X PBS buffer and dried in air. The surface density of both probe biomolecules (i.e., ssDNA and antibodies) was assessed and optimized by

fluorescence measurements. Standard solutions of Cy3-modified ssDNA probes (ranging from 0.001 to 50 μM) and antibodies (from 1:1 to 1:2500) were spotted onto GTA functionalized 2D-PhC nanocavities. By confocal microscopy analyses (Leica, TCS-SP5 AOBS), we found out that the highest fluorescence signal was obtained with 1 μM for DNA and a dilution of 1:200 for the antibody.

Bibliography

[1] Feynman, R. *The strange theory of light and matter* (Princeton University Press, 1985). URL http://catdir.loc.gov/catdir/samples/prin031/85042685.pdf.

[2] Rossetti, R., Ellison, J., Gibson, J. & Brus, L. Size effects in the excited electronic states of small colloidal CdS crystallites. *The Journal of chemical physics* **80**, 4464 (1984). URL http://jcp.aip.org/resource/1/jcpsa6/v80/i9/p4464_s1.

[3] Ekimov, A. & Onushchenko, A. Quantum size effect in the optical spectra of semiconductor microcrystals. *Sov. Phys. Semicond* **16**, 775–778 (1982).

[4] Alivisatos, A. Perspectives on the physical chemistry of semiconductor nanocrystals. *The Journal of Physical Chemistry* **100**, 13226–13239 (1996). URL pubs.acs.org/doi/abs/10.1021/jp9535506.

[5] Alivisatos, A. Semiconductor clusters, nanocrystals, and quantum dots. *Science* **271**, 933 (1996). URL http://www.sciencemag.org/content/271/5251/933.abstract.

[6] Colvin, V., Schlamp, M. & Alivisatos, A. Light-emitting diodes made from cadmium selenide nanocrystals and a semiconducting polymer. *Nature* **370**, 354–357 (1994). URL http://www.nature.com/nature/journal/v370/n6488/pdf/370354a0.pdf.

[7] Dabbousi, B., Bawendi, M., Onitsuka, O. & Rubner, M. Electroluminescence from CdSe quantum-dot/polymer composites. *Applied Physics Letters* **66**, 1316 (1995). URL http://apl.aip.org/resource/1/applab/v66/i11/p1316_s1.

[8] Bruchez, M., Moronne, M., Gin, P., Weiss, S. & Alivisatos, A. Semiconductor nanocrystals as fluorescent biological labels. *Science* **281**, 2013 (1998). URL http://www.sciencemag.org/content/281/5385/2013.abstract.

[9] Klein, D., Roth, R., Lim, A., Alivisatos, A. & McEuen, P. A single-electron transistor made from a cadmium selenide nanocrystal. *Nature* **389**, 699 (1997). URL http://www.nature.com/nature/journal/v389/n6652/full/389699a0.html.

[10] Feldheim, D. & Keating, C. Self-assembly of single electron transistors and related devices. *Chem. Soc. Rev.* **27**, 1–12 (1998). URL http://pubs.rsc.org/en/Content/ArticleLanding/1998/CS/a827001z.

[11] Michler, P., Imamoglu, A., Mason, M. D., Carson, P. J., Strouse, G. F. & Buratto, S. K. Quantum correlation among photons from a single quantum dot at room temperature. *Nature* **406**, 968 (2000). URL http://www.nature.com/nature/journal/v406/n6799/abs/406968a0.html.

[12] Babinec, T., Hausmann, B., Khan, M., Zhang, Y., Maze, J., Hemmer, P. & Loncar, M. A diamond nanowire single-photon source. *Nature nanotechnology* **5**, 195 (2010). URL http://www.nature.com/nnano/journal/v5/n3/full/nnano.2010.6.html.

[13] Claudon, J., Bleuse, J., Malik, N., Bazin, M., Jaffrennou, P., Gregersen, N., Sauvan, C., Lalanne, P. & Gérard, J. A highly efficient single-photon source based on a quantum dot in a photonic nanowire. *Nature Photonics* **4**, 174–177 (2010). URL http://www.nature.com/nphoton/journal/v4/n3/full/nphoton.2009.287.html.

[14] Lee, K., Chen, X., Eghlidi, H., Kukura, P., Lettow, R., Renn, A., Sandoghdar, V. & Götzinger, S. A planar dielectric antenna for directional single-photon emission

and near-unity collection efficiency. *Nature Photonics* (2011). URL http://www.nature.com/nphoton/journal/v5/n3/full/nphoton.2010.312.html.

[15] Nirmal, M., Dabbousi, B., Bawendi, M., Macklin, J., Trautman, J., Harris, T. & Brus, L. Fluorescence intermittency in single cadmium selenide nanocrystals. *Nature* **383**, 802–804 (1996). URL http://www.nature.com/nature/journal/v383/n6603/abs/383802a0.html.

[16] Mahler, B., Spinicelli, P., Buil, S., Quelin, X., Hermier, J. & Dubertret, B. Towards non-blinking colloidal quantum dots. *Nature Materials* **7**, 659–664 (2008). URL http://www.nature.com/nmat/journal/vaop/ncurrent/full/nmat2222.html.

[17] Wang, X., Ren, X., Kahen, K., Hahn, M. A., Rajeswaran, M., Maccagnano-Zacher, S., Silcox, J., Cragg, G. E., Efros, A. L. & Krauss, T. D. Non-blinking semiconductor nanocrystals. *Nature* (2009). URL http://www.nature.com/nature/journal/v459/n7247/abs/nature08072.html.

[18] Joannopoulos, J. *Photonic crystals: molding the flow of light* (Princeton Univ Pr, 2008). URL http://ab-initio.mit.edu/book/photonic-crystals-book.pdf.

[19] Makarova, M., Vuckovic, J., Sanda, H. & Nishi, Y. Silicon-based photonic crystal nanocavity light emitters. *Applied physics letters* **89**, 221101–221101 (2006). URL apl.aip.org/resource/1/applab/v89/i22/p221101_s1.

[20] Shambat, G., Rivoire, K., Lu, J., Hatami, F. & Vučković, J. Tunable-wavelength second harmonic generation from GaP photonic crystal cavities coupled to fiber tapers. *Optics Express* **18**, 12176–12184 (2010). URL http://www.opticsinfobase.org/abstract.cfm?URI=oe-18-12-12176.

[21] Corcoran, B., Monat, C., Grillet, C., Moss, D., Eggleton, B., White, T., O'Faolain, L. & Krauss, T. Green light emission in silicon through slow-light

enhanced third-harmonic generation in photonic-crystal waveguides. *Nature Photonics* **3**, 206–210 (2009). URL http://www.nature.com/nphoton/journal/v3/n4/full/nphoton.2009.28.html.

[22] Amo, A., Sanvitto, D., Laussy, F., Ballarini, D., Del Valle, E., Martin, M., Lemaître, A., Bloch, J., Krizhanovskii, D., Skolnick, M. *et al.* Collective fluid dynamics of a polariton condensate in a semiconductor microcavity. *Nature* **457**, 291–295 (2009). URL http://www.nature.com/nature/journal/v457/n7227/abs/nature07640.html.

[23] Amo, A., Lefrère, J., Pigeon, S., Adrados, C., Ciuti, C., Carusotto, I., Houdré, R., Giacobino, E. & Bramati, A. Superfluidity of polaritons in semiconductor microcavities. *Nature Physics* **5**, 805–810 (2009). URL http://www.nature.com/nphys/journal/v5/n11/abs/nphys1364.html.

[24] Lagoudakis, K., Wouters, M., Richard, M., Baas, A., Carusotto, I., Andre, R., Dang, L. & Deveaud-Plédran, B. Quantized vortices in an exciton-polariton condensate. *Nature Physics* **4**, 706–710 (2008). URL http://www.nature.com/nphys/journal/v4/n9/full/nphys1051.html.

[25] Nardin, G., Grosso, G., Léger, Y., Pi?tka, B., Morier-Genoud, F. & Deveaud-Plédran, B. Hydrodynamic nucleation of quantized vortex pairs in a polariton quantum fluid. *Nature Physics, DOI: 10.1038/NPHYS1959* (2011). URL http://www.nature.com/nphys/journal/vaop/ncurrent/full/nphys1959.html#/superfluidity-and-turbulence-in-microcavities.

[26] Amo, A., Pigeon, S., Sanvitto, D., Sala, V., Hivet, R., Carusotto, I., Pisanello, F., Lemenager, G., Houdre, R., Giacobino, E. *et al.* Hydrodynamic solitons in polariton superfluids. *Science* 1167–1170 (2011). URL http://www.sciencemag.org/content/332/6034/1167.full.

[27] Deng, H., Weihs, G., Snoke, D., Bloch, J. & Yamamoto, Y. Polariton lasing vs. photon lasing in a semiconductor microcavity. *Proceedings of the National Academy of Sciences of the United States of America* **100**, 15318 (2003). URL http://www.pnas.org/content/100/26/15318.short.

[28] Bajoni, D., Senellart, P., Wertz, E., Sagnes, I., Miard, A., Lemaître, A. & Bloch, J. Polariton laser using single micropillar GaAs-GaAlAs semiconductor cavities. *Physical review letters* **100**, 47401 (2008). URL http://prl.aps.org/abstract/PRL/v100/i4/e047401.

[29] Verger, A., Ciuti, C. & Carusotto, I. Polariton quantum blockade in a photonic dot. *Physical Review B* **73**, 193306 (2006). URL http://prb.aps.org/abstract/PRB/v73/i19/e193306.

[30] Dingle, R., Wiegmann, W. & Henry, C. Quantum States of Confined Carriers in Very Thin $Al_xGa_{1-x}As - GaAs - -Al_xGa_{1-x}As$ Heterostructures. *Phys. Rev. Lett* **33**, 827–830 (1974). URL http://prl.aps.org/abstract/PRL/v33/i14/p827_1.

[31] Agranovich, V. & Dubovskii, O. Effect of retarded interaction on the exciton spectrum in one-dimensional and two-dimensional crystals. *JETP Lett* **3**, 223–226 (1966). URL http://www.jetpletters.ac.ru/ps/1618/article_24767.pdf.

[32] Andreani, L., Tassone, F. & Bassani, F. Radiative lifetime of free excitons in quantum wells. *Solid state communications* **77**, 641–645 (1991). URL http://dx.doi.org/10.1016/0038-1098(91)90761-J.

[33] Wertz, E. *Formation spontanée de condensats de polaritons dans des microcavités à base de GaAs*. Ph.D. thesis, Laboratoire de Photonique et de Nanostructures – CNRS UPR 20, Université Paris - Sud 11 (2010).

[34] Burstein, E. & Weisbuch, C. *Confined electrons and photons* (Plenum Press New York, NY, 1995).

[35] Arakawa, Y. & Sakaki, H. Multidimensional quantum well laser and temperature dependence of its threshold current. *Applied Physics Letters* **40**, 939–941 (1982). URL http://apl.aip.org/resource/1/applab/v40/i11/p939_s1.

[36] Stranski, I. N. & Von Krastanow, L. Abhandlungender Mathematisch Naturwissenschaftlichen Klasse. *Applied Physics Letters* **146**, 797 (1939).

[37] Akiyama, T., Sugawara, M. & Arakawa, Y. Quantum-dot semiconductor optical amplifiers. *Proceedings of the IEEE* **95**, 1757–1766 (2007). URL http://ieeexplore.ieee.org/xpls/abs_all.jsp?arnumber=4362699.

[38] Ledentsov, N., Bimberg, D. & Alferov, Z. Progress in epitaxial growth and performance of quantum dot and quantum wire lasers. *Journal of Lightwave Technology* **26**, 1540–1555 (2008). URL http://www.opticsinfobase.org/abstract.cfm?URI=jlt-26-11-1540.

[39] Salhi, A., Raino, G., Fortunato, L., Tasco, V., Visimberga, G., Martiradonna, L., Todaro, M., De Giorgi, M., Cingolani, R., Trampert, A. *et al.* Enhanced performances of quantum dot lasers operating at 1.3*mu* m. *Selected Topics in Quantum Electronics, IEEE Journal of* **14**, 1188–1196 (2008). URL http://ieeexplore.ieee.org/xpls/abs_all.jsp?arnumber=4582390.

[40] Murray, C., Norris, D. & Bawendi, M. Synthesis and characterization of nearly monodisperse cde (e= sulfur, selenium, tellurium) semiconductor nanocrystallites. *Journal of the American Chemical Society* **115**, 8706–8715 (1993). URL http://pubs.acs.org/doi/abs/10.1021/ja00072a025.

[41] Kako, S., Santori, C., Hoshino, K., Götzinger, S., Yamamoto, Y. & Arakawa, Y. A gallium nitride single-photon source operating at 200 K. *Nature materials* **5**, 887–892 (2006). URL http://www.nature.com/nmat/journal/v5/n11/full/nmat1763.html.

[42] Lounis, B. & Moerner, W. E. Single photons on demand from a singlemolecule at room temperature. *Nature* **407**, 291 (2000). URL http://www.nature.com/nature/journal/v407/n6803/pdf/407491a0.pdf:PDF.

[43] Efros, A., Rosen, M., Kuno, M., Nirmal, M., Norris, D. & Bawendi, M. Band-edge exciton in quantum dots of semiconductors with a degenerate valence band: Dark and bright exciton states. *Physical Review B* **54**, 4843 (1996). URL http://prb.aps.org/abstract/PRB/v54/i7/p4843_1.

[44] Reboredo, F., Franceschetti, A. & Zunger, A. Dark excitons due to direct coulomb interactions in silicon quantum dots. *Physical Review B* **61**, 13073 (2000). URL http://prb.aps.org/abstract/PRB/v61/i19/p13073_1.

[45] Qualtieri, A. *Photonic devices based on colloidal nanocrystals embedded in polymeric resist*. Ph.D. thesis, Scuola Superiore Isufi, Università del Salento, National Nanotechnology Laboratory, Lecce, Italy (2010).

[46] Empedocles, S. & Bawendi, M. Influence of spectral diffusion on the line shapes of single cdse nanocrystallite quantum dots. *The Journal of Physical Chemistry B* **103**, 1826–1830 (1999). URL http://pubs.acs.org/doi/abs/10.1021/jp983305x.

[47] Neuhauser, R., Shimizu, K., Woo, W., Empedocles, S. & Bawendi, M. Correlation between fluorescence intermittency and spectral diffusion in single semiconductor quantum dots. *Physical Review Letters* **85**, 3301–3304 (2000). URL http://link.aps.org/doi/10.1103/PhysRevLett.85.3301.

[48] Efros, A. & Rosen, M. Random telegraph signal in the photoluminescence intensity of a single quantum dot. *Physical review letters* **78**, 1110–1113 (1997). URL http://link.aps.org/doi/10.1103/PhysRevLett.78.1110.

[49] Schlegel, G., Bohnenberger, J., Potapova, I. & Mews, A. Fluorescence decay time of single semiconductor nanocrystals. *Physical review letters* **88**, 137401 (2002). URL http://link.aps.org/doi/10.1103/PhysRevLett.88.137401.

[50] Fisher, B., Eisler, H., Stott, N. & Bawendi, M. Emission intensity dependence and single-exponential behavior in single colloidal quantum dot fluorescence lifetimes. *The Journal of Physical Chemistry B* **108**, 143–148 (2004). URL http://pubs.acs.org/doi/abs/10.1021/jp035756%2B.

[51] Brokmann, X., Messin, G., Desbiolles, P., Giacobino, E., Dahan, M. & Hermier, J.-P. Colloidal cdse/zns quantum dots as single-photon sources. *New journal of physics* **6**, 99 (2004). URL http://www.iop.org/EJ/article/1367-2630/6/1/099/njp4_1_099.pdf:PDF?request-id=fa601655-14a7-4daf-8b7e-a5983559d261.

[52] Johnson, S. G. MIT open course URL http://ab-initio.mit.edu/photons.

[53] Ounsi, E. *0D Microcavity polaritons trapping light-matter quasiparticles*. Ph.D. thesis, École polytechnique fédérale de Lausanne (2007).

[54] Purcell, E., Torrey, H. & Pound, R. Resonance absorption by nuclear magnetic moments in a solid. *Physical review* **69**, 37–38 (1946). URL http://link.aps.org/doi/10.1103/PhysRev.69.37.

[55] Weisbuch, C., Nishioka, M., Ishikawa, A. & Arakawa, Y. Observation of the coupled exciton-photon mode splitting in a semiconductor quantum microcavity. *Physical review letters* **69**, 3314–3317 (1992). URL http://link.aps.org/doi/10.1103/PhysRevLett.69.3314.

[56] Andreani, L., Panzarini, G. & Gérard, J. Strong-coupling regime for quantum boxes in pillar microcavities: Theory. *Physical Review B* **60**, 13276 (1999). URL http://prb.aps.org/abstract/PRB/v60/i19/p13276_1.

[57] Gerard, J. Solid-state cavity-quantum electrodynamics with self-assembled quantum dots. *Single Quantum Dots, Topics Appl. Phys.* 269–314 (2003). URL http://www.springerlink.com/content/4nn94hfbm1gpmyxq/.

[58] Maxwell, J. C. *On physical lines of force* (Philosophical Magazine, 1861). URL http://upload.wikimedia.org/wikipedia/commons/b/b8/On_Physical_Lines_of_Force.pdf.

[59] Einstein, A. Über einen die erzeugung und verwandlung des lichtes betreffenden heuristischen gesichtspunkt. *Annalen der Physik* **17**, 132 (1905). URL http://www.physik.uni-augsburg.de/annalen/history/einstein-papers/1905_17_132-148.pdf.

[60] Gisin, N., Ribordy, G., Tittel, W. & Zbinden, H. Quantum cryptography. *Reviews of Modern Physics* **74**, 145–195 (2002). URL http://rmp.aps.org/abstract/RMP/v74/i1/p145_1.

[61] Brouri, R., Beveratos, A., Poizat, J.-P. & Grangier, P. Single photon generation by pulsed excitation of a single dipole. *Phys. Rev. A* **62**, 063817 (2000). URL http://pra.aps.org/abstract/PRA/v62/i6/e063817.

[62] Kimble, H., Dagenais, M. & Mandel, L. Photon antibunching in resonance fluorescence. *Phys. Rev. Lett.* **39**, 691–695 (1977). URL http://prl.aps.org/abstract/PRL/v39/i11/p691_1.

[63] Diedrich, F. & Walther, H. Non classical radiation from a single stored ion. *Phys. Rev. Lett.* **58**, 203–206 (1987). URL http://prl.aps.org/abstract/PRL/v58/i3/p203_1.

[64] Cohen-Tannoudji, C. & Dalibard, J. Single-atom laser spectroscopy. looking for dark periods in fluorescence light. *EPL (Europhysics Letters)* **1**, 441 (1986). URL http://iopscience.iop.org/0295-5075/1/9/004.

[65] Plenio, M. & Knight, P. The quantum-jump approach to dissipative dynamics in quantum optics. *Reviews of Modern Physics* **70**, 101 (1998). URL http://rmp.aps.org/abstract/RMP/v70/i1/p101_1.

[66] Bardou, F. *Levy statistics and laser cooling: how rare events bring atoms to rest* (Cambridge Univ Pr, 2002).

[67] Brokmann, X. *Propriétés de fluorescence de nanocristaux de CdSe individuels*. Ph.D. thesis, Laboratoire Kastler Brossel (2004). URL http://tel.archives-ouvertes.fr/tel-00007873/.

[68] Loudon, R. *The quantum theory of light* (Oxford University Press, USA, 2000). URL http://books.google.com/books?hl=en&lr=&id=AEkfajgqldoC&oi=fnd&pg=PA1&dq=the+quantum+theory+of+light&ots=JjJOUowNEo&sig=5ejP0kM0auNacOA8oYzSrARbziM.

[69] Brokmann, X., Giacobino, E., Dahan, M. & Hermier, J. Highly efficient triggered emission of single photons by colloidal CdSe/ZnS nanocrystals. *Applied Physics Letters* **85**, 712 (2004). URL http://apl.aip.org/resource/1/applab/v85/i5/p712_s1.

[70] Brown, R. & Twiss, R. Correlation between photons in two coherent beams of light. *Nature* **177**, 27–29 (1956). URL http://siba.unipv.it/fisica/articoli/N/Nature1956_177_27.pdf.

[71] Grangier, P., Roger, G., Aspect, A., Heidmann, A. & Reynaud, S. Observation of photon antibunching in phase-matched multiatom resonance fluorescence. *Physical review letters* **57**, 687–690 (1986). URL http://prl.aps.org/abstract/PRL/v57/i6/p687_1.

[72] Maiwald, R., Leibfried, D., Britton, J., Bergquist, J., Leuchs, G. & Wineland, D. Stylus ion trap for enhanced access and sensing. *Nature Physics* **5**,

551–554 (2009). URL http://www.opticsinfobase.org/abstract.cfm?URI=EQEC-2011-EA_P1.

[73] Kuhn, A., Hennrich, M. & Rempe, G. Deterministic single-photon source for distributed quantum networking. *Physical review letters* **89**, 67901 (2002). URL http://prl.aps.org/abstract/PRL/v89/i6/e067901.

[74] McKeever, J., Boca, A., Boozer, A., Miller, R., Buck, J., Kuzmich, A. & Kimble, H. Deterministic generation of single photons from one atom trapped in a cavity. *Science* **303**, 1992 (2004). URL http://www.sciencemag.org/content/303/5666/1992.abstract.

[75] Hijlkema, M., Weber, B., Specht, H., Webster, S., Kuhn, A. & Rempe, G. A single-photon server with just one atom. *Nature Physics* **3**, 253–255 (2007). URL http://www.nature.com/nphys/journal/v3/n4/abs/nphys569.html.

[76] Brunel, C., Lounis, B., Tamarat, P. & Orrit, M. Triggered source of single photons based on controlled single molecule fluorescence. *Physical Review Letters* **83**, 2722–2725 (1999). URL http://prl.aps.org/abstract/PRL/v83/i14/p2722_1.

[77] Treussart, F., Clouqueur, A., Grossman, C. & Roch, J. Photon antibunching in the fluorescence of a single dye molecule embedded in a thin polymer film. *Optics Letters* **26**, 1504–1506 (2001). URL http://www.opticsinfobase.org/abstract.cfm?&id=65327.

[78] Treussart, F., Alléaume, R., Floc'h, V. L. & Roch, J. F. Single photon emission from a single molecule. *Comptes Rendus Physique* **3**, 501–508 (2002). URL http://linkinghub.elsevier.com/retrieve/pii/S1631070502013312.

[79] Treussart, F., Alléaume, R., Le Floc'h, V., Xiao, L., Courty, J. & Roch, J. Direct measurement of the photon statistics of a triggered single photon source.

Physical review letters **89**, 93601 (2002). URL http://link.aps.org/doi/10.1103/PhysRevLett.89.093601.

[80] Brouri, R., Beveratos, A., Poizat, J. & Grangier, P. Photon antibunching in the fluorescence of individual color centers in diamond. *Optics letters* **25**, 1294–1296 (2000). URL http://www.opticsinfobase.org/abstract.cfm?id=62152.

[81] Beveratos, A., Brouri, R., Gacoin, T., Poizat, J. & Grangier, P. Nonclassical radiation from diamond nanocrystals. *Physical Review A* **64**, 061802 (2001). URL http://pra.aps.org/abstract/PRA/v64/i6/e061802.

[82] Beveratos, A., Kühn, S., Brouri, R., Gacoin, T., Poizat, J. & Grangier, P. Room temperature stable single-photon source. *The European Physical Journal D-Atomic, Molecular, Optical and Plasma Physics* **18**, 191–196 (2002). URL http://www.springerlink.com/content/ketq0lamw458ebxd/.

[83] Wu, E., Jacques, V., Zeng, H., Grangier, P., Treussart, F. & Roch, J.-F. Narrow-band single-photon emission in the near infrared for quantum key distribution. *Optics Express* **14**, 1296–1303 (2006). URL http://www.opticsinfobase.org/abstract.cfm?id=87799.

[84] Wu, E., Rabeau, J., Roger, G., Treussart, F., Zeng, H., Grangier, P., Prawer, S. & Roch, J. Room temperature triggered single-photon source in the near infrared. *New Journal of Physics* **9**, 434 (2007). URL http://iopscience.iop.org/1367-2630/9/12/434.

[85] Barth, M., Nüsse, N., Löchel, B. & Benson, O. Controlled coupling of a single-diamond nanocrystal to a photonic crystal cavity. *Optics letters* **34**, 1108–1110 (2009). URL http://www.opticsinfobase.org/abstract.cfm?URI=ol-34-7-1108.

[86] Englund, D., Shields, B., Rivoire, K., Hatami, F., Vuckovic, J., Park, H. & Lukin, M. Deterministic coupling of a single nitrogen vacancy center to a photonic crystal cavity. *Nano letters* (2010). URL pubs.acs.org/doi/abs/10.1021/nl101662v.

[87] Ampem-Lassen, E., Simpson, D., Gibson, B., Trpkovski, S., Hossain, F., Huntington, S., Ganesan, K., Hollenberg, L. & Prawer, S. Nano-manipulation of diamond-based single photon sources. *Optics Express* **17**, 11287–11293 (2009). URL http://www.opticsinfobase.org/abstract.cfm?URI=oe-17-14-11287.

[88] URL http://www.qcvictoria.com.

[89] Beveratos, A., Brouri, R., Gacoin, T., Villing, A., Poizat, J. & Grangier, P. Single photon quantum cryptography. *Physical Review Letters* **89**, 187901 (2002). URL http://prl.aps.org/abstract/PRL/v89/i18/e187901.

[90] Alléaume, R., Treussart, F., Messin, G., Dumeige, Y., Roch, J., Beveratos, A., Brouri-Tualle, R., Poizat, J. & Grangier, P. Experimental open-air quantum key distribution with a single-photon source. *New Journal of Physics* **6**, 92 (2004). URL http://iopscience.iop.org/1367-2630/6/1/092.

[91] Tribu, A., Sallen, G., Aichele, T., Andre, R., Poizat, J.-P., Bougerol, C., Tatarenko, S. & Kheng, K. A high-temperature single-photon source from nanowire quantum dots. *Nano Letters* **8**, 4326–4329 (2008). URL http://pubs.acs.org/doi/abs/10.1021/nl802160z?ai=55eampaf=Rhttp://pubs.acs.org/doi/abs/10.1021/nl802160z?ai=55eampaf=R.

[92] Englund, D., Fattal, D., Waks, E., Solomon, G., Zhang, B., Nakaoka, T., Arakawa, Y., Yamamoto, Y. & Vučković, J. Controlling the spontaneous emission rate of single quantum dots in a two-dimensional photonic crystal. *Physical review letters* **95**, 13904 (2005). URL http://link.aps.org/doi/10.1103/PhysRevLett.95.013904.

[93] Michler, P., Kiraz, A., Becher, C., Schoenfeld, W., Petroff, P., Zhang, L., Hu, E. & Imamoglu, A. A quantum dot single-photon turnstile device. *Science* **290**, 2282 (2000). URL http://www.sciencemag.org/content/290/5500/2282.short.

[94] Moreau, E., Robert, I., Gérard, J., Abram, I., Manin, L. & Thierry-Mieg, V. Single-mode solid-state single photon source based on isolated quantum dots in pillar microcavities. *Applied Physics Letters* **79**, 2865 (2001). URL http://link.aip.org/link/?APPLAB/79/2865/1.

[95] Dousse, A., Lanco, L., Suffczyński, J., Semenova, E., Miard, A., Lemaître, A., Sagnes, I., Roblin, C., Bloch, J. & Senellart, P. Controlled light-matter coupling for a single quantum dot embedded in a pillar microcavity using far-field optical lithography. *Physical Review Letters* **101**, 267404 (2008). URL http://link.aps.org/doi/10.1103/PhysRevLett.101.267404.

[96] Dousse, A., Suffczyński, J., Beveratos, A., Krebs, O., Lemaître, A., Sagnes, I., Bloch, J., Voisin, P. & Senellart, P. Ultrabright source of entangled photon pairs. *Nature* **466**, 217–220 (2010). URL http://www.nature.com/nature/journal/v466/n7303/full/nature09148.html.

[97] Faraon, A., Fushman, I., Englund, D., Stoltz, N., Petroff, P. & Vuckovic, J. Coherent generation of non-classical light on a chip via photon-induced tunnelling and blockade. *Nature physics* **4**, 859 (2008). URL http://www.nature.com/nphys/journal/v4/n11/full/nphys1078.html.

[98] Birnbaum, K., Boca, A., Miller, R., Boozer, A., Northup, T. & Kimble, H. Photon blockade in an optical cavity with one trapped atom. *Nature* **436**, 87–90 (2005). URL http://www.nature.com/nature/journal/v436/n7047/full/nature03804.html.

[99] Liew, T. & Savona, V. Single photons from coupled quantum modes. *Physical Review Letters* **104**, 183601 (2010). URL http://prl.aps.org/abstract/PRL/v104/i18/e183601.

[100] Bamba, M., Imamoğlu, A., Carusotto, I. & Ciuti, C. Origin of strong photon antibunching in weakly nonlinear photonic molecules. *Physical Review A* **83**, 021802 (2011). URL http://pra.aps.org/abstract/PRA/v83/i2/e021802.

[101] Martiradonna, L., Stomeo, T., Giorgi, M., Cingolani, R. & Vittorio, M. Nanopatterning of colloidal nanocrystals emitters dispersed in a PMMA matrix by e-beam lithography. *Microelectronic Engineering* **83**, 1478–1481 (2006). URL http://dx.doi.org/10.1016/j.mee.2006.01.134.

[102] Martiradonna, L., Carbone, L., Tandaechanurat, A., Kitamura, M., Iwamoto, S., Manna, L., Vittorio, M. D., Cingolani, R. & Arakawa, Y. Two-dimensional photonic crystal resist membrane nanocavity embedding colloidal dot-in-a-rod nanocrystals. *Nano Letters* **8**, 260–264 (2008). URL http://pubs.acs.org/doi/abs/10.1021/nl0725751.

[103] Qualtieri, A., Morello, G., Spinicelli, P., Todaro, M., Stomeo, T., Martiradonna, L., Giorgi, M., Quélin, X., Buil, S., Bramati, A. *et al.* Nonclassical emission from single colloidal nanocrystals in a microcavity: a route towards room temperature single photon sources. *New Journal of Physics* **11**, 033025 (2009). URL http://iopscience.iop.org/1367-2630/11/3/033025/.

[104] Qualtieri, A., Martiradonna, L., Stomeo, T., Todaro, M., Cingolani, R. & Vittorio, M. Multicolored devices fabricated by direct lithography of colloidal nanocrystals. *Microelectronic Engineering* **86**, 1127–1130 (2009). URL http://linkinghub.elsevier.com/retrieve/pii/S0167931708005340.

[105] Klimov, V., Mikhailovsky, A., McBranch, D., Leatherdale, C. & Bawendi, M. Quantization of multiparticle Auger rates in semiconductor quantum dots. *Sci-*

ence **287**, 1011 (2000). URL http://www.sciencemag.org/content/287/5455/1011.abstract.

[106] Spinicelli, P., Buil, S., Quélin, X., Mahler, B., Dubertret, B. & Hermier, J. Bright and grey states in cdse-cds nanocrystals exhibiting strongly reduced blinking. *Physical review letters* **102**, 136801 (2009). URL http://prl.aps.org/abstract/PRL/v102/i13/e136801.

[107] Park, Y., Malko, A., Vela, J., Chen, Y., Ghosh, Y., García-Santamaría, F., Hollingsworth, J., Klimov, V. & Htoon, H. Near-unity quantum yields of biexciton emission from cdse= cds nanocrystals measured using single-particle spectroscopy. *Physical Review Letters* **106**, 187401 (2011). URL http://link.aps.org/doi/10.1103/PhysRevLett.106.187401.

[108] Pisanello, F., Qualtieri, A., Stomeo, T., andRoberto Cingolani, L. M., Bramati, A., & Vittorio, M. D. High-purcell-factor dipolelike modes at visible wavelengths in h1 photonic crystal cavity. *Optic Letters* **35**, 1509–1511 (2010). URL http://www.opticsinfobase.org/ol/abstract.cfm?URI=ol-35-10-1509.

[109] Nair, G., Zhao, J. & Bawendi, M. Biexciton quantum yield of single semiconductor nanocrystals from photon statistics. *Nano letters* **11**, 1136–1140 (2011). URL http://pubs.acs.org/doi/abs/10.1021/nl104054t.

[110] Poitras, C., Lipson, M., Du, H., Hahn, M. & Krauss, T. Photoluminescence enhancement of colloidal quantum dots embedded in a monolithic microcavity. *Applied physics letters* **82**, 4032 (2003). URL http://link.aip.org/link/?APPLAB/82/4032/1.

[111] Martiradonna, L., Carbone, L., De Giorgi, M., Manna, L., Gigli, G., Cingolani, R. & De Vittorio, M. High q-factor colloidal nanocrystal-based vertical microcavity by hot embossing technology. *Applied physics letters* **88**, 181108 (2006). URL http://link.aip.org/link/?APPLAB/88/181108/1.

[112] Kahl, M., Thomay, T., Kohnle, V., Beha, K., Merlein, J., Hagner, M., Halm, A., Ziegler, J., Nann, T., Fedutik, Y. *et al.* Colloidal quantum dots in all-dielectric high-q pillar microcavities. *Nano letters* **7**, 2897–2900 (2007). URL http://pubs.acs.org/doi/abs/10.1021/nl071812x.

[113] Artemyev, M., Woggon, U., Wannemacher, R., Jaschinski, H. & Langbein, W. Light trapped in a photonic dot: Microspheres act as a cavity for quantum dot emission. *Nano Letters* **1**, 309–314 (2001). URL http://pubs.acs.org/doi/abs/10.1021/nl0155451.

[114] Le Thomas, N., Woggon, U., Schöps, O., Artemyev, M., Kazes, M. & Banin, U. Cavity QED with semiconductor nanocrystals. *Nano letters* **6**, 557–561 (2006). URL http://link.aps.org/doi/10.1103/PhysRevLett.99.136802.

[115] Qualtieri, A., Morello, G., Spinicelli, P., Todaro, M., Stomeo, T., Martiradonna, L., De Giorni, M., Quélin, X., Buil, S., Bramati, A. *et al.* Room temperature single-photon sources based on single colloidal nanocrystals in microcavities. *Superlattices and Microstructures* **47**, 187–191 (2010). URL http://linkinghub.elsevier.com/retrieve/pii/S0749603609001074.

[116] Yokoyama, H. Physics and device applications of optical microcavities. *Science* **256**, 66 (1992). URL http://www.sciencemag.org/content/256/5053/66.short.

[117] Efros, A. Luminescence polarization of CdSe microcrystals. *Physical Review B* **46**, 7448–7458 (1992). URL http://prb.aps.org/abstract/PRB/v46/i12/p7448_1.

[118] Empedocles, S., Neuhauser, R. & Bawendi, M. Three-dimensional orientation measurements of symmetric single chromophores using polarization microscopy. *Nature* **399**, 126–130 (1999). URL http://www.nature.com/nature/journal/v399/n6732/abs/399126a0.html.

[119] Peng, X., Manna, L., Yang, W., Wickham, J., Scher, E., Kadavanich, A. & Alivisatos, A. Shape control of CdSe nanocrystals. *Nature* **404**, 59–61 (2000). URL http://www.nature.com/nature/journal/v404/n6773/abs/404059a0.html.

[120] Chen, X., Nazzal, A., Goorskey, D., Xiao, M., Peng, Z. A. & Peng, X. Polarization spectroscopy of single cdse quantum rods. *Physical Review B* **64**, 2453041–2453044 (2001). URL http://prb.aps.org/abstract/PRB/v64/i24/e245304.

[121] Hu, J., Li, L.-S., Yang, W., Manna, L., Wang, L.-W. & Alivisatos, A. P. Linearly polarized emission from colloidal semiconductor quantum rods. *Science* **292**, 2060 (2001). URL http://www.sciencemag.org/content/292/5524/2060.abstract.

[122] Mokari, T. & Banin, U. Synthesis and properties of CdSe/ZnS core/shell nanorods. *Chem. Mater* **15**, 3955–3960 (2003). URL http://pubs.acs.org/doi/abs/10.1021/cm034173%2B.

[123] Manna, L., Milliron, D., Meisel, A., Scher, E. & Alivisatos, A. Controlled growth of tetrapod-branched inorganic nanocrystals. *Nature materials* **2**, 382–385 (2003). URL http://www.nature.com/nmat/journal/v2/n6/abs/nmat902.html.

[124] Talapin, D., Koeppe, R., Götzinger, S., Kornowski, A., Lupton, J., Rogach, A., Benson, O., Feldmann, J. & Weller, H. Highly emissive colloidal CdSe/CdS heterostructures of mixed dimensionality. *Nano Lett.* **3**, 1677–1681 (2003). URL http://pubs.acs.org/doi/abs/10.1021/nl034815s.

[125] Talapin, D., Nelson, J., Shevchenko, E., Aloni, S., Sadtler, B. & Alivisatos, A. Seeded growth of highly luminescent CdSe/CdS nanoheterostructures with rod and tetrapod morphologies. *Nano Lett.* **7**, 2951–2959 (2007). URL http://pubs.acs.org/doi/abs/10.1021/nl072003g.

[126] Sitt, A., Salant, A., Menagen, G. & Banin, U. Highly emissive nano rod-in-rod heterostructures with strong linear polarization. *Nano Letters* **11**, 2054–2060 (2011). URL http://pubs.acs.org/doi/abs/10.1021/nl200519b.

[127] Carbone, L., Nobile, C., Giorgi, M. D., Sala, F. D., Morello, G., Pompa, P., Hytch, M., Snoeck, E., Fiore, A., Franchini, I. R., Nadasan, M., Silvestre, A. F., Chiodo, L., Kudera, S., Cingolani, R., Krahne, R. & Manna, L. Synthesis and micrometer-scale assembly of colloidal cdse/cds nanorods prepared by a seeded growth approach. *Nano Letters* **7**, 2942–2950 (2007). URL http://pubs.acs.org/doi/pdf/10.1021/nl0717661.

[128] Morello, G., Sala, F. D., Manna, L. C. L., Maruccio, G., Cingolani, R. & Giorgi, M. D. Intrinsic optical nonlinearity in colloidal seeded grown cdse/cds nanostructures: Photoinduced screening of the internal electric field. *Physical Review B* **78**, 195313 (2008). URL http://link.aip.org/getpdf/servlet/GetPDFServlet?filetype=pdf&id=PRBMDO000078000019195313000001.

[129] Deka, S., Quarta, A., Lupo, M., Falqui, A., Boninelli, S., Giannini, C., Morello, G., De Giorgi, M., Lanzani, G., Spinella, C. *et al.* CdSe/CdS/ZnS double shell nanorods with high photoluminescence efficiency and their exploitation as biolabeling probes. *Journal of the American Chemical Society* **131**, 2948–2958 (2009). URL http://pubs.acs.org/doi/abs/10.1021/ja808369e.

[130] Hewa-Kasakarage, N. N., Kirsanova, M., Nemchinov, A., Schmall, N., El-Khoury, P. Z., Tarnovsky, A. N. & Zamkov, M. Radiative recombination of spatially extended excitons in (znse/cds)/cds heterostructured nanorods. *J. Am. Chem. Soc.* **131**, 1328–1334 (2009).

[131] Muller, J., Lupton, J. M., Lagoudakis, P. G., Schindler, F., Koeppe, R., Rogach, A. L., Feldmann, J., Talapin, D. V. & Weller, H. Wave function engineering in elongated semiconductor nanocrystals with heterogeneous carrier confinement.

Nano Letters **5**, 2044–2049 (2005). URL http://pubs.acs.org/doi/abs/10.1021/nl051596x.

[132] Muller, J., Lupton, J., Rogach, A., Feldmann, J., Talapin, D. & Weller, H. Monitoring surface charge migration in the spectral dynamics of single CdSe/CdS nanodot/nanorod heterostructures. *Physical Review B* **72**, 205339 (2005). URL http://prb.aps.org/abstract/PRB/v72/i20/e205339.

[133] Steiner, D., Dorfs, D., Banin, U., Sala, F. D., Manna, L. & Millo, O. Determination of band offsets in heterostructured colloidal nanorods using scanning tunneling spectroscopy. *Nano Letters* **8**, 2954–2958 (2008). URL http://pubs.acs.org/doi/abs/10.1021/nl801848x.

[134] Lupo, M. G., Sala, F. D., Carbone, L., Zavelani-Rossi, M., Fiore, A., Luer, L., Polli, D., Cingolani, R., Manna, L. & Lanzani, G. Ultrafast electron-hole dynamics in core/shell cdse/cds dot/rod nanocrystals. *Nano Letters* **8**, 4582–4587 (2008). URL http://pubs.acs.org/doi/pdf/10.1021/nl8028366.

[135] Sitt, A., Sala, F. D., Menagen, G. & Banin, U. Multiexciton engineering in seeded core/shell nanorods: Transfer from type-i to quasi-type-ii regimes. *Nano Letters* **9**, 3470 (2009). URL http://pubs.acs.org/doi/abs/10.1021/nl901679q.

[136] Zavelani-Rossi, M., Lupo, M., Tassone, F., Manna, L. & Lanzani, G. Suppression of Biexciton Auger Recombination in CdSe/CdS Dot/Rods: Role of the Electronic Structure in the Carrier Dynamics. *Nano letters* 59–61 (2010). URL http://pubs.acs.org/doi/abs/10.1021/nl101930z.

[137] Nethercot Jr, A. Prediction of Fermi energies and photoelectric thresholds based on electronegativity concepts. *Physical Review Letters* **33**, 1088–1091 (1974). URL http://prl.aps.org/abstract/PRL/v33/i18/p1088_1.

[138] Trager-Cowan, C., Parbrook, P., Henderson, B. & O'Donnell, K. Band alignments in Zn (Cd) S (Se) strained layer superlattices. *Semiconductor Science and Technology* **7**, 536 (1992). URL http://iopscience.iop.org/0268-1242/7/4/016.

[139] O'Donnell, K., Parbrook, P., Yang, F., Chen, X., Irvine, D., Trager-Cowan, C., Henderson, P. *et al.* The optical properties of wide bandgap binary II-VI superlattices. *Journal of Crystal Growth* **117**, 497–500 (1992). URL http://linkinghub.elsevier.com/retrieve/pii/002202489290800X.

[140] Kuno, M., Fromm, D., Hamann, H., Gallagher, A. & Nesbitt, D. Nonexponential "blinking" kinetics of single cdse quantum dots: A universal power law behavior. *The journal of chemical physics* **112**, 3117 (2000). URL http://link.aip.org/link/?jcp/112/3117.

[141] Verberk, R., van Oijen, A. & Orrit, M. Simple model for the power-law blinking of single semiconductor nanocrystals. *Physical Review B* **66**, 233202 (2002). URL http://prb.aps.org/abstract/PRB/v66/i23/e233202.

[142] Rainò, G., Stöferle, T., Moreels, I., Gomes, R., Kamal, J., Hens, Z. & Mahrt, R. Probing the Wave Function Delocalization in CdSe/CdS Dot-in-Rod Nanocrystals by Time-and Temperature-Resolved Spectroscopy. *ACS nano, DOI: 10.1021/nn2005969* URL http://pubs.acs.org/doi/abs/10.1021/nn2005969.

[143] Pisanello, F., Martiradonna, L., Leménager, G., Spinicelli, P., Fiore, A., Manna, L., Hermier, J., Cingolani, R., Giacobino, E., De Vittorio, M. *et al.* Room temperature-dipolelike single photon source with a colloidal dot-in-rod. *Applied Physics Letters* **96**, 033101 (2010). URL http://link.aip.org/link/?APPLAB/96/033101/1.

[144] Tanabe, T., Notomi, M., Mitsugi, S., Shinya, A. & Kuramochi, E. All-optical switches on a silicon chip realized using photonic crystal nanocavities. *Ap-*

plied Physics Letters **87**, 151112–151112 (2005). URL http://apl.aip.org/resource/1/applab/v87/i15/p151112_s1.

[145] Stomeo, T., Van Laere, F., Ayre, M., Cambournac, C., Benisty, H., Van Thourhout, D., Baets, R. & Krauss, T. Integration of grating couplers with a compact photonic crystal demultiplexer on an inp membrane. *Optics letters* **33**, 884–886 (2008). URL http://www.opticsinfobase.org/abstract.cfm?id=157233.

[146] Van Laere, F., Stomeo, T., Cambournac, C., Ayre, M., Brenot, R., Benisty, H., Roelkens, G., Krauss, T., Van Thourhout, D. & Baets, R. Nanophotonic polarization diversity demultiplexer chip. *Lightwave Technology, Journal of* **27**, 417–425 (2009). URL http://ieeexplore.ieee.org/xpl/freeabs_all.jsp?arnumber=4785438.

[147] Stomeo, T., Grande, M., Rainò, G., Passaseo, A., D'Orazio, A., Cingolani, R., Locatelli, A., Modotto, D., De Angelis, C. & De Vittorio, M. Optical filter based on two coupled phc gaas-membranes. *Optics letters* **35**, 411–413 (2010). URL http://www.opticsinfobase.org/abstract.cfm?URI=ol-35-3-411.

[148] Choi, Y., Hennessy, K., Sharma, R., Haberer, E., Gao, Y., DenBaars, S., Nakamura, S., Hu, E. & Meier, C. Gan blue photonic crystal membrane nanocavities. *Applied Physics Letters* **87**, 243101 (2005). URL http://apl.aip.org/resource/1/applab/v87/i24/p243101_s1.

[149] Rivoire, K., Faraon, A. & Vuckovic, J. Gallium phosphide photonic crystal nanocavities in the visible. *Applied Physics Letters* **93**, 063103 (2008). URL http://apl.aip.org/resource/1/applab/v93/i6/p063103_s1.

[150] Gong, Y. & Vučković, J. Photonic crystal cavities in silicon dioxide. *Applied Physics Letters* **96**, 031107 (2010). URL http://apl.aip.org/resource/1/applab/v96/i3/p031107_s1.

[151] Yoon, D., Yoon, S. & Kim, Y. Refractive index and etched structure of silicon nitride waveguides fabricated by pecvd. *Thin Solid Films* **515**, 5004–5007 (2007). URL http://dx.doi.org/10.1016/j.tsf.2006.10.059.

[152] Mui, D., Liaw, H., Demirel, A., Strite, S. & Morkoc, H. Electrical characteristics of si3n4/si/gaas metal-insulator-semiconductor capacitor. *Applied physics letters* **59**, 2847–2849 (1991). URL http://apl.aip.org/resource/1/applab/v59/i22/p2847_s1.

[153] Chen, A., Young, M., Li, W., Ma, T. & Woodall, J. Metal-insulator-semiconductor structure on low-temperature grown gaas. *Applied physics letters* **89**, 233514 (2006). URL http://link.aip.org/link/?APPLAB/89/233514/1.

[154] Gao, H., Luginbuhl, R. & Sigrist, H. Bioengineering of silicon nitride. *Sensors and Actuators B: Chemical* **38**, 38–41 (1997). URL http://linkinghub.elsevier.com/retrieve/pii/S0925400596021259.

[155] Diao, J., Ren, D., Engstrom, J. & Lee, K. A surface modification strategy on silicon nitride for developing biosensors. *Analytical biochemistry* **343**, 322–328 (2005). URL http://linkinghub.elsevier.com/retrieve/pii/S0003269705003714.

[156] Dauphas, S., Ababou-Girard, S., Girard, A., Le Bihan, F., Mohammed-Brahim, T., Vié, V., Corlu, A., Guguen-Guillouzo, C., Lavastre, O. & Geneste, F. Stepwise functionalization of sinx surfaces for covalent immobilization of antibodies. *Thin Solid Films* **517**, 6016–6022 (2009). URL http://linkinghub.elsevier.com/retrieve/pii/S0040609009009328.

[157] Barth, M., Kouba, J., Stingl, J., Löchel, B. & Benson, O. Modification of visible spontaneous emission with silicon nitride photonic crystal nanocavities. *Optics Express* **15**, 17231–17240 (2007). URL http://www.opticsinfobase.org/abstract.cfm?id=148387.

[158] Barth, M., Nüsse, N., Stingl, J., Löchel, B. & Benson, O. Emission properties of high-q silicon nitride photonic crystal heterostructure cavities. *Applied Physics Letters* **93**, 021112 (2008). URL http://link.aip.org/link/?APPLAB/93/021112/1.

[159] Eichenfield, M., Camacho, R., Chan, J., Vahala, K. & Painter, O. A picogram- and nanometre-scale photonic-crystal optomechanical cavity. *Nature* **459**, 550–555 (2009). URL http://www.nature.com/nature/journal/vaop/ncurrent/abs/nature08061.html.

[160] Gong, Y., Makarova, M., Yerci, S., Li, R., Stevens, M., Baek, B., Nam, S., Dal Negro, L. & Vuckovic, J. Observation of transparency of erbium-doped silicon nitride in photonic crystal nanobeam cavities. *Optics Express* **18**, 13863–13873 (2010). URL http://www.opticsinfobase.org/abstract.cfm?id=202239.

[161] Khan, M., Babinec, T., McCutcheon, M., Deotare, P. & Lončar, M. Fabrication and characterization of high-quality-factor silicon nitride nanobeam cavities. *Optics letters* **36**, 421–423 (2011). URL http://www.opticsinfobase.org/abstract.cfm?URI=ol-36-3-421.

[162] Kitamura, M., Iwamoto, S. & Arakawa, Y. Enhanced light emission from an organic photonic crystal with a nanocavity. *Applied Physics Letters* **87**, 151119 (2005). URL http://link.aip.org/link/?APPLAB/87/151119/1.

[163] Bennett, C., Brassard, G. *et al.* Quantum cryptography: Public key distribution and coin tossing. In *Proceedings of IEEE International Conference on Computers, Systems and Signal Processing*, vol. 175 (Bangalore, India, 1984). URL http://dm.ing.unibs.it/giuzzi/corsi/2010-11/Brescia/Algebra_Codici_Crittografia/papers/bennettc198469790513.pdf.

[164] Yee, K. Numerical solution of initial boundary value problems involving maxwell's equations in isotropic media. *Antennas and Propagation, IEEE Trans-*

actions on **14**, 302–307 (1966). URL http://ecee.colorado.edu/~mcleod/teaching/nmip/references/Numerical%20Solution%20of%20Initial%20Value%20Problems%20of%20Maxwells%20Equations%20Yee%201966.pdf.

[165] Tandaechanurat, A., Iwamoto, S., Nomura, M., Kumagai, N. & Arakawa, Y. Increase of q-factor in photonic crystal h1-defect nanocavities after closing of photonic bandgap with optimal slab thickness. *Optics Express* **16**, 448–455 (2008). URL http://www.opticsinfobase.org/abstract.cfm?id=148707.

[166] Larqué, M., Karle, T., Robert-Philip, I. & Beveratos, A. Optimizing h1 cavities for the generation of entangled photon pairs. *New Journal of Physics* **11**, 033022 (2009). URL http://iopscience.iop.org/1367-2630/11/3/033022.

[167] Martiradonna, L., Pisanello, F., Stomeo, T., Qualtieri, A., Vecchio, G., Sabella, S., Cingolani, R., De Vittorio, M. & Pompa, P. Spectral tagging by integrated photonic crystal resonators for highly sensitive and parallel detection in biochips. *Applied Physics Letters* **96**, 113702 (2010). URL http://link.aip.org/link/?APPLAB/96/113702/1.

[168] Painter, O., Srinivasan, K., O'Brien, J., Scherer, A. & Dapkus, P. Tailoring of the resonant mode properties of optical nanocavities in two-dimensional photonic crystal slab waveguides. *Journal of Optics A: Pure and Applied Optics* **3**, S161 (2001). URL http://iopscience.iop.org/1464-4258/3/6/367.

[169] Frédérick, S., Dalacu, D., Aers, G., Poole, P., Lapointe, J. & Williams, R. Optical characterisation of inas/inp quantum dot photonic cavity membranes. *Physica E: Low-dimensional Systems and Nanostructures* **32**, 504–507 (2006). URL http://linkinghub.elsevier.com/retrieve/pii/S1386947705005898.

[170] Hennessy, K., Högerle, C., Hu, E., Badolato, A. & Imamoğlu, A. Tuning photonic nanocavities by atomic force microscope nano-oxidation. *Applied physics letters* **89**, 041118 (2006). URL http://link.aip.org/link/?APPLAB/89/041118/1.

[171] Akahane, Y., Asano, T., Song, B. & Noda, S. Fine-tuned high-q photonic-crystal nanocavity. *Optics Express* **13**, 1202–1214 (2005). URL http://www.opticsinfobase.org/abstract.cfm?&id=82669.

[172] Srinivasan, K. & Painter, O. Momentum space design of high-q photonic crystal optical cavities. *Optics Express* **10**, 670–684 (2002). URL http://authors.library.caltech.edu/276/.

[173] Vuckovic, J., Loncar, M., Mabuchi, H. & Scherer, A. Optimization of the q factor in photonic crystal microcavities. *Quantum Electronics, IEEE Journal of* **38**, 850–856 (2002). URL http://ieeexplore.ieee.org/xpls/abs_all.jsp?arnumber=1017597.

[174] Rico-Garcia, J., Lopez-Alonso, J. & Alda, J. Multivariate analysis of photonic crystal microcavities with fabrication defects. In *Proceedings of SPIE*, vol. 5840, 562 (2005). URL http://link.aip.org/link/?PSISDG/5840/562/1.

[175] Adawi, A. & Lidzey, D. A design for an optical-nanocavity optimized for use with surface-bound light-emitting materials. *New Journal of Physics* **10**, 065011 (2008). URL http://iopscience.iop.org/1367-2630/10/6/065011.

[176] Ganesh, N., Zhang, W., Mathias, P., Chow, E., Soares, J., Malyarchuk, V., Smith, A. & Cunningham, B. Enhanced fluorescence emission from quantum dots on a photonic crystal surface. *Nature Nanotechnology* **2**, 515–520 (2007). URL http://www.nature.com/nnano/journal/vaop/ncurrent/full/nnano.2007.216.html.

[177] Skivesen, N., Tŕtu, A., Kristensen, M., Kjems, J. *et al.* Photonic-crystal waveguide biosensor. *Optics Express* **15**, 3169–3176 (2007). URL http://www.opticsinfobase.org/abstract.cfm?URI=oe-15-6-3169.

[178] Li, M., He, F., Liao, Q., Liu, J., Xu, L., Jiang, L., Song, Y., Wang, S. & Zhu, D. Ultrasensitive dna detection using photonic crystals. *Angewandte*

Chemie **120**, 7368–7372 (2008). URL http://onlinelibrary.wiley.com/doi/10.1002/ange.200801998/full.

[179] Fan, J., Chee, M. & Gunderson, K. Highly parallel genomic assays. *Nature Reviews Genetics* **7**, 632–644 (2006). URL http://www.nature.com/nrg/journal/vaop/ncurrent/full/nrg1901.html.

[180] Schena, M., Shalon, D., Davis, R. & Brown, P. Quantitative monitoring of gene expression patterns with a complementary dna microarray. *Science* **270**, 467 (1995). URL http://www.sciencemag.org/content/270/5235/467.short.

[181] Spurgeon, S., Jones, R. & Ramakrishnan, R. High throughput gene expression measurement with real time pcr in a microfluidic dynamic array. *PLoS One* **3**, e1662 (2008). URL http://dx.plos.org/10.1371/journal.pone.0001662.

[182] Noda, S., Fujita, M. & Asano, T. Spontaneous-emission control by photonic crystals and nanocavities. *Nature photonics* **1**, 449–458 (2007). URL http://www.nature.com/nphoton/journal/v1/n8/abs/nphoton.2007.141.html.

[183] Painter, O., Lee, R., Scherer, A., Yariv, A., O'brien, J., Dapkus, P. & Kim, I. Two-dimensional photonic band-gap defect mode laser. *Science* **284**, 1819 (1999). URL http://www.sciencemag.org/content/284/5421/1819.short.

[184] Pisanello, F., De Vittorio, M. & Cingolani, R. Modal selective tuning in a photonic crystal cavity. *Superlattices and Microstructures* **47**, 34–38 (2010). URL http://linkinghub.elsevier.com/retrieve/pii/S0749603609001141.

[185] Fan, S. & Joannopoulos, J. Analysis of guided resonances in photonic crystal slabs. *Physical Review B* **65**, 235112 (2002). URL http://prb.aps.org/abstract/PRB/v65/i23/e235112.

[186] Crozier, K., Lousse, V., Kilic, O., Kim, S., Fan, S. & Solgaard, O. Air-bridged photonic crystal slabs at visible and near-infrared wavelengths. *Physical Re-*

view B **73**, 115126 (2006). URL http://prb.aps.org/abstract/PRB/v73/i11/e115126.

[187] Yoshie, T., Scherer, A., Hendrickson, J., Khitrova, G., Gibbs, H., Rupper, G., Ell, C., Shchekin, O. & Deppe, D. Vacuum Rabi splitting with a single quantum dot in a photonic crystal nanocavity. *Nature* **432**, 200–203 (2004). URL http://www.nature.com/nature/journal/v432/n7014/abs/nature03119.html.

[188] Reithmaier, J., Sek, G., Loffler, A., Hofmann, C., Kuhn, S., Reitzenstein, S., Keldysh, L., Kulakovskii, V., Reinecke, T. & Forchel, A. Strong coupling in a single quantum dot-semiconductor microcavity system. *Nature* **432**, 197–200 (2004). URL http://www.nature.com/nature/journal/vaop/ncurrent/abs/nature02969.html.

[189] Peter, E., Senellart, P., Martrou, D., Lemaître, A., Hours, J., Gérard, J. & Bloch, J. Exciton-photon strong-coupling regime for a single quantum dot embedded in a microcavity. *Physical Review Letters* **95**, 67401 (2005). URL http://link.aps.org/doi/10.1103/PhysRevLett.95.067401.

[190] Hennessy, K., Badolato, A., Winger, M., Gerace, D., Atatüre, M., Gulde, S., Fält, S., Hu, E., Imamo&gbreve, A. *et al.* Quantum nature of a strongly coupled single quantum dot–cavity system. *Nature* **445**, 896–899 (2007). URL http://www.nature.com/nature/journal/vaop/ncurrent/full/nature05586.html.

[191] Leistikow, M., Johansen, J., Kettelarij, A., Lodahl, P. & Vos, W. Size-dependent oscillator strength and quantum efficiency of cdse quantum dots controlled via the local density of states. *Physical Review B* **79**, 045301 (2009). URL http://link.aps.org/doi/10.1103/PhysRevLett.103.045301.

[192] Laussy, F., Del Valle, E. & Tejedor, C. Luminescence spectra of quantum dots in microcavities. i. bosons. *Physical Review B* **79**, 235325 (2009). URL http://prb.aps.org/abstract/PRB/v79/i23/e235325.

[193] Deng, H., Weihs, G., Santori, C., Bloch, J. & Yamamoto, Y. Condensation of semiconductor microcavity exciton polaritons. *Science* **298**, 199 (2002). URL http://www.sciencemag.org/content/298/5591/199.short.

[194] Kasprzak, J., Richard, M., Kundermann, S., Baas, A., Jeambrun, P., Keeling, J., Marchetti, F., Szyma&nacute, M., Andre, R., Staehli, J. *et al.* Bose–Einstein condensation of exciton polaritons. *Nature* **443**, 409–414 (2006). URL http://www.nature.com/nature/journal/v443/n7110/abs/nature05131.html.

[195] Dirk Englund, A., Ilya Fushman, N., Pierre Petroff, J. *et al.* Controlling cavity reflectivity with a single quantum dot. *Nature* **450**, 857–861 (2007). URL http://www.nature.com/nature/journal/v450/n7171/abs/nature06234.html.

[196] Göppert-Mayer, M. Über elementarakte mit zwei quantensprüngen. *Annalen der Physik* **401**, 273–294 (1931). URL http://onlinelibrary.wiley.com/doi/10.1002/andp.19314010303/abstract.

[197] Kaiser, W. & Garrett, C. Two-Photon Excitation in CaF_ {2}: Euˆ{2+}. *Physical Review Letters* **7**, 229–231 (1961). URL http://prl.aps.org/abstract/PRL/v7/i6/p229_1.

[198] Terenziani, F., Katan, C., Badaeva, E., Tretiak, S. & Blanchard-Desce, M. Enhanced Two-Photon Absorption of Organic Chromophores: Theoretical and Experimental Assessments. *Advanced Materials* **20**, 4641–4678 (2008). URL http://onlinelibrary.wiley.com/doi/10.1002/adma.200800402/abstract.

[199] Denk, W., Strickler, J. & Webb, W. Two-photon laser scanning fluorescence microscopy. *Science* **248**, 73 (1990). URL http://www.sciencemag.org/content/248/4951/73.short.

[200] Gaus, K., Gratton, E., Kable, E., Jones, A., Gelissen, I., Kritharides, L. & Jessup, W. Visualizing lipid structure and raft domains in living cells with two-photon

microscopy. *Proceedings of the National Academy of Sciences of the United States of America* **100**, 15554 (2003). URL http://www.pnas.org/content/100/26/15554.short.

[201] Helmchen, F. & Denk, W. Deep tissue two-photon microscopy. *Nature methods* **2**, 932–940 (2005). URL http://www.nature.com/nmeth/journal/v2/n12/abs/nmeth818.html.

[202] Bajoni, D., Peter, E., Senellart, P., Smirr, J., Sagnes, I., Lemaître, A. & Bloch, J. Polariton parametric luminescence in a single micropillar. *Applied physics letters* **90**, 051107 (2007). URL http://link.aip.org/link/?APPLAB/90/051107/1.

[203] El Daïf, O., Baas, A., Guillet, T., Brantut, J., Kaitouni, R., Staehli, J., Morier-Genoud, F. & Deveaud, B. Polariton quantum boxes in semiconductor microcavities. *Applied Physics Letters* **88**, 061105 (2006). URL http://apl.aip.org/resource/1/applab/v88/i6/p061105_s1.

[204] Gérard, J., Barrier, D., Marzin, J., Kuszelewicz, R., Manin, L., Costard, E., Thierry-Mieg, V. & Rivera, T. Quantum boxes as active probes for photonic microstructures: The pillar microcavity case. *Applied physics letters* **69**, 449 (1996). URL http://apl.aip.org/resource/1/applab/v69/i4/p449_s1.

[205] Kavokin, K., Kaliteevski, M., Abram, R., Kavokin, A., Sharkova, S. & Shelykh, I. Stimulated emission of terahertz radiation by exciton-polariton lasers. *Applied Physics Letters* **97**, 201111–201111 (2010). URL http://apl.aip.org/resource/1/applab/v97/i20/p201111_s1.

[206] Paraïso, T., Sarchi, D., Nardin, G., Cerna, R., Leger, Y., Pietka, B., Richard, M., El Daïf, O., Morier-Genoud, F., Savona, V. *et al.* Enhancement of microcavity polariton relaxation under confinement. *Physical Review B* **79**, 045319 (2009). URL http://prb.aps.org/abstract/PRB/v79/i4/e045319.

[207] Dasbach, G., Schwab, M., Bayer, M. & Forchel, A. Parametric polariton scattering in microresonators with three-dimensional optical confinement. *Physical Review B* **64**, 201309 (2001). URL http://prb.aps.org/abstract/PRB/v64/i20/e201309.

[208] Maragkou, M., Grundy, A., Wertz, E., Lemaitre, A., Sagnes, I., Senellart, P., Bloch, J. & Lagoudakis, P. Spontaneous nonground state polariton condensation in pillar microcavities. *Physical review B. Condensed matter and materials physics* **81** (2010). URL http://prb.aps.org/abstract/PRB/v81/i8/e081307.